

Optics and Cryogenics for the 1.1 THz Heterodyne Array Receiver for the APEX Telescope

Inaugural-Dissertation
zur
Erlangung des Doktorgrades
der Mathematisch-Naturwissenschaftlichen Fakultät
der Universität zu Köln



vorgelegt von

Norma Hurtado

aus Antofagasta, Chile

Köln 2015

Berichterstatter: Prof. Dr. Jürgen Stutzki
(Gutachter) Prof. Dr. Jan Jolie

Tag der mündlichen Prüfung: 23 June 2015

Abstract

This thesis is about the development of the optics and the cryogenics for the 1.1 THz Heterodyne Array Receiver to be mounted in the Nasmyth A cabin of the Atacama Pathfinder Experiment (APEX) telescope.

The THz range is a still largely unexplored area in astrophysics because of the technological challenge for the receiver and telescope as well as the difficult atmospheric conditions.

The APEX telescope, a modified Atacama Large Millimeter Array (ALMA) prototype antenna, with its 12 m dish is the largest submillimeter single-dish telescope in the world for THz frequencies, allowing a spatial resolution of few arcseconds, due to its location on the Chajnantor plateau, at 5100 m altitude in the Chilean Andes, and its surface accuracy of 17 μm r.m.s.

Observations in the 1.1 THz atmospheric window (1000 - 1080 GHz) from the ground have difficulties, but are still possible and productively usable if done with APEX. These difficulties, in addition to the fact that single pixel sensitivity is constrained by the quantum limit, make even more important the development of array receivers in this frequency band.

Several important molecular transitions are located in this frequency range, observing them with high spectral resolution ($> 10^6$) will improve our understanding of the chemical and physical conditions in hot cores in the galactic Interstellar Medium (ISM) and, especially, in starburst galaxies and active galactic nuclei of external galaxies. The CO 9-8 line at 1036.9 GHz is a tracer for the warm and dense gas. OH⁺ at 1033 GHz and NH⁺ at 1012.6 GHz are important for the study of chemical networks in the ISM. These observations will contribute decisively to answer questions such as “How do galaxies form and evolve?” and “How do stars form?”.

The 1.1 THz Array Receiver is a cartridge-type receiver because of the several benefits that this concept provides which was first introduced for the ALMA receivers. It mainly means that several individual receivers, or cartridges, share one main cryostat. Among the benefits that this modularity provides is the fact that each cartridge can be assembled and maintained independently to the cryostat, reducing observing downtime at the telescope. The receiver could optionally be upgraded, in the future, with different mixer technology, operation frequency and number of pixels. Two easily removable cartridges were designed and built, each containing one sub-array of 9 pixels, organized in a 3x3 arrangement, observing the same frequency in orthogonal polarizations.

The detecting elements will be Superconductor-Isolator-Superconductor (SIS) balance mixers which required an operation temperature below 4.5 K for their optimum performance. They are being developed in our institute and are not part of this thesis. However, their requirements are important inputs for the design of the cryogenics and the optics of the receiver. A

cryostat that can house both cartridge modules and that provides the infrastructure together with the necessary low cryogenic temperature to the mixers was developed.

To connect the cartridges to the cryostat thermally and mechanically we developed a new all-metal Thermal Link (TL). It consists of a crown-like ring made of aluminum and an Invar ring.

All the receiver optics is fully reflective, thus avoiding the absorption and reflection losses of dielectric lenses and reducing standing waves in the receiver. To guarantee internal optics alignment, we employ, where possible, a monolithic integrated optics approach.

The optics that is installed inside the cryostat and the cryogenics were built, mostly in our workshop, and assembled to be tested in the laboratory. Beam measurements of the optics were performed, in direct-detection mode, with our in house available single-ended Superconducting Hot Electron Bolometer (HEB) mixers. The provided temperature to both focal plane arrays was 4.4 K, in the latest tests, largely sufficient for the HEB mixers which operation temperature was around 6.5 K. The results of the optics tests have shown some misalignment inside of the cryostat. The source of the problem is most probably due to the cartridges positioning and not to the optics itself, but additional tests are needed. One of the two optics assemblies involved was tested individually and shows good results.

Zusammenfassung

Diese Arbeit handelt von der Entwicklung der Optik und der Kühleinheit (“cryogenics”) für den 1.1 THz Heterodyn Array Empfänger, der in der Nasmyth A Kabine des Atacama Pathfinder Experiment (APEX) Teleskops installiert werden soll.

Der THz Bereich ist ein immer noch größtenteils unerforschtes Gebiet in der Astrophysik aufgrund der technologischen Herausforderungen für Empfänger und Teleskop sowie aufgrund der schwierigen atmosphärischen Bedingungen. Das APEX Teleskop, eine modifizierte Prototyp-Antenne des Atacama Large Millimeter Array (ALMA), ist mit seinem 12m Durchmesser das größte sub-mm Einzel-Antennen (single-dish) Teleskop der Welt für THz Frequenzen. Es hat eine räumliche Auflösung von einigen Bogensekunden aufgrund seiner Lage auf dem Chajnantor Plateau, 5100 m hoch gelegen in den Chilenischen Anden, und aufgrund seiner Oberflächengenauigkeit von $17\mu\text{m}$ r.m.s..

Bodengebundene Beobachtungen in dem atmosphärischen Fenster bei 1.1 THz (1000-1080 GHz) sind schwierig, sind aber möglich und können produktiv mit APEX durchgeführt werden. Diese Schwierigkeiten, zusätzlich zu der Tatsache, dass die Empfindlichkeit der einzelnen Pixel durch das Quantenlimit begrenzt ist, machen die Entwicklung von Array-Empfängern in diesem Frequenzband noch wichtiger.

Einige wichtige Energieübergänge von Molekülen liegen in diesem Frequenzbereich. Diese mit hoher spektraler Auflösung zu beobachten ($> 10^6$) ist wichtig für das Verständnis der physikalischen und chemischen Bedingungen in sogenannten “hot cores” im galaktischen Interstellaren Medium (ISM) und insbesondere auch in Starburst Galaxien sowie aktiven Kernen entfernter Galaxien (AGN). Die CO 9-8 Linie bei 1036.9 GHz ist ein Tracer für dichtes, warmes Gas. OH^+ bei 1033 GHz und NH^+ bei 1012.6 GHz sind wichtig beim Studium chemischer Netzwerke im ISM. Diese Beobachtungen werden entscheidend zur Beantwortung von Fragen wie “Wie entstehen Galaxien und wie entwickeln sie sich?” und “Wie entstehen Sterne?” beitragen.

Der 1.1 THz Array-Empfänger ist ein sogenannter “cartridge-type” Empfänger, aufgrund der verschiedenen Vorzüge dieses, erstmals für die ALMA Empfänger eingeführten, Konzepts. Es bedeutet hauptsächlich, dass sich mehrere einzelne Empfänger, die sogenannten “cartridges”, sich einen Haupt-Kryostat teilen. Zu den Vorteilen dieser Modularität gehört auch, dass jedes “cartridge” einzeln in den Kryostaten eingebaut und dort unterhalten werden kann, was Beobachtungsunterbrechungen am Teleskop reduziert. Der Empfänger kann optional in der Zukunft aufgerüstet werden, z.Bsp. mit anderer Mischer-technologie, anderen Beobachtungsfrequenzen und einer anderen Anzahl von Pixeln. Zwei, leicht austauschbare “cartridges” wurden entworfen und gebaut, jedes enthält ein Sub-Array mit 9 Pixeln, angeordnet in einer 3x3 Konfiguration, die bei gleicher Frequenz in orthogonalen

Polarisationen messen.

Die Detektorelemente werde Supraleiter-Isolator-Supraleiter (SIS) balancierter Mischer sein, die zur optimalen Performance bei Temperaturen unter 4.5 K betrieben werden müssen. Sie werden an unserem Institut entwickelt und sind nicht Teil dieser Arbeit. Allerdings ist ihr Anforderungsprofil ein wichtiger Input für das Design der Kühleinheit (cryogenics) und der Optik des Empfängers. Ein Kryostat, der beide “cartridge” Module aufnehmen kann und gleichzeitig die gesamte Infrastruktur, zusammen mit den erforderlichen niedrigen Temperaturen für die Mischer zur Verfügung stellt wurde von mir entwickelt.

Um die “cartridges” thermisch und mechanisch mit dem Kryostaten zu verbinden entwickelten wir eine neue thermische Kopplung (TL) ausschließlich aus Metall, bestehend aus einem kronenartigen Aluminiumring und einem Ring aus Invar.

Die gesamte Empfängeroptik ist voll reflektierend und vermeidet damit Absorptions- und Reflektionsverlust von dielektrischen Linsen und reduziert damit Stehwellen innerhalb des Empfängers. Um eine optimal Ausrichtung der internen Optik zu garantieren verwendeten wir, wenn möglich, eine monolithisch integrierte Optik.

Die Optik, die innerhalb des Kryostaten verwendet wird, sowie die Kühleinheit (“cryogenics”) wurden größtenteils in unserer Werkstatt gebaut und in unserem Labor getestet. Strahlungsmessungen der Optik wurden im “direct-detection” Modus mit Hilfe hausgener Hot Electron Bolometer (HEB) Mischer (single-ended) durchgeführt. In beiden Fokalebene-Arrays wurde bei den letzten Tests eine Temperatur von 4.4 K erreicht - ausreichend für die supraleitenden HEB Mischer, deren Arbeitstemperatur bei ca. 6.5 K lag. Die Ergebnisse der Optikttests zeigten einige Fehlausrichtungen innerhalb des Kryostaten. Deren Ursache ist sehr wahrscheinlich die Positionierung der “cartridges” und nicht eine fehlerhafte Optik. Allerdings sind weitere Tests zu Abklärung nötig. Eine der beiden verwendeten Optik-Komponenten wurde separat getestet und zeigte gute Ergebnisse.

Contents

Abstract	i
Zusammenfassung	iii
1 Introduction	1
1.1 Submillimeter Astronomy	2
1.2 Detectors for submillimeter astronomy	5
1.2.1 Direct Detectors	5
1.2.2 Heterodyne detectors	6
1.2.3 Coherent (heterodyne) or Incoherent detection?	7
1.3 The 1.1 THz Heterodyne Array Receiver Project	7
1.3.1 Science Objectives	8
1.3.2 Other Instruments Working in this Band	10
1.3.3 The Site and the Telescope	10
1.3.4 Instrument Concept	12
2 The 1.1 THz Heterodyne Array Receiver Cryostat	19
2.1 Requirements for the Cryostat	20
2.2 Design and Construction of the Cryostat	22
2.2.1 Description of the Cryostat	22
2.2.2 The Cartridge	28
2.2.3 The Entrance Window and IR Filter	34
2.2.4 The Cooling System	40
2.3 Heat Load Analysis	43
2.4 Cryostat Performance	54
2.4.1 Vacuum Tests	54
2.4.2 Temperature Tests	55
2.5 Summary	66
3 The Thermal Links	67
3.1 Thermal Links Description	68
3.2 Thermal Links Design	71
3.3 Thermal Links Versions	77
3.4 Thermal Conductance of the Thermal Links	80

3.5	Thermal Links Performance	82
3.5.1	Temperature Test Results	83
3.5.2	Thermal Conductance Measurements	87
3.6	Summary	92
4	The 1.1 THz Heterodyne Array Receiver Optics	95
4.1	Heterodyne Array Receiver Optics	95
4.1.1	Design Principle	96
4.2	The Relay Optics and the Cold Optics	102
4.2.1	The Cold Optics	105
4.2.2	APEX Tertiary Optics	108
4.3	The Focal Plane Unit (FPU) Optics	111
4.4	LO Power Distribution	118
4.4.1	LO Distribution Optics	119
4.4.2	LO Distribution Plate	121
4.5	Optics Tests	122
4.5.1	Beam Measurements	122
4.5.2	Alignment Tests and Analysis	128
4.5.3	FPU Optics Beam Measurements	132
4.6	Summary	135
5	Conclusions and Outlook	137
A	Cryostat Temperature Data	141
B	Thermal Links Data	143
	Bibliography	164
	Acronyms	167
	Acknowledgment	170
	Financial Support	171
	Erklärung	172
	Lebenslauf	174

Chapter 1

Introduction

This chapter provides the context of this thesis which deals with the development of the optics and the cryogenics for an instrument that will operate in the submillimeter frequency range and that will perform the observations from the ground. It starts with a description of submillimeter astronomy (section 1.1), including its difficulties, science goals and the important astronomical projects of recent years. After this, the detection modes, coherent and incoherent, that are available in the submillimeter regime are briefly explained, and their major differences are highlighted in the framework of their use in submillimeter astronomy. It continues with the description of the 1.1 THz Heterodyne Array Receiver project in section 1.3, starting with the particular science enabled by the THz astronomy, with focus in the 1.1 THz atmospheric window. Then, other instruments that have observed in this band are presented. After the Herschel space observatory has completed its operations, there is no instrument observing in this frequency band. Afterward, the observing facility that will accommodate this receiver is presented and the receiver description including its components, and the reason for their incorporation or choice, is explained.

The detectors of the receiver are not part of this thesis. However, their requirements in temperature, space and other particular needs for their right functioning are important inputs for the design of the cryogenics and the optics of the receiver. Therefore relevant information about them is given in this chapter, in particular when describing the instrument concept in section 1.3.4.

After the introduction, this thesis is presented divided in two main parts, two chapters give an account of the cryogenics and a third one explains the optics. Each chapter includes a presentation of the subject with the related requirements, the description of the design and the explanation of the laboratory tests with the corresponding results. Chapter 2 refers to the cryostat and the cartridges, chapter 3 is about the thermal links and chapter 4 gives an explanation of the receiver optics. The conclusions and outlook are given in chapter 5. To finish, two appendices are included. The first one

shows two figures with the receiver temperatures during the cool-down cycle and the second one shows the thermal links behavior during 31 cool-downs, out of a total of 35 performed during this thesis, presented chronologically.

1.1 Submillimeter Astronomy

Observational astronomy is focused on acquiring data from observations of astronomical objects where the source of information is the electromagnetic radiation. It may be divided according to the observed region of the electromagnetic spectrum. Some parts of the electro-magnetic spectrum can be observed from the Earth's surface, while other parts are only observable from either high altitudes or outside the Earth's atmosphere.

At the beginning of the 1990s, the submillimeter regime which approximately spans the frequencies from 0.3 to 3 THz was still very unexplored. This can be explained by two major limitations: the atmosphere, mainly opaque in this spectral range, except in some windows of transmission accessible only from dry sites either in altitude (see figure 1.1) or on the Antarctica plateau; and the developed instruments that had limited sensitivities and were generally equipped with only one single detector or receiver.

The main goal of submillimeter astronomy is to observe the warm rather than hot (such as stars) and cold (such as the cosmic background radiation) sources, e.g. the Interstellar Medium (ISM) which is made of gas and dust, star formation regions. Broadband thermal radiation from small dust grains - re-radiating absorbed shorter wavelength radiation - is the most common continuum emission process in this band; and gases with temperatures between 10 and a few hundred K emit their brightest molecular and atomic emission lines here.

Submillimeter astronomy is then the prime technique to unveil the formation and evolution of stars, galaxies and the interaction with the ISM.

To avoid most of the atmospheric absorption due to water vapor, specially at THz frequencies, airborne observatories have been used since the 70s. The Kuiper Airborne Observatory (KAO), equipped with a 91 cm telescope, was operational from 1974 to 1995. It included an heterodyne receiver for the range from 600 to 3000 GHz which was in operations from 1985 [Roeser et al., 1990]. The front end of this receiver contained Schottky diode mixer operating at ambient temperature. The useful application of the high resolution heterodyne receiver was limited by the sensitivity of the detector¹.

In the last decades, the progress made in technology of the semiconductors as well as in superconductivity made it possible to set the bases of a promising submillimeter instrumentation. Thus, ambitious projects have been developed, such as the Herschel Space Observatory [Pilbratt et al.,

¹System noise temperature of 25.000 (SSB) or 12.500 (DSB) achieved at 120 μm

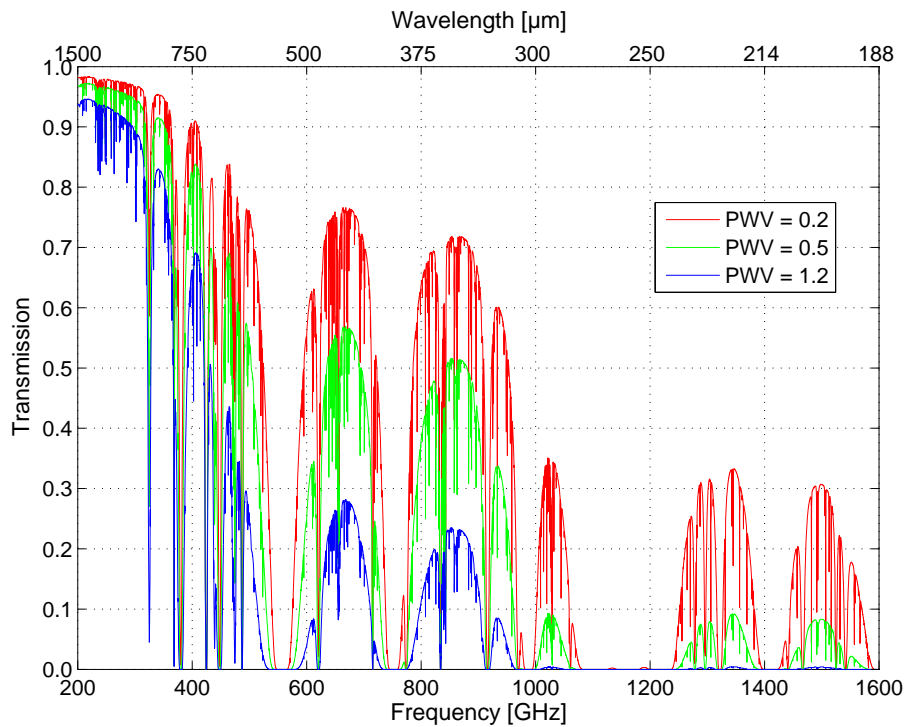


Figure 1.1: Zenith atmospheric transmission on the Chajnantor Plateau (Chile). At the Atacama Pathfinder Experiment (APEX) telescope site on the Chajnantor Plateau, the amount of PWV^a is typically 1.0 mm and falls below 0.5 mm up to 25% of the time. The image shows the atmospheric transmission between 200 GHz and 1.6 THz for different PWV values. It is based on the ATM^b model written by Juan Pardo [APEX telescope,].

^aPWV = Precipitable Water Vapor

^bATM = Atmospheric Transmission at Microwaves

2010], a submillimeter space observatory and one of the major projects of the world astrophysical community of the last years. It was launched on 14 May 2009 and was operational until 29 April 2013, but scientific work on the data will continue for many years. The observatory offered unprecedented observational capabilities in the far-infrared and submillimeter spectral range from 55 to 671 μm . The telescope's primary mirror was 3.5 m, more than four times bigger than any previous infrared space telescope. The payload had three advanced science instruments: Photodetecting Array Camera and Spectrometer (PACS) and Spectral and Photometric Imaging Receiver (SPIRE), two direct detection cameras/medium resolution (few thousands) spectrometers and Heterodyne Instrument for the Far Infrared (HIFI), a very high-resolution heterodyne spectrometer (up to 10^8).

Developed on the legacy of KAO, the Stratospheric Observatory For Infrared Astronomy (SOFIA) [Becklin and Moon, 2004] is another important project. It consists of a Boeing 747SP modified to carry a 2.5 m telescope, is operational since end of 2010. SOFIA is a joint project between USA and Germany. Nine first generation instruments were selected and are developed by institutions in both involved countries, including imaging cameras and spectrographs with spectral resolutions ranging from 100 to 10^8 , covering the wavelength range from 0.3 to 600 μm with an emphasis on the spectral regions inaccessible from the ground such as the 6-8 μm and 30-300 μm regions. One of the first generation instruments is the German Receiver for Astronomy at Terahertz Frequencies (GREAT), a dual channel heterodyne instrument working at 1.4, 1.9 and 2.5 THz. GREAT detected first light on April 2011, and performed successfully 14 science flights during SOFIA's Early Science phase. Science results based on these observations are contained in an Astronomy & Astrophysics special issue [Walmsley et al., 2012].

The submillimeter regime can be observed from space observatories, aircraft or balloons without (or with less) the limitations caused by the atmosphere and, most importantly, are not limited to few windows, but ground-based submillimeter observations can provide better angular resolutions down to a few arcseconds with single dish observations, are considerably cheaper and easier to service than satellites, and may provide more observing time than can be obtained from an aircraft. THz observations from the ground have difficulties, but it has been demonstrated that they are possible (see section 1.3). These difficulties make even more important the development of array receivers in this frequency range. Ground observations are also important to follow up the investigation, where possible, of the discoveries done with the Herschel's instruments and are a good complement to the observations performed with SOFIA.

1.2 Detectors for submillimeter astronomy

Detectors used in submillimeter astronomy can be classified in two groups depending on the detection principle: coherent and incoherent (direct) detection. These two principles are briefly described in the following sections.

1.2.1 Direct Detectors

In direct or incoherent detection the energy of the photons incident on the detector releases free carriers (electrons), or leads to heating of a thermal device. Consequently the phase information of the electromagnetic wave is lost. The fundamental, and usually dominating, noise contribution in this detection principle is due to statistical fluctuations in the arrival rate of the photons (photon noise).

Bolometers are type of direct detectors, they are basically very sensitive thermometers. The operation of a bolometer makes use of the effect that the resistance, R , of a material varies with the temperature. When radiation is absorbed by the bolometer material, the temperature varies; this temperature change is a measure of the intensity of the incident radiation. Because this thermal effect is rather independent of the frequency of the radiation absorbed, bolometers are intrinsically broadband devices. Bolometers are sensitive to both polarizations.

In the submillimeter range (from around 200 μm to 1 mm wavelength), the bolometer is the most sensitive type of detector for any continuum (broadband) measurements. Nevertheless, to achieve the best sensitivity, they must be cooled down to a fraction of a degree above absolute zero (typically from 50 to 300 mK); this makes their operation technically somewhat challenging.

To resolve the input signal spectroscopically, the optics of the direct-detector systems has to include filters (low resolution) or dispersive elements (mid-resolution) such as a Michelson or Fabry-Pérot interferometers, diffraction grating, etc. to distribute the different wavelengths on different detector elements.

Some examples of bolometer cameras with a large number of pixels are the PACS imager [Poglitsch et al., 2010] operating from 60 to 210 μm and the SPIRE photometer [Griffin et al., 2010] covering the range from 208 to 583 μm , both on the Herschel Space Observatory. From the ground, LABOCA operates at 870 μm since 2007 and ArTeMiS 350 μm band was commissioned on 2013, both at the Atacama Pathfinder Experiment (APEX) telescope [APEX telescope,].

In the last decade, research has extended to a new type of direct detector called Microwave Kinetic Inductance Detector (MKID) [Day et al., 2003]. They are wideband superconducting photon detectors suitable for a wide frequency range from the THz up to the X-ray. These devices operate at cryogenic temperatures, typically below 300 mK.

1.2.2 Heterodyne detectors

Coherent detectors measure amplitude and phase of the electromagnetic field at the same time, due to the Heisenberg uncertainty principle, their maximum sensitivity restricts to the quantum limit:

$$T_{N,min} = \frac{h\nu}{k_B} \approx 47 \text{ K/THz} \quad (1.1)$$

where $T_{N,min}$ is the minimum noise temperature that a mixer can achieved, in other words, is its maximum possible sensitivity, h is the Planck's constant, ν is the frequency and k_B is the Boltzmann's constant.

To observe at frequencies where no suitable amplifiers exist (above 100 GHz), the heterodyne principle is used. Instead of filtering and amplifying the incoming astronomical signal (RF) as such, it is down-converted to a lower Intermediate Frequency (IF). The weak RF to be detected ν_{RF} , together with a stronger Local Oscillator (LO) signal ν_{LO} , of only slightly different frequency, are fed into a mixer where a multiplication of the two signal takes place creating signals at many different frequencies. The IF frequency band $|\nu_{RF} - \nu_{LO}|$, which usually lies in the range of 1-10 GHz, is separated from other mixing products and can be amplified by commercial cryogenic Low Noise Amplifiers (LNAs) and processed e.g. digitalized with less technological effort. There are two more advantages of the down conversion: one is the high spectral resolution $> 10^6$ and the other one, is that since the phase of the signal is preserved during the conversion, coherent detection can be used in the submillimeter range for interferometry (e.g. Atacama Large Millimeter Array (ALMA) [[ALMA observatory](#),]). In contrast to direct detection, coherent detection allows amplification of the signal before correlation.

There are different kinds of mixing devices such as a Superconductor-Insulator-Superconductor (SIS) tunnel junction or a Superconducting Hot Electron Bolometer (HEB).

In submillimeter astronomy, SIS mixers are used up to frequencies of 1.4 THz and receivers for higher frequencies employ HEB mixers [[Zmuidzinas and Richards, 2004](#)]

Currently, operation of single-ended SIS mixers in astronomical receivers, at least up to 700 GHz, is a well known technique where the sensitivity cannot be improved anymore since the detector has reached the quantum limit. Thus, further improvement in sensitivity can be accomplished by the use of detector arrays.

On average, HEB mixers have sensitivities 6-10 times the quantum limit, thus they are less sensitive than SIS mixers. The advantage of HEBs rely on the fact that they do not need a magnetic field and have a simpler tuning structure. Then, when is possible to work with SIS mixers for a certain frequency band, these devices are preferred over HEBs even if this results in more receiver complexity. An advantage of SIS mixers, besides higher

sensitivity, is the much larger IF bandwidth.

Some examples of heterodyne receivers: HIFI [de Graauw et al., 2010] on the Herschel Space Observatory, GREAT [Heyminck et al., 2012] on SOFIA and the SubMillimeter Array Receiver for Two Frequencies (SMART) [Graf et al., 2003] at the NANTEN2 telescope.

1.2.3 Coherent (heterodyne) or Incoherent detection?

Both detection methods have advantages and disadvantages. The disadvantages of coherent-detection are the fact that their maximum sensitivity restricts to the quantum limit, that only 1 polarization is detected and that the maximum coherently detected bandwidth is a few GHz. In addition, building an heterodyne arrays is complicated - each pixel has to be coupled to the telescope, the need of a LO signal per pixel, etc. - then, these receivers are mainly single pixel or up to several tens of pixels. As a result, the Field of View (FOV) is smaller than in direct detectors. On the other hand, some of the disadvantages of the incoherent detection are the very low cryogenic temperatures required by the detectors, < 300 mK for the bolometer arrays; and the fact that when used as spectrometers they can reach spectral resolutions of only up to few thousands because of the need of dispersive elements - such as a Fabry-Pérot interferometers, a diffraction grating, etc. - in front of them, coherent detection can offer resolutions $> 10^6$.

At the end, the decision on which detector system is going to be used has to be decided in relation to the astronomical question to answer and the available technology. Bolometer cameras are usually chosen to measure broadband radiation, e.g. map the dust emission. Coherent detectors on the other hand, get a high spectral resolution at a desired frequency allowing to obtain e.g. kinematic information of astronomical objects and the astrochemical properties of the source. Thus, when the main factor is the spectral resolution, heterodyne receivers are a better choice.

1.3 The 1.1 THz Heterodyne Array Receiver Project

In this section, the receiver project will be extensively explained. Starting with the science goals that motivated its development, continuing with the description of other instruments that have worked in this frequency regime (no instrument is currently working in this band), following by the description of the site and the telescope, and ending with the receiver description where we explain its components and the reason for their incorporation or choice.

1.3.1 Science Objectives

Part of the submillimeter regime, the THz frequency range, from 1 to 3 THz (100 - 300 μm), is still a largely unexplored area in astrophysics because of the technological challenge for the receiver and telescope as well as the difficult atmospheric conditions. Recently, a tremendous effort has been made in order to fill in the called “THz gap”.

The poor atmospheric transmission for ground based observations at THz frequencies limits the observable bands to three windows centered at 1.03 THz, 1.32 THz and 1.5 THz (see figure 1.1) from high altitude sites in northern Chile. However, many astronomical interesting lines can be found in this range.

The 1.1 THz Heterodyne Array Receiver will cover the spectral range of 1000-1080 GHz, which corresponds to the 1.03 THz atmospheric window (also called “1.1 THz” in this work), where there are several important molecular transitions, whose observations with high-resolution spectroscopy will bring new knowledge about the chemical and physical conditions of the gas, especially in starburst galaxies and active galactic nuclei of external galaxies, but also in hot cores in the galactic ISM. The CO 9-8 line at 1036.9 GHz is a tracer for the warm and dense gas. OH⁺ at 1033 GHz and NH⁺ at 1012.6 GHz are important for the study of chemical networks in the ISM. The observations with APEX in this frequency range are outstanding additions of the observations performed with the Herschel Space Observatory and SOFIA.

After the first submillimeter and far-Infrared (IR) spectral lines observations in early 1980s, it became clear that the UV radiation from nearby massive, young stars can heat the gas, dissociate the molecules and partly ionize the atoms [Stutzki, 1994]. Abundances of different chemical species depend on the strength of the radiation UV field. Carbon, for example, shows a complex behavior. Depending on the radiation field it forms molecules - mainly the important CO -, it appears as atomic C, or is ionized.

CO has a rotational transition line every approximately 115 GHz and is the most abundant tracer of molecular gas. Intensive studies have been performed mainly at rotational transitions below 1 THz. Thus, in complement to the observations of mid-J CO transitions which are the routine observation in the accessible atmospheric windows at 345, 460, 660 and 810 GHz, observations at 1.1 THz will enable to determine the physical conditions (density, temperature) in star-forming regions and active galactic nuclei with unique spatial resolution, the Half Power Beam Width (HPBW) of the antenna beam at 1.1 THz is 5.9 arcseconds. In addition, the high spectral resolution of the heterodyne observations will allow to unambiguously assign the emission to shock fronts or Photon Dominated Regions (PDRs). Thus, the 1.1 THz Heterodyne Array Receiver will contribute decisively to answer questions such as “How do galaxies form and evolve?” and “How do stars form?”.

CO 9-8 has been already detected in ground based observations (see sec-

tion 1.3.2) and also from Herschel with SPIRE, e.g. [van der Werf et al., 2010] which presents a Fourier Transform Spectrometer (FTS) spectrum of the nearby ultraluminous infrared galaxy Mrk 231, including as well other transitions between CO 5-4 to CO 13-12; and with HIFI, e.g. [Pon et al., 2015] where mid-J CO transitions towards four dense, starless clumps within Infrared dark clouds (IRDCs) are shown.

Current chemistry models of the ISM composition suggest that most of chemical reactions in it are controlled by ion-molecule reactions which begins with the ionization of H and H₂ by cosmic rays, responsible for generating many of the diatomic and small polyatomic molecules observed in the ISM. A few such species - OH⁺, H₂O⁺ and H₃⁺, in particular - are formed and destroyed by rather simple processes, making them powerful probes of the cosmic ray ionization rate [Indriolo et al., 2015]. With Herschel HIFI all three transitions of OH⁺ (909 GHz, 971 GHz and 1033 GHz) have been detected. However, the first interstellar detection of OH⁺ was done from the ground, APEX was used to observe the ground-state transition at 909.1588 GHz with The Carbon Heterodyne Array of the MPIfR (CHAMP⁺). The transition at 1033 GHz could be observed with the 1.1 THz Array Receiver.

Other line of interested in the 1.03 THz window is the 1012.6 GHz transition of NH⁺, an undetected molecular ion in the formation chain of ammonia. With the launch of Herschel, HIFI has allowed, for the first time, searches for spectrally resolved, rotational transitions involving the ground states of NH⁺, NH, NH₂ and NH₃ with the same instrument. [Persson et al., 2012] reports the non-detection of NH⁺, the other species were detected. However, this lowest rotational transition of NH⁺ has been detected in laboratory [Verhoeve et al., 1986], astronomers will be able to continue searching for this transition with the 1.1 THz Array Receiver from the ground.

As a consequence of the science goals described above and the detector technologies explained in section 1.2.3, the best suited detector technology for the 1.1 THz Receiver is the heterodyne detection. This detectors can achieve spectral resolution $> 10^6$.

Starburst galaxies rotate with velocities (v_{rot}) in the range of 120 to 200 km/sec. Due to the Doppler effect, the observed emission line of the molecule inside the galaxy will be broadened by $\Delta\nu = 2\nu v_{rot}/c$, where ν is the observed frequency from the molecule and c is the speed of light. $\Delta\nu$ could be additionally Doppler shifted because of a relative motion of the source with respect to the observer, this would only cause a shift of the line in the observed band. Observing one of these galaxies at $\nu = 1$ THz would result in a molecular line width of approximately 1 GHz, adding to this the necessity of sufficient spectral baseline to measured the observed line, there was decided to require 4 GHz of IF bandwidth for the 1.1 THz Receiver.

1.3.2 Other Instruments Working in this Band

Currently there are no instruments observing in the frequency band of the 1.1 THz Array Receiver and, to our knowledge, there is no other instrument being developed. However, there have been instruments that have observed in this band from space, aircraft and also from the ground.

A single-pixel dual-channel heterodyne receiver, operating in the 460 GHz and 1.03 THz atmospheric windows, was commissioned in 2009 at APEX [Leinz et al., 2010]. As part of the science demonstration of this receiver, the CO (9-8) emission towards the high-mass star forming region, NGC 6334 I, was mapped with a 6.4 arcsecs resolution [Qiu et al., 2011].

Previously, another experiment was done to assess the feasibility of ground-based THz astronomy. The Receiver Lab Telescope (RLT) [Blundell et al., 2002], a 0.8 m antenna, was located 40 km north of the ALMA site, at an altitude of 5525 m on Cerro Sairecabur, Chile. It was equipped with HEB mixers for observations in four atmospheric windows between 800 GHz and 1.6 THz. The telescope was operational from late 2002 to, at least, 2005. The distribution of CO (9-8) emission was mapped in the OMC²-1 region of the Orion A molecular cloud with a spatial resolution of 84 arcsec [Marrone et al., 2004a]. This telescope also detected CO (7-6), CO (9-8) and CO (11-10) emission in M17 [Marrone et al., 2005]. The CO (9-8) line in OMC-1 was previously observed with KAO.

Two of the three instruments of Herschel have operational bandwidth that include the frequency band of the 1.1 THz Array Receiver, HIFI band 4 (2 SIS mixers operate on orthogonal polarizations) corresponds to the range 960 - 1120 GHz (268 - 313 μm) [de Graauw et al., 2010] and one of the two medium resolution spectrometers of SPIRE which corresponds to the band 194 - 313 μm [Griffin et al., 2010].

After Herschel was decommissioned in 2012 and until Cerro Chajnantor Atacama Telescope (CCAT) is in operations, the lines in the 1.1 THz bands, among others, will only be observable from the ground with the APEX telescope.

1.3.3 The Site and the Telescope

The APEX telescope (see figure 1.2 left) is a collaboration between Max-Planck-Institut für Radioastronomie (MPIfR) at 50 %, the European Southern Observatory (ESO) at 27 % and the Onsala Space Observatory (OSO) at 23 % to construct and operate a modified ALMA prototype antenna as a single dish on the high altitude site of Llano Chajnantor. The telescope was officially inaugurated on September 25, 2005 [Güsten et al., 2006]. As the name suggests, it fulfills a function as a pathfinder, finding targets that

²Orion Molecular Cloud

can be studied in greater detail by the ALMA observatory which is an interferometer of 64 antennas covering the frequency range from 31 to 950 GHz installed at the same site. The first antenna of the array came to Llano Chajnantor on 2009.

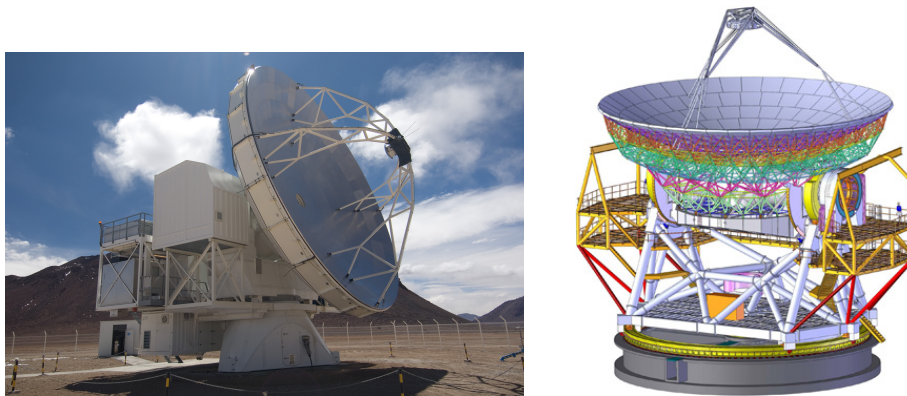


Figure 1.2: Left: The Atacama Pathfinder Experiment (APEX) telescope at 5100 m altitude on Llano Chajnantor. Right: Cerro Chajnantor Atacama Telescope (CCAT) CAD^a model. The planned location of the site is at 5612 m altitude just below the summit of Cerro Chajnantor. Image from [CCAT observatory,]. Both in the high Chilean Andes.

^aComputer-Aided Design

APEX is designed to work in the submillimeter range, from 200 to 1500 GHz, between infrared light and radio waves. Submillimeter astronomy provides a window into the cold, dusty and distant Universe, but the faint signals from space are heavily absorbed by water vapor in the Earth's atmosphere. Llano Chajnantor at 5100 m altitude in the high Chilean Andes, was chosen as the location for such a telescope because the area offers one of the driest and more stable atmospheric conditions on Earth.

This is of particular interest for the 1.1 THz Array Receiver which frequency band corresponds to one of the three THz windows (centered at 1.03, 1.32 and 1.5 THz) that opens only on extremely dry ground sites, such as the South Pole and high in the Atacama desert [Marrone et al., 2004b] and references therein. At APEX, the Precipitable Water Vapor (PWV) is typically 1.0 mm and drops below 0.5 mm up to 25 % of the time. During best weather conditions an atmospheric transmission of up to 35 % (see figure 1.1) in the 1.03 THz window is possible, where statistics show that the atmosphere is this transparent only in approximately 5 % of the nights.

Besides the atmosphere, the surface accuracy of the telescope and its pointing capabilities, able to handle the rather small beams of THz receivers, also play an important role to produce good beam efficiencies on sky.

The main dish of the APEX telescope has a diameter of 12 meters and consists of 264 aluminum panels with an average surface accuracy of 17 μm

(r.m.s.). These characteristics, in addition to its location at 5000 m, make of APEX the largest submillimeter single-dish telescope world-wide for THz frequencies. It provides 2 Nasmyth and 1 Cassegrain receiver cabins. More information on the telescope and on its current instrumentation can be found in [[APEX telescope](#),].

Even though the 1.1 THz Array Receiver is being developed to perform observations with the APEX telescope, it could also work with other telescopes, in particular with the future CCAT observatory (see figure [1.2 right](#)). It is planned to be located on Cerro Chajnantor, at 5600 m altitude, in the Chilean Atacama Desert where the transparency of the atmosphere is unique; and have a primary mirror of 25 m, an operation wavelength band from 200 to 2200 μm and a field of view of one degree [[CCAT observatory](#),].

1.3.4 Instrument Concept

The 1.1 THz Heterodyne Array Receiver will operate in the frequency band from 1000 to 1080 GHz. It will be installed in the Nasmyth A Cabin of the APEX telescope and as a consequence it must adhere to the constraints defined in the document [[Heyminck et al., 2004](#)] which defines the mechanical and optical constraints for the receiver design (see figure [1.3](#)). All the receiver parts, cryostat plus optics, must stay within this envelope limits to avoid collision with other installations inside the cabin. In addition, it gives information about the refocusing system called Tertiary Optics that modifies the APEX Cassegrain-telescope for Nasmyth instrumentation, the optical path to the telescope and its narrowest part.

Because of the difficult atmosphere conditions within this frequency band (see figure [1.1](#)), the observation time must be optimally used. The traditional scanning of the sources with a single detector is too ineffective. Especially due to the fact that the single pixel sensitivity cannot be improved by much anymore since it is approaching the quantum limit. Therefore, we developed a multi-pixel receiver that is equipped with 2 sub-arrays of 9 pixels each, organized in a 3x3 arrangement, observing the same frequency band in orthogonal polarizations, both sub-arrays have their beams coincident on sky.

The 1.1 THz Array Receiver will be a cartridge-type receiver because of the several benefits that provides this concept which was first introduced for the ALMA receivers by Rutherford Appleton Laboratory (RAL) in the United Kingdom [[Wild and Payne, 2002](#)]. It mainly means that several individual receivers, or cartridges, share one main cryostat. Among the benefits that this modularity provides is that each cartridge can be assembled independently to the cryostat, it also allows easy maintenance and troubleshooting since it is possible to remove and repair cartridge components without having to open the whole cryostat neither to dismount it from the telescope and thus reduce observing downtime. The same advantages are also valid

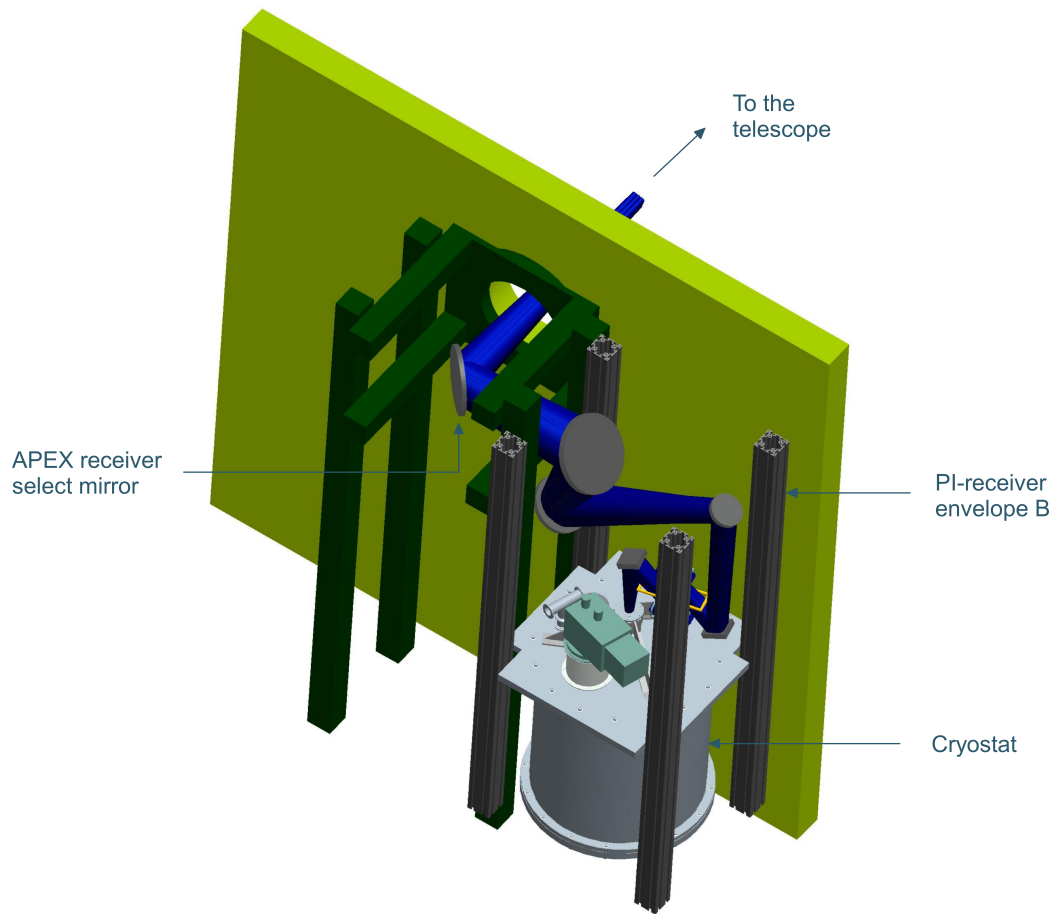


Figure 1.3: CAD drawing of the 1.1 THz Receiver set up in the Nasmyth A cabin at the APEX telescope. The four gray beams delimit the allocated envelope, called PI-receiver envelope B, which size is: 1900 mm in height, 800 mm in width and 650 mm in depth (towards the wall).

while testing in the laboratory. In addition, it should permit future flexibility to replace mixer technology, operation frequency and number of pixels. The cartridge description together with their design and components, are explained in section 2.2.2).

The detectors will be SIS mixers because they offer both, high sensitivity and a larger instantaneous IF bandwidth than HEB mixers. An IF bandwidth of minimum 4 GHz is needed to be able to detect the wide lines of external galaxies.(see section 1.3.1). The array spectrometer back ends will be the ones available at APEX. The receiver uses synthesizer-driven solid-state LO [VDI Virginia Diodes, Inc.,], which is an established LO technology in this frequency range. Excess receiver noise issues related to these LO sources are circumvented when they are operated together with balanced mixers [Westig et al., 2012]. Balanced mixers, in addition, have a separate port for the LO signal making them very well suited for array receivers since the sky signal and the LO radiation can be combined without the need of using a diplexer which permits to exploit effectively the LO power. Another advantage, is the fact that the IF bandwidth provided by the mixer device is not affected by the transmission band of the optical diplexer. For these reasons, the receiver mixers will be balanced SIS mixers, which will be essentially based on the design of the on-chip balanced SIS mixers at 490 GHz [Westig et al., 2011] developed in our institute (see figure 1.4). On the other hand, this requires a separate distribution network to supply with LO signal to each of the 9 pixels of the sub-array. Even though this dedicated network is not part of this thesis, a proposed solution is given in section 4.4, and the necessary space has been allocated for it on the cartridge module.

A cryostat that can house both cartridges and that satisfies all the receiver requirements was developed and is described in detail in chapter 2. The main objective of the cryostat is to provide the infrastructure to house the detecting elements together with the necessary low cryogenic temperature indispensable for their optimum performance. The SIS balanced mixers will use superconducting NbTiN contact leads and a Nb-AlOx-Nb SIS junction for mixing the LO signal and the RF [Westig et al., 2013]. The sensitivity of the SIS mixers is temperature dependent, increasing at decreasing operation temperature, but does not change significantly below $T_c/2$, where T_c is the critical temperature of the superconductor. The lowest T_c in the device, that of Niobium, is approximately 9 K [Ashcroft and Mermin, 1976]. Thus, a cooling temperature below 4.5 K was defined for the focal plane sub-arrays where the mixers will be mounted. Therefore, a cooling system such as a 2-stage Pulse Tube (PT) (see section 2.2.4) had to be incorporated into the cryostat.

Thermal connection from the cryostat to each cartridge assembly heat sink stage is provided via a thermally activated link arrangement that requires no permanent mechanical attachment. This mechanism, called Thermal Link (TL), provides a significant operational advantage in that a with-

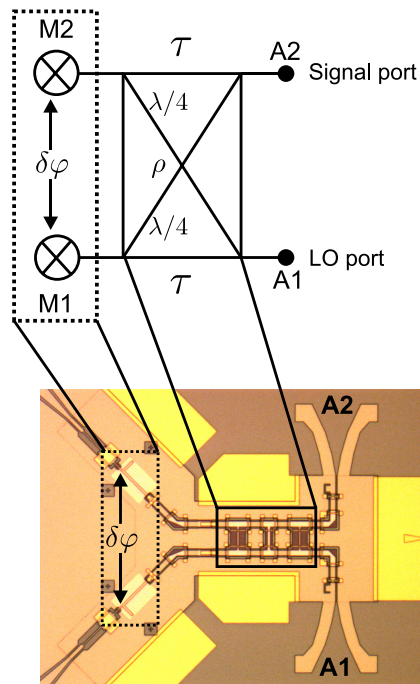


Figure 1.4: Top: Balanced mixer circuit diagram showing the two mixer input ports A1 and A2, the 90° hybrid coupler (crossed rectangle) and the two SIS mixers M1 and M2 having gains G_{M1} and G_{M2} . τ^2 and ρ^2 are power coupling factors and $\delta\phi$ is the phase error of a possibly not ideal 90° hybrid coupler. Bottom: Detail photograph of the mixer chip focussing on the RF part of the circuit. Figure and text from [Westig et al., 2012].

drawal of a cartridge, can be simply performed at room temperature and ambient atmospheric pressure without disturbing the rest of the receiver. The design of the TL developed during this thesis was inspired by two previously created thermal links. The first one was proposed by RAL for use in the ALMA receivers [Orlowska et al., 2002], and the second one was designed in [Sugimoto et al., 2003] for a 3-cartridge test cryostat for ALMA. The design and performance of our new all-metal TL is presented in detail in chapter 3.

The 1.1 THz Heterodyne Array Receiver optics is fully reflective to avoid the absorption and reflection losses of refractive optics. To reduce the need for optical alignment, we machine, as far as possible, complete sub-units from monolithic blocks of aluminum. Since heterodyne mixers are sensitive to one polarization only, a dual-polarization receiver can be made by dividing the incident beams into two perpendicular polarizations. As a consequence, the Relay Optics (or re-imaging optics) in charge of transforming the focal plane of the telescope into the focal plane of the receiver includes a wire-grid polarizer that splits the incident beams into transmitted and reflected beams depending on their polarization. Thereafter, each set of beams is directed to one of the two cartridges. Thus, the focal plane array of the receiver is divided into two sub-arrays. On each cartridge, the receiver focal plane is located at the Focal Plane Unit (FPU) optics which is in charge of coupling the RF to each mixer-horn pixel. It is here that the beam spacing on sky is defined. The design of the optics is widely explained in chapter 4. Beam measurements of the optics were performed with our in house available single-ended HEB mixers [Pütz et al., 2011], working in direct-detection mode. The result of these tests are presented in section 4.5.

During this work, it was decided to leave open the possibility of using single-ended HEBs or SIS mixers, in which case the LO beams have to be coupled to the RF beams before arriving into the mixing elements. Accordingly, the Relay Optics includes a diplexer. Nevertheless, we are developing SIS balanced mixers and the LO power distribution and expect in the near future change this optical LO coupling. To take this diplexer out and adjust the warm optics presents no problem.

To have an overview of the receiver installed in the Nasmyth A Cabin of the APEX telescope, including a view of the inside of the cryostat, see the Computer-Aided Design (CAD) drawing shown in figure 1.5. The different subsystems are explained throughout the chapters of this thesis.

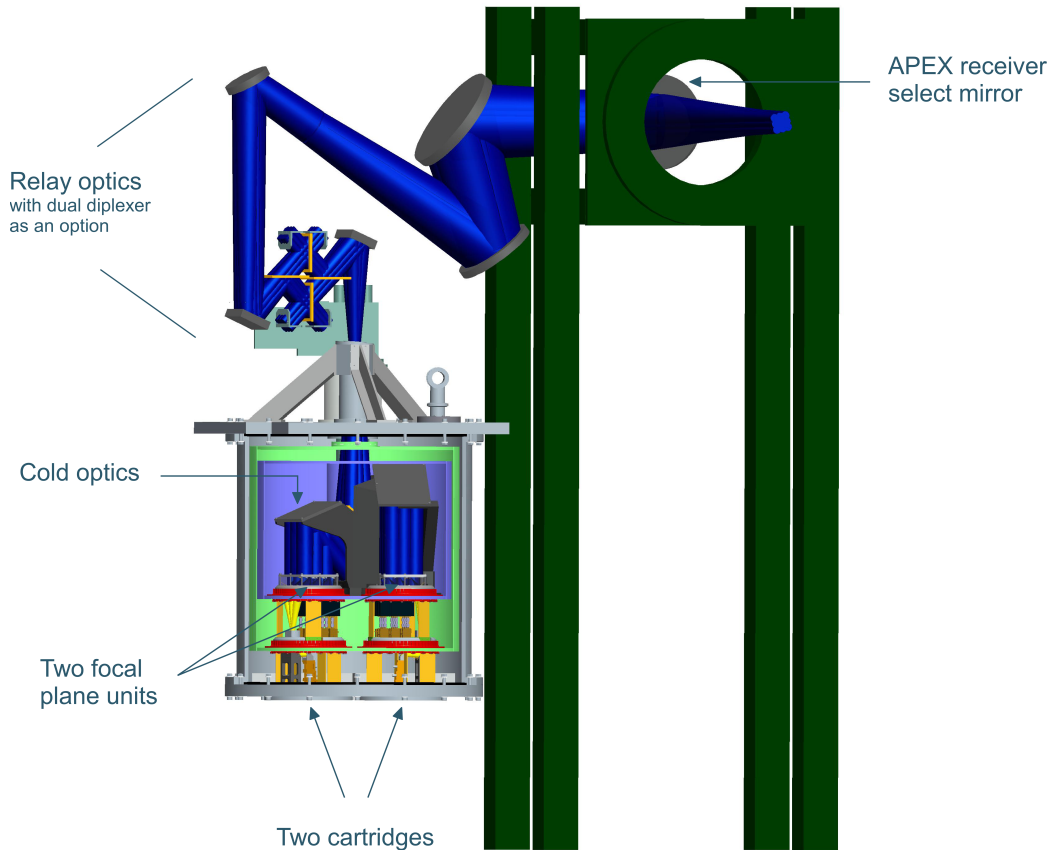


Figure 1.5: CAD drawing of the 1.1 THz Array Receiver setup in the Nasmyth A cabin at the APEX telescope as seen from the cabin wall. The inside of the cryostat is also shown and the sub-systems such as the cartridges and the Cold Optics (part of the Relay Optics) are identified. The 5w beam contour of the RF beams are presented in dark blue. The distance from the bottom of the cryostat to the APEX receiver select mirror is 1610 mm.

Chapter 2

The 1.1 THz Heterodyne Array Receiver Cryostat

To have a complete account of the 1.1 THz Array Receiver and mainly because it is one of the central parts of this thesis, it is needed to describe the cryostat, the device used to furnish the infrastructure to house the detecting components and to supply them with the necessary low cryogenic temperature indispensable for their right functioning. In our receiver, it should provide an operations temperature lower than 4.5 K to the SIS balance mixers. For this reason, a cooling system such as a PT (see section 2.2.4) was incorporated into the cryostat. The heat load inside the cryostat has to be lower than the PT cooling capacity (1 W at 4.2 K), this is analyzed in detail in section 2.3.

Even though the cryostat has to isolate the detecting elements from the outside to keep them cold, it also needs the appropriate interfaces to allow the astronomical beams to go in and the IF signals to go out and towards the APEX telescope facility back ends. The first point is made by means of an entrance window and the second one with coaxial cables and connectors. In addition, wires and cables are also needed for the temperature sensors, the bias supply and the LO signal. The entrance window and IR filter are described in detail in section 2.2.3 while in section 2.1, the requirements for the cryostat of the 1.1 THz Array Receiver, including the wires and connectors, are explained. Then, the cryostat design and its performance are presented in sections 2.2 and 2.4 respectively.

The 1.1 THz Array Receiver was chosen to be a cartridge-type receiver system including two cartridges. The reason for this choice, their design and components are explained in section 2.2.2.

2.1 Requirements for the Cryostat

Since the cryostat is a cartridge-type cryostat that fits 2 cartridges containing 9 detecting elements each, the cartridges and the necessary TLs (see chapter 3) had to be developed and incorporated in the design of the cryostat. Two TLs per radiation shield are needed.

The cryostat also has to provide the necessary space and support to the receiver optics assemblies (see chapter 4) that are installed inside of it.

The cryostat was developed considering the requirements in size, mass, low temperature, interfaces and weight. Furthermore, it was also taken into account the need of a strong structure to avoid pressure and gravitational deformation as well as high stability to mechanical vibration. Maintenance issues were also considered.

Temperature

The main purposes of the cryostat is to provide a temperature lower than 4.5 K to the detecting elements which is essential to their right operational behavior. Therefore, a cooling system such as a PT (see section 2.2.4) has to be incorporated into the cryostat. To allow this temperature to be reached, the limited cooling power of the PT (1 W at 4.2 K) cannot be exceeded. The cryostat has to isolate the detectors from the outside heat and the elements inside the cryostat (amplifiers, wires, etc.) have to produce a small amount of heat. First of all, the cryostat has to be vacuum tight, to allow the required isolating vacuum of few 10^{-6} mbar, then the materials used inside the cryostat have to be carefully selected. The thermal conductivity and thermal expansion of the materials, together with their emissivity, are among the most important properties to be taken into account.

Size and Mass

The 1.1 THz Array Receiver will be installed in the Nasmyth A Cabin of the APEX telescope, consequently it has to respect the requirements defined in the document [Heyminck et al., 2004] provided by APEX. The 1.1 THz Receiver was allocated with the area named PI-receiver envelope B shown in figure 1.3. All parts of the receiver must stay inside the envelope to exclude collision with other installations inside the cabin. A separate space for an electronics rack is also available. The maximum weight to be placed on the receiver support structure must not exceed 120 kg. If this weight is exceeded, supporting legs must be used.

The limit described above is the maximum limit in size because the receiver must fit into this envelope. Nevertheless, the cryostat should be as small as possible for easy handling and shorter cooling time. The minimum size will be given by the fact that the cryostat has to permit the installation

of the two cartridges (with its 9 SIS balance mixers each), the dedicated LO distribution network, the required cold optics, as well as the cooling system, LO multipliers, TLs and all the necessary components (wires, electronic connectors, vacuum port, etc.) to function correctly.

Interfaces

The cryostat has to be equipped with the appropriate interfaces for the inputs and outputs from and to the outside. A vacuum or entrance window has to be incorporated to the cryostat to permit the RF to pass from the telescope to the detecting components. The entrance window has to be transparent for the desired frequency band, but block the IR radiation to diminish the heat load into the cryostat. As a consequence, IR filters have to be added in the optical path to minimize the IR radiation that can pass through the entrance window and also to block the black body radiation from the cryostat vessel into the cold stage. Appropriate connectors have to be available for the IF signals to go out from the cryostat towards the APEX facility back ends (Fast Fourier Transform Spectrometer (FFTS)).

Besides, the cryostat has to be provided with the corresponding electronic connectors for the wires and cables required in the receiver. They are needed for the temperature sensors, the biasing of the detectors and amplifiers, and the LO multipliers. The thermal conductivity and dissipation of the wires has to be minimized.

At least one vacuum port has to be available to evacuate the cryostat, monitor the vacuum continuously and break the vacuum when necessary. It has to be furnished with a valve and a vacuum gauge. All the interfaces have to be vacuum tight.

The transmission of the PT mechanical vibrations through the cryostat should be prevented. The connections between the cooling system cold heads and the shields have to be done by means of soft and flexible interfaces.

Other mechanical issues

The effect of the pressure difference, gravitation and acceleration while pre-setting the telescope has to be considered, this will define the thickness of the sidewall and the two cover plates of the vacuum vessel. The radiation shields also have to be analyzed.

The design should also consider the maintenance of the receiver, changing components should be easy, reducing maintenance and troubleshooting time especially when at the telescope. The fact that this is a cartridge-type cryostat already helps in this respect because most of the elements are installed in the cartridges being accessible by removing the cartridge from the cryostat.

2.2 Design and Construction of the Cryostat

In this section, the cryostat designed and built for the 1.1 THz Array Receiver is described. It was conceived to accomplish the requirements presented in the previous section.

2.2.1 Description of the Cryostat

The vacuum vessel of the cryostat consists of a metal cylinder closed on both ends with metal covers that on the top side support the signal input window, the cryocooler system and the vacuum port and on the bottom side, only the two cartridges. The construction material of the vacuum vessel is aluminum (Al) and was fabricated in accordance with a pressure vessel design. The dimensions of the vacuum vessel are 614 mm in diameter and 715 mm in height including the top and bottom covers. The side wall of the cylinder is 10 mm thick and both covers thickness are 30 mm in order to keep their deflection below 0.5 mm when the system is evacuated. It is foreseen that the entrance window and the cartridge access holes will weaken the end plates, particularly at the bottom plate, hence additional mechanical stiffening is provided. The top cover of the vacuum vessel has a square shape to facilitate the installation in the laboratory for tests and, in the future, at the receiver support structure in the telescope. Figure 1.3 show a CAD model of the cryostat installed in the telescope Nasmyth A Cabin and figure 2.1 *Bottom right* show a picture of the cryostat in the laboratory.

The cryostat is composed by the external vacuum vessel and 2 radiation shields. These two shields are crucial to reduce the radiative thermal load on the 4 K stage, the heat radiation is proportional to $(T_2^4 - T_1^4)$. Each shield corresponds to a temperature stage of the cooling system and has a cylindrical shape, it is formed by two plates, a top or Cold Head (CH) plate and a bottom or TL plate, and a side wall that connects them. See figure 2.2 for a simplify CAD model of the cryostat that allows a better look of its cooling path, and figures 2.1 *Top left* and *Top right* for complete versions of it.

The 4 K TL plate was made of Al5N high purity aluminum (99.999% purity) to provide a thermal conduction with the least possible loss to the 4 K TLs [Woodcraft, 2005b] because they are responsible for the cool down of the 4 K cartridge plate where the mixers are mounted; see figure 2.3 for the thermal conductivity of high purity aluminums. Its thickness is 8 mm and has an additional 'X' shape reinforcement due to the fact that the Cold Optics which weighs 13 kg is mounted on it. The other three top and bottom plates of the shields also have 8 mm in thickness, but were made out of aluminum 5083 because less critical with respect of thermal conductivity; see figure 2.4 for the thermal conductivity of this and other materials mentioned in this section.

2.2. Design and Construction of the Cryostat

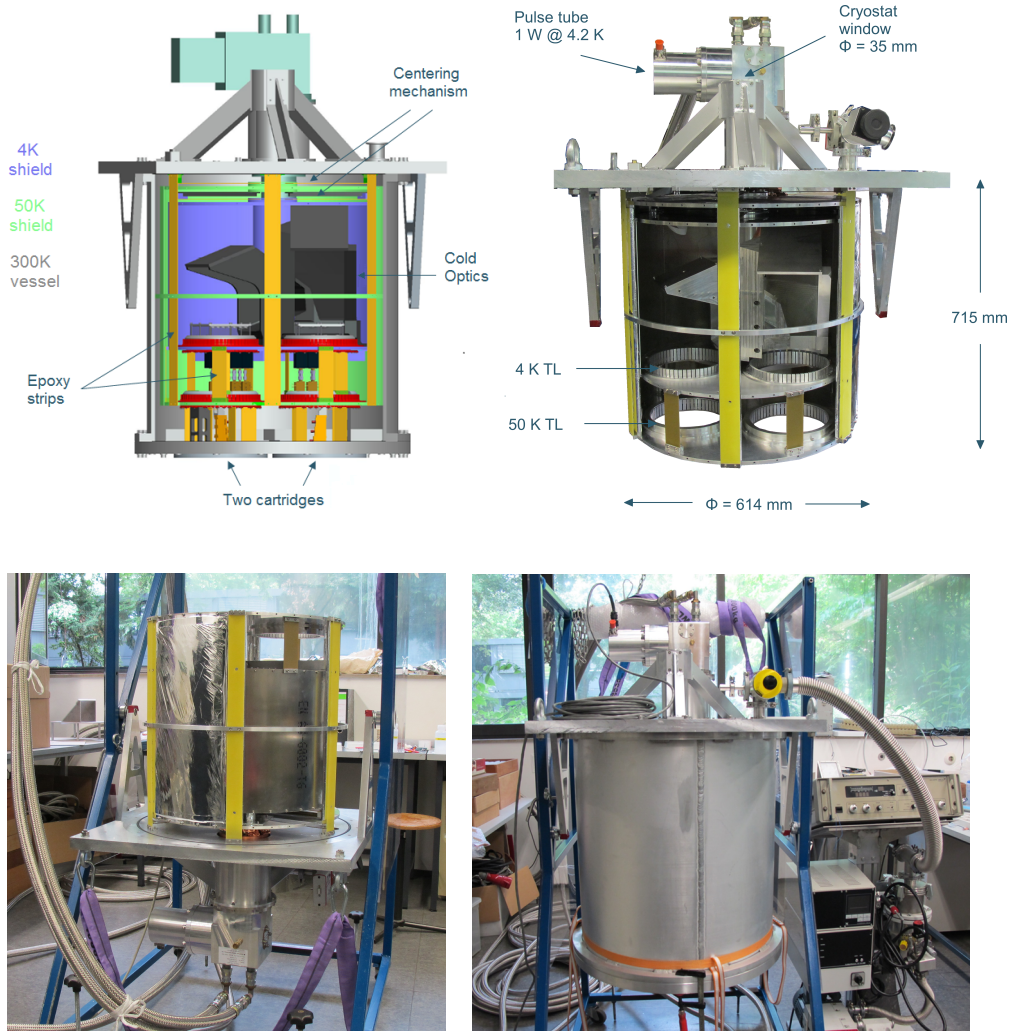


Figure 2.1: The 1.1 THz Array Receiver cryostat. Top left: CAD drawing of the receiver cryostat with a cut in the vessel and radiation shields to view the interior including the cartridges, TLs, cold optics and epoxy G10 strips. Top right: Picture of the receiver cryostat without the vacuum vessel and the cartridges. Two of the 6 parts that form the 50 K and 4 K radiation shield walls are removed to allow the view of the inside. The 50 K TL have their covers on to block the heat load from the 300 K pass through the fingers into the 4 K stage. The dimensions indicate the size of the vessel. Bottom: Photographs of the cryostat in the laboratory. Left: The cryostat in the mounting position, the 4 K and 50 K shields (with the 10 layer Multi Layer Insulation (MLI)) can be seen partially mounted. Right: The cryostat closed and in operation position .

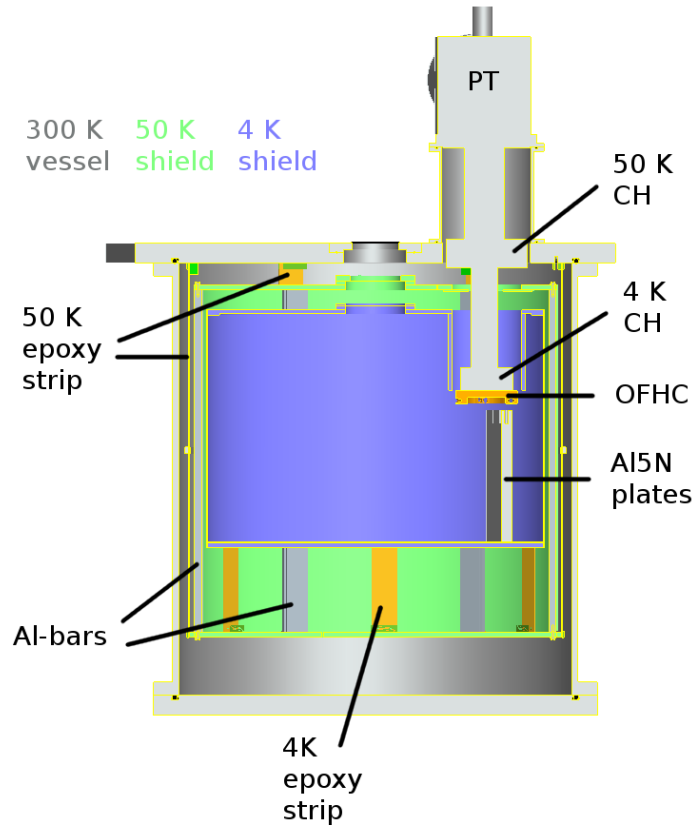


Figure 2.2: The cooling paths of the cryostat are shown in a simplified cryostat CAD model. The vessel and the radiation shields are identified by colors. All three have a cylindrical shape and are formed by a wall and two plates, the top plate (also called PT plate) is connected to the corresponding PT CH and the bottom plate (also called TL plate) is connected to the cartridge via the TLs (not shown). The 50 K cooling path to the bottom plate is done by the wall and the 6 Al-bars, 2 of these bars are identified. The 4 K cooling path to the bottom plate is done by the wall and by a direct connection from the CH. This connection is made of Oxygen Free High Conductivity Copper (OFHC) and Al5N plates. Both shields are hold by 6 epoxy strips. The 50 K epoxy strips hold the shield from the bottom plate, they hung from the top vessel plate, 2 of them are identified. The 4 K epoxy strips are shorter and are mounted between the bottom plates of both shields, 1 strip is identified, 3 are shown in the figure. See figure 2.1 for a complete CAD model, and pictures, of the cryostat.

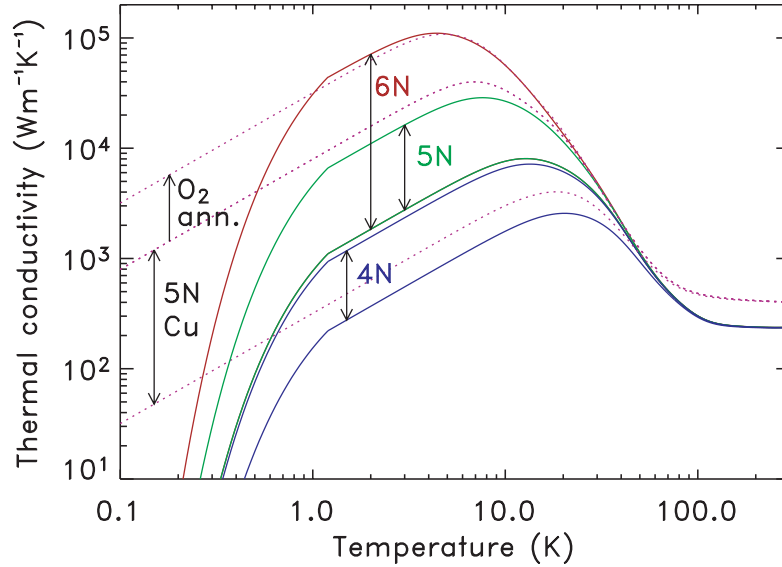


Figure 2.3: Conductivity of annealed aluminum with 4N (99.99%), 5N (99.999%) and 6N (99.9999%) purity, from [Woodcraft, 2005b].

The side walls of the shields which are made of aluminum 6082, have a thickness of 2 mm and are divided into six segments to ease access and assembly (figure 2.1 *Bottom left*). Aluminum 6082 has a higher thermal conductivity (see figure 2.5) than the aluminum 5083 and this was needed particularly in the 50 K shield to increase the thermal conduction from the top plate, connected to the PT CH, to the TL plate which does not have a direct connection to the CH. For the same reason, 6 bars made of aluminum 6082 were mounted, in the 50 K shield, between the side walls. The length of the bars is 517.5 mm and their area 40 x 10 mm².

The ideal is to always use the aluminum with the highest thermal conductivity, but the suitability for each part, availability in the market and price has to be taken into account as well.

Both shields are kept in place by means of fiberglass epoxy strips, this material was chosen because of its low thermal conductivity (see figure 2.4) combined with its high stiffness and lightness. The shields have to be held by a material that keeps them thermally isolated and that do not bend neither brake. The 50 K screen is hanging from the vessel (300 K) top cover via 6 epoxy strips of a size of 568 x 40 x 1.5 mm³ and the connection is done, on the other side, to the 50 K bottom plate because it allows longer epoxy strips to diminish the thermal conduction. These epoxy strips are installed just in front of the aluminum bars to avoid blocking the shield wall segments. To hold the 4 K shield, 6 fiberglass epoxy strips are installed between the 50 K bottom plate and 4 K bottom plate, their size is 137 x 40 x 1.5 mm³. Two TLs (chapter 3) are installed in the bottom plates (also called TL plates) of each radiation shield.

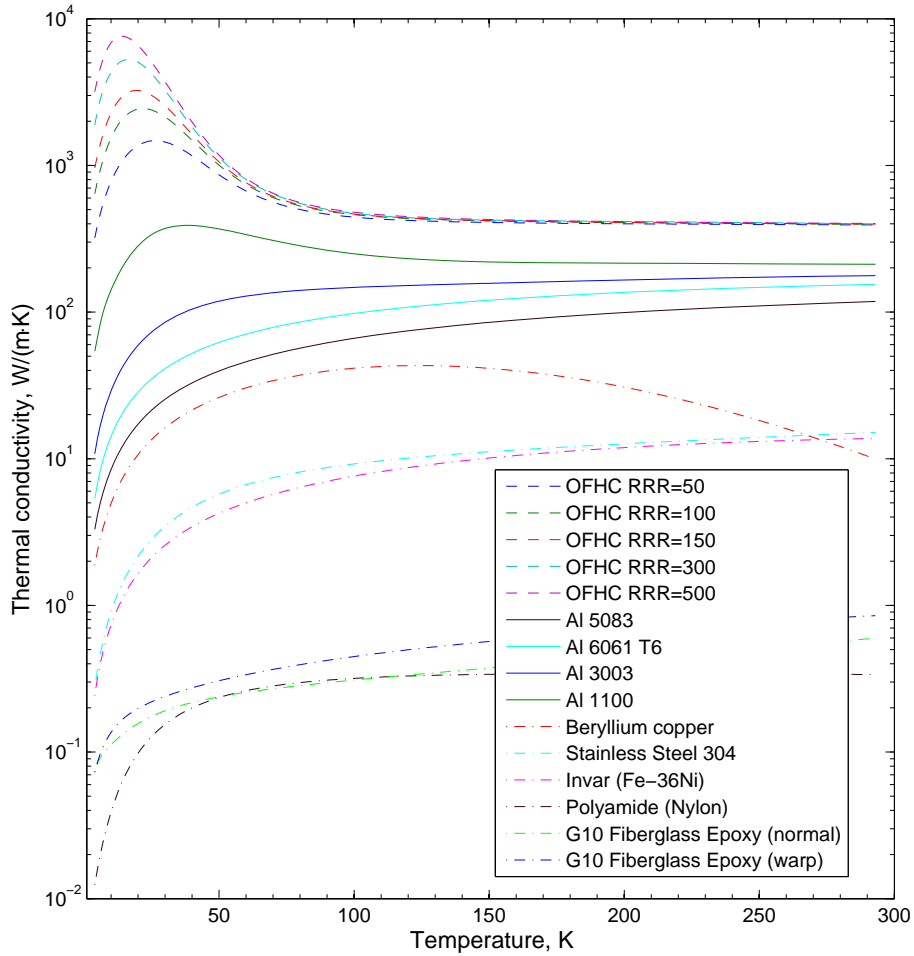


Figure 2.4: Thermal conductivity of various materials. Data based on literature, from [Marquardt et al., 2000] and the NIST^a web page [NIST Cryogenics,].

^aNational Institute of Standards and Technology

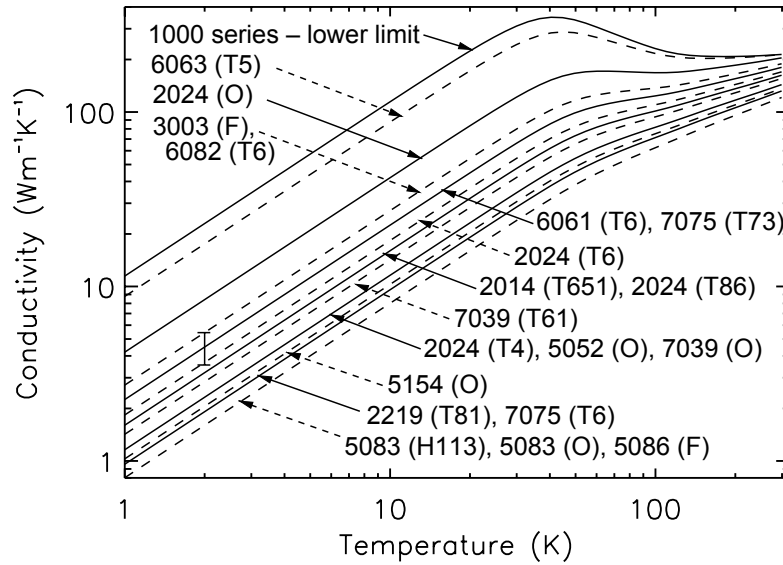


Figure 2.5: Recommended values for the thermal conductivity of various aluminum alloys, using the prediction method described in [Woodcraft, 2005a], the figure is from the same paper. Here, Al-6082 has a similar thermal conductivity as the Al-3003 which is also shown in figure 2.4.

The alignment of the two radiation shields is essential for the mounting of the cartridges and also to keep the optical path free of vignetting. The mechanical loads that could affect the alignment are the deflection of the vacuum vessel covers after evacuation, thermal contraction during cool down and also the fact that after mounting, the cryostat has to be rotated 180° to operate. First, the deflection of the 30 mm thick vessel top and bottom plates were estimated and measured (section 2.4.1) smaller than 0.5 mm, thus in agreement with the requirement. Second, the thermal expansion properties of the aluminum radiation shields were taken into account by building scaled parts that considered the shrinking of the piece from manufacturing temperature to operations temperature; see figure 3.2 for the thermal expansion of the aluminum and other materials. Besides, centering mechanisms are installed in the top plates of both shields to preserve the alignment of the entrance window, in the vessel, and the IR filters on each shield. Both are described in detail in section 2.2.3. The fact of using 6 epoxy strips is also to help in this respect, to only hold the shields, less would suffice.

The heat radiation depends on the temperature and also on the emissivity of the facing surfaces. In this respect, having two shields of aluminum is not sufficient to reduce it as much as needed. To overcome this problem, the 50 K shield has to be covered with a layer of a material with a smaller emissivity. This can be achieved by either coating the shield with for example nickel or gold, or covering it with a Multi Layer Insulation (MLI). In our case we opted for the second option, wrapping the 50 K shield with one sheet of COOLCAT

2NW MLI (see figure 2.1 *Bottom left*) that we bought from [RUAG Space Division,]. Each sheet contains 10 layers of double side aluminized, 6 μm polyester film, interleaved with 10 layers polyester non-woven spacer.

Each radiation shield is connected by the top plate to the 1st (50 K) and 2nd (4 K) CHs of the cooling system which is a 2-stage Sumitomo PT (described in section 2.2.4). These connections are done by soft and flexible Oxygen Free High Conductivity Copper (OFHC) braids to reduce the transmission of the PT mechanical vibrations to the shields, and thus to the receiver focal plane. Heat losses are also reduced due to the high thermal conductivity of the OFHC.

In the 4 K shield, an additional flexible connection is done directly from the 4 K CH to the TL plate. The 4 K stage interface is made of OFHC for the CH side and of high purity aluminum, Al5N for the 4 K TL plate, made of the same material, due to its high thermal conductivity. We avoid as much as possible different material interfaces due to their different thermal expansion characteristics. Figure 2.6 shows 4 K CH interface installed in the cryostat.

The total weight of the cryostat, including the 2 cartridges, the PT and the Cold Optics is estimated in 180 kg. The cryostat fits well inside the allocated envelope at the APEX Nasmyth A cabin, but the total weight is more than the limit of 120 kg making necessary the use of air dampers for extra support.

2.2.2 The Cartridge

The cartridge-type receiver concept was first proposed for the ALMA cryostat by RAL in United Kingdom [Orlowska et al., 2002]. This concept means that several individual receivers, or cartridges, share one main cryostat.

The adoption of a receiver cartridge philosophy provides the following benefits:

- The main cryostat can accommodate a variety of receiver configurations.
- Individual cartridges can be assembled, integrated to the cryostat and maintained independently to main cryostat.
- Reduces the maintenance time and avoids a potentially long and difficult readjustment of the external optical assembly, the parts that are not maintained are not touched. It also minimizes the risk of damage to the remaining receiver parts.
- Minimizing internal cable and harnessing inside the cryostat since all individual IF signal coaxial cables and most of the electrical connections are located on the base of the cartridge.

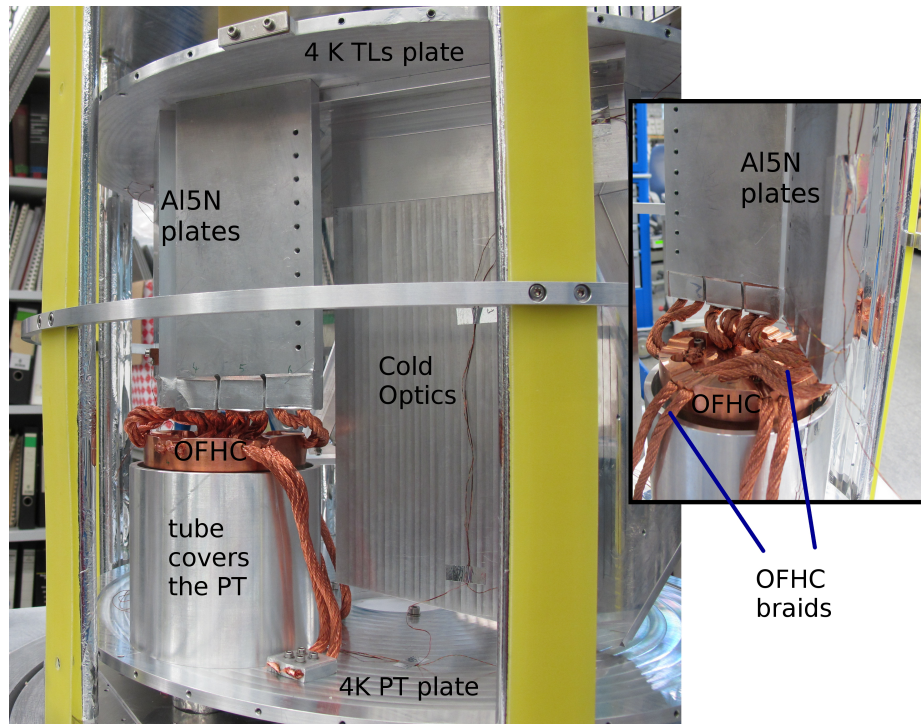


Figure 2.6: The 4 K CH interface. The interface is made of high conductivity aluminum and copper to avoid contact of different materials due to their different thermal expansion properties. In this way, the OFHC CH is connected to the OFHC part of the interface and the 4 K TLs plate made of Al5N is connected to two Al5N plates. The connection between the OFHC and AL5N parts of the interface are provided by soft braids of OFHC (to avoid the transmission of vibrations to the 4 K stage radiation shield) which are pressed in the two Al5N plates. Three small Al5N pieces are installed on the 4 K PT plate. The insert shows a view from the other side of the interface.

- Flexibility for future upgrades that could include modifications in mixer technology, number of pixels and wavelength.

Thermal connection from the cryostat to each cartridge assembly heat sink stage is provided via a thermally activated link arrangement that requires no permanent mechanical attachment. This mechanism, mounted on the 50 K and 4 K cryostat stages and called thermal link (see chapter 3), is the responsible for one significant operational advantage in that a withdrawal of a cartridge can be simply performed without disturbing the rest of the receiver.

The 1.1 THz Array Receiver is a cartridge-type receiver system containing two easily removable cartridges. The focal plane array of the receiver consists of two sub-arrays, one per cartridge.

The structural form of a cartridge module comprises a room temperature base plate that mates with the cryostat vessel and two cartridge stages to match the cryostat's 50 K and 4 K shields respectively. From the base plate, four thermal insulator (epoxy) strips hold the 50 K stage plate and from this one, three epoxy strips hold the 4 K cartridge stage (see figure 2.7right).

Like every state-of-the-art low noise astronomical detector, the SIS balanced mixer devices that will be used in the 1.1 THz Array Receiver need cryogenic temperatures. Accordingly, these devices are accommodated behind the FPU optics (section 4.3) - the cartridge's 4 K stage - and mounted on the LO Distribution Plate, part of the dedicated network required for the LO signal distribution to each of the balanced mixers (see section 4.4). Besides, due to the low level of the IF signal, the 1st amplifier has to operate at a cryogenic temperature as well so that the added amount of noise is small. Thus, these devices are also accommodated in the cartridge's 4 K stage. On the contrary, the LO multiplier chain, with the corresponding LO optics mirrors, needs to be installed on the 300 K stage. All these components together with the wires, cables and connectors form each cartridge assembly and are identified in figures 2.7 left and 4.13.

The diameter of the cartridge was defined by the estimated size of the balanced mixer blocks being currently developed. An area of 30x30 mm² was allocated for each of them. The height of each stage was determined by the components requirements in space and operating temperature. For the mixers a height of 60 mm was considered.

Both cartridges are identical in shape and composed by identical components. The orientation in which the cartridges have to be mounted is defined by the Relay Optics (section 4.2) which is in charge of transforming the telescope focal plane into the receiver focal plane, located in the two FPU optics. Thus, to have coincident beams on sky, both FPU optics have to be mounted with a relative rotation of 21 degrees (see figure 2.8). In addition, due to the shields' thermal contraction of 0.58 mm (in radius) when cooled down, two epoxy strips, mounted in the room temperature base plate, are aligned with

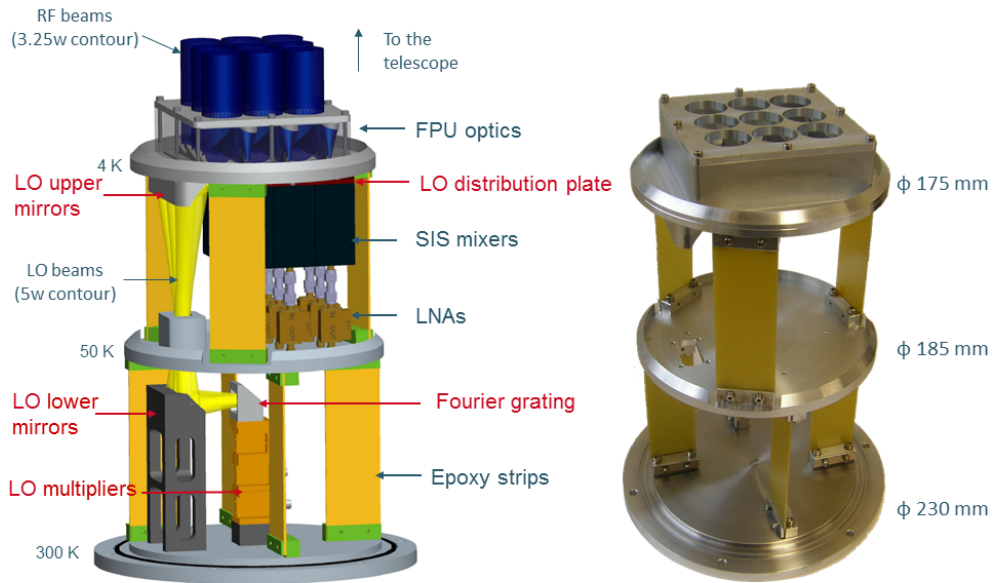


Figure 2.7: Left: CAD model of a fully populated cartridge showing the $3.25w$ beam contour of the RF beams in dark blue and the $5w$ beam contour of the LO beams in yellow. The mixers and amplifiers are only representations to show their location and allocated space. The red text points out the LO power distribution sub-system. The wires, cables and connectors are not represented. Right: Photograph of the fabricated empty cartridge. All parts are made of aluminum and held with epoxy strips. The diameter of each plate is indicated. The distance between the 300 K and 50 K stage plates is 140 mm and 136 mm from this plate to the 4 K stage plate.

the radial direction of the shield plate to allow a small displacement in this sense. This is the reason to have four epoxy strips in the 300 K cartridge plate (see figure 2.7 right).

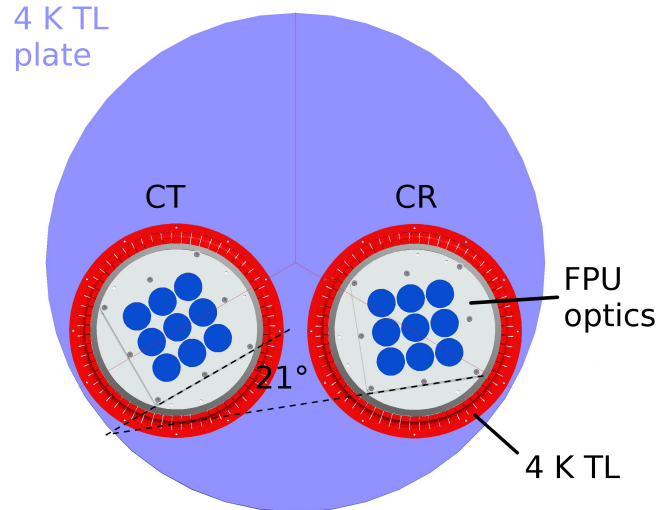


Figure 2.8: The 1.1 THz Array Receiver focal plane sub-arrays layout. It shows the relative rotation in which the FPU optics (section 4.3), and thus the cartridges, have to be mounted into the cryostat to have the Cartridge of Reflected beams (CR) and the Cartridge of Transmitted beams (CT) coincide on sky. The three red radial lines point the center of the 4 K TL plate and divide the plate in three identical parts, two of them used to position the cartridges and the third one used for the PT, present only in the top plate of this shield, therefore not in this figure.

Other Components of the Cartridge

For completion, the components of the cartridges that are not described in other sections of this thesis are briefly described below.

Low Noise Amplifiers

The LNAs should amplify the IF signal produced by the balanced mixer with low noise contribution, low power consumption and good bandwidth. Most probably this amplifiers will be of a kind such us the High Electron Mobility Transistor (HEMT) WBA-13 developed by the Caltech group and which characteristics are a noise temperature of 5 K and more than 35 dB of gain in the operations frequency bandwidth of 4-12 GHz. It requires a drain current and a gate voltage in the range of 20 mA and 1.2 V respectively, and to have this performance, the low noise amplifier has to be cooled down

to 15 K. The optimum noise performance is obtained at 20 mW of power dissipation and stays nearly constant down to 5 mW with a bias setting of 9 mA and 0.6 V [Rodriguez-Morales et al., 2004].

The Local Oscillator

One LO source is needed for each cartridge of the 1.1 THz Array Receiver. The chosen model is the solid state LO source model 1 THz Amplified Multiplier Chain (AMC), serial number VDI-AMC-S177. Its output power is between 30 and 100 μ W in the output frequency band of 1000 - 1070 GHz. The product is developed by [VDI Virginia Diodes, Inc.,]. Figure 2.9 shows a picture of the Virginia Diodes Inc. (VDI) source. The output signal is provided by a diagonal horn which defines the input beam waist, size and position, for the LO distribution optics explained in section 4.4.1.

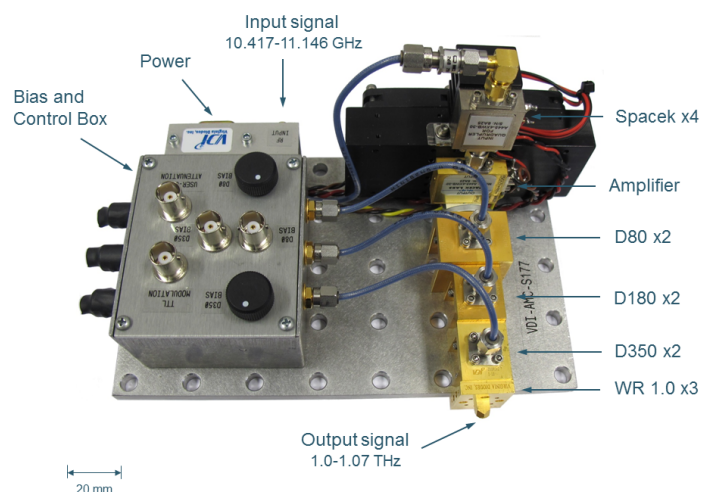


Figure 2.9: Photograph of the VDI LO source, serial number VDI-AMC-S177 which includes a 1000 - 1070 GHz amplified multiplier chain with an integrated horn output. The output power is between 30 and 100 μ W. The Bias and Control Box contains the bias adjustments, the TTL Modulation input and the User Control Attenuation Ports. The E-field of the output signal is linearly polarized vertically, perpendicular to the plate.

Wires and Connectors

Five D-type connector are planned, one on the cryostat top flange and two on each cartridge bottom plate. The ones on the cartridges should cover the need for all the wires required by the SIS balanced mixers (10 x 9), the LNAs (5 x 9), the magnets (2 x 9) and two 4-wire temperature sensors, one on each sub-array which is crucial to monitor the operation temperature of

the mixers. This makes a total of 161 wires per cartridge; as a consequence, two high density D-type connector of 104 pins are needed on each cartridge. Additionally, 13 coaxial cables and SubMiniature version A (SMA) connectors are planned on the bottom plate of each cartridge, 9 for the IF outputs and four for the LO chain. On the vessel top plate, we placed one 25 pins D-type connector which is enough for the temperature monitoring of the PT 4 K CH and of some places of the inner shields such as the 4 K TLs.

Currently, the bottom plate of each cartridge has installed two 25 pins D-type connectors and three SMA connectors which covers the needs of the receiver in the actual state and during all the tests performed as part of this thesis.

2.2.3 The Entrance Window and IR Filter

It is essential that appropriate windows are incorporated into the cryostat to permit the RF to pass between the telescope and the detectors. The type of window material selected will be determined by its transmissivity at the observing frequencies. Two types of windows are identified, the vacuum or entrance window and the IR filters. For the first one, in addition, the material can't be porous and has to be solid to withstand the pressure difference to ensure the vacuum. The IR filters are placed in the internal cooling screens to minimize the radiation heat load on the next cold stage.

The entrance window and IR filters have to be as small as possible, but big enough to let the beams go through. For the 1.1 THz Receiver, their aperture diameters were required to allow, for all 9 beams, 5 width diameter Gaussian beam propagation. To fulfill this criteria, the position selected for the entrance window is at 205 mm above the cryostat vessel top cover where the total beam cross section is smallest (see figure 2.10). This position is defined in the optical design explained in section 4.2.

The Entrance Window

Among large variety of available polymers there are some of excellent THz transparencies with relatively low reflectivity. The best material in this sense are Polytetrafluoroethylene (teflon) (PTFE), High Density Polyethylene (HDPE) and Polymethylpentene (TPX). Ultra High Molecular Weight polyethylene (UHMW) is also used. At the longer sub-millimeter wavelengths, the transmission of these polymers is structureless and flat. Going to shorter wavelengths, mainly below 200 μm , characteristic bands of intrinsic vibrations appear and scattering due to inhomogeneities increases. Polymers generally become increasingly opaque at shorter wavelengths.

Properly prepared PTFE has the lowest loss at frequencies below 200-300 GHz. It becomes lossier at higher frequencies, but the reported frequency range where the loss increases varies between different publications, probably

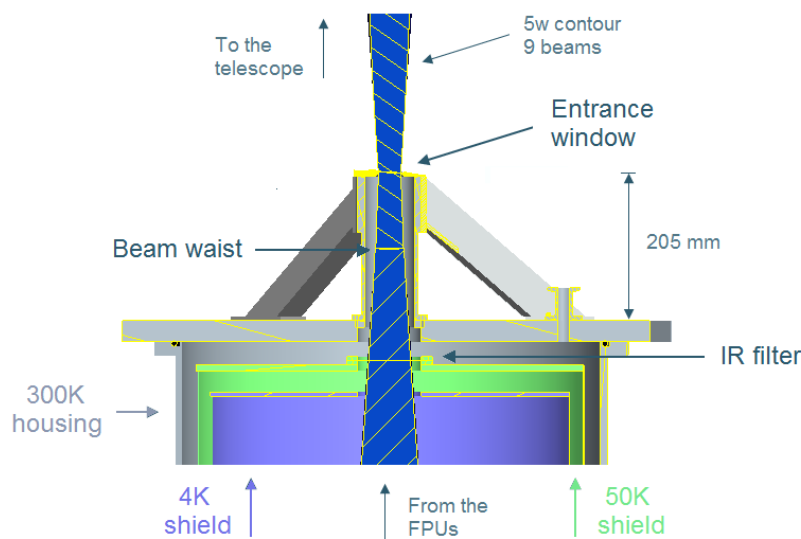


Figure 2.10: Cut view of the CAD design of the entrance window and the IR filter mounted in the cryostat. Their aperture diameters allow, for all 9 beams, 5 width Gaussian beam propagation. The entrance window is mounted on a tube at the position of the smallest beam cross section, thus avoiding the cryostat to get bigger. Here, only the 50 K shield has a IR filter installed, but in the receiver we also use an IR filter in the 4 K shield.

because of differences in the manufacturing process. Physically, it is denser than HDPE. At higher frequencies, HDPE has significantly lower loss. See figure 2.11 and [Tydex Optics,] for graphics and information about the transmission of these polymers at sub-millimeter wavelengths. In table 2.1, information about the permeability and tensile strength of these polymers is presented. SMART (490 and 810 GHz), has its entrance window made out of PTFE.

Material	σ_F [MPa]	D_{CO_2} $\cdot \frac{cm^2}{s \cdot Pa} 10^{-13}$	D_{O_2} $\cdot \frac{cm^2}{s \cdot Pa} 10^{-13}$	D_{N_2} $\cdot \frac{cm^2}{s \cdot Pa} 10^{-13}$	D_{H_2O} $\cdot \frac{cm^2}{s \cdot Pa} 10^{-13}$
PTFE	10-40	7	3	1	25
HDPE	15-40	0.3-2	0.4	0.1	10
LDPE	5-25	10	2	0.7	70
TPX	25.5	70	20	5	-

Table 2.1: The Tensile strength σ_F and the permeability at 298 K of a selection of polymers [Goodfellow,] that could act as entrance window.

Crystals such as silicon, quartz, diamond and sapphire can also be used for entrance windows in the THz regime, but they are more expensive to fabricate

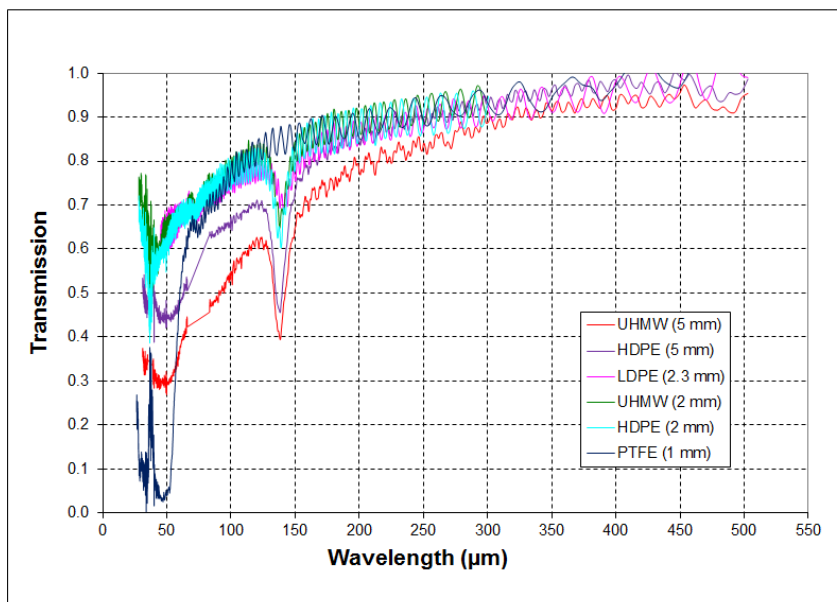


Figure 2.11: Transmission of several polymers at ambient temperatures in the sub-millimeter range. Note that the thickness of the samples is not the same. There are two sets of data for the HDPE and UHMW for comparison. Data taken from the technical report [Hurtado et al., 2007] done in the context of the ArTeMiS project.

and the high dielectric constant makes necessary an anti-reflection coating or an etched structure on the surface to minimize the reflection [Gatesman et al., 2000]. See figure 2.12 and [Tydex Optics,] for graphics and information about the transmission of these crystals at sub-millimeter wavelengths. GREAT has an etched silicon entrance window [Wagner-Gentner et al., 2005].

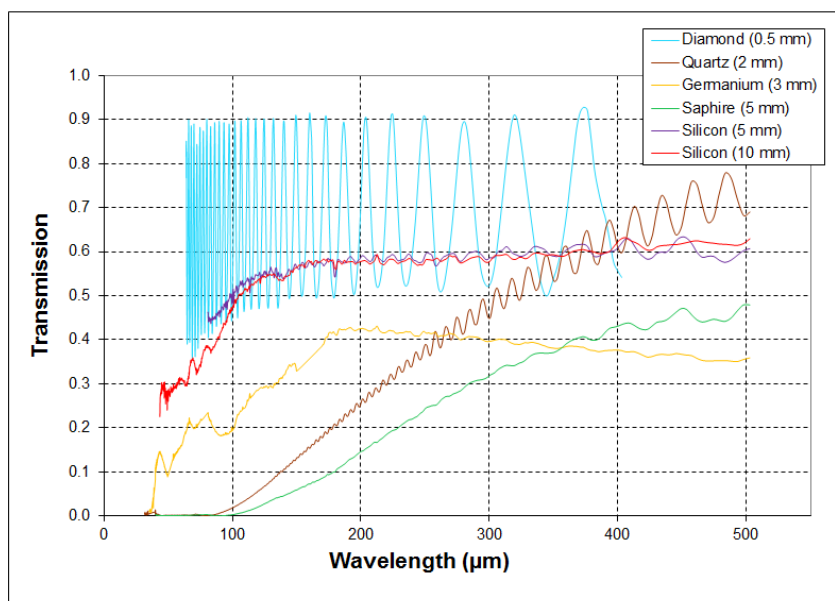


Figure 2.12: Transmission of several crystals at ambient temperatures in the sub-millimeter range. Not all the fringes are resolved, this could be misleading. All these materials would need an anti-reflection treatment unless it used in the band range of a maximum transmission. Note that the thickness of the samples is not the same. Data taken from the technical report [Hurtado et al., 2007] performed in the context of the ArTeMiS project.

We chose HDPE as the material for the entrance window of the 1.1 THz Receiver. This material satisfies the requirements already mentioned: very good transmission at the operations frequency band, lower gas permeability than, for example, PTFE and high tensile strength, see table 2.1. In addition, an entrance window made of HDPE is cheaper and easier to make than the ones made out of the previously mentioned crystals. HDPE will then be used in the following calculations to define the thickness of the window.

One would want the window to be as thin as possible to reduce absorption, but the minimum thickness is defined by the material stiffness. Nevertheless, other parameters are also involved in the definition of the window thickness. The reflection on the surfaces of the window, together with the absorption, reduce the transmission. One way to reduce the effect of the reflection is to add an anti-reflection coating, another way is to use a window thickness d of m -times half of the wavelength ($\lambda/2$), which ensures that the reflections at the

outer and inner surfaces are superposed and cancel each other, minimizing the reflected radiation. We use the second option, then the thickness should follow:

$$d_m(\lambda) = \frac{\lambda}{2n_\lambda \cos \gamma} m \quad (2.1)$$

where λ is the observing wavelength, n_λ the refractive index of the material at the observing wavelength, γ the angle of incidence and m is an integer.

Different windows thickness cause a variation of the fringe bandwidth and change of the maximum position. This makes it possible to build windows for the desired observing frequencies by varying the windows thickness and also, the tilt of the window to reduce the standing waves. Therefore precise material information and a reliable manufacture process are required. Both are not obvious. On one side, published HDPE refractive index at 1.1 THz varies from values of 1.518 [Wieching, 2006] up to 1.534 [Jin et al., 2006], passing by values of 1.524 [Lamb et al., 2001] and 1.53 [Lee, 2009]. On the other side, it's hard to manufacture a piece of HDPE with an accuracy of few microns.

In spite of this, an HDPE entrance window design was specified for the 1.1 THz Receiver. The thickness and tilt angle were chosen such that the maximum transmission is placed where the important observation lines are found. The fact that the reflectivity and transmissivity depend on the polarization of the incident wave was also considered. Thus, the calculations of the transmitted and reflected wave were done using the Fresnel formulae [Born and Wolf, 1989]. A range of refractive index from $n_{HDPE} = 1.52$ to $n_{HDPE} = 1.53$ was used in the computations, these values are the most representative found in literature. The result of the calculations using this range of refractive index, a thickness of 0.962 ± 0.005 mm and a tilt angle of 4° is plotted in figure 2.13. It can be seen that the 3 main astronomical lines are located at 95% of transmission. An entrance window of these characteristics was built in our workshop. The thickness is bigger than the minimum required to resist the pressure without breaking.

The IR filter

The IR filter must have a good transmission at the observing frequencies and good absorption in the mid-IR radiation range (the radiation of a 300 K black body peaks at $10 \mu\text{m}$).

At (sub-)millimeter wavelengths Zitex[®]¹, is commonly used as IR filter. Zitex[®] is a membrane made out of PTFE and is available in different thickness and pore size. To increase IR absorption and decrease the IR radiation by the warm IR filter, at least two layers should be used.

¹Zitex[®], manufactured by Saint-Gobain Performance Plastics

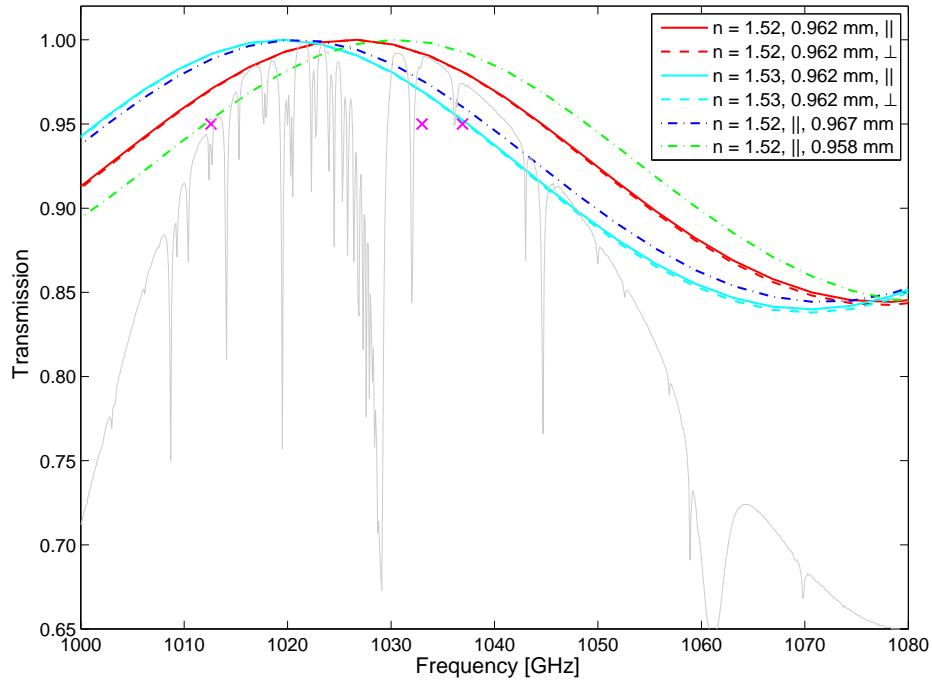


Figure 2.13: Calculated transmission of an HDPE entrance window. The first two group of lines show the transmission of parallel (entire lines) and perpendicular polarization (dash lines) for the same values of thickness (0.962 mm) and of tilt angle (4°) for a n_{HDPE} of 1.52 and 1.53. Then, since the transmissions of both polarizations are very similar, only one of them is plotted for a n_{HDPE} of 1.52 and different thickness of 0.967 and 0.958 mm. In all these variations, the important astronomical lines represented by crosses, are at a transmission of 95%. The gray line shows the estimated atmospheric transmission at APEX for 0.2 mm PWV.

Measurements of the infrared and sub-millimeter transmission of Zitex[®] has been made by [Benford et al., 2003], showing that Zitex[®] is better than teflon (thickness = 0.75mm) as IR filter, in particular the kind G108 and G110, transmitting less than 1 % in the 1-50 μm wavelength range. Other literature indicate that the transmission drops only to less than 10 % at 50 μm ([Bründermann et al., 2012]).

Transmission measurements of three types of Zitex[®] can also be seen on figure 2.14. On [Wieching, 2006] PhD thesis, the transmission at frequencies higher than 1 THz of Zitex[®] G108 and G104 were measured at 300K and 120 K for 1 and 2 layers of material. At the operations frequency band of the 1.1 THz Array Receiver, all the mentioned Zitex[®] have similar high transmission (> 95%). We decided to use 2 layers of Zitex[®], one G108 and one G110 as the IR filter in the 50 K stage and 2 layers of Zitex[®] G104 in the 4 K stage (see figure 2.10).

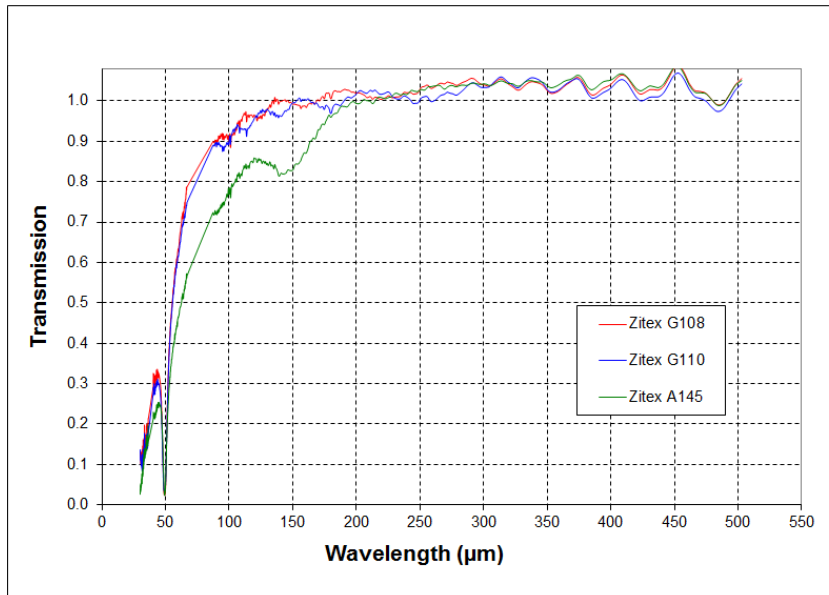


Figure 2.14: Transmission of three types of Zitex[®] at ambient temperatures in the sub-millimeter range. Data taken from the technical report [Hurtado et al., 2007] performed in the context of the ArTeMiS project.

2.2.4 The Cooling System

In the list of requirements for the cryostat (section 2.1), it is said that an appropriate cooling system has to be provided with the cryostat. This is needed to supply temperatures below 4.5 K to the SIS balanced mixers (section 1.3.4), key components of the 1.1 THz Array Receiver.

Prior to the introduction of 4 K closed-cycle cooler which use pressurized Helium gas, liquid helium was most commonly used to cool down equipment and experiments to 4.2 K. This kind of cooling mechanism has some advantages such as a cold stage temperature intrinsically stable, no need of additional power supply and no mechanical vibration are produced. On the other side, there are also some disadvantages, namely the need of liquid Helium supply, its high cost and the need of man power for refilling. As a consequence, the operating cost of a typical liquid helium cooled instrument is very high, especially in long term operations.

Closed-cycled coolers use a cyclic process to generate the cryogenic temperatures. Below some characteristics of two types of cryocoolers which are commonly used in astronomical instruments. Two-stage Gifford-McMahon (GM) refrigerator systems have been in widespread use for several decades. Room temperature helium gas is first compressed, and then supplied to the refrigerator via flexible gas lines. The compressed helium is cooled by expansion, and provides cooling to two heat stations (or CHs) on the refrigerator. After cooling the refrigerator, the gas is returned to the compressor to repeat the cycle.

PT refrigerator systems use a similar compression/expansion cycle, but eliminate the moving displacer found in GM cryocoolers. PT cryocoolers often have reduced vibration levels at the vacuum interface flange as compared with GM systems. A more detailed explanation on how the PT works together with a description of the PT chosen for the 1.1 THz Array Receiver are given below in this section.

Three main differences exist between PT and GM cryocoolers [[SHI Cryogenics Group](#),]:

- Price. In general, GM cryocoolers are somewhat less expensive than PT cryocoolers of similar cooling power.
- Vibration. Both GM and PT cryocoolers are mechanical refrigerators that do have some level of vibration, but the vibration level of a PT system is of the order of 4 - 7 μm along the axis of the cold head and $\sim 2 \mu\text{m}$ perpendicular to this axis against 20 μm and $\sim 5 \mu\text{m}$ respectively for a GM system.
- Orientation. The performance of PT cryocoolers is orientation dependent. PT cryocoolers only function properly when they are operated in a purely vertical orientation (in line with gravitation force) with the 2nd stage pointing down. GM cryocoolers will lose some cooling power when the cold head is not operated vertically, but the base temperature will not be affected. GM cryocoolers can operate in any orientation.

In the PT refrigerator, the use of an orifice and a reservoir volume to store the gas during a half cycle achieves the proper gas motion (see figure

2.15). The oscillating flow through the orifice splits the heating and cooling effects just as the displacer does for the GM refrigerators.

Available PTs use different designs, the following description should be taken as the general principle [Radebaugh, 2000]. The PT refrigerator works ideally with adiabatic compression and expansion in the pulse tube. The cycle consists of four steps:

- The helium gas in the pulse tube is compressed by a pressure pulse produced by the piston moving down.
- The compressed gas flows through the orifice into the reservoir, where the average pressure is lower, and exchanges heat with the ambient environment through the warm heat exchanger. The flow continues until the pressure in the pulse tube is reduced to the average pressure.
- Moving the piston up causes the gas to expand adiabatically in the pulse tube.
- The cooled, expanded gas in the pulse tube is forced by the gas flow from the reservoir towards the cold heat exchanger picking up heat from the object being cooled. The flow stops when the pressure in the pulse tube is increased to the average pressure. The cycle then repeats.

The function of the regenerator is the same as in the GM refrigerators; it has to precool the incoming high-pressure gas before it reaches the cold end. The function of the pulse tube is to insulate the processes at its two ends; there is gas in the middle portion of the pulse tube that never leaves the pulse tube and forms a temperature gradient that insulates the two ends.

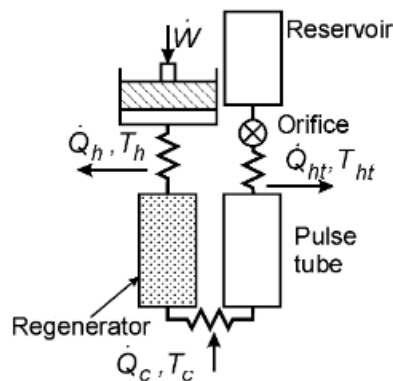


Figure 2.15: Schematics of a single stage Pulse Tube [Radebaugh, 2000].

The 1.1 THz Array Receiver Cryocooler

The RP-082B Cold Head from Sumitomo Heavy Industries (SHI) Cryogenics Group [[SHI Cryogenics Group](#),], a two-stage PT cryo-refrigerator is the chosen one for the 1.1 THz Receiver (see figure 2.16). Its function is to produce continuous closed-cycle refrigeration at temperatures, depending upon the heat load imposed, in the range of 30 K to 45 K for the first-stage cold station and in the range of 3.0 K to 4.2 K for the second-stage cold station. The RP-082B has its 2nd stage refrigerator capacity of 1.0 W at 4.2 K and 1st stage refrigeration capacity of 40 W at 45 K. See figure 2.17 for a detailed capacity map.

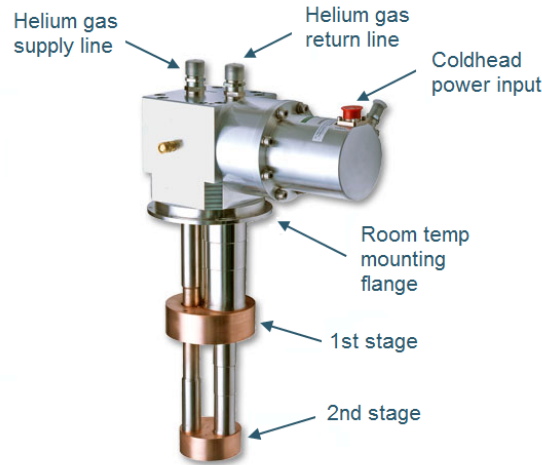


Figure 2.16: Picture of the Sumitomo RP-082B Pulse Tube, its main parts are identified [[SHI Cryogenics Group](#),].

The fact that the performance of the PT cryocooler is orientation-dependent (see figure 2.18) causes no problem for the 1.1 THz Array Receiver because it will be operated only in vertical position and the cryostat design incorporates the PT with the CH facing down when in the operation position.

The RP-082B is driven by water-cooled F-70H compressor which provides refined oil and gas management to the PT and offers a 30.000-hour service interval. For a full recapitulation of the specifications of the RP-082B PT and the F-70H compressor see table 2.2.

2.3 Heat Load Analysis

The cryostat of the 1.1 THz Multi-pixel Receiver has been described in detail in this chapter. In this section, we will do the thermal analysis of the cryostat. This is necessary to check that the heat load into the PT's stages are within

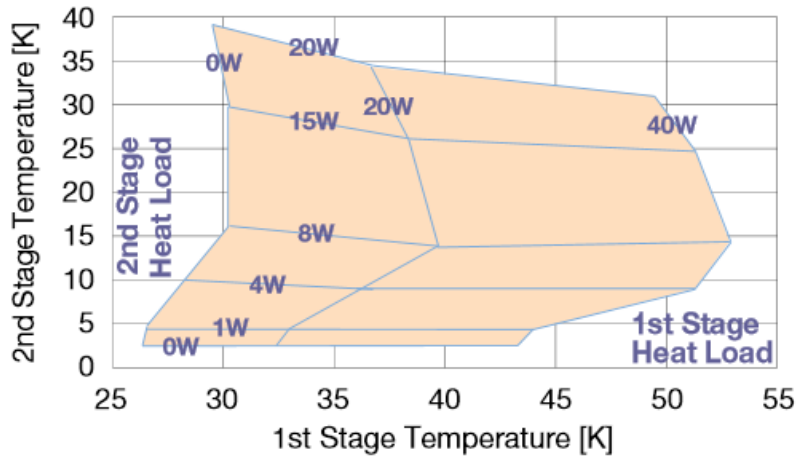


Figure 2.17: The Sumitomo RP-082B Pulse Tube Capacity Map (50 Hz). Provided by [SHI Cryogenics Group,]

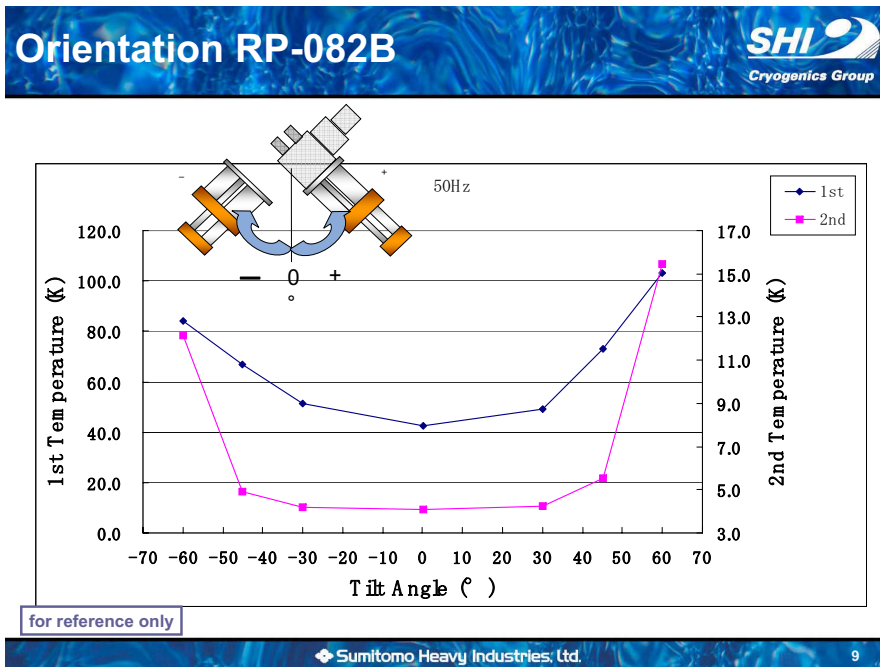


Figure 2.18: The Sumitomo RP-082B Pulse Tube capacity in function of the orientation. Provided by [SHI Cryogenics Group,]

SRP-082B-F70H	
Refrigeration Capacity ^a	
1 st Stage	40 W @ 45 K
2 nd Stage	1.0 W @ 4.2 K
Lowest Temperature 2 nd Stage	< 3 K
Cool down Time 2 nd Stage	< 80 min.
Orientation	Vertical only ^b
Ambient Operating Temperature	5 to 40 °C ^c
Vibration level	
1 st Stage	± 7 μm
2 nd Stage	± 9 μm
Helium Gas Pressure	
Static	1.65 MPa at 20°C
Operating ^d	1.90 - 2.20 MPa
Pressure Relief Valve Setting	2.61 - 2.75 MPa
Pulse Tube RP-082B	
Dimension (HxWxD)	581 x 190 x 347 mm ³
Weight	26 kg
Maintenance interval	20.000 hrs
Compressor	
Model F-70H ^e	Indoor, water-cooled
Cooling water (inlet)	6 - 9 L/min, 5 - 25°C
Flexline Length	20 m Helium Gas Lines
Dimension (HxWxD)	576 x 444 x 529 mm ³
Weight	100 kg
Maintenance interval	30.000 hrs
Electrical Power	3 phase, AC 380 - 415 V, 50 Hz
Power Consumption	7.2 kW

Table 2.2: Specifications of the RP-082B Pulse Tube and the F-70H compressor working together. Data provided by [SHI Cryogenics Group,]

^aThe refrigeration capacity is the value in the vacuum.

^b2nd stage pointing down.

^cCooling capacity may degrade by max. 5% if ambient temperature is above 28°C.

^dThe operating pressure varies according to the heat load of cold head and temperature around the equipment.

^eHigh voltage model.

their capacity so that the temperatures provided to the SIS mixers can be below 4.5 K.

The analysis is done in the steady state, when the system has reached its equilibrium. In the case of the cryostat it means when the cryostat has reached the operation temperature.

Heat transfer at low temperatures is governed by the same three mechanisms present at ambient and elevated temperatures: radiation, conduction and convection. The latter, which is the transfer of heat from a fluid to a colder surface by means of fluid particle motion is not present in the cryostat because of the vacuum. The other two ways of heat transfer are calculated in the following paragraphs. The formulas used for the calculations are mentioned and briefly described here, for more details there are many good books in the subject such as [Lienhard IV and Lienhard V, 2008] and [Flynn, 2005].

The thermal radiation is the heat exchange between two surfaces separated by a medium considered transparent. The net rate of heat transfer from the hotter surface at T_1 to cooler surface at T_2 can be calculated from:

$$\Phi_r = \sigma SF(T_1^4 - T_2^4) \quad (2.2)$$

where $\sigma = 5.67 \cdot 10^{-8} \text{ W/m}^2 \cdot \text{K}^4$ is the Stefan-Boltzman constant, S is the surface area in which the exchange happens and F is the view factor (sometimes called configuration, form or shape factor) which may be regarded as the fraction of energy leaving object 1 that is intercepted by object 2.

The view factor for close surfaces (parallels or concentric) is:

$$F = \frac{1}{\frac{1}{\varepsilon_1} + \frac{1}{\varepsilon_2} - 1} \quad (2.3)$$

where ε_1 and ε_2 are the emissivity of each surface which depend in the material and its temperature.

The heat transfer by conduction is the heat exchange between two points of a solid, liquid or immobile gas. When we are in the permanent regime, with T_1 and T_2 the respective temperatures of the two points in the solid, the heat flux is given by:

$$\Phi_c = \frac{S}{l} \lambda (T_1 - T_2) \quad (2.4)$$

where S is the area in which the heat exchange happens, l is the distance between the two points and λ (sometimes identified with the letter k) is the thermal conductivity of the material, its dimensions are W/m·K. But, λ is almost always temperature dependent, so we will use the following expression to be more precise:

$$\Phi_c = \frac{S}{l} \int_{T_1}^{T_2} \lambda(T) dT \quad (2.5)$$

where $\int \lambda(T)dT$ is the thermal conductivity integral which dimensions are W/m.

In table 2.3 the calculated radiative and conductive heat transfer from the cryostat and cartridges to the two cooling stages of the PT are listed. The heat load produced by the LO, one per cartridge, is approximately 100 μ W [VDI Virginia Diodes, Inc.,] which is negligible.

una temperatura efectiva a lo largo del epoxy de 215

We also have to calculate the heat load via the wires that are needed by the following components inside the cryostat:

- Balanced SIS mixers: The Direct Current (DC) bias current ($\approx 100 \mu$ A) is applied via a bias-T to each mixer. To monitor and adjust the bias current a set of 5 wires is required, thus 10 wires per balanced SIS.
- Magnets: A carefully adjusted magnetic field is needed to suppressed the Josephson current. It is supplied by an electro-magnet that needs a current between 50 - 100 mA, thus 2 wires per magnet.
- LNAs: The amplifier requires a DC current (10 - 20 mA), thus 2-5 wires, and a coaxial cable carrying the IF per LNA.
- Temperature sensors: Each sensor requires 4, low current (10 μ A), wires. In total the cryostat is equipped with at least 4 sensors and each cartridge has two more.
- Heaters: each one requires two wires with low resistance and high current capabilities. The cryostat is provided with three heaters. Not considered for the heat load analysis, because they are used only if the temperature has to be increase for operations or to reduce the warming up time.

The wire material should have a low thermal conductivity to minimize the heat transfer from the outside (at ambient temperature) to the inside (at cryogenic temperature) of the cryostat. And, the material should also have low electric resistance to minimize the heat input due to the current running in the wire. Table 2.4 has the thermal conductivity and the electric resistivity of some materials commonly used in cryogenic wires. In addition, the materials used for the wires have to be selected depending on the required electric current.

The Wiedemann-Franz law states that the ratio of the thermal conductivity ($\lambda(T)$) to the electrical conductivity ($\sigma = 1/\rho$), with ρ the electrical resistivity, of a metal is proportional to the temperature (T). The proportionality constant L, known as the Lorenz number, is:

$$L = \frac{\lambda(T)}{\sigma(T)T} = \frac{\pi^2 k_B}{3 e} = 2.44 \cdot 10^{-8} \text{ W}\Omega\text{K}^{-2} \quad (2.6)$$

Cryostat	T_1 K	T_2 K	S m^2	$F(\varepsilon)$	Φ_r W
Vessel \rightarrow 50 K shield	300	60	1.914	0.088 ^a	77.419
Vessel \rightarrow 50 K shield	300	60	1.914	0.013 ^b	22.759
50 K \rightarrow 4 K shield	60	4	0.988	0.046 ^c	0.048
Centering mechanism	300	60	0.009	0.247	3.130
Centering mechanism	60	4	0.009	0.119	0.002
6 G10-Epoxy strips	300	60	0.023	0.247 ^d	4.048
6 G10-Epoxy strips	60	4	0.005	0.119	0.003
Entrance window (HDPE)	300	60	0.006	0.680 ^e	1.984
IR filter (Zitex [®])	60	4	0.007	0.515	0.003
18 LNAs ^f		4			0.090
2 Cartridges					
300 K plate \rightarrow 50 K plate	300	60	0.027	0.088	2.175
50 K plate \rightarrow 4 K plate	60	4	0.024	0.046	0.002
8 G10-Epoxy strips	300	60	0.005	0.247	1.225
6 G10-Epoxy strips	60	4	0.005	0.119	0.003
			Subtotal	300 \rightarrow 60	35.321
				60 \rightarrow 4	0.151

Cryostat	T_1 K	T_2 K	S m^2	l m	$\int \lambda(T)dT$ W/m	Φ_c W
6 G10-Epoxy strips	300	60	$6 \cdot 10^{-5}$	0.568	146.800 ^g	0.093
6 G10-Epoxy strips	60	4	$6 \cdot 10^{-5}$	0.137	12.470	0.033
Centering mechanism	300	60	$6 \cdot 10^{-5}$	0.231	146.800	0.115
Centering mechanism	60	4	$6 \cdot 10^{-5}$	0.215	12.470	0.010
2 Cartridges						
8 G10-Epoxy strips	300	60	$6 \cdot 10^{-5}$	0.132	146.800	0.534
6 G10-Epoxy strips	60	4	$6 \cdot 10^{-5}$	0.130	12.470	0.035
			Subtotal	300 \rightarrow 60	0.742	
				60 \rightarrow 4	0.078	

Table 2.3: Cryostat heat exchange analysis. T_1 and T_2 are the temperature of the two surfaces or points, S is the area in which the heat exchange happens, $F(\varepsilon)$ is the form factor obtained from equation 2.3. The radiative (Φ_r) and conductive (Φ_c) heat transfer are obtained from equations 2.2 and 2.5 respectively.

^a ε_{Al} at 300 K is 0.25 and at 50 K 0.10, values for commercial unpolished aluminum [Verdier and Locatelli, 1986].

^bThe 50 K shield with a 10 layer MLI, $\approx 15\%$ of the surface is not covered. ε_{MLI} is 0.013 [RUAG Space Division,].

^c ε_{Al} at 4 K is 0.06, for commercial unpolished aluminum [Verdier and Locatelli, 1986].

^dIn the literature, ε_{epoxy} goes from 0.80 to 0.95. We use 0.95 [Everest Interscience,]. An effective temperature of 215 K along the epoxy strip is used in the calculation.

^eThe entrance window is mounted in a 90 mm diameter tube made of aluminum, cavity of emissivity ≈ 1 and. $\varepsilon_{zitex} = 0.68$ in [Clark and D'Addario, 1999].

^fConsidering that each LNA dissipates 5 mW, the mixers dissipation is negligible.

^g $\int \lambda(T)dT$ calculated from the $\lambda(T)$ values of epoxy taken from [NIST Cryogenics,]. In [Frey et al., 1981], the $\lambda(T)$ for $T > 60$ are smaller than the ones used here.

	T K	Phosphor Bronze	Manganin	Copper	Stainless Steel 304
Electrical resistivity	4.2	$1.08 \cdot 10^{-7}$	$4.38 \cdot 10^{-7}$	$1.52 \cdot 10^{-10}$	
	77	$1.12 \cdot 10^{-7}$	$4.62 \cdot 10^{-7}$	$2.03 \cdot 10^{-9}$	$5.60 \cdot 10^{-7}$
$\Omega \frac{\text{m}^2}{\text{m}}$	305	$1.30 \cdot 10^{-7}$	$4.92 \cdot 10^{-7}$	$1.63 \cdot 10^{-8}$	$10.25 \cdot 10^{-7}$
	4	1.6	0.5	300	0.3
Thermal conductivity	10	4.6	2	700	0.9
	20	10	3.3	1100	2.2
$\frac{\text{W}}{\text{m}\cdot\text{K}}$	80	25	13	600	8.2
	150	34	16	410	11.2
	300	48	22	400	15.1

Table 2.4: Electrical resistivity and thermal conductivity for some materials used in cryogenic wires. Stainless Steel’s electrical resistivity and thermal conductivity from [Flynn, 2005] and [NIST Cryogenics,] respectively. The rest of the data is from [Lake Shore Cryogenics, Inc.,].

where k_B is the Boltzmann’s constant and e is the charge of an electron. This law is helpful in obtaining a value of λ , which is usually rather difficult to measure, from an easily measured quantity. But, it usually valid only for temperatures above 100 K.

To help select the most appropriate wires, that would fulfill the requirements with minimum heat load, the common rule is to decide the length of the wire in a way that the heat load by both mechanism, dissipation and thermal conductivity, are equal. This may not always be possible, but it can be an useful starting point.

The thermal conductivity is obtained with equation 2.4 or 2.5 and the dissipation (Q) by:

$$Q = RI^2 \quad (2.7)$$

with R the resistance and I the current. This gives a wire length given by:

$$l^2 = \frac{S^2 \lambda(T) \Delta T}{I^2 \rho(T)} \quad (2.8)$$

Depending on the characteristics of the material, sometimes the recommended length of the wire will be longer than needed to diminish the thermal conductivity load. It is also recommended to heat sink the wires at the 50 K stage to reduce the heat input in the 4 K stage of the cryostat.

The calculations of the heat load produced by the wires is presented in table 2.5. The wiring of the 1.1 THz Array Receiver, when fully populated with the SIS balanced mixers, has not been defined yet and it is not part

of this thesis, so it may end up consisting of different wires than the ones selected here. However, these calculations are included to have an estimation of what could be the heat load produced by the many wires needed for this receiver, and then be able to have a complete heat load input per temperature stage to compare them with the capacities of the PT.

We also present the heat load produced by the wiring used in the current configuration of the receiver (see table 2.6), which is the status of the receiver at the end of this thesis. At this stage, there are 9 temperature sensors (5 in the cryostat and 2 on each cartridge) and 4 single-ended HEB mixers in total. Each sensor requires 4, low current ($10 \mu\text{A}$), wires and to monitor and adjust the DC bias current ($< 1 \text{ mA}$) of each HEB, 5 wires are needed.

The total heat input per temperature stage in both cases, current status and final receiver, are smaller than the capacity of the PT and can be seen in table 2.7. This cryocooler should be enough for the 1.1 THz Array Receiver in its final version. Nevertheless, these calculations are ideal, the choice of wire material and length are critical to stay below the 1 W capacity of the PT in the 4 K stage.

Heat load mechanism [W]		Φ_c	Q	Φ_c	Q
Temperature [K]		300 → 60	300 → 60	60 → 4	60 → 4
Balanced SIS					
Material	PB				
Diameter [mm]	0.127				
Length [mm]	500	$4.2 \cdot 10^{-2}$	$9.2 \cdot 10^{-6}$	$3.8 \cdot 10^{-3}$	$8.0 \cdot 10^{-6}$
# of wires	10				
# of devices	18				
Temperature sensors					
Material	PB				
Diameter [mm]	0.127				
Length [mm]	500	$7.5 \cdot 10^{-3}$	$1.6 \cdot 10^{-8}$	$6.7 \cdot 10^{-4}$	$1.4 \cdot 10^{-8}$
# of wires	4				
# of devices	8				
Magnets					
Material	Cu				
Diameter [mm]	0.160				
Length [mm]	1000	$7.4 \cdot 10^{-2}$	$2.9 \cdot 10^{-1}$	$4.0 \cdot 10^{-2}$	$3.6 \cdot 10^{-2}$
# of wires	2				
# of devices	18				
LNAs					
Material	Cu				
Diameter [mm]	0.160				
Length [mm]	1000	$1.9 \cdot 10^{-1}$	$2.9 \cdot 10^{-2}$	$1.0 \cdot 10^{-1}$	$3.6 \cdot 10^{-3}$
# of wires	5				
# of devices	18				
IF					
Material	Coaxial ^a				
Diameter [mm]	2.200				
Length [mm]	500	$1.9 \cdot 10^{-1}$	negligible	$1.6 \cdot 10^{-2}$	negligible
# of wires	1				
# of devices	18				
Subtotal		$5.0 \cdot 10^{-1}$	$3.2 \cdot 10^{-1}$	$1.6 \cdot 10^{-1}$	$4.0 \cdot 10^{-2}$
Total			$8.2 \cdot 10^{-1}$		$2.0 \cdot 10^{-1}$

Table 2.5: Heat exchange via the wires on each of the two temperature stages in the 1.1 THz Array Receiver final version.

^aThe coaxial cable has a center and outer conductor (in SS) diameter of 0.51 mm and 2.2 mm respectively and a dielectric (PTFE) diameter of 1.68 mm.

Heat load mechanism [W]		Φ_c	Q	Φ_c	Q
Temperature [K]		300 \rightarrow 60	300 \rightarrow 60	60 \rightarrow 4	60 \rightarrow 4
Ribbon cables ^a					
Material	Cu				
Thickness [mm]	0.05				
Width [mm]	0.32	$8.7 \cdot 10^{-1}$	$4.8 \cdot 10^{-6}$	$1.6 \cdot 10^{-1}$	$6.7 \cdot 10^{-10}$
Length [mm]	170				
# of wires	30 ^b				
Wires					
Material	PB				
Diameter [mm]	0.127				
Length [mm]	500	$7.1 \cdot 10^{-3}$	$4.1 \cdot 10^{-9}$	$1.5 \cdot 10^{-3}$	$8.8 \cdot 10^{-5}$
# of wires	4				
# of devices	8				
Subtotal		$8.8 \cdot 10^{-1}$	$4.8 \cdot 10^{-6}$	$1.6 \cdot 10^{-1}$	$8.8 \cdot 10^{-5}$
Total		$8.8 \cdot 10^{-1}$		$1.6 \cdot 10^{-1}$	

Table 2.6: Heat exchange via the wires on each of the two temperature stages in the 1.1 THz Array Receiver current status. In this case, a combination of ribbon cables and phosphor bronze wires are used on the cryostat for the temperature sensors; the latter only from the 4 K stage to the sensors. In the cartridge side, the wiring for the mixers is done from the 300 K to 60 K with ribbon cables and from the 60 K on with PB wires. In addition, PB wires are used for the sensors and heaters on both stages. Only the conduction is accounted for the heaters because they produce heat by dissipation when needed to increase the temperature

^aFFC (Flat-Flex-Cable) from [ES&S Solutions GmbH,]

^bWires per ribbon cable

	Heat transfer mechanism	300 K \rightarrow 60 K W	60K \rightarrow 4 K W
Cryostat+ cartridges	Conductive	0.742	0.078
	Radiative	35.321 ^a	0.151
Wires			
Final version	Conductive	0.500	0.160
	Dissipative	0.320	0.040
Current version	Conductive	0.880	0.160
	Dissipative	$4.8 \cdot 10^{-6}$	$8.8 \cdot 10^{-5}$
Receiver final version total		36.883	0.429
Receiver current version total		36.943	0.389

Table 2.7: Total heat load for the 1.1 THz Array Receiver in its final and current versions. The heat load is presented separately for the two temperature stages.

^aWith 10 layer MLI.

2.4 Cryostat Performance

The results were not the expected ones after the first cool down, several things had to be improved or modified until the required temperatures were reached. A total of approximately 15 cool downs were performed before reaching satisfactory results. With respect of vacuum, the results were as expected since the beginning of the tests. In this section, we present some of these cool downs and the tests done in the process of troubleshooting.

The results concerning the thermal links performance and the optics tests are presented in sections 3.5 and 4.5 respectively.

2.4.1 Vacuum Tests

During the tests in the laboratory, a pressure of few 10^{-7} mbar was generally reached. This pressure did not change when the cryostat started to be tested, open to external radiation, with the HDPE entrance window (see section 2.2.3). Previously, before lower temperatures were reached, the cryostat was tested closed, with an aluminum plate instead of the HDPE. See figure 2.19.

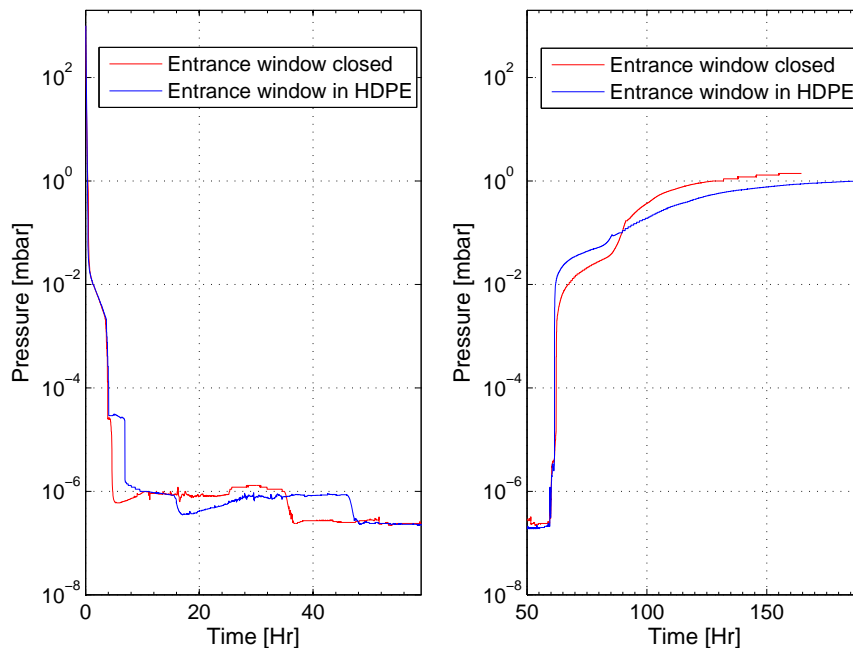


Figure 2.19: Pressure measurements during the cool down and warm up cycles. The red line data was taken with the cryostat closed to external radiation and the blue line with the entrance window in HDPE, therefore open to the RF. The PT was started after 4.4 and 15.6 hours respectively, on both cases a pressure of few 10^{-7} mbar is reached. In the warm up cycle, it can be seen that the pressure goes up to $\approx 10^0$ mbar, to reach the ambient pressure one has to open the vacuum valve (not shown here).

The cryostat was evacuated with a turbo-molecular pump during 4 hours to reach a vacuum of $\approx 4 \cdot 10^{-5}$ mbar. When this vacuum is reached, the PT is started. Then, during the cool down, the vacuum improves due to the freeze-out of residual gases, reaching 10^{-7} mbar and remaining at this value or better during the tests in the laboratory.

2.4.2 Temperature Tests

The temperature sensors installed in the cryostat and cartridges are silicon diodes, series DT-670, from [Lake Shore Cryogenics, Inc.,]. We use non-calibrated and calibrated sensors with an accuracy of 0.5 K and 0.1 K respectively.

Cooling down and warming up time

The cooling down cycle of the cryostat is shown in figure 2.20, it takes approximately 32 hours to reach the operation temperature when the Cold Optics is installed, increasing the cool-down time by approximately 10 hours. The warming up cycle can be seen in the same figure, the cryostat takes approximately 80 hours to reach ambient temperature, but after 50 hours the temperature is high enough to be able to open it. With heaters, this time can be reduced.

Temperature ripple

PT coolers have a cyclic cooling process that provoke temperature oscillations on its first and second stages which correspond to the 50 K and 4 K CHs respectively. The 4 K CH and focal plane temperatures were measured with a time resolution of 16 Hz to be able to resolve the temperature variations. The corresponding data can be seen in figures 2.21 and 2.22 respectively. The temperature oscillations in the 4 K CH are of ≈ 300 mK at 1.7 Hz and they are reduced, in the focal plane, to less than 6 mK at a much slower rate. The latter was measured when the TL Al-5083 (see chapter 3) was used, when a TL with a higher thermal conductance is used a better coupling with the temperature oscillations of the CH would be present. In the case of the TL Al-1050 with the nylon ring, a temperature oscillation of 25 mK - in average in 30 minutes - was measured in the focal plane with a data sampling of 1 Hz (see figure 2.23) which should be a good representation of the situation with respect of temperature, but it can not resolve the oscillations period.

Longer time variations can be seen in figure 2.24 which shows measurements taken during 40 and 60 hours with the cryostat open and close to external radiation respectively, but with no extra heat load. The maximum variations are of 1 K in the 50 K cartridge stage and of 60 mK in the 4 K cartridge stage. Temperature variations of this kind and value do not affect

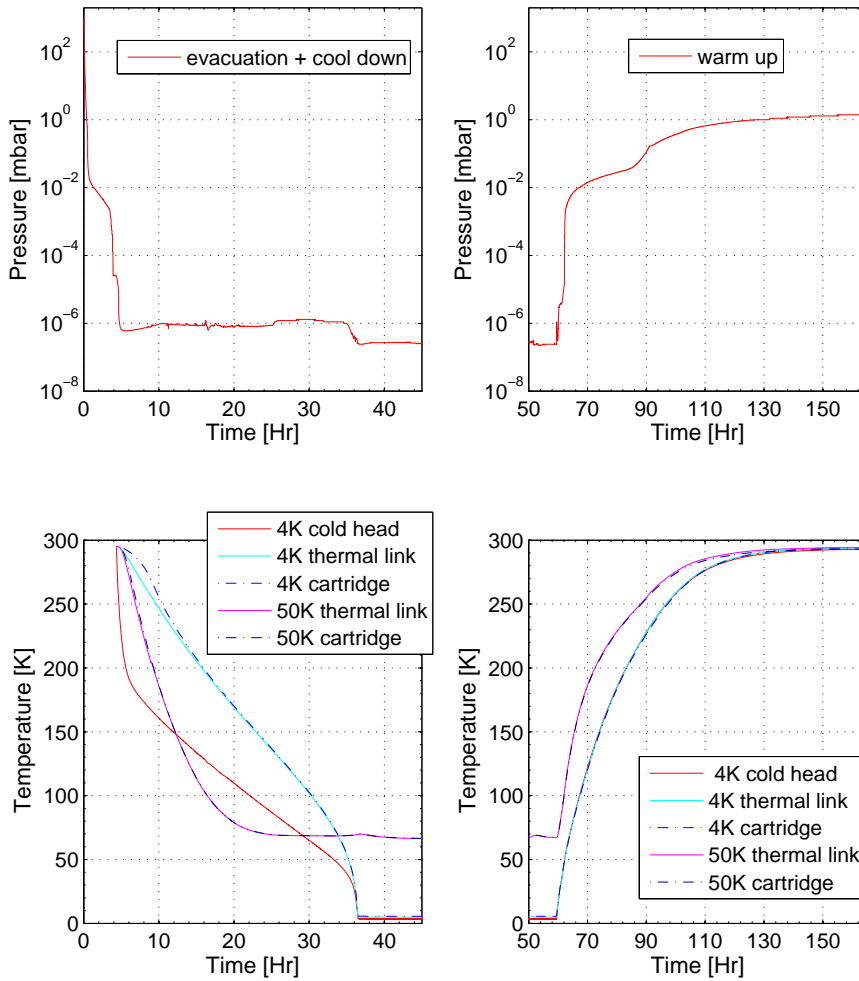


Figure 2.20: Cool down and warm up cycles, pressure (top) and temperature (bottom) versus time. The time scale is the same for both plots which helps to see that the PT is started after 4 hours, when the pressure is 10^{-5} mbar, and how the vacuum improves when the PT is started. The cool down takes 32 hours, it was performed on the 09.12.2013 with the Cold Optics installed and the cryostat closed to external radiation (aluminum plate instead of the HDPE entrance window). Only the temperatures of the CR were measured.

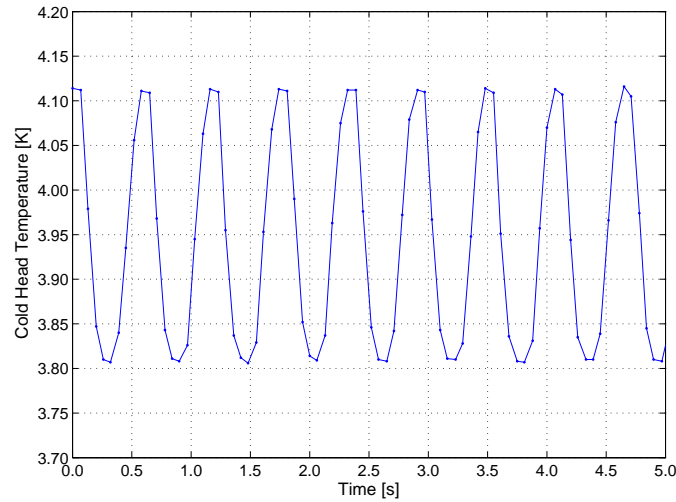


Figure 2.21: Temperature oscillations at the 2nd stage CH of the PT measured with a time resolution of 16 Hz, the points show the taken data. The temperature oscillations are of approximately 300 mK and at a rate of 1.7 Hz.

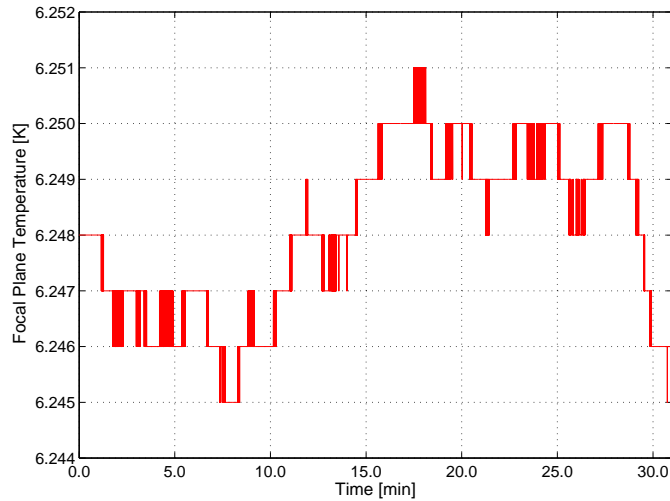


Figure 2.22: Temperature oscillations at the focal plane measured with a time resolution of 16 Hz. The plot shows the data taken during 30 minutes. Noiseless periods can be seen, for example 100 secs, where the temperature oscillations of the CH, shown in figure 2.21, are not present. In addition, mid-term behavior can be observed with a temperature variation of 6 mK instead of the 300 mK shown in the previously mentioned figure. Data taken when the TL Al-5083 (see chapter 3) was installed, when a TL with higher thermal conductance is used, a better coupling with the CH temperature oscillations would occur (see figure 2.23).

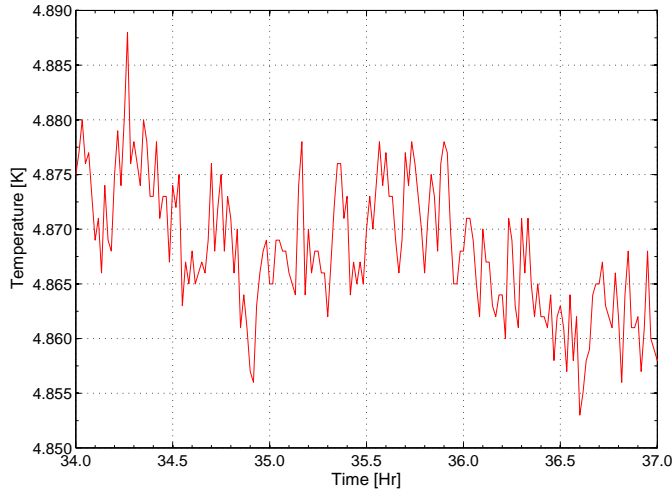


Figure 2.23: Temperature oscillations at the focal plane measured with a time resolution of 1 Hz when using the TL Al-1050 with the nylon ring (see chapter 3). The plot shows the data taken during 3 hours. Mid-term behavior can be observed with a temperature variation of up to 25 mK in 30 minutes instead of the 6 mK shown in figure 2.22. Even if measured with a smaller sampling rate, it shows the better coupling with the CH temperature oscillations (variations are bigger), but it can not resolve the period of these oscillations.

the operations of the receiver. These variations may be related to the tap water temperature difference between day and night with which the PT is cooled down.

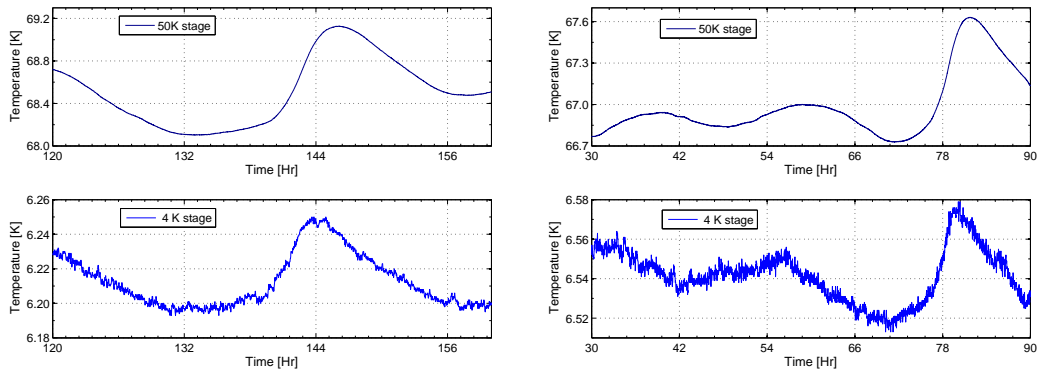


Figure 2.24: Long term temperature fluctuations on the cartridge stages taken with a time resolution of 1 Hz. The plots show the variation in 40 hours (left) and 60 hours (right), without extra heat load, of the 50 K and 4 K cartridge plates. The maximum variations are of 1 K and 60 mK respectively. Temperature variations of this kind and value do not affect the operations of the receiver.

Heat load tests of the PT

Due to the difficulties to reach 4.2 K on the second stage of the PT, it was necessary to do a heat load test on this stage to understand the behavior of the PT and check if the higher temperatures were a consequence of unexpected higher heat load and not due to a malfunctioning. A heat load test of the first stage was also done to see the behavior of the 4 K stage when the first one bears higher heat load.

Heat load on the 4 K stage

The test was done in the following way: the 4 K shield of the cryostat was disconnected from its corresponding CH. In this way, the latter would not be loaded with the shield, but instead with a resistor of $R = 100 \Omega$ placed on the 4 K CH of the PT. The resistor was connected to a power source which was able to load it with up to a voltage (V) of 30 V. The temperature of the 4 K cold head as well as 7 other positions in the cryostat were measured by DT-670 silicon diodes. The test started with the measurements of the initial state, when no voltage is applied to the resistor. The temperatures were measured every 60 seconds and during 20 minutes before increasing the voltage in 2.5 V. This procedure was repeated until reaching 20 V equivalent to a power ($P = V^2/R$) of 4 W.

The measurements were done twice meaning that the described procedure was repeated 40 hours later to let the 4 K shield get colder and in this way reduce its radiative heat load onto the 4 K CH. Between both measurements the 4 K shield got 30 K colder, from 222 K to 191 K. It can be seen in figure 2.25 that the 4 K shield is getting colder continuously.

The result of the test, zooming into the 4 K stage temperatures, is shown in figure 2.26. Afterward, to estimate the heat load difference between both set of measurements, the data was plotted and fitted with a straight line in figure 2.27. The answer is that the temperature difference of the 4 K shield means 260 mW less heat load in the second test, enough to reduce the heat load below 1 W (down to ≈ 740 mW) and accordingly diminish the 2nd stage CH temperature to 3.7 K. The capacity map of the PT does not allow us to say that this level of heat load corresponds to this exact temperature, it doesn't provide enough resolution to do this, but we can confirm that the PT can provide temperatures ≤ 4.2 K which was the objective of this test.

In figure 2.25, it can be seen a correlation in both shields temperatures. The 50 K shield temperature increases when the 4 K CH is being loaded during both tests. This is confirmed with the test explained in the next

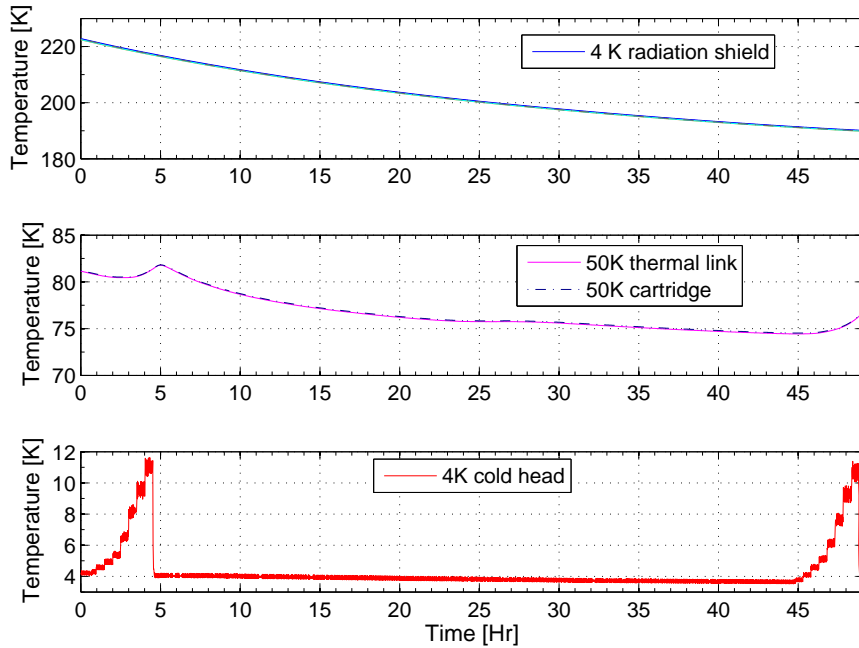


Figure 2.25: 4 K stage heat load tests results. Test done with the cryostat closed to external radiation. The 4 K CH of the PT is not connected to the 4 K shield, instead it is loaded via a resistor of 100Ω installed on it. The voltage was increased in steps of 2.5 V and the temperature was registered every minute. The plot shows all the measured temperatures during both tests separated by 40 hours. In red (bottom), it can be seen the response of the 4 K CH temperature as consequence of the increment in the heat load, separated by the period of time indicated above. The other 5 temperature curves that were measured in the 4 K radiation shield can not be identify separately (top), their temperature difference is less than 1 K. Same thing for the two measurements of the 50 K stage (middle). The 4 K stage was continuously reducing its temperature as well as the 50 K stage. However, it can be seen that the 50 K stage TL and cartridge increase their temperature as a consequence of the 4 K heat load increments. This correlation in the temperature of both stages is observed during both tests.

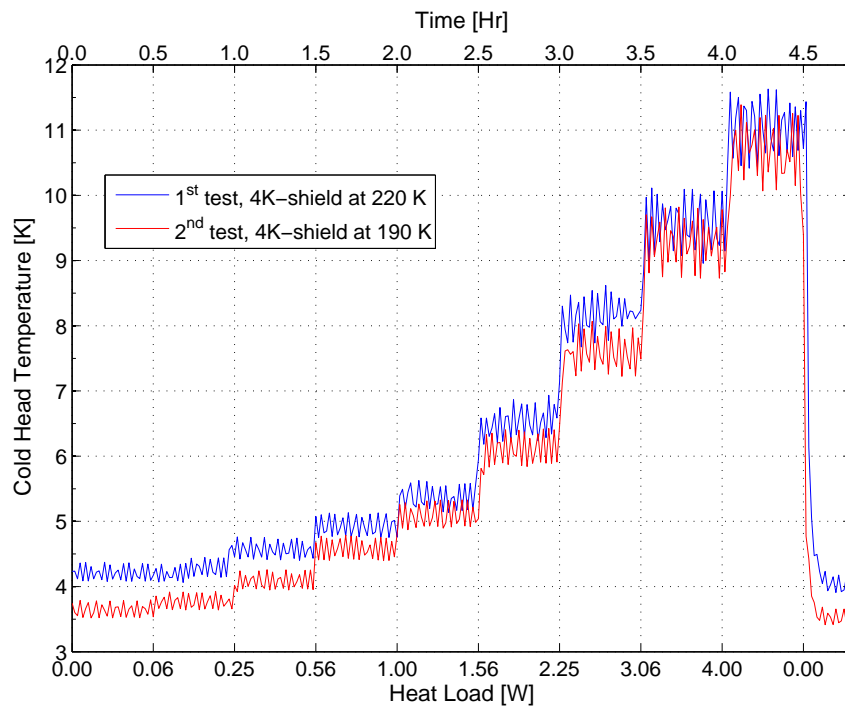


Figure 2.26: 4 K heat load tests results, zooming on the 4 K CH temperature. Both measurements were taken with 40 hours difference to let the 4 K shield get colder and have measurements at a different heat load level. At the beginning of the first test, the CH temperature is 4.2 K, therefore the heat load in the second stage is already 1 W according to the capacity map (see figure 2.17). At the beginning of the second test, the PT CH temperature is 3.7 K, thus the heat load is less than 1 W. To have an estimation of the heat load difference see figure 2.27. However, we can already conclude that the PT is able to provide temperatures ≤ 4.2 K and thus, that it works properly.

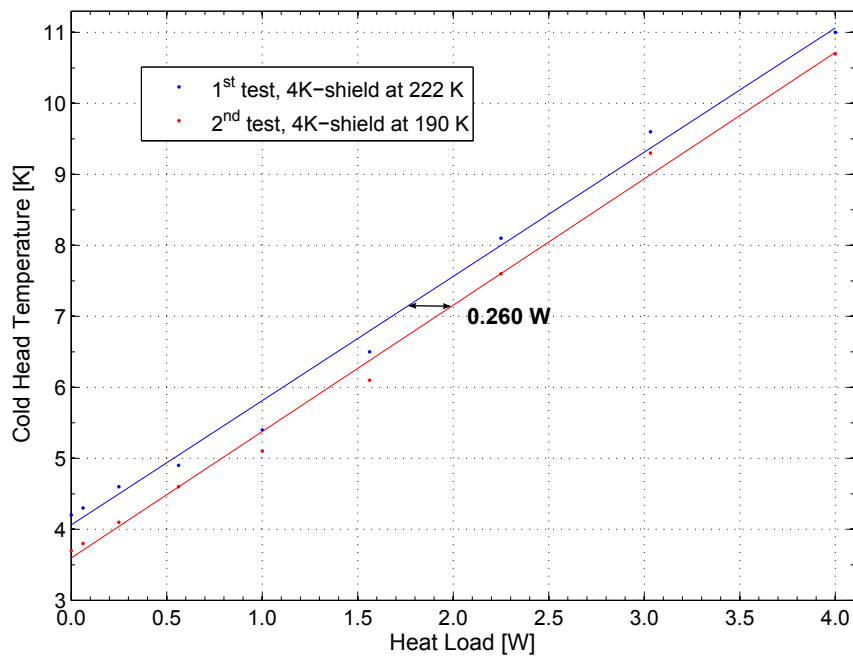


Figure 2.27: The points correspond to the data plotted in figure 2.26 and the lines are the fitted curves. The load difference between both tests is approximately 260 mW which corresponds to the difference in heat load (horizontal-axis) from both curves. From these curves we can also conclude that the 4 K CH, at this load conditions, has an increase of cooling capacity of 565 mW per Kelvin.

paragraphs.

Heat load on the 50 K stage

The heat load test of the 50 K stage was done in a similar way as the one for the 4 K stage, but in this case the 50 K shield was not disconnected from its corresponding CH, neither was the 4 K shield. A resistor, of 75Ω , was placed in the 50 K CH of the PT to produce the additional heat load. The test was done from the initial state, when no voltage is applied to the resistor, to the final state, when a maximum of 25 V is applied, equivalent to a load of 8.3 W. The increment in voltage was done in steps of 5.0 V.

Figure 2.28 shows the results of this test where it can be confirmed the correlation between both stages. This means that, at the current levels of heat loads in the PT, when one of the two stages is loaded, the temperature of the other stage also rises. Thus, the heat load in the 50 K stage also has to be reduced (or not increased) to be able to reach the needed 4.2 K in the second stage of the PT. In the PT capacity map, it can be seen that this is the behavior when the first stage has temperatures between 33 K and 50 K, when the temperatures are < 33 K, this correlation is no longer valid and a decrease in this temperature would produce an increment in the second stage temperature which is something we have to avoid.

It has been shown that the PT works properly, thus the problem for reaching colder temperatures during our tests were due to some unexpected, undesirable, heat load sources in the cryostat. Thus, after these tests, we looked for any unexpected load particularly the ones that could come directly from the 300 K into the 4 K stage.

Three main strategies were followed to obtain the needed improvement. First, improve the thermal conduction on each shield by the use of aluminum and/or copper with higher thermal conductivity and also by improving the interface between the PT CHs and the shields. Figure 2.6 shows the 4 K CH interface. Second, look for and reduce all possible unwanted radiation heat load that could come directly from the 300 K into the 4 K stage. Among others, the hole for the PT in the 50 K radiation shield was covered with an aluminum plate, the small gaps left between the 50 K wall segments and the aluminum bars were closed by wrapping the bars with a 10 layer MLI sheet and the space between the 50 K TL fingers were closed by means of a special cover designed for this purpose (see figure 3.7). And last, correct any possible thermal leak caused by an unwanted contact between the shields.

Figure 2.29 presents the temperatures in the cryostat of a selection of 7 cool downs to show the evolution toward operation temperatures. The two cool downs, in which both cartridges temperatures were measured, show that the TLs have reached temperatures ≤ 4.2 K which is very good, but the temperatures in the cartridges plates still needed improvements to be able to operate with SIS mixers. After that, a nylon ring was installed around the

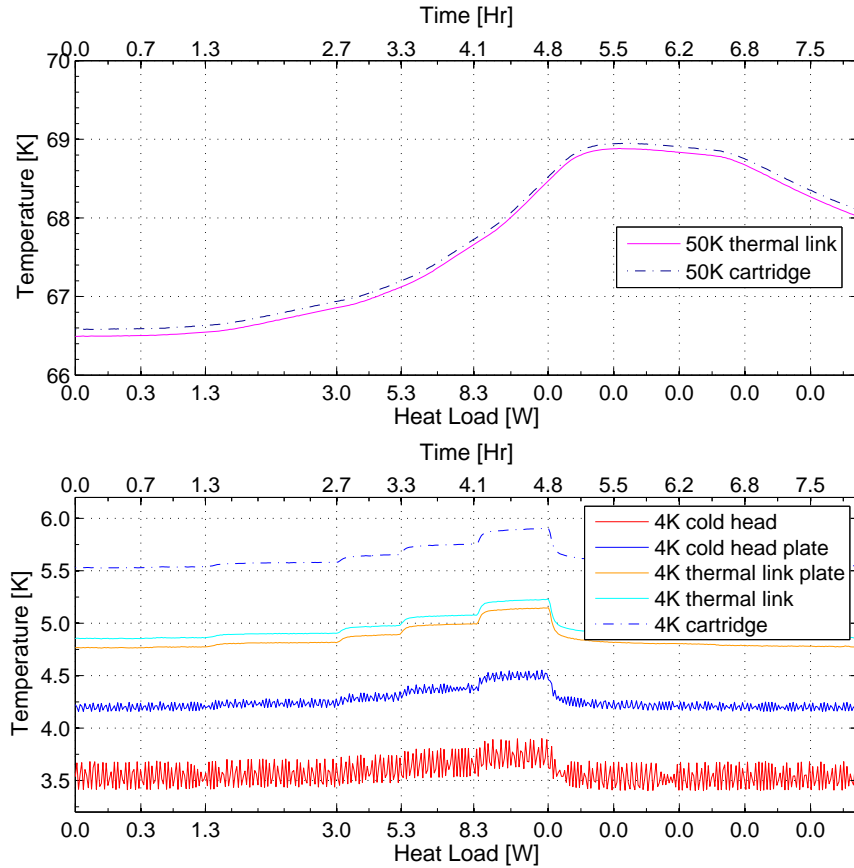


Figure 2.28: 50 K stage heat load test. For this test the cryostat was closed to external radiation and, in addition, both shield's entrance were also covered with an aluminum plate. A 75Ω resistor was installed in the 50 K CH of the PT and loaded in steps of 5 V up to 25 V, equivalent to 8.3 W. The load increment did not happen at regular intervals, but this does not affect the information obtained from the test. It can be seen that an increment in the heat load applied to the 50 K CH, also causes an increment in temperature of the 4 K stage. The temperature sensors in the 50 K stage are in the TL and the cartridge plate, thus far from the CH (without direct thermal connection to it). This explains why the temperature changes takes longer to be observed in this stage than in the second stage of the cryostat. The temperature in the 50 K CH is approximately 30 K lower.

TL Al-1050 to improve its thermal conductance (see section 3.5.2) with very good results. The last measurement included in this figure shows the best performance of the cryostat. Here, the cartridge plate temperature reached 4.4 K. Unfortunately, only the 4 K stage temperatures of the Cartridge of Reflected beams (CR) are presented because, during this cool down, the FPU optics of the Cartridge of Transmitted beams (CT) was being tested (beam measurements) and thus it was mounted just below the entrance of the 4 K radiation shield (see section 4.5.3).

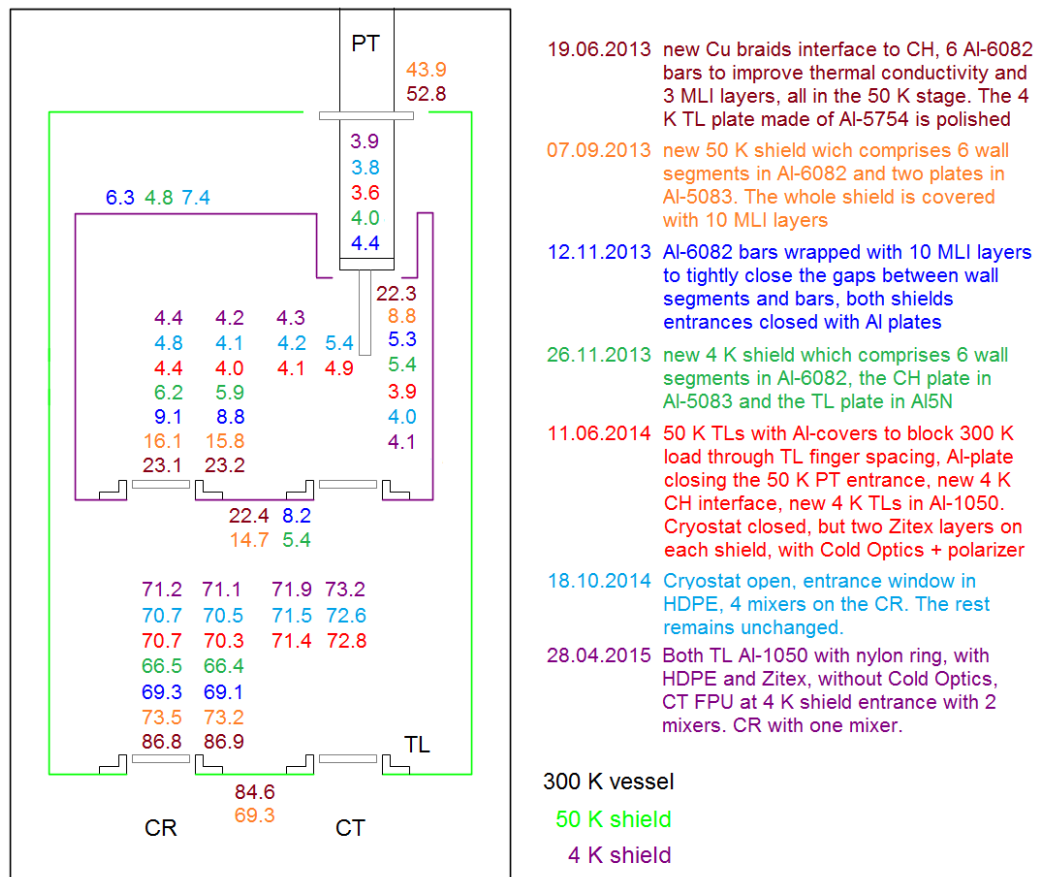


Figure 2.29: A selection of seven cool downs to show the main steps towards the operation temperature. In the cryostat, the PT is at the same distance from both cartridges, here it is closer to the CT due to a display choice. Because of a limited number of temperature sensors, the measured temperatures are not always the same, they vary through the cool downs for diagnose purposes. From the 11.06.2014 we had the necessary equipment to also measured the CT temperatures. The best performance of the cryostat is when the CR cartridge plate temperature reached 4.4 K. the CT temperature on the 4 K-stage could not be measure this time, this was the last test performed during this thesis. The Cold Optics has a temperature of 4.6 K, in average, when measured in the last cool downs (not in the figure).

2.5 Summary

A cryostat that fits the two cartridge with all the necessary components - described in this chapter - has been built, assembled and tested in the laboratory. Most of the parts of this cryostat were built in our workshop.

The cartridge philosophy allows easy maintenance and troubleshooting since it is possible to remove and repair cartridge components without having to open the whole cryostat neither to dismount it from the telescope and thus reduce observing downtime. The same advantages are also valid when testing in the laboratory.

Due to the SIS balanced mixers' requirement of low cryogenics temperature, a 2-stage PT was incorporated in the cryostat. Flexible connections from the PT cold heads to the radiation shields were designed to prevent the transmission of mechanical vibrations to the receiver focal plane, where the mixers are mounted.

An entrance window made of HDPE was developed, this material was selected due to its high transmission at the operation frequencies, low gas permeability and strength to withstand the pressure difference. Zitex[®] was chosen as the material for the IR-filters because of its good absorption in the mid-IR and good transparency in the receiver frequency band. 2 layers of Zitex[®] are use in the 50 K and 4 K shields.

Approximately 15 cool downs were performed before reaching temperatures that could allow operation with the HEB mixers. In this chapter, it was explained the strategy followed to reach the required lower temperatures, e.g. reduced the unanticipated direct 300 K radiation into the 4 K stage, replaced parts of the radiation shields with higher conductivity aluminum.

The final temperature provided to the FPUs also depends in the thermal conductance of the TLs (see chapter 3), the best results were obtained during the latest cool downs when using the TL made of aluminum 1050 with the nylon ring. In this case, a temperature of 4.4 K was reached in the CR. Unfortunately, the temperature of the other cartridge could not be measured.

The calculated heat load of the current receiver version is similar to the one estimated for the final state, when the receiver will be fully populated with 18 SIS balanced mixers. One of the reasons for this, is that in the current version, the heat load produced by the wiring (white ribbon cables) can be reduced and has to be changed. Therefore, we can conclude that the cryostat is suitable for the use with HEB mixers and it should also be the case with SIS balanced mixers, provided that the adequate wiring is used.

Chapter 3

The Thermal Links

The 1.1 THz Array Receiver is a cartridge-type instrument. Its cryostat fits two easily removable cartridges containing 9 SIS balanced mixers each. The mixers require an operation temperature below 4.5 K (section 1.3.4). The cryostat and the cartridges developed during this thesis are described in chapter 2 and section 2.2.2 respectively.

The cooling of the cartridges, where the detectors are mounted, is provided from the cryostat via a thermally activated link arrangement (the TL) that requires no permanent mechanical attachment, that is to say, it does not need to be physically bolted to a cartridge stage. This concept provides a significant operational advantage in that the withdrawal of a cartridge, to be maintained or repaired, can be simply performed at room temperature and ambient atmospheric pressure without disturbing the rest of the receiver and cryogenics systems. This minimizes the risk of damage to the remaining receiver parts, reduces observing downtime and maintenance time because it avoids a potentially lengthy and difficult readjustment of the external optics since there is no need to dismount or separate the other parts from the vacuum vessel, which can remain mounted in the laboratory or in the telescope cabin.

In this chapter, we present the new all-metal TL that was developed, during this thesis, to connect the cartridges to the cryostat thermally and mechanically. We start by describing the TL in section 3.1, followed by the explanation of its design (section 3.2) and the description of the different TLs that were built (section 3.3). Then, we calculate their thermal conductance (section 3.4) and lastly, in section 3.5, we show the results from the laboratory tests including the thermal conductance measurements of the three TL types that were built.

3.1 Thermal Links Description

The design of the TL is inspired by the concept first proposed by RAL for use in the ALMA receivers [Orlowska et al., 2002], which was slightly large and complicated in its first iteration. An updated design, suitable for all the 170 mm - diameter - cartridges is shown in figure 3.1 *top*. A simplified version was then designed in [Yokogawa et al., 2003] as part of the development of a 3-cartridge test cryostat for ALMA. This TL is composed of a crown-like ring made of OFHC and a clamping belt made of nylon (figure 3.1 *bottom*).

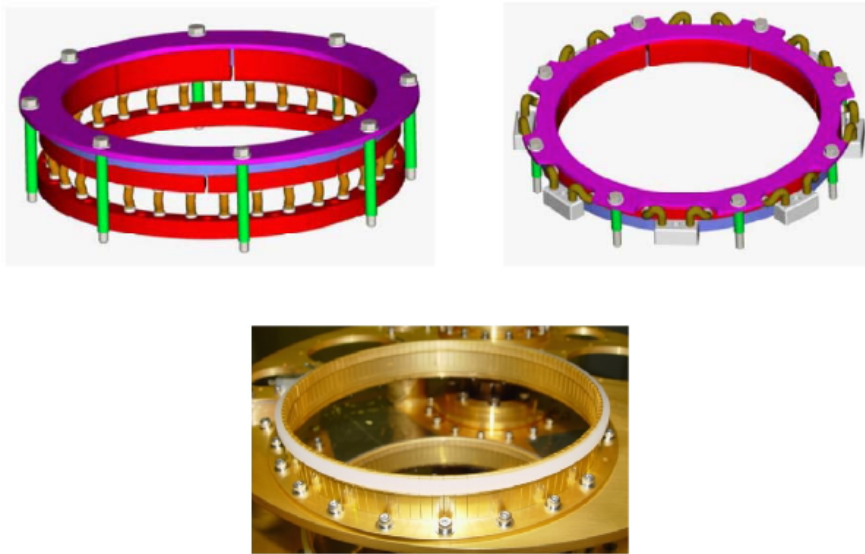


Figure 3.1: Top: Two models of the ALMA thermal link arrangement, the 4 K TL (left) and the 12 K and 70 K TLs (right). Bottom: Picture of the TL composed of a OFHC crown-like ring and a nylon clamping belt (white ring) used in the 3-cartridge test cryostat for ALMA. Figures from [Orlowska et al., 2002] and [Sekimoto et al., 2003] respectively.

In the case of the OFHC-nylon model, the fingers close into the cartridge plates with an external force provided by the nylon ring produced due to its higher thermal contraction under low temperature. The nylon ring is installed in the higher part of the fingers, embracing them. This produces the needed contact for the thermal conduction.

One of the important characteristics required for the new TL that developed for the 1.1 THz Array Receiver was that it could not include any plastic, thus requiring an all-metal design. The reason for this is that material properties of metals are better known and more reproducible (from different providers) and that the plastic may age faster.

In the case of the all-metal design, a metal ring is placed in the inner diameter of the lower part of the TL (see figure 3.3). Its purpose is to block

the thermal contraction of the lower part of the fingers, forcing rotation and bending reactions in different parts of the fingers. As a consequence, the higher part of the TL fingers will close the gap and make contact with the cartridge plates. This is explained in detail in section 3.2.

As a consequence, the employed materials should have the largest possible difference with respect of thermal expansion characteristics. We needed one material that would exhibit a large dimensional change with temperature changes for the crown-like ring and one that would react as little as possible for the metal ring.

As first material, we chose aluminum instead of copper because it has a higher thermal expansion coefficient. See figure 3.2 for the thermal expansion characteristics of different materials. In addition, it was also decided to avoid, where possible, interfaces between different materials and since the TL plates of both cryostat's radiation shields as well as the FPU optics in the cartridges are made of aluminum (see chapter 2), the decision to use aluminum was confirmed. However, the thermal conductivity of the material (see figure 2.4) of which is made the crown-like ring is also important because a main objective of the TL is to cool down the receiver focal plane below 4.5 K. The latter should guide the decision about which kind of aluminum to use.

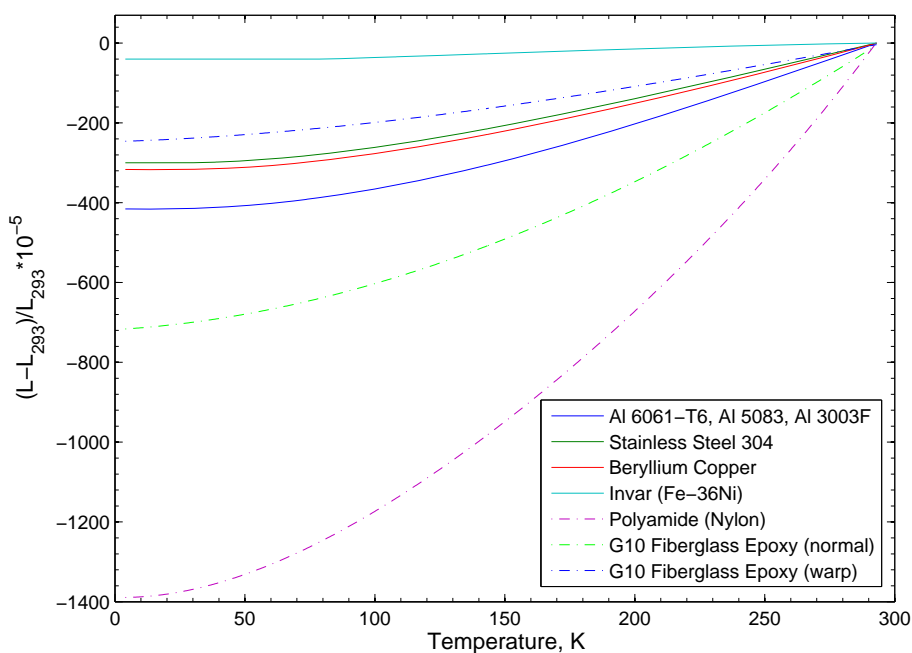


Figure 3.2: Integrated linear thermal expansion of various materials. Data based on literature, from [Marquardt et al., 2000] and the NIST web page [NIST Cryogenics,].

Invar was an obvious choice as second material. It's a nickel-iron alloy also known as FeNi36, notable for its unique low coefficient of thermal expansion

(see figure 3.2). Its name comes from the word *invariable*, referring to its lack of expansion or contraction with temperature changes.

The current receiver needs four TLs, one per cartridge in the 4 K and 50 K stages. Our TL is formed by a crown-like ring made of aluminum - divided into 60 fingers - and an Invar metal ring (see figure 3.3). The design principle (section 3.2) of the TLs for both stages is the same, the only difference is their size. The inner diameter of the TLs are 185.5 mm and 175.5 mm for the 50 K and 4 K stages respectively. The ones on the 50 K stage are only larger to facilitate the mounting. Each TL weighs ≈ 300 gr.

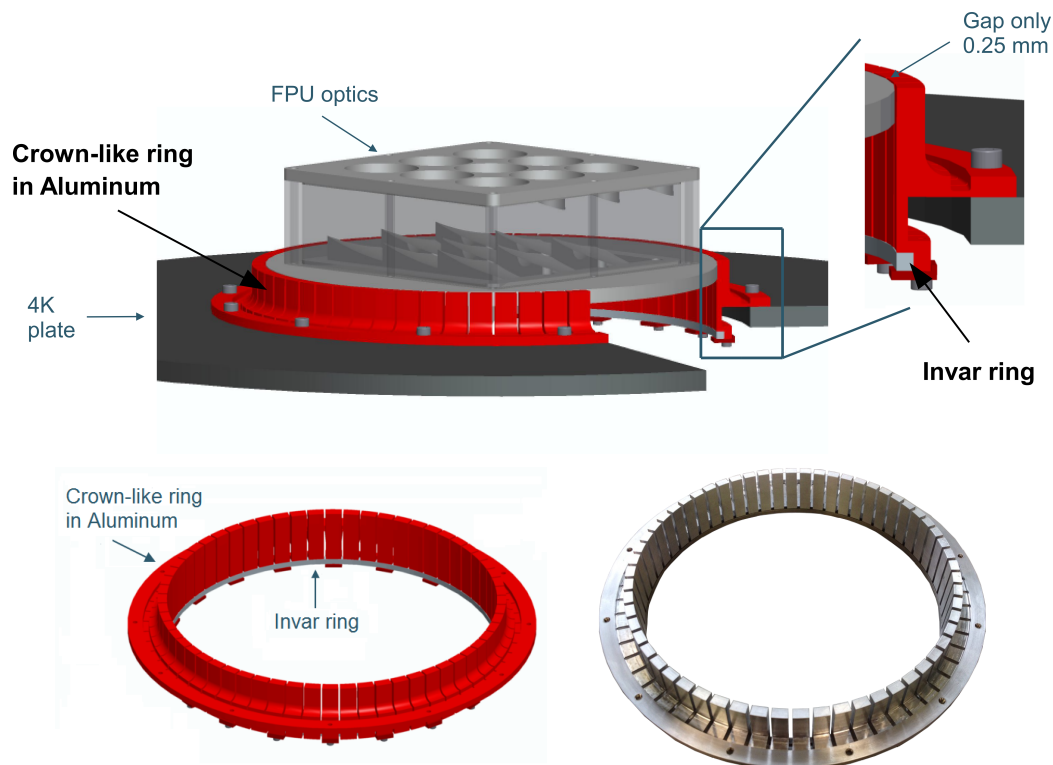


Figure 3.3: Top: CAD drawing showing the ensemble cryostat 4 K plate - TL - FPU optics with a cut to see the inner part and a zoomed view for details. Bottom left: CAD drawing of the all-metal TL which is composed of a crown-like ring made of aluminum divided into 60 "fingers" and an Invar ring. Bottom right: Picture of the crown-like ring made of Al-1050, its inner diameter is 175.5 mm and the distance between fingers is 2 mm. Each TL weighs ≈ 300 gr.

The gap left between the cartridge plate and the TL is 0.25 mm (figure 3.3 top). This space is sufficient for the mounting of the cartridges at ambient temperature. The TL should be designed in such a way that this gap is closed when cooled down and in this way, the cartridge plates can reach the desired operating temperatures. The most important temperature is the one reached by the 4 K stage plate of the cartridges where all the mixers are connected

to.

3.2 Thermal Links Design

To proceed with the explanation of the design we have to concentrate on one finger; all the calculations were done for one of the 60 identical fingers. For the analysis, each finger is divided in three beams, two vertical and one horizontal, named: higher beam (L_s), lower beam (L_i) and horizontal beam (L_h) respectively. See figure 3.4 to identify the beams more clearly. This figure also shows the dimensions and real profile of the finger, it may be too soon to see all of this, but this figure will help understand the method used in the TL design.

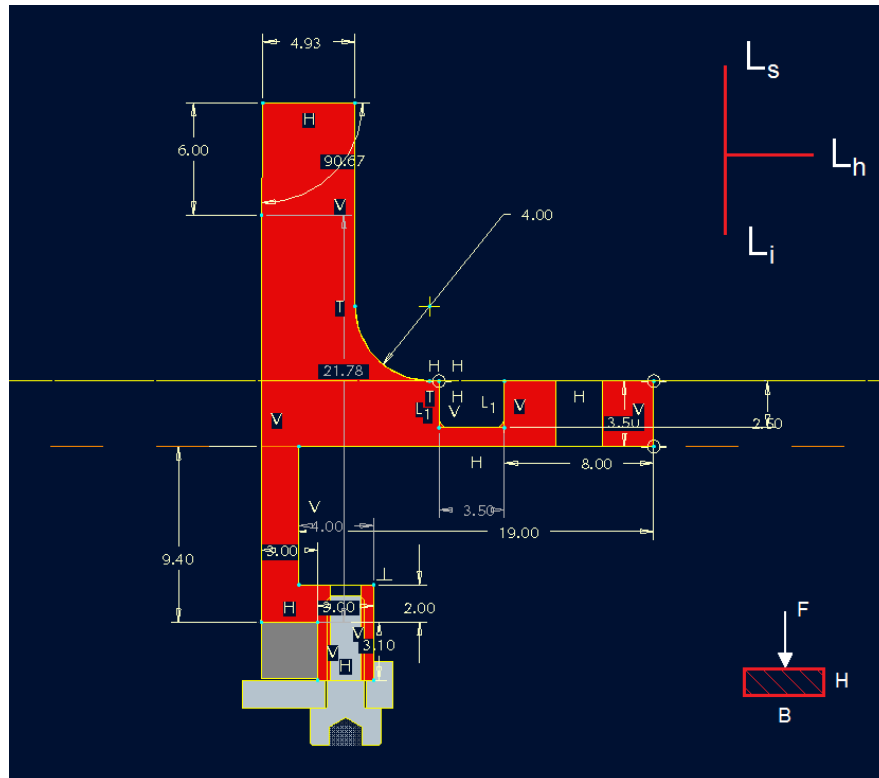


Figure 3.4: Drawing of the TL profile. In red, its profile and dimensions are shown. In dark gray, the square section of the Invar ring and in light gray, the Invar ring support made of small aluminum plates and its corresponding screw. Only six of these plate are actually used. Two small schemata are present, the top right one identifies the beams that form each finger and the bottom right one shows the section of the beam with its two sides and an applied force. In the main drawing, B is perpendicular to the paper. These dimensions are valid for the 4 K and 50 K TLs made of Al-5083. Due to their difference in diameter, only the width of the finger (B) is different, being bigger in the 50 K model.

The closing of the gap by the fingers is done via three components: displacement due to thermal shrinking of the aluminum, bending of the thinnest part of L_h , which causes the rotation of L_s , and L_i , until the former is stopped by the corresponding cartridge plate, thus closing the gap; and the bending of the L_i provoked by the fact that the aluminum contracts when cold and the Invar ring (almost) does not (see figure 3.5). This difference in contraction is not completely covered by the rotation of L_i , thus bending occurs. The bending of L_i is needed to have a clamping force on L_s when it closes the gap.

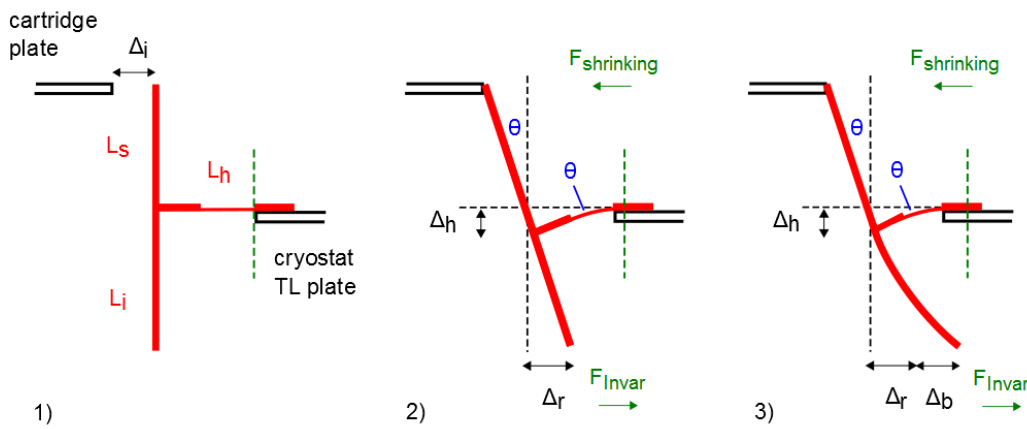


Figure 3.5: TLs working principle. 1) Initial state: cryostat is at ambient temperature and the gap between the TL and the cartridge (Δ_i) is 0.25 mm. 2) Cooling down starts: aluminum starts to shrink ($F_{\text{shrinking}}$) and the Invar does not (F_{Invar}), this displacement produces the bending of the thinnest part of L_h (Δ_h) which provokes a rotation of L_s and L_i , until the former touches the cartridge plate. The amount of L_i rotation (Δ_r) can be calculated by geometry. 3) Final state: the cryostat is cooled down, the rest of the shrinking difference between the aluminum and Invar ($\Delta_t = \Delta_r + \Delta_b$) is absorbed by the bending of L_i (Δ_b). Table 3.3 shows all these Δ values for the TLs built during this thesis.

Table 3.1 shows the thermal expansion calculations done for the cartridge plates and the TLs at ambient and operation temperatures. The first two lines of the table, for each stage, show that when cold, the gap between the cartridge plates and the TL will be similar to the gap when at ambient temperatures. Thus, the shrinking of the cartridge plates can be ignored. The third line of the table shows the difference in contraction of both materials where the Invar ring is in contact with the L_i . The difference in contraction (Δ_t) is 0.35 mm and 0.34 mm for the 50 K and 4 K TLs respectively.

The bending of the L_h thinnest part and of L_i means stress in the material (aluminum and Invar) and materials undergo strain when they are subject to stress. Stress is the force applied to the material per unit of cross-sectional area and strain is the deflection per unit length. When stress is applied to

Stage	ϵ_A $\cdot 10^{-5}$	ϵ_I $\cdot 10^{-5}$	$\Delta\epsilon$ $\cdot 10^{-5}$	R_h [mm]	ΔL [mm]	R_c [mm]
50 K						
cartridge ^a	-407.3			92.50	-0.38	92.12
cryostat ^b	-407.3			92.75	-0.38	92.37
thermal link ^c	-407.3	-40	-367.3	95.75	-0.35	
4 K						
cartridge	-415.5			87.50	-0.36	87.14
cryostat	-415.5			87.75	-0.36	87.39
thermal link	-415.5	-40	-375.5	90.75	-0.34	

Table 3.1: The thermal expansion of the aluminum and Invar in the TLs. The integrated thermal expansion of aluminum (ϵ_A), Invar (ϵ_I) and the difference between them ($\Delta\epsilon$) are given at 50 K and 4 K. ϵ is defined as $\Delta L/L_{293} = (L - L_{293})/L_{293}$, where L_{293} is the length at room temperature and L the length when cold. The radius of each part at room temperature (R_h) and when cold (R_c) are also given. The values in bold are the shrinking difference between aluminum and Invar (Δ_t). In the TLs, this difference is absorbed by rotation (Δ_r) and bending (Δ_b) of L_i (see figure 3.5 for the explanation of the TLs working principle). ϵ data are based on literature, from [Marquardt et al., 2000] and the NIST web page [NIST Cryogenics,].

^aRadius of the cartridge plate.

^bInner Radius of the TL.

^cRadius where the lower beams (L_i) are in contact with the Invar ring.

a metal the initial strain is elastic and the metal will return to its original dimensions if stress is removed. Beyond a certain stress however, plastic strain occurs and the metal is permanently deformed. We have to make sure that the beams of the TL stay in the elastic range to avoid permanent deformation.

The relationship between stress and strain is different for different materials and depends on properties such as the modulus of elasticity (E), also known as Young's modulus, and the yield strength (σ_y). The modulus of elasticity is a measure of the stiffness of an elastic material and is a quantity used to characterize materials. It is defined as the slope of its stress-strain curve in the elastic deformation region ($E = \text{stress}/\text{strain}$), where stress is the force causing the deformation divided by the area to which the force is applied and strain is the ratio of the change in some length parameter caused by the deformation to the original value of the length parameter. Stiffer materials have higher elastic modulus. The σ_y is a very important parameter for the design because it is the stress required to produce small plastic strain in the metal, usually 0.2 % permanent deformation, thus the maximum stress that the material can withstand without a permanent deformation occurring. For more details in this topic, please refer to any of the many good books written about it, for example [Young and Budynas, 2002] and [Moore et al., 1989].

The size of each aluminum beam is analyzed in terms of the needed geometry and of its undergone bending. Geometry will give a starting point for the lengths of the beams, then with these values one can calculate the rectangular cross section (described below) that would be needed to stay within the elastics limit (avoiding permanent deformation of the metal) and if not realistic (for example, too big), try with other lengths until both criteria are satisfied.

First, the bending of the L_i will be analyzed. The amount of Δ_t taken by the rotation (Δ_r) of L_i can be calculated by geometry (see figure 3.5) and depends on the lengths of L_s , L_i and the initial gap of 0.25 mm between the TL and the corresponding cartridge plate. Then, the bending of L_i is given by:

$$\Delta_b = \Delta_t - \Delta_r. \quad (3.1)$$

This bending corresponds to the case of a beam fixed at one end and the load (F) concentrated on the other end. The maximum displacement (Δ_b) is produced where F is applied and it is given by:

$$\Delta_b = \frac{Fl^3}{3EI} \quad (3.2)$$

Obtained from [Moore et al., 1989], where l is the length of the beam, E is the Young's modulus of the material and I is the centroidal moment of

inertia of a beam with rectangular cross section. I is calculated by:

$$I = \frac{BH^3}{12} \quad (3.3)$$

with B and H as the sides of the rectangle (see figure 3.4 bottom right). B is the width of the finger and is defined by the diameter of the TL, the number of fingers and their spacing. Then, from equation 3.2, the force that would produce Δ_b is calculated. Additionally, the maximum bending moment which is located at the support of the beam, is calculated by:

$$M_{\max} = Fl \quad (3.4)$$

After this, we have to calculate the maximum force F_{\max} that resists the beam to stay into the desired elastic range. One way to continue would be to use the bending moment at yield strength, also known as yield moment (M_y) which is the bending moment when the first part of the section reaches the yield stress, it is calculated by $M_y = \sigma_y BH^2/6$. But this method is too conservative and it would have resulted in beams unnecessarily big.

Instead, we use the method of *plastic, or ultimate strength* which is a preferred method of design, applicable to rigid frames and statically indeterminate beams made of materials capable of plastic action [Young and Budynas, 2002]. First, the plastic moment M_p , defined as the moment at which the entire cross section has reached its yield stress (maximum bending moment that a section can resist before moving in the plastic range), is calculated with:

$$M_p = \sigma_y Z = \frac{\sigma_y BH^2}{4} \quad (3.5)$$

where Z is called the plastic section modulus. Second, one simply sets M_p equals to the expression for the maximum value of the bending moment on the beam M_{\max} (equation 3.4) and solves for the force which gives:

$$F_{\max} = M_p/l \quad (3.6)$$

M_p is always larger than M_y , this causes that the allowed F_{\max} is, in this case, 1.5 times bigger, resulting in smaller beams for the TL.

To continue, one has to compare both force values and check that the beam dimensions satisfy the condition of $F/F_{\max} \leq 1$. Using equations 3.2 and 3.6, the rapport can be expressed as follows:

$$\frac{F}{F_{\max}} = \frac{\Delta_b EH}{\sigma_y l^2} \quad (3.7)$$

One could also check that $F \leq F_{\max}$, but doing the rapport helps to noticed that the depth or width of the beam (B) is not present, in other words, changing this dimension does not help to improve this rapport. If the condition

is not satisfy, one can modify the dimensions of H , l and Δ_b of L_i . H is an independent parameter, but the other two are related with each other and with the length of L_h (see figure 3.5).

Secondly, we will analyzed L_h . In this case, the important part for the stress-strain analysis is the thin part of the beam which is where bending occurs. It has to be analyzed with the same procedure described above for the L_i analysis. First we calculate the M_p and the F/F_{max} ratio to find the values of the l and H that allow elastic bending. The corresponding Δ_h is calculated by geometry since the bending angle of L_h is the same as the rotation angle for L_s (see figure 3.5). Equation 3.5 shows that a longer l and a smaller H are the direction to go, but that goes in exactly the opposite direction when considering the thermal conductance (equation 3.10) which is very important in the TLs. Thus, we chose the shortest l and largest H that satisfy $F \leq F_{max}$ for the part of L_h that bends and completed the L_h length with a larger H (see figure 3.4) to add some thermal conductance.

The definition of the L_s dimensions are only done by geometry, this part does not undergo any stress. The total length is defined so it touches the cartridge plate which is 0.25 mm away and allows an appropriate Δ_b for L_i (equation 3.1), B is given by the finger width and H follows the shape of L_h which is wider at this end (bigger cross section) to improve the thermal conductance after the thin part (see previous paragraph). At the top of the L_s , a small cut is done to increase the surface contact between the finger and the cartridge plate.

The diameter of the Invar ring is defined by the TL inner radio, at the bottom of the L_i beams, where is it mounted (see figure 3.4). Thus, analyzing the bending of the Invar ring, we will only define its cross section. To start, the ring is divided into 60 virtual beams where each beam corresponds to the part facing one finger. Consequently, the length of each Invar beam is given by the B parameter (width) of the aluminum fingers.

The bending of the Invar beam corresponds to the case of a beam supported at both ends with an applied force in the center. Here, F is the force produced by L_i on the Invar beam, obtained from equation 3.2. Using the beam load equations [Moore et al., 1989] that corresponds to this case, we have the maximum moment at the point of the load given by:

$$M_{max} = Fl/4 \quad (3.8)$$

Afterward, the procedure is similar to the one described before for the L_i bending analysis. First, we set M_p (from equation 3.5) equal to M_{max} and solve for the F_{max} to obtain:

$$F_{max} = \frac{\sigma_y B H^2}{l} \quad (3.9)$$

Then, the condition $F \leq F_{max}$ must be satisfied by the Invar beam B and H

dimensions.

The dimensions of all the beams, as well as the rotation and bending values, for the TLs that were built during this thesis are presented in table 3.3 and described in section 3.3.

3.3 Thermal Links Versions

Two versions of TLs were designed using the method explained in section 3.2. The first version was made of Aluminum 5083, a standard aluminum used in our workshop. Four TLs were made, two for the 50 K stage and two for the 4 K stage.

After that, driven by the desire of a higher thermal conductance (see section 3.4), it was decided to make the 4 K TLs of an aluminum with higher thermal conductivity. We wanted to make these TLs in Al-1100 (see figure 2.4), but its smaller yield strength of 34.5 MPa [Schwarzwalder Metallhandel GmbH,] made it impossible (see equation 3.7). However, we managed to design a new TL in Al-1050, which is the purest aluminum with a yield strength big enough to allow a new design in the space already allocated for it. Two TLs were made for the 4 K stage.

The yield strength and the modulus of elasticity of the materials used in the two versions of the TLs are shown in table 3.2.

The dimensions of the TL beams together with the values of their corresponding rotation and bending, for both versions, are presented in table 3.3. The real profile of one finger can be seen in figure 3.4.

	E [N/m ²]	σ_y [N/m ²]
Al-5083 ^a	$7.10 \cdot 10^{10}$	$2.80 \cdot 10^8$
Al-1050 ^b	$6.90 \cdot 10^{10}$	$9.50 \cdot 10^7$
Invar ^c	$1.45 \cdot 10^{11}$	$1.65 \cdot 10^8$

Table 3.2: Modulus of elasticity (E) and yield's strength (σ_y) used in the calculations of the TLs design (see section 3.2).

^aData from [ASM Aerospace Specification Metals, Inc.,].

^bData from [Schwarzwalder Metallhandel GmbH,].

^cData from [Moore et al., 1989].

Before building the TLs, the design was validated with a finite element analysis done, with ProMechanica [PTC,], on one of the 60 identical fingers of the TL. The corresponding results for the TL Al-5083 model are shown in figure 3.6.

Beam	l [mm]	H [mm]	B [mm]	Δ_t [mm]	Δ_r [mm]	Δ_b [mm]
50 K TL Al-5083						
L_i	12.5	2.0	8.0	0.35	0.17	0.18
L_h	4.5	3.5	8.0			
$L_{h \text{ thin}}$	3.5	1.0	8.0			0.05
L_s	18.4	5.0	8.0			
4 K TL Al-5083						
L_i	12.5	2.0	7.5	0.34	0.17	0.17
L_h	4.5	3.5	7.5			
$L_{h \text{ thin}}$	3.5	1.0	7.5			0.05
L_s	18.4	5.0	7.5			
4 K TL Al-1050						
L_i	14.5	1.6	7.5	0.34	0.20	0.14
L_h	8.0	0.8	7.5			0.11
L_s	18.4	5.0	7.5			

Table 3.3: Thermal link (TL) beam dimensions for the two versions of TLs built in our workshop, made of Al-5083 and Al-1050. The later was used to build only the 4 K TLs to improve the thermal conductance of the stage. The characteristics of the three aluminum beams are given, $L_{h \text{ thin}}$ is the thin part of L_h (see figure 3.4). In the TL made of Al-1050 there is no thinner part, thus only a value for L_h is given. B is defined by the diameter of the TL, the number of fingers and the space between the fingers. In these versions, a spacing of 2 mm was considered. The shrinking difference (Δ_t), of the aluminum and Invar, where L_i is in contact with the Invar ring is 0.35 mm and 0.34 mm for the 50 K and 4 K TLs respectively (see table 3.1). The amount of Δ_t absorbed by rotation (Δ_r) and by bending (Δ_b) are also presented (see figure 3.5). The Invar ring beam length (for the calculations) is equal to the corresponding TL B and its cross-section area is $3 \times 3 \text{ mm}^2$. The performance of the TLs is presented in section 3.5.1.

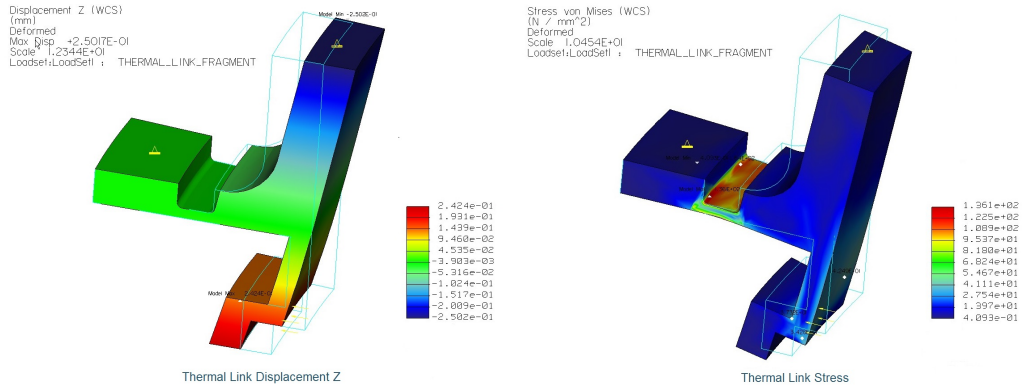


Figure 3.6: TL design validated by the finite element analysis done using ProMechanica [PTC,] in one of the 60 identical fingers. Left: The TL displacement, being the maximum displacement of 0.25 mm. Right: The TL stress, being the maximum stress equal to 136 N/mm² which is smaller than the limit of 150 N/mm² (equation 3.6) in this beam to stay within the elastic range. It shows the thin part of L_h as the part of maximal care of the TL. This analysis was done to validate the design of the Al-5083 TL before its fabrication.

The force produced by the TL on the cartridge plate does not need to hold anything, only do the contact to allow the thermal conduction. Nevertheless, it is necessary to have a clamping force to assure a good contact. The estimation of the clamping force was done using the Law of the Lever which relates the input and output forces with the inverse of their distances from the fulcrum where they are applied. In the case of the TL, the input force (F_i) is the one applied by the Invar ring in L_i , the output force (F_s) is the clamping force, the distances are the lengths of the corresponding beams and the fulcrum, defining the rotation point, is L_h . Consequently, $F_s = F_i l(L_i)/l(L_s)$, F_i was calculated using equation 3.2. To have the total force, F_s has to be multiplied by 60. The fingers apply a force estimated in 4500 N for the first model, made of Al-5083, and a force of 1700 N for the version made of Al-1050. In the first design of the ALMA TLs, the clamping force was estimated in 2200 N [Orlowska et al., 2002] .

In the original design of the TL, the separation of the fingers was 1 mm. A prototype for the 4 K stage was built with this characteristic, but because of critical manufacturing it was decided that the separation was going to be increased to 2 mm. This change did not mean any additional modification in the design. Nevertheless, this larger finger separation in the 50 K TLs has a negative impact on the 4 K stage temperature. The larger spacing allows more radiation from the 300 K vessel to pass directly to the 4 K stage, resulting in a higher temperature of this stage. This was solved by a TL cover made of aluminum and mounted on each of the 50 K TLs. Figures 2.1 *Top right* and 3.7 show the 50 K TLs, with their covers, mounted in the receiver.

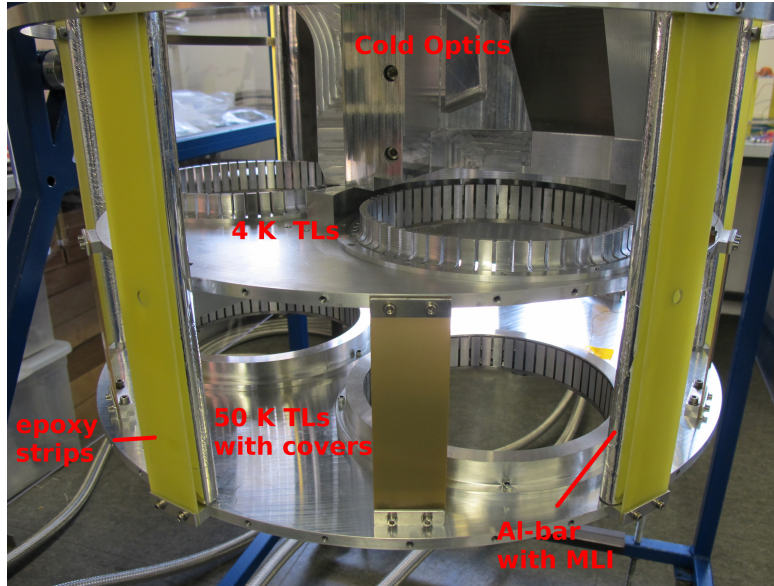


Figure 3.7: Picture taken during the mounting of the receiver, it shows the 4 K TLs and both 50 K TLs with their covers. This is the orientation in which the receiver operates. Some aluminum bars wrap in MLI can be seen behind the longer epoxy strips and part of the Cold Optics is seen in the back and on top of the 4 K TLs.

The TLs designed during this thesis for the 1.1 THz Array Receiver can be used in other projects. As an example of this, figure 3.8 shows the new receiver of the Laboratory Spectroscopy Group of our institute where two TLs are used.

3.4 Thermal Conductance of the Thermal Links

Another modification that was done to the TL was to try to increase its thermal conductance, particularly in the case of the 4 K stage TLs. To investigate in this respect, we started by estimating the thermal conductance of the TL built of Al-5083.

We do the calculation for one of the 60 identical fingers of the TL. We start by dividing the finger in three parts or portions. The first one corresponds to the $L_{h \text{ thin}}$, the second one to L_h and the third one to L_s (see figure 3.4). For each part we calculate its thermal conductance using the following formula (see equation 2.4):

$$\lambda' = \frac{S}{l} \lambda(T) \quad (3.10)$$

where $\lambda(T)$ is the thermal conductivity of the material at the temperature

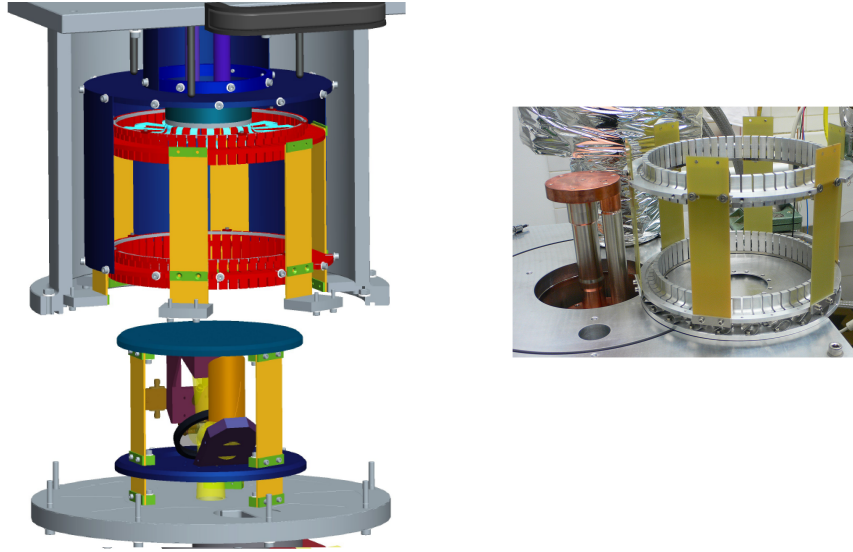


Figure 3.8: TLs used in the new receiver of the Laboratory Spectroscopy Group of our institute. Left: CAD drawing of the receiver. The TLs are drawn in red, the lower one corresponds to the 50 K TL and the upper one to the 4 K TL. Right: Picture of the two TLs hold together with three epoxy strips. Part of the PT can be seen next to them.

T , S the cross section area perpendicular to the thermal flux and l is the length of the corresponding part.

In a serial configuration, the resistances ($1/\lambda'$) are added and then inverted to get the total thermal conductance of each finger. In this way, the different aluminum types can be compare. It was estimated that the thermal conductance obtained with the current aluminum type (Al-5083), calculated in 0.252 W/K, could be improved by a factor of 6 with the aluminum alloy 1050.

However, another thermal conductance (or resistance) has to be added, this is the one that represents the contact between the TL and the corresponding cartridge plate. By using the measured thermal conductance of the TL Al-5083 which is 0.182 W/K (figure 3.16), the thermal conductance of the contact was calculated to be 0.655 W/K. Considering this value to also be the contact thermal conductance of the TL Al-1050, the previous improvement factor drops to 2.5. Nevertheless, we decided to build the new TLs for the 4 K stage.

Unfortunately, the measured thermal conductance of the TL AL-1050 is not as good as expected. It is only 0.186 W/K (figure 3.16), similar to the one of the TL Al-5083. This means, that the thermal conductance is dominated by the contact between the TL and the cartridge, which is not improved by a different choice of aluminum. The thermal conductance of the contact this time is calculated to be only 0.211 W/K. However, it improved

the temperature of the TL itself.

The thermal conductance of the TL made of Al-1050 has the problem of being more affected by the bad thermal conductance of the contact TL - cartridge plate. The contact behaves worse than the one of the Al-5083 model. The contact geometry is very hard to handle in the construction process and softer materials, like the Al-1050, are more difficult in this respect.

For the time being, we decided to improve the thermal conductance of the TLs by the use of a Nylon ring installed around the top of the fingers, similar to the one in the copper-nylon TL model (see figure 3.1 *bottom*). A ring made of nylon (polyamide 66) was designed for the 4 K TLs made of Al-1050; its inner diameter is 185.5 mm and has a thickness of 4 mm. Figure 3.9 shows a picture of both TLs, with the nylon ring, mounted in the 4 K TL plate. All the thermal conductance results and the way they were measured are presented in the next section.

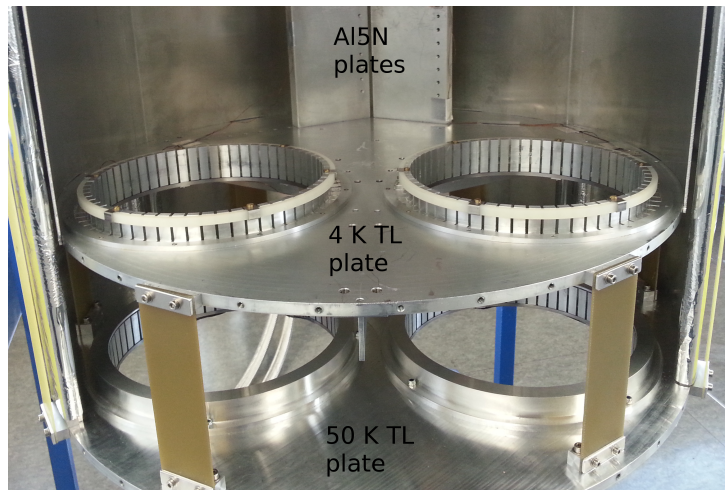


Figure 3.9: Both TLs made of Al-1050 with their nylon ring are installed in the 4 K TL plate. The 50 K TLs, with their covers, are also present. The Cold Optics is not installed and the Al5N plates, part of the 4 K CH interface, can be seen in the back.

3.5 Thermal Links Performance

In this section, we will present the results of the receiver tests done, in our laboratory, with a focus in the thermal links behavior. The results concerning the cryostat performance and the optics tests are presented in sections 2.4 and 4.5 respectively.

3.5.1 Temperature Test Results

The TLs - cartridge plates cooling behavior, for the 50 K and 4 K stages can be seen in figure 3.10 which shows 5 of the first set of cool downs, when we were trying to reach 4.2 K or less in the second stage of the PT. During this time, the cryostat was closed to external radiation (entrance window with a aluminum plate instead of the HDPE), the Cold Optics was not installed yet and the 50 K TLs had no covers. It can be observed that the TLs close at an average temperature of 250 K which is higher than the expected (≈ 150 K) because the design was done considering the final state, when the total shrinking has happened already for both, the radiation shields and the cartridge, but the latter starts shrinking only after the contact is established.

It can also be seen that the first TLs to close are the 50 K ones, doing it after 2 hours of cool down. The 4 K TLs close after 3.5 hours in average. This can be explained by the fact that the former cools down faster as shown in figure 2.20. Other plots of cool downs can be seen in appendix A and similar plots of the thermal links behavior of all the cool downs, a total of 30, are presented in the appendix B.

The TLs - cartridge plates cooling behavior when the Cold Optics is installed can be seen in figure 3.11 which shows 3 of the cool downs with different cryostat configuration (open/closed to external radiation, with/without 50 K TLs covers) and before the mixers were installed. Both models of TLs are presented. The Cold Optics guides the beams from the outside of the cryostat to the FPU's optics increasing their temperature. Accordingly, the temperature difference between the TLs and the cartridges, at the steady state, is higher than when the Cold Optics is not installed.

To see the temperature difference between the TL and the corresponding cartridge plate only when the steady state is reached see figure 3.12 which shows most of the cool downs done during this thesis. Only 6 are not included either because they were a particular kind of test or due to a problem with the data collection. In this figure, it can be seen that the CT temperatures are always higher than the CR ones, on both stages. Unfortunately, we have almost no data of the CT before the Cold Optics was installed, thus we can not say much about that case, but at least part of the reason of this temperature difference, is that even if the Cold Optics should affect both FPU's optics - and cartridges - in a similar way, the CT gets most of the ambient temperature radiation, because at this wavelength ($10 \mu\text{m}$) the polarizer reflect less of it. In addition, it can also be seen that the mixers also increase the temperature of the cartridges 4 K stage, particularly of the one on which they are installed due to the heat load conduction by the wires.

To have a better look at the usefulness of the 50 K TL's covers see figure 3.13. They work correctly, the 4 K stage reaches the needed lower temperatures when the covers are installed, this means that the heat load it is effectively stopped by the cover, warming up the 50 K stage by few kelvins

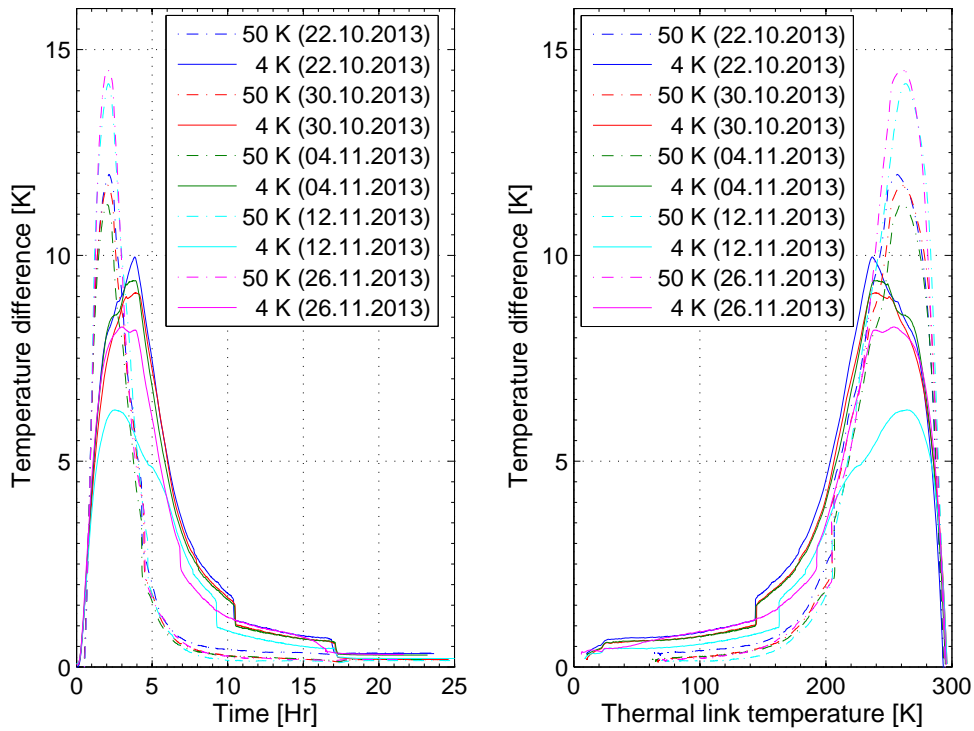


Figure 3.10: Thermal links behavior while cooling down. The vertical-axis indicates the temperature difference between the TLs and the corresponding cartridge stage and the x-axis the cooling down time (left) and the TL temperature (right). In this way, it can be seen when and at which TL temperature this one starts to close and thus cool down the cartridge plate. Here are presented 5 of the first cool downs, when the cryostat was closed, the Cold Optics was not installed yet and the 50 K TLs had no covers.

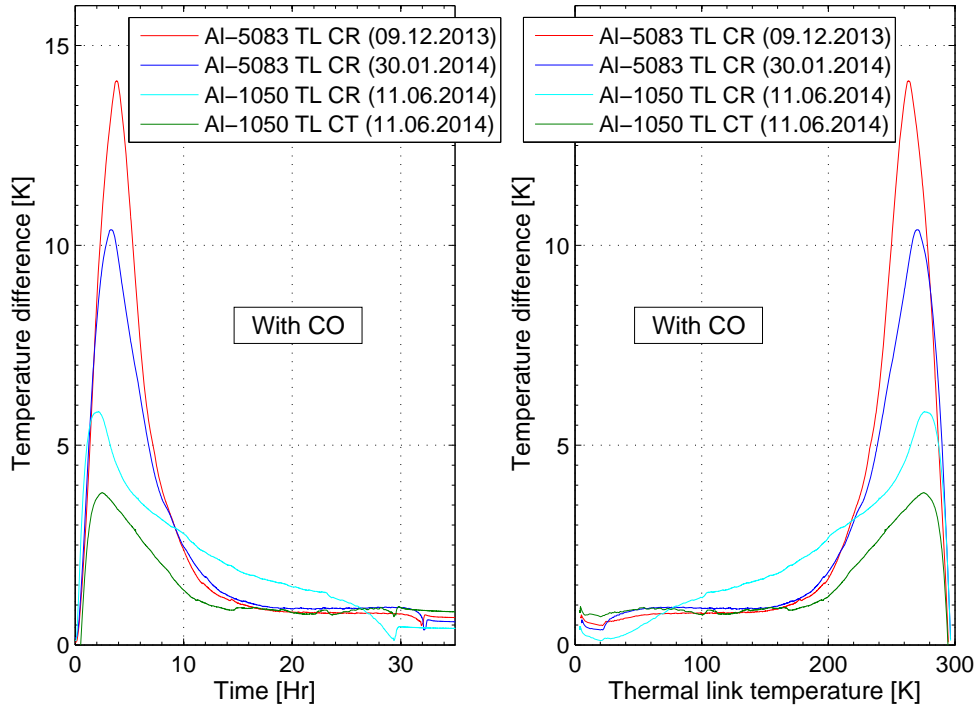


Figure 3.11: Thermal links behavior while cooling down when the Cold Optics is installed. The vertical-axis indicates the temperature difference between the TLs and the corresponding cartridge stage and the horizontal-axis the cooling down time (left) and the TL temperature (right). A sample of 3 cool downs with different cryostat configuration (open/close, with/without 50 K TLs covers) and before the mixers were installed. Both models of TLs are also present. The temperature difference between the TL and the corresponding cartridge plate when the steady state is reached is higher than when the Cold Optics is not installed because this one guides the beams from the outside of the cryostat to the FPU's optics increasing their temperature.

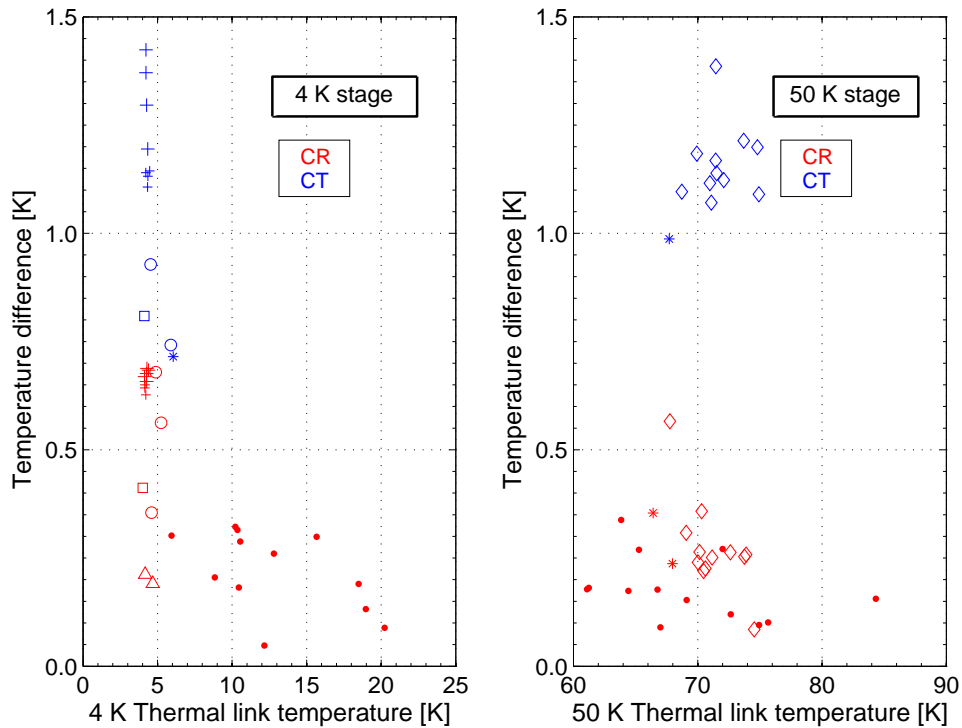


Figure 3.12: Steady state temperature difference between the TLs and their corresponding cartridge plates. On both stages the temperature difference of the CR (red) is smaller than the one of CT (blue). Left: 4 K stage data. The points show the measurements taken with the cryostat entrance window closed to external radiation, and before the Cold Optics was installed using the Al-5083 TLs. The circles indicate measurements taken with the Cold Optics installed and the star some measurements while it was off again. The rest of the data show the performance of the Al-1050 TLs: the square represents data taken with the Cold Optics and the plus signs with mixers, the smaller plus means that the mixers are in the other cartridge. The triangle indicate the best performance, when the Al-1050 TLs have the nylon ring installed. Right: 50 K stage data. The points show the first data taken without the 50 K TL covers, the diamonds indicate the data taken with the covers and the stars some data while the covers were removed again. The 50 K TLs are always the same, made of Al-5083.

which is not a problem.

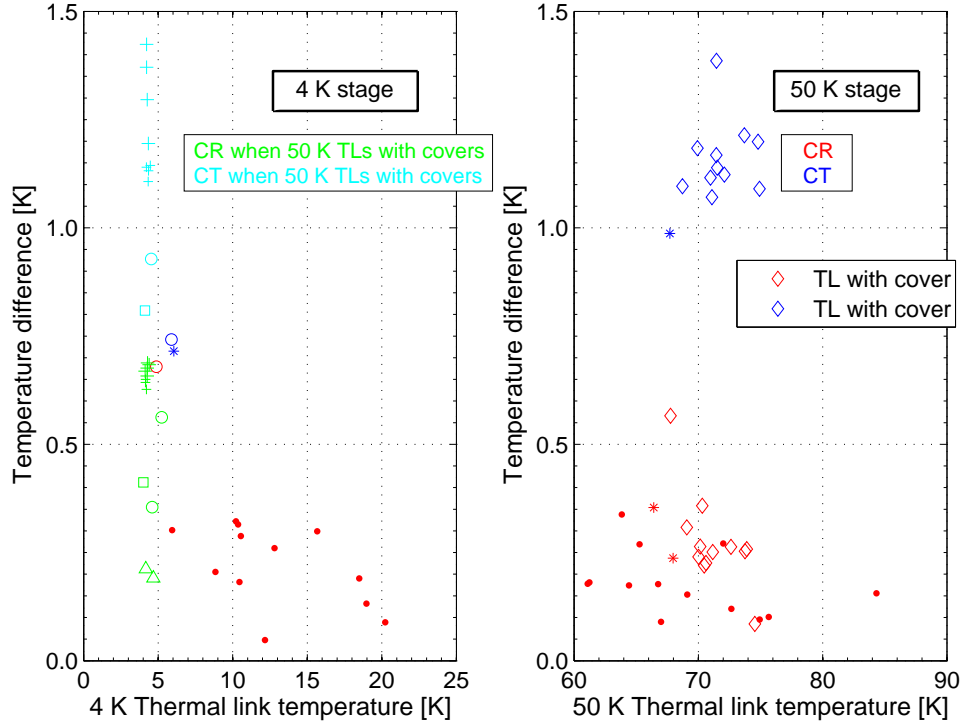


Figure 3.13: Steady state temperature difference between the TLs and their corresponding cartridge plates. Same as figure 3.12, but showing the effect of the 50 K TL's covers in the 4 K stage. Left: The green and cyan data indicate when the 50 K TLs had their covers installed. In these cases, the TL temperature is below 5 K on both cartridges. Right: The points and the diamonds show the measurements when the 50 K TLs had their covers off and on respectively; and the stars some measurements while they were off again. The covers do not have an impact in the temperature difference, but the stage stays at higher temperature. This shows that the covers do their job of blocking the 300 K radiation, preventing it to load the 4 K stage, and thus, allowing it to reach lower temperatures.

3.5.2 Thermal Conductance Measurements

To have a more complete understanding of the TLs performance, we need to know their thermal conductance. The estimation of this value was done in section 3.4. Here, we show the results of the measured thermal conductance of three types of TLs, which are the TL made of Al-5083, the TL made of Al-1050 and the TL prototype, also called first version TL (V.1), which only difference with the former is that it has a finger spacing of 1 mm.

The thermal conductance of the TLs was measured as follows: 1) A resistor of 1000 Ω and of 100 Ω were placed on the 4 K and 50 K cartridge

stages respectively. 2) The temperatures of the cartridge plate (T_a) and the TL (T_b) were measured with silicon diodes. 3) the heat load (in W) was increased by changing the voltage applied to the resistor 4) the temperature difference ($T_a - T_b$) is obtained and 5) these data points are then fitted with a first degree polynomial. The thermal conductance is the inverse of the slope of the latter. One TL is tested at a time.

As examples of these tests, figure 3.14 shows the test data for the TL Al-5083 installed in the 4 K stage as they are taken (point 2 and 3 of the procedure) and figure 3.15 shows the calculated temperature difference from the 4 K TL (V.1) and the 50 K TL test data (point 4).

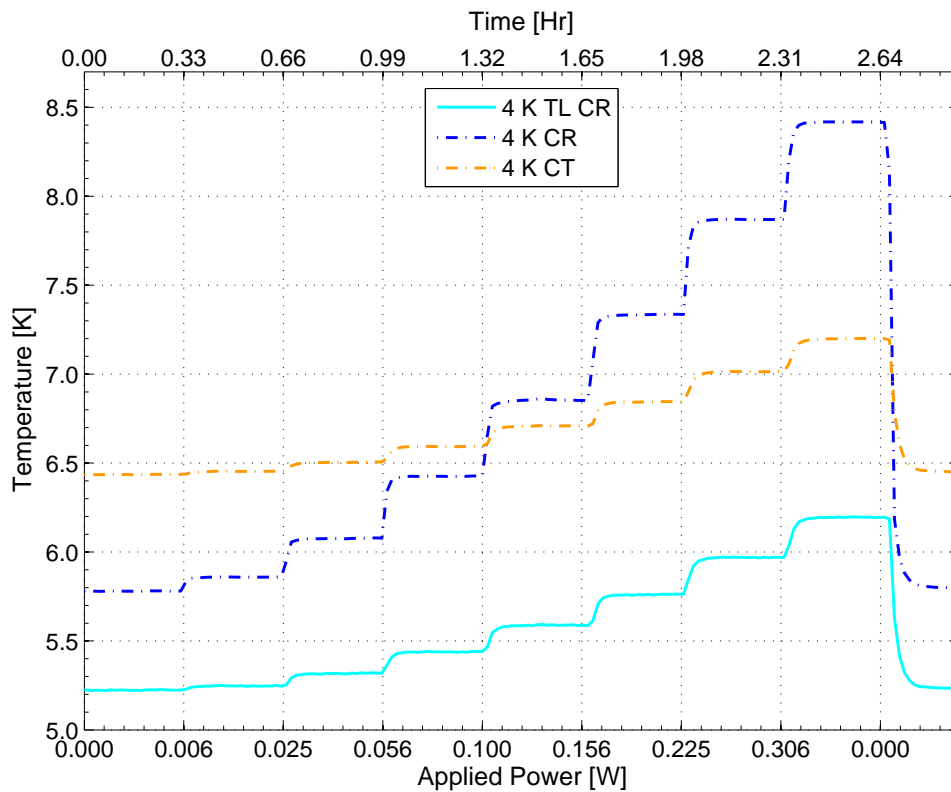


Figure 3.14: Thermal conductance test of the 4 K TL made of Al-5083. The horizontal-axis indicates the applied power in the resistor installed in the 4 K CR plate and the vertical-axis the temperature. The temperature of the TL as well as the temperatures of both cartridge's 4 K plates are shown. Data taken on the 01.30.2014.

All the data with their corresponding fitted curves are displayed in figure 3.16 (point 5), thus giving the information of the thermal conductance of all the tested TLs. These values together with the thermal conductance of other TLs are presented in table 3.4 for comparison.

The worst thermal conductivity is the one of the prototype TL (V.1). Then, TLs made of Al-5083 and Al-1050 have similar results even though

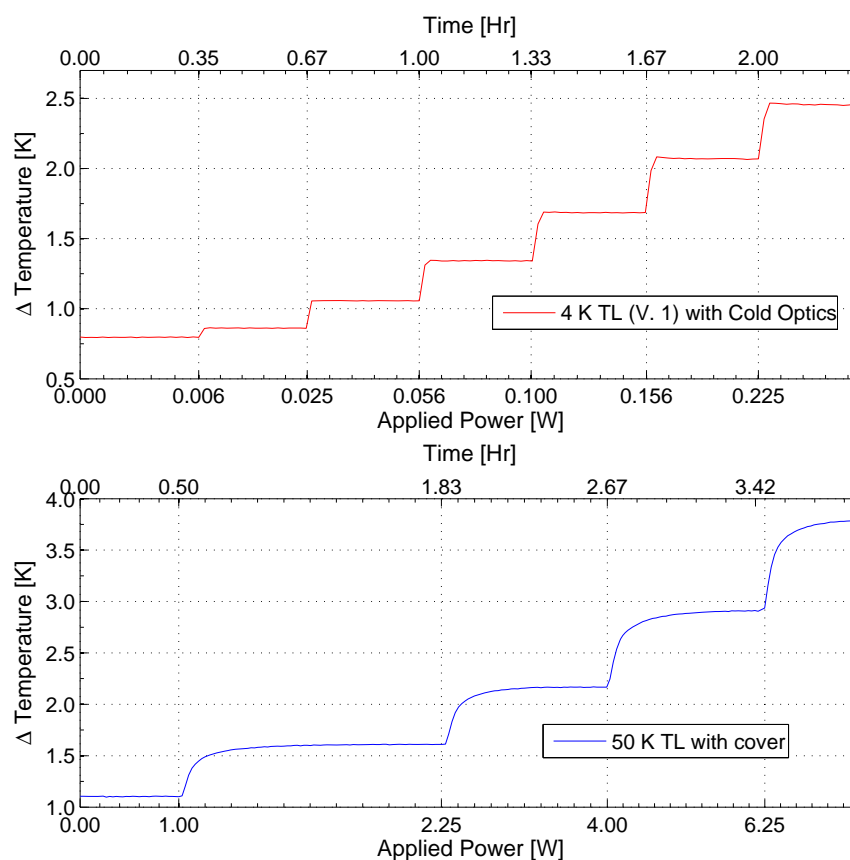


Figure 3.15: The TL - cartridge plate temperature difference (vertical-axis) calculated, from a data set similar to the one presented in figure 3.14, for the 4 K TL (V.1) test (top) and for the 50 K TL made of Al-5083 (bottom). The horizontal-axis indicates the applied power in the resistor installed in the corresponding cartridge plate. From data taken on 11.02.2014.

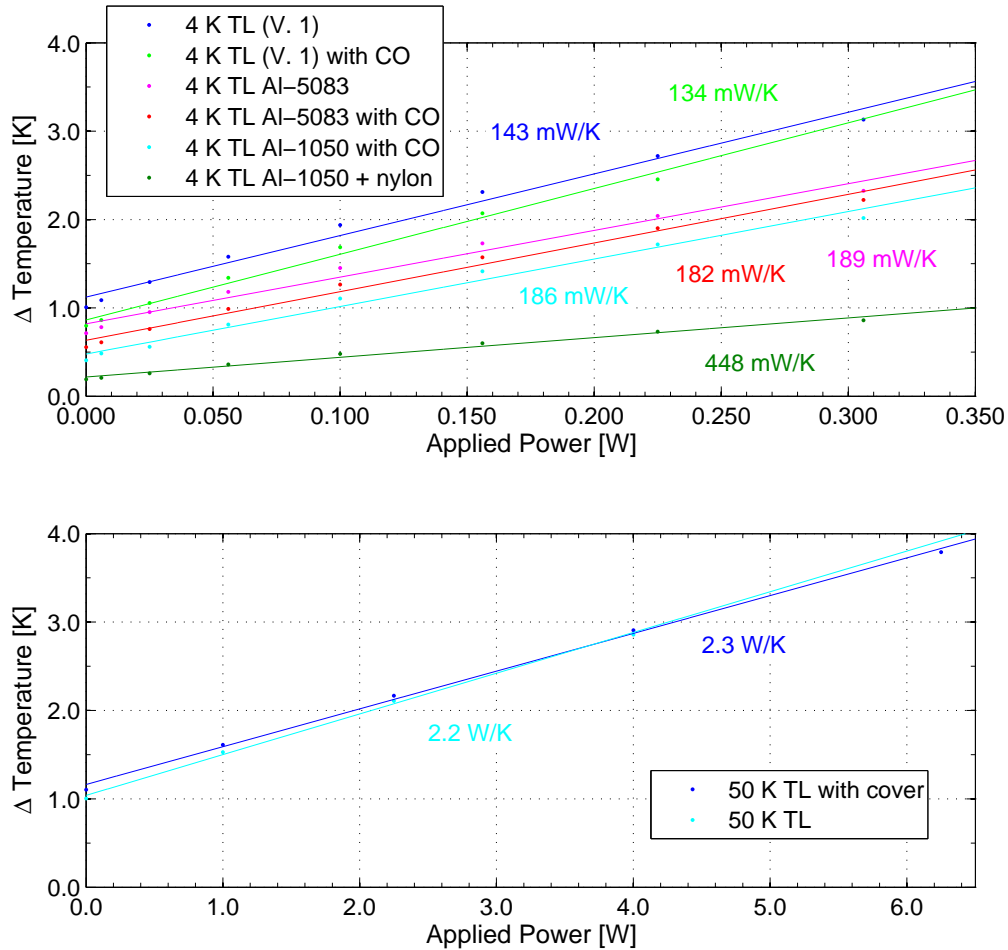


Figure 3.16: Thermal conductance measurements results. The horizontal-axis indicates the applied power in the cartridge plate and the vertical-axis the temperature difference between the TL and the cartridge plate. The points are the data and the lines the fitted curves. The thermal conductance is written in the matching color. Top: It can be observed that the performance of the prototype (TL V.1) is the worst one. However, we expected a better conductance for the TL Al-1050, being only similar to the one of the TL Al-5083. The thermal conductance of the former is dominated by the contact between the TL and the cartridge, which is not improved by a different choice of aluminum and, in addition, very hard to control in the manufacturing process. For this reason, we added a nylon ring to the TL Al-1050 and the result is very positive, the thermal conductance is more than 2 times bigger. Bottom: The thermal conductance of the 50 K TL Al-5083 is similar with or without cover as expected. The cover can affect the initial temperature difference, but not the thermal conductance. For the 4 K TLs, the third measured was the only one performed in the CT, on the other hand, for the 50 K TLs only this cartridge was measured.

	V. 1	Al-5083 Al-1050	Al-1050 +nylon	ALMA ^a	Test ^b Cryostat	Test ^c Cryostat
ϕ [mm]	175.5	175.5	175.5		170/140	170/140
	W/K	W/K	W/K	W/K	W/K	W/K
4 K	0.14	0.19	0.45	0.12	1.7/1.4	1.2/2.0
50 K		2.30 ^d	-	1.30	3.3/3.1	5.0/4.0

Table 3.4: TLs thermal conductance measurement results, including data from other TLs for comparison. The thermal conductance of our thermal links are better than the one of the ALMA prototype, but worse than the ones obtained in the Test Cryostat even in the case of the TL Al-1050 where it is more than doubled when the nylon ring around the fingers is used. The lower performance of our TLs is due mainly to the fact of a poor contact with the cartridge plate, this is the weak point in our design. The fact that the FPU optics, which is the 4 K stage in the cartridge, is not made of pure aluminum may have an impact in their lower thermal conductance. For the time being we added a nylon ring to improve its performance.

^aValues of a first ALMA TL prototype [Orlowska et al., 2002]. An updated design was built as final version for the ALMA cryostat (see figure 3.1), but not thermal conduction values are given for this model.

^bValues of the OFHC-nylon TL developed for the 3-cartridge test cryostat for ALMA, taken from [Sugimoto et al., 2003].

^cValues of the OFHC-nylon TL developed for the 3-cartridge test cryostat for ALMA, taken from [Sekimoto et al., 2003].

^dTL diameter 185.5 mm. Only a TL Al-5083 is used in this stage.

we expected a higher value for the latter. The thermal conductance of our TLs is dominated by the contact between the TL and the cartridge, which is not improved by a different choice of aluminum and hard to control during fabrication, it is the weak point of our design. However, the use of Al-1050 improved the temperature of the TL itself, getting the 4 K TL plate temperature with less loss than the version made of Al-5083.

The thermal conductance was improved by more than the double by means of a Nylon ring installed around the top of the fingers of the TL Al-1050. Taking into account the estimated thermal conductivity of the TL Al-1050 which was 1.6 W/K, the thermal conductance of the contact is improved from 0.22 W/K to 0.63 W/K. Maybe it could be better to build the TLs without the cut on top of the fingers, supposed to improve the contact between them and the cartridge plate, when the nylon ring is going to be used.

If one needs this Nylon ring will depend in the amount of heat load that will be present in the focal plane of the receiver when in operations and the temperature required by the detectors. In other words, if the temperature provided to the TLs and their thermal conductance is enough for the receiver to operate, there is no need to add the nylon ring. The 1.1 THz Array Receiver will need the TLs with their nylon rings to be able to operate with SIS mixers. Currently, it can operate with HEB mixers without the need of the nylon rings and probably it will also be able to, in the future, when the receiver is fully populated, if care is taken in minimizing the wiring and the amplifiers heat load.

3.6 Summary

We have designed and built a new all-metal TL to be used with the cartridge-type receiver, reducing maintenance complexity and allowing the required future flexibility.

The thermal conductance of the TL made of Al-5083 was 0.19 W/K, lower than the calculated 0.252 W/K. Since the performance of the TLs affects the temperature obtained in the receiver focal plane, located in the cartridges, it was decided to improve the thermal conductance of the 4 K TLs by making them of an aluminum with higher thermal conductivity. We designed a new TL made of Al-1050, which is the purest aluminum with a yield strength big enough to allow a new design in the space already allocated for it. Unfortunately, the result was not as good as expected, obtaining a thermal conductance only similar to the initial version. The difference in performance is partly due to the material, but mainly due to the contact, between the TL and the cartridge plate, which is hard to control during fabrication and is the weak point in our design. This can be improved by a Nylon ring installed around the top of the fingers, similar to the one in

the copper-nylon TL-model made for the ALMA test cryostat. The thermal conductance was increased to 0.45 W/K and allowed the best performance of the cryostat (chapter 2), where a temperature of 4.4 K was obtained in the CR.

If one needs this Nylon ring on the 4 K TLs will depend in the amount of heat load that will be present in the receiver focal plane and the required operation temperature for the detectors. In other words, if the thermal conductance of our all-metal TLs is enough for the receiver to operate, there is no need to add the nylon ring.

A cover made of aluminum had to be designed to be used with the 50 K TLs because the 2 mm finger spacing allows too much radiation from the 300 K vessel to pass directly into the 4 K stage, increasing the temperature of the latter. This solution worked very well and helped reduced the temperature of the 4 K stage.

Chapter 4

The 1.1 THz Heterodyne Array Receiver Optics

The receiver was designed as a cartridge-type receiver to, among other things, allow flexibility by being able to operate, in the future, at different frequencies and, within some limits, with different number of pixels. This is an important input for the decision of the optics-array design philosophy that should also permit this interchangeability.

In this chapter a detailed overview of the 1.1 THz Heterodyne Array Receiver optics is given. The Relay Optics, in charge of directing the beams from the two FPU optics outside of the cryostat and towards the Nasmyth A focal plane of the APEX telescope, is described in section 4.2. The FPU optics, in charge of coupling the radiation from the receiver focal plane into the feed horns of the mixing elements, is explained extensively in section 4.3, it is here that the beam distance on sky is defined.

A direct consequence of the decision to use SIS balanced mixers (section 1.3.4) instead of single-ended mixers, is the need of a LO Power Distribution accommodated behind the FPU optics which should provide an independent LO-signal path to the dedicated LO-port of each of the 9 mixers in the sub-array. A proposed design is presented in section 4.4.

To avoid absorption and reflection losses of lenses, the entire optics of the receiver is composed only of mirrors. However, all the optics-related schematic drawings included in this work show lenses instead of mirrors because lenses are better adapted for these representations to be understood.

The multi-beam optics tests were performed using HEB mixers, the results are presented in section 4.5.

4.1 Heterodyne Array Receiver Optics

Heterodyne array receivers have the important requirement that each beam must have optimum coupling to the telescope, to avoid signal loss. This, in

addition to the effects of diffraction, have the consequence that the astronomical source is not fully sampled¹ because one can not put the pixels closer than $\approx 2.5F\lambda$ (see section 4.3), where $F = f/D$ is the focal number of the telescope, f the effective focal length (including all common mirrors), λ the wavelength and D the diameter of the primary mirror. The optimum coupling to the telescope is taken care of by the heterodyne array receiver optics which can be divided in two parts:

- the Relay Optics or re-imaging optics in charge of transforming the focal plane of the telescope into the focal plane of the receiver
- the FPU optics, in charge of coupling the radiation from the focal plane of the receiver to the feed horns of the mixing elements.

The telescope focal plane can be the Cassegrain or one of the two Nasmyths focal planes and the receiver focal plane is located in the FPU optics which is described in detail in section 4.3. See figure 4.1 to have a clear overview of the location of these focal planes and the optics sub-assemblies that are described in this thesis.

In the following sections, the attention is given to the description of the Relay Optics, including the Cold Optics as part of it. The design principle of such optics is presented in section 4.1.1 and the design developed and built for the 1.1 THz Array Receiver is presented in section 4.2.

4.1.1 Design Principle

Due to the need of introducing Quasioptics and its mathematical statement, required for the design of the receiver optics, and also to set the notation used in this thesis, we replicate [Goldsmith, 1998] at the beginning of this section.

The optics of the sub-millimeter and millimeter heterodyne receivers, like it is the case for the 1.1 THz Array Receiver ($\lambda = 293 \mu\text{m}$, $50 - 500 \lambda \approx$ system dimensions), can not be described with geometrical optics which deals with radiation in the limit that the wavelength $\lambda \ll$ system dimensions. When $\lambda \approx$ system dimensions, diffraction effects dominate the propagation of radiation. In these situations a complex formalism to analyze the beam behavior is required.

Quasioptics gets into the middle of these two limiting cases and treats a realistic situation of system dimensions being only moderately larger when measured in wavelengths. This allows the theory of Gaussian beam modes and Gaussian beam propagation to be employed [Goldsmith, 1998]. This formalism includes the effects of diffraction within the limits of this case. The beam is described by a Gaussian intensity profile, having a beam radius

¹Nyquist criterion: $0.5F\lambda$

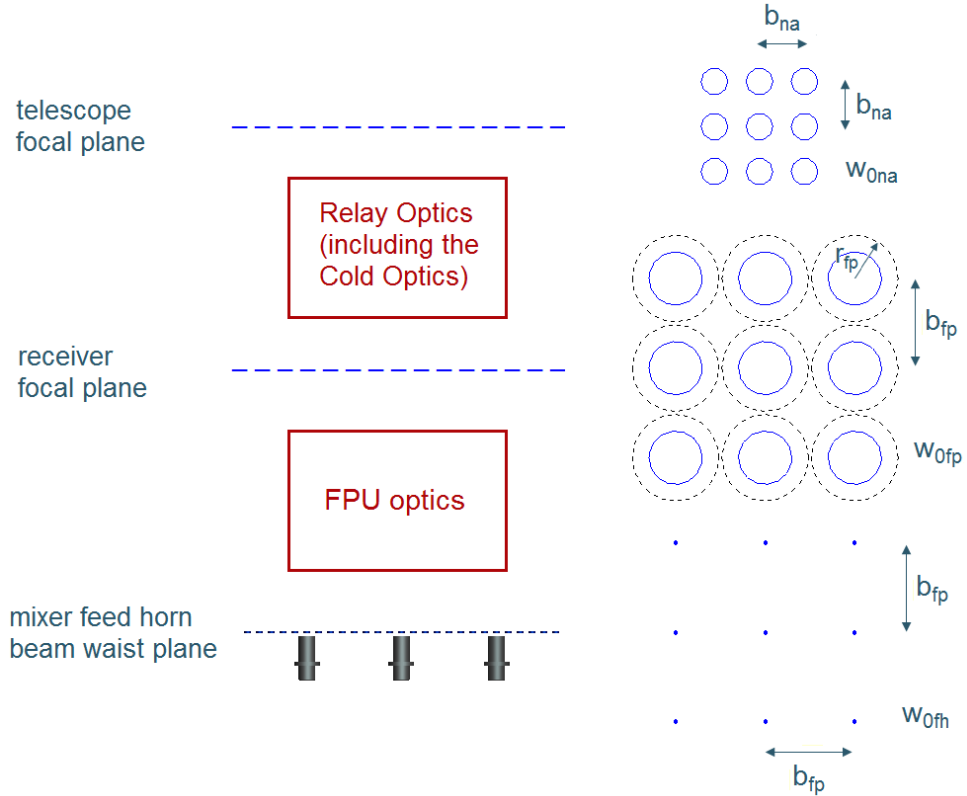


Figure 4.1: Schematic representation of the three important planes for the optical design and their layouts. Starting from the top, we have the telescope focal plane, then the receiver focal plane and finally the mixer-feed-horn beam-waist plane right in front of the feed horns. The beam waists (represented with blue circles) and the beam spacing on each plane are drawn in the same scale and are called: w_{0na} , b_{na} , w_{0fp} , b_{fp} , w_{0fh} and b_{fp} (same as the previous one) respectively. In addition, in the receiver focal plane, the size of the apertures ($3.25w_{0fp} = 2r_{fp}$, see section 4.3) are shown in dashed black lines. The optical sub-assembly required to convert from one plane to the next one is named in the red rectangles.

w , which is the value of the radius at which the field falls to $1/e$ relative to its on-axis value. Using the Gaussian beam formalism, the beam is fully determined by the beam waist radius (w_0) and its position $z = 0$. The beam radius at a distance z from the waist can be expressed as:

$$w(z) = w_0 \sqrt{1 + \left(\frac{\lambda z}{\pi w_0^2} \right)^2} \quad (4.1)$$

The propagation of Gaussian beams deals with the growth of the beam of radiation away from a beam waist, where the amplitude distribution perpendicular to the direction of propagation is most concentrated and the phase front is planar (figure 4.2 *left*). The process of altering the properties of a Gaussian beam is called beam transformation. While there are clear similarities to focusing in geometrical optics, it has to be reminded that in quasioptics there is no focus in the sense of radiation being concentrated to a point. What is done here is to transform one beam waist into another, as shown schematically in figure 4.2 *right*. The Gaussian beam transformation by a thin lens can be calculated by:

$$w_{0\text{out}} = \frac{w_{0\text{in}}}{[(d_{\text{in}}/f - 1)^2 + (\pi w_{0\text{in}}^2 / \lambda f)^2]^{1/2}} \quad (4.2)$$

$$\frac{d_{\text{out}}}{f} = 1 + \frac{d_{\text{in}}/f - 1}{(d_{\text{in}}/f - 1)^2 + (\pi w_{0\text{in}}^2 / \lambda f)^2} \quad (4.3)$$

The output beam waist $w_{0\text{out}}$ and the output distance d_{out} depend on the input beam waist $w_{0\text{in}}$ and the input distance d_{in} , as well as the focal length f and the wavelength λ .

After stating the basics of Gaussian beam propagation, we can focus on the Relay Optics and its design principle. First, it has to be said that a Relay Optics is in charge of converting the telescope focal plane into the receiver focal plane (see figure 4.1). In this thesis, we are dealing with an array receiver which is more challenging, but the same principle can be applied to a single-pixel receiver by considering it equivalent to the central pixel of the array receiver. Its design must include:

- Off-axis reflecting surfaces should be used to avoid absorption and reflection losses of dielectric lenses. The mirrors should be large enough to fulfill at least the $4w$ -criterion (see below), goal is $5w$, for all beams.
- The Gaussian beam coupling to the desired telescope focal plane illumination pattern should be as uniform and as high as possible across the complete FOV and the entire bandwidth.

The $4w$ -criterion means a minimum aperture diameter equal to $4w$ where w is the beam radius at the aperture (real aperture, lens or mirror). This

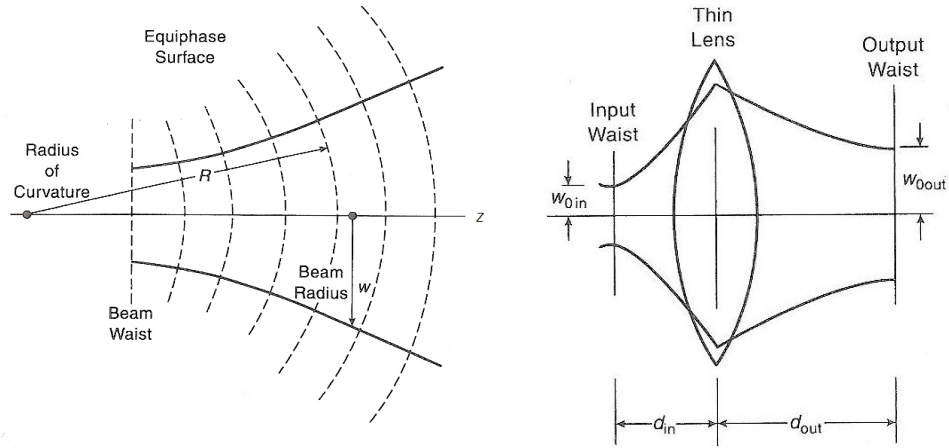


Figure 4.2: Left: Schematic diagram of Gaussian beam propagation: cut through beam showing equiphase surfaces with broken lines, beam radius w , and radius of curvature R . The beam waist is also identified. Right: Schematic of Gaussian beam transformation by thin lens. Both images from [Goldsmith, 1998].

truncates the beam at an edge taper T_e of 34.7 dB (defined by equation 4.12) and includes 99.97 % of the power in the fundamental mode Gaussian beam. In order to gain some margin for alignment tolerances we prefer to use, when possible (e.g. enough space for bigger apertures), the $5w$ -criterion, which includes 99.9996 % of the power corresponding to $T_e = 54$ dB. To calculate the right size of the mirrors and apertures, the beam spacing has to be considered. In the design of the Relay Optics for the 1.1 THz Array Receiver, the $5w$ -criterion was used. The topic of truncation and dimensions of the optical elements is treated again in section 4.3.

The telescope that will host the array receiver must also meet several requirements:

- The FOV must be wide enough to cover the entire $n \times m$ array of beams (in the 1.1 THz Array Receiver $n = m = 3$, the total number of beams is 9).
- The performance over the FOV must have minimal gain variation.
- The structure and mechanical design should offer an optical path free of vignetting and sufficiently-large intermediate mirrors (when needed) to fit all the beams with at least the $4w$ -criterion.

A good solution for the design of a Relay Optics for a multi-pixel heterodyne receiver is the use of a Gaussian Beam Telescope (*GBT*)². This device,

²*GBT* in *italics* to differentiate from the Green Bank Telescope (GBT)

illustrated in figure 4.3 top left), consists of a pair of focusing elements separated by the sum of their focal lengths ($f_1 + f_2$), has interesting properties that are presented below. From equations 4.2 and 4.3, the characteristics of the output beam can be determined as:

$$w_{0\text{out}2} = \frac{f_2}{f_1} w_{0\text{in}1} \quad (4.4)$$

$$d_{\text{out}2} = \frac{f_2}{f_1} \left(f_1 + f_2 - \frac{f_2}{f_1} d_{\text{in}1} \right) \quad (4.5)$$

where the output beam waist of the second mirror $w_{0\text{out}2}$ depends only on the input beam waist of the first mirror $w_{0\text{in}1}$ and the focal lengths ratio. Then, it has wavelength-independent magnification:

$$\mathcal{M} = \frac{w_{0\text{out}2}}{w_{0\text{in}1}} = \frac{f_2}{f_1} \quad (4.6)$$

In addition, the output beam-waist location after the second mirror ($d_{\text{out}2}$) depends only on ($d_{\text{in}1}$) and the focal lengths, and is equal to the focal length of the second element (f_2) for $d_{\text{in}1} = f_1$ (the focal length of the first mirror). Hence, $d_{\text{out}2}$ is also wavelength independent. The *GBT* is very useful in systems that must operate over broad bandwidths [Goldsmith, 1998].

For the conception of the Relay Optics, first, geometrical optics is used. The beam axis of each of the array pixels are traced, from the feed horns to the telescope and of course, through the *GBT*s, by using the ray tracing method [Hecht, 1987]. Afterward, Gaussian beams are propagated along each ray to take into account the diffraction.

Few words about the ray tracing method seem necessary, not only because it is used in the optics design of a heterodyne array receiver, but also to set the nomenclature used in this thesis. In any case, this will not be treated extensively since there are plenty of good books that describe it in detail [Born and Wolf, 1989], [Hecht, 1987].

The ray tracing method is used to determine the path of the light rays accurately with the help of elementary geometry, by successive application of the law of refraction (or reflection). Each ray is uniquely defined by position (distance from the optical axis) and angle (with respect of the optical axis), the paraxial approximation permits to express the angle as a slope. The position (b_{out}) and slope (θ_{out}) of the rays after passing a thin lens or mirror can be express as:

$$b_{\text{out}} = \left(1 - \frac{d_{\text{out}}}{f} \right) b_{\text{in}} + \left(d_{\text{in}} + d_{\text{out}} \left(1 - \frac{d_{\text{in}}}{f} \right) \right) \theta_{\text{in}} \quad (4.7)$$

$$\theta_{\text{out}} = \frac{-b_{\text{in}}}{f} + \left(1 - \frac{d_{\text{in}}}{f} \right) \theta_{\text{in}} \quad (4.8)$$

both depending on the position (b_{in}) and slope (θ_{in}) of the rays before the mirror, the distances before (d_{in}) and after (d_{out}) the mirror, as well as on its focal length f .

This ray tracing analysis has to be done for both mirrors forming the *GBT* (see figure 4.3 *top right*) and after that it is found that the same magnification is also valid for the position of the beams:

$$\mathcal{M} = \frac{b_{out2}}{b_{in1}} \quad (4.9)$$

The position of the beam is equivalent to the distance between beams (or beam spacing), i.e. the distance between the off-axis beam and the on-axis one. Here b_{out2} is the beam spacing after the second mirror and the b_{in1} is the distance between the beams entering the first mirror of the *GBT*. Equations 4.6 and 4.9 imply that:

$$\frac{w_{0out2}}{b_{out2}} = \frac{w_{0in1}}{b_{in1}} \quad (4.10)$$

This is a very important feature for the design of array optics for heterodyne receivers, it says that the ratio between the beam waist and the distance between the beams is the same in the input and output plane of a *GBT*, this ratio remains constant.

A particular situation is when $d_{in1} = f_1$, causing that $d_{out2} = f_2$; in this case, the beam waist position between the two mirrors is in the same place as the geometrical focus. This condition is not always possible due to mechanical constraints (e.g. assigned space in the receiver cabin) that limits the choice of the input or output distances. When w_{0in1} is closer to the first mirror ($d_{in1} < f_1$), then the w_{0out2} will be farther from the second mirror ($d_{out2} > f_2$). The contrary happens when $d_{in1} > f_1$. This can be easily seen in equation 4.5.

To conclude, an optical design schematic of a 3 pixel heterodyne receiver is presented in figure 4.3 *bottom* where it can be seen the ray tracing method for all the beam axes and the Gaussian beam propagation along each ray to consider the diffraction. The size of the mirrors is determined by at least the $4w$ -criterion (goal is $5w$) which means that the mirrors should be large enough to fit a beam diameter of $4w$ for each of the beams plus the beam spacing.

As can be seen, the *GBT* has the desirable features for the Relay Optics development. Nevertheless, it must be noted that this characteristics are strictly valid only for the beam propagation on-axis. In the case of a focal plane array, the *GBT* conditions can not be simultaneously met by the central pixel and the off-axis pixels. The off-axis beams propagate parallel to the axis connecting the geometrical foci to the center of the mirrors. In this thesis, this effect is neglected as well as no aberrations are calculated, the total FOV of the 1.1 THz Array Receiver is very small (33" x 33").

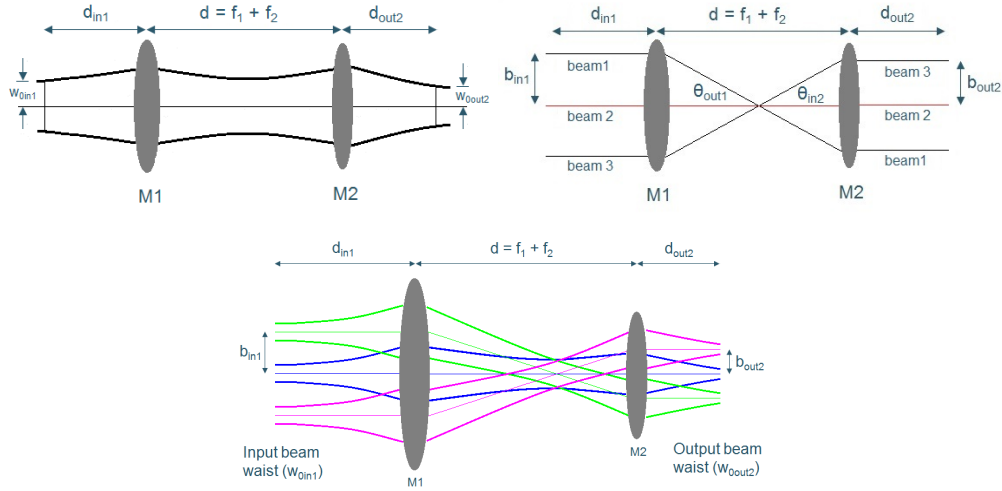


Figure 4.3: Top left: A single pixel GBT consisting of two focusing elements, with focal lengths f_1 and f_2 , separated by the sum of their focal lengths. Top right: The same pair of focusing elements using geometrical optics analysis for three beams, optical axis in red. Bottom: A combination of the two previous images describing the way heterodyne arrays optics is treated. This image shows an example with 3 pixels, the thin lines represent the beam axis and the thicker lines the Gaussian beam radius contour. The magnification is wavelength independent ($\mathcal{M} = f_2/f_1$) and is also equal to the ratio of beam waists (w_{0out2}/w_{0in1}) and beam distances (b_{out2}/b_{in1}).

In many cases, as well as in the case of the 1.1 THz Array Receiver, it is not possible to match the required magnification with one *GBT*, then a second one is incorporated to the Relay Optics design. This can be seen in the next section, where the Relay Optics of the 1.1 THz Array Receiver is described in detail.

4.2 The Relay Optics and the Cold Optics

The Relay Optics for the 1.1 THz Array Receiver was designed using the method described in the previous section. The Cold Optics is part of the Relay Optics, but is also explained separately because it is the optics assembly inside the cryostat, cooled down to 4 K, and machined quasi monolithically using Computer Numerical Control (CNC) milling techniques to guaranty internal alignment. The Cold Optics will be explained thoroughly in section 4.2.1, for the moment the description will be done for the Relay Optics as a whole.

The 1.1 THz Array Receiver will be installed in the Nasmyth A Cabin of the APEX telescope. The document [Heyminck et al., 2004], provided by the APEX team, defines the mechanical and optical constraints for the receiver

design. On one hand, it means that all the receiver parts, cryostat plus optics, must stay within the allocated area to avoid disturbing other installations inside the cabin (see figure 1.3). And, on the other hand, it gives information about the telescope focal plane beam waist and its location. In addition, it describes the refocusing system called Tertiary Optics (see figure 4.8) that modifies the APEX Cassegrain-telescope for Nasmyth instrumentation, the optical path to the telescope and its narrowest part.

The size of the Tertiary Optics mirrors together with the aperture of the optical path between the Nasmyth A and the Cassegrain focus of the telescope has to be considered, in the design of the Relay Optics, to be sure that they can fulfill at least the $4w$ -criterion (goal $5w$ -criterion) for the 9 beams of the array receiver. See section 4.2.2 for the details on what was achieved in this respect.

The focal plane array of the receiver consists of two sub-arrays, each formed by one FPU with 9 elements (section 4.3), and with sensitivity to perpendicular signal polarizations. In this receiver, both sub-arrays have their beams coincident on sky. The sub-arrays are coupled to the telescope via a wire-grid polarizer, in which the incoming signal from the telescope is split into two orthogonal polarization components, one per sub-array.

The operational band of the receiver is between 1000 and 1080 GHz, but it was decided to use a design frequency of 1025 GHz ($\lambda = 293 \mu\text{m}$), a better value with respect of the interesting lines found in this range, instead of the center of the band. At this design frequency, on the focal plane of the receiver which is located and defined in both FPU optics assemblies, the Gaussian beam waist is $w_{\text{ofp}} = 8.923 \text{ mm}$ and the distance between the beams is $b_{\text{fp}} = 30 \text{ mm}$ (see section 4.3 for a detailed explanation of these values). On the telescope focal plane, the Gaussian beam waist at the APEX Nasmyth A focal plane is, using $f/D = 20.5$ [Heyminck et al., 2004] and an edge taper (T_e) of 12 dB (see below), $w_{\text{0na}} = 4.505 \text{ mm}$ (equation 4.13) and as a consequence of equation 4.10, the beam distance is $b_{\text{na}} = 15.15 \text{ mm}$ (see figure 4.1). So, the required magnification of the Relay Optics to be able to reimage the receiver focal plane into the Nasmyth A focal plane is $\mathcal{M} = 0.505$ (equation 4.6).

Sub-millimeter receivers usually use edge tapers between 10 and 14 dB [Goldsmith, 1998], [Graf et al., 1998] laying between the optima given by the aperture efficiency and the main beam efficiency which increases when the aperture illumination becomes more highly tapered because of the reduce energy on the sides lobes of the antenna pattern. We use an edge taper of 12 dB to illuminate the APEX telescope; going to a higher value would mean that not all the Tertiary Optics mirrors can fulfill the $4w$ -criterion for all the beams (figure 4.8, table 4.2).

To be able to match this magnification together with the optical path length within the limits of the allocated area in the Nasmyth A cabin and the geometry inside the cryostat, the Relay Optics has to be formed by two

GBTs made of three ellipsoidal and one hyperboloidal mirrors. To work on the Relay Optics design using the method explained in section 4.1.1, the Gaussian beam optics formulation together with the ray tracing calculus were implemented in ProEngineer, a 3D CAD-software. In Table 4.1, the characteristics of these four mirrors are presented and figure 4.4 shows a schematic drawing of the Relay Optics design. The mirrors are numbered from 1 to 4 starting from the ones inside the cryostat and then following the beams towards the telescope. Inside the cryostat there are only two active mirrors which are $M1_t$ for the transmitted beams after the polarizer and $M1_r$ for the reflected ones. However, some descriptions in the following paragraphs are done in the opposite direction.

Name	f mm	$angle_r$ degree	d_{in} mm	w_{in} mm	b_{in} mm	d_{out} mm	w_{out} mm	b_{out} mm
$M1_t$	600.00	41.6	375.03	8.923	30.00	496.10	6.064	5.20
$M1_r$	600.00	74.5	375.03	8.923	30.00	496.10	6.064	5.20
M2	263.59	45.0	367.49	6.064	5.20	307.00	3.920	13.18
M3	811.42	45.0	307.00	3.920	13.18	-368.02	5.994	19.16
M4	932.51	73.0	2111.95	5.994	19.16	1598.72	4.505	15.15

Table 4.1: Characteristics of the Relay-Optics and Cold-Optics active mirrors. The two pairs of mirrors that form the two *GBTs* are both $M1$ s with M2 ($\mathcal{M} = 0.44$) and M3 with M4 ($\mathcal{M} = 1.15$). All mirrors are ellipsoidal except M3 which is hyperboloidal. In the columns, f is the focal length, $angle_r$ the reflection angle, d_{in} the input distance, w_{in} the input beam waist, b_{in} the input beam distance. The same repeats for the outputs.

The Relay Optics includes a diplexer to leave open the possibility of using single-ended HEBs or SIS, in which case the LO beams have to be coupled to the RF beams before arriving into the mixing elements. Nevertheless, we are developing SIS balanced mixers and the LO Power Distribution and expect in the near future change this optical LO coupling. To take this diplexer out and adjust the warm optics presents no problem.

The use of two *GBTs* make possible to have a more compact arrangement of the diplexer because it allows a smaller beam diameter and beam spacing. This is a good reason to put the diplexer after the first set of two mirrors, besides here the beams are parallel. In this way, the first *GBT* re-images the telescope focal plane to one of the roof-top mirrors of the dual diplexer. Then, the second *GBT* converts the diplexer waists to the receiver focal plane inside the cryostat. To assure its smallest size, the entrance window of the cryostat is positioned where the beams cross between these last two mirrors, its diameter is 35 mm and it is made of HDPE (see section 2.2.3 for details). Once inside the cryostat, the first optical element is the polarizer

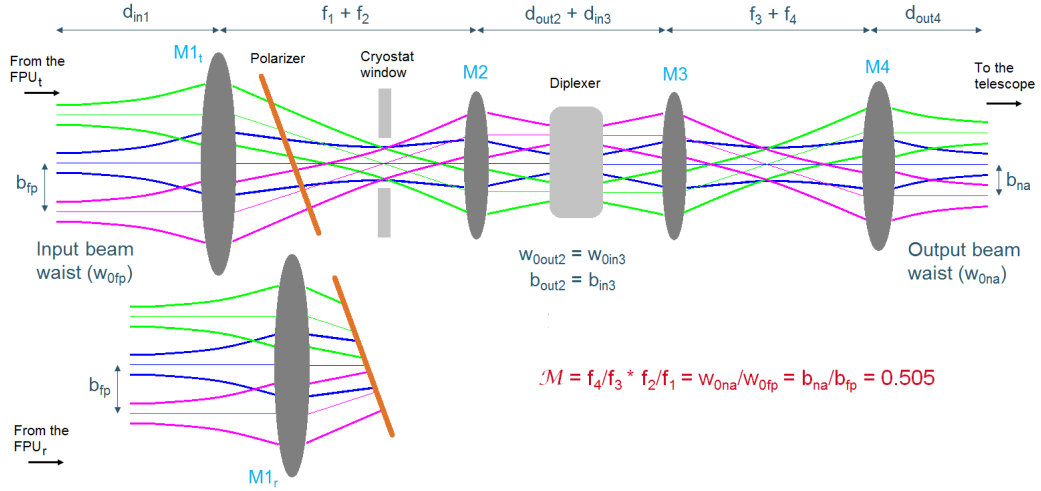


Figure 4.4: Schematic of the Relay Optics the two *GBTs* and the location of the entrance window, the diplexer (as an option) and the polarizer. This image shows only 3 pixels, the thin lines represent the beam axis and the thicker lines the Gaussian beam radius contour. The optical elements present to the left of the entrance window form the Cold Optics. Only one polarizer is used, but two are drawn to facilitate the representation. To the left of the polarizer, the top part represents the transmitted beams that come from FPU_t and the bottom one stands for the reflected beams that come from FPU_r . The beam spacing in the FPU s optics (i.e. in the receiver focal plane) is b_{fp} , being b_{na} , the beam spacing in the Nasmyth A focal plane, w_{ofp} and w_{0na} are the corresponding beam waists and f_1 to f_4 the focal lengths of each mirror. \mathcal{M} is the total magnification. The plane mirrors needed to fold the beams are not included.

(the last common element to all the beams) which splits the incoming signal into two orthogonally polarized sets of 9 beams. The polarizer can be seen in figure 4.7 and is described in this section 4.2.1. After that, the transmitted and reflected beams continue different paths to their corresponding second mirror ($M1_t$ and $M1_r$) of this *GBT* and then all the way to each sub-array (FPU optics). Plane mirrors had to be introduced for the bending and redirectioning of the beams inside the cryostat as well as outside of it to keep the optical path inside the allocated envelope. Figure 4.5 shows a complete 3D CAD model of the Relay Optics and figure 2.8 shows the receiver focal plane sub-arrays layout as defined by this Relay Optics. This is important because it defines the orientation in which the cartridges have to be mounted into the cryostat.

4.2.1 The Cold Optics

Now the Cold Optics can be introduced and explained as a separate unit. It is formed by all the optical elements of the Relay Optics that are inside the

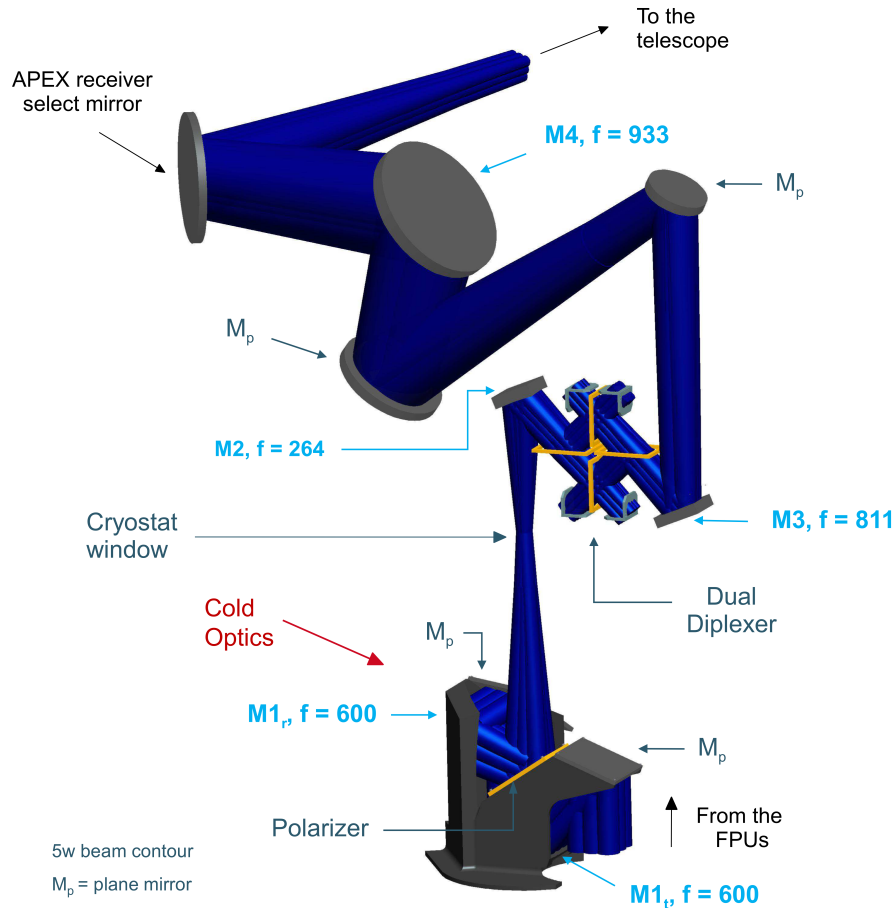


Figure 4.5: CAD drawing of the Relay Optics showing the 5w beam contour of the RF beams in dark blue. The four mirrors named in light blue are the active mirrors that form the two *GBTs* which transform the receiver focal-plane Gaussian beam waists into the Nasmyth A focal-plane beam waists. The Cold Optics is the part of the Relay Optics which is inside of the cryostat. A diplexer is present as an option in case of using single ended mixers, however the LO beams and the Fourier grating that would be needed are not present in the drawing. To take away the dual diplexer and adjust the position of the mirrors to operate with balanced mixers presents no problem. The distance from the bottom of the Cold Optics to the APEX receiver select mirror is 1350 mm, the dimensions of the Cold Optics are shown in figure 4.6.

cryostat and cooled down to 4 K. It consists of the polarizer (described below in this section) and the mirrors for the transmitted and reflected beams. This means, two active mirrors, $M1_t$ and $M1_r$ (see table 4.1), which have the same focal length, but different reflection angle to cope with the space inside the cryostat and two plane mirrors to fold the beams and direct them towards the corresponding FPU optics.

Figure 4.6 shows a 3D CAD illustration (*Left*) and a photograph (*Right*) of the Cold Optics alone. Additionally, see figure 2.1 for a 3D CAD model (*Top left*) and a picture (*Top right*) of the Cold Optics, with the plane mirrors and polarizer, mounted on the cryostat.

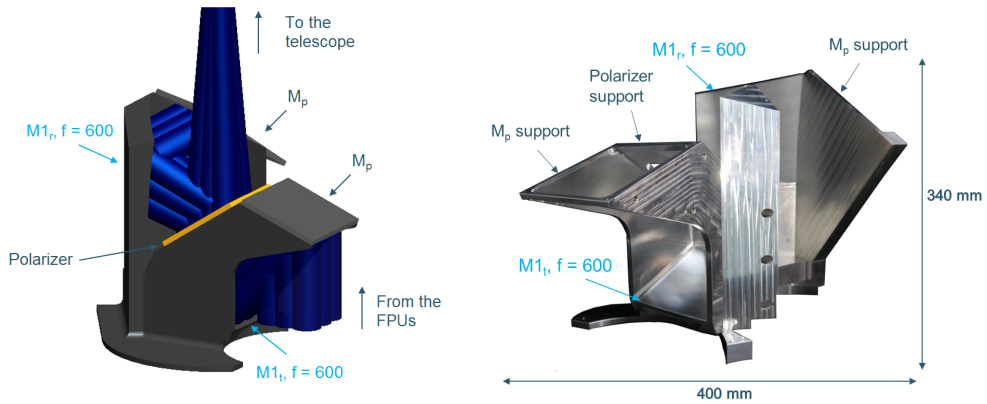


Figure 4.6: Two views of the Cold Optics. Left: CAD drawing of the monolithic Cold Optics including the polarizer in yellow and the two plane mirrors (M_p). The 5w beam contour of the RF beams in dark blue can also be seen. Right: Photograph of the manufactured Cold Optics, made in aluminum as a quasi monolithic piece which weighs 11.7 kg. The weight including the two M_p and the polarizer is 13 kg. The dimensions are included.

To compensate for the shrinking of the Cold Optics when cooled down, a scaled version of it is manufactured at ambient temperature. The scaling factor is calculated taking into account the aluminum thermal expansion values and the difference between the manufacturing and operating temperatures. In this way, the Cold Optics has the right size when at 4 K. The manufacturing could not be done fully monolithically due to its large size, thus it was built in three separate parts that were mounted and put back together in the CNC machine to mill precisely the active mirrors surfaces. To get the best-quality surface on the two plane mirrors, they were manufactured separately and then mounted to the main monolithic part.

The use of a crossed wire grid would have allowed a much simpler and easier Cold Optics design because of symmetry. Crossed grids allow an unpolarized beam to be separated into orthogonal components with both beams being deflected by 90 degrees. A further advantage of this arrangement is that remaining IR radiation passes directly through the crossed grid and thus

is not directed toward the detectors. This can be very useful in reducing the thermal loading on cryostat cold plates. [Schuster et al., 2004] shows a 230 GHz heterodyne receiver array that includes a crossed grid in its optics, but at the 1.1 THz Array Receiver wavelengths, we were not sure to have a product of the required quality and so, we decided to go ahead with the use of a single wire-grid polarizer.

The Cold Optics was tested together with the two FPU optics by doing beam measurements with HEB mixers working in direct mode. The results of these measurements together with other Cold Optics tests are reported in section 4.5.

The Polarizer

A polarizer is needed as part of the Cold Optics to combined the 9 beams that come from both FPUs. The characteristics of this polarizer are a clear aperture of 94 mm x 117 mm, 10 μm diameter wirewound with 25 μm center spacing. The wire is wound parallel to the short side of the aperture. In addition, it is composed of an Invar two-piece rectangular frame (4 mm thick keeper frame over the wires) which makes a total size of 118 mm x 141 mm. A polarizer of this characteristics was ordered from [QMC Instruments Ltd.,] in Cardiff, United Kingdom and it can be seen in figure 4.7.

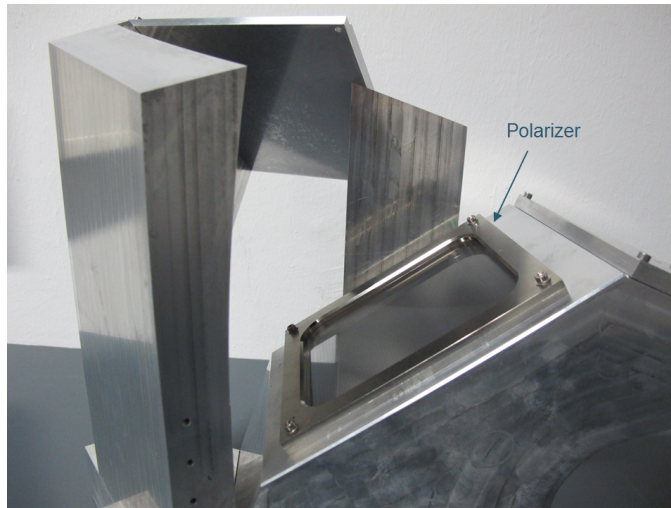


Figure 4.7: Picture of the polarizer mounted in the Cold Optics, its size including the Invar frame is 118 mm x 141 mm. The thickness of the two-piece rectangular frame is 8 mm.

4.2.2 APEX Tertiary Optics

APEX is a Cassegrain telescope modified for Nasmyth instrumentation. Thus, a refocusing system has been introduced to transform the telescope

waist into a Nasmyth waist located in the Nasmyth cabin(s). The refocusing system, called Tertiary Optics and described in [Heyminck et al., 2004], was conceived using a *GBT* that makes the optics frequency independent and that would also allow operation of (small) multi-pixel receiver systems. The number of pixels is limited, among others, by the size of the Tertiary-Optics mirrors and the observing wavelength. The mirror-sizes were defined to fulfill at least the $4w$ -criterion for a single-pixel receiver working at 211 GHz ($\lambda = 1.4$ mm).

The Tertiary Optics characteristics were utilized for the design of the Relay Optics of the 1.1 THz Array Receiver (section 4.2). Here, we show the 9 beams of the receiver propagate through the Nasmyth tube and the Tertiary Optics towards the telescope.

The results are shown in figure 4.8 and in table 4.2 where the mirror sizes and the fulfill criterion are stated. It can be seen that all 9 RF beams go through the Nasmyth tube and the elevation encoder (narrowest aperture in the optical path) without vignetting and fulfilling the $5w$ -criterion (goal) for all the beams and all mirrors do better than the $4w$ -criterion. To summarize, the 1.1 THz Array Receiver can operate in the Nasmyth A cabin of the APEX telescope.

	Available size mm	Reflection angle degree	Fulfill criterion
Tertiary Mirror M3			
size 1	200		
size 2	250 (239)	34	$4.2w$
Flat Mirror F4			
size 1	200		
size 2	280 (247)	56	$4.8w$
Flat Mirror F5			
size 1	180		
size 2	220 (156)	90	$4.7w$
Tertiary Mirror M6			
size 1	180		
size 2	220 (156)	90	$4.8w$

Table 4.2: APEX Tertiary Optics, the size of its mirrors and the 1.1 THz Array Receiver Relay Optics fulfilled criterion. Size 1 and size 2 are the dimensions of the rectangular tertiary mirrors, the first one is perpendicular to the page. The mirror projection on the optical path, calculated from its reflection angle, is also considered and given in parenthesis. At least the $4w$ -criterion is achieved for all the mirrors. See figure 4.8 for a CAD model of the Tertiary Optics with the 9 beams.

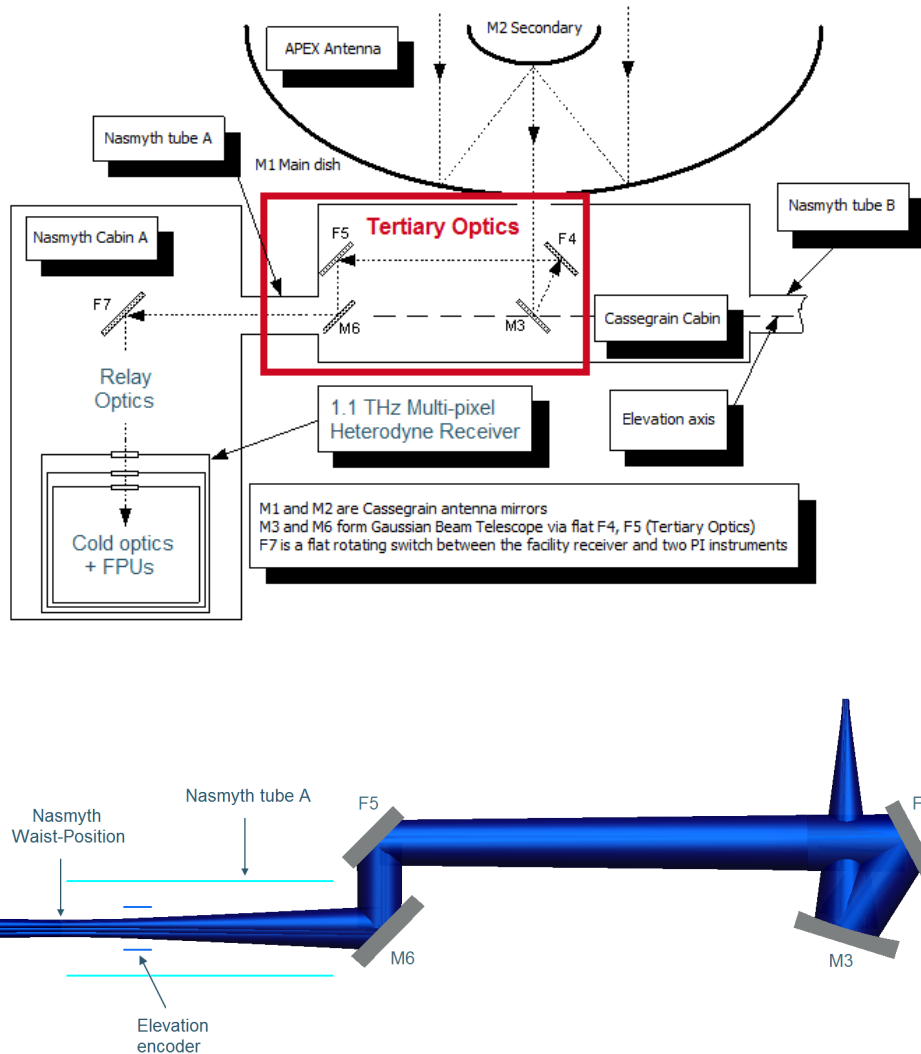


Figure 4.8: Top: Optical layout for the APEX Nasmyth Cabin A receivers. The 1.1 THz Array Receiver location and its optics are identified, the receiver is chosen by the receiver select mirror (F7). The refocusing system called Tertiary Optics is highlighted with a red rectangle. Based on the drawing from SHEFI^a documentation [APEX telescope,]. Bottom: The $5w$ -contour of the 9 astronomical beams of the 1.1 THz Array Receiver go through the Nasmyth tube A and the narrowest aperture in the optical path (elevation encoder) without vignetting and through the Tertiary Optics fulfilling at least the $4w$ -criterion (see table 4.2 for details).

^aSwedish Heterodyne Facility Instrument

4.3 The Focal Plane Unit (FPU) Optics

Previously, in section 4.1.1, the design principle of the re-imaging optics needed to transform the heterodyne array-receiver focal plane into the telescope focal plane was discussed. After that, in section 4.2, the specific Relay Optics and Cold Optics of the 1.1 THz Array Receiver was told in detail. This re-imaging system transforms the receiver focal plane into the Nasmyth A focal plane of the APEX telescope. Thereafter, also explained in the last mentioned section, the propagation of the RF beams continue through the Tertiary Optics all the way to the Cassegrain focus of the telescope. Thus, the propagation to the telescope and, as a consequence, to the sky is done. Now, we have to take care of the propagation of the beams from the receiver focal plane towards the mixer feed horns.

In the 1.1 THz Array Receiver, the focal plane is composed by two sub-arrays, one per cartridge. Each sub-array is formed by one FPU (in literature also find as mixer unit or focal plane array) that consists of some optics and 9 detecting elements (feed horns, mixers, low noise amplifiers, etc) arranged in a 3x3 configuration. In this section, the focus will be given to the description of the FPU optics. Both sub-arrays are identical, they will be only mounted with a relative rotation of 21 degrees. Consequently, the description of the FPU optics will continue indistinctly.

Heterodyne detectors preserve the phase³ of the received wave field and are sensitive only to a single polarization. Therefore, precautions are taken to focus the radiation entirely into each mixer horn to minimize integration time and so, the target is not Nyquist-sampled directly, but with the appropriate observation procedure. The goals of the FPU optics are:

- to maximize the overlap integral of the two radiation patterns in the receiver focal plane: the one of the Relay Optics and the one of the mixer feed horn.
- to pack the beams together as close as possible, fulfilling the $3.25w$ -criterion (explain below in this section), in order to keep the beam spacing on sky to a minimum.

The first point means that the FPU optics adapts the individual beam of the mixer feed horn to the common optics and ensures the required illumination of the telescope for each of the sub-array pixels. The second point comes from the fact that the relative spacing of the array pixels on the sky is determined by the ratio of the beam spacing (b_{fp}) to the beam waist (w_{ofp}) at the point where the beams enter the common receiver optics. Both points will be developed in extense in the following paragraphs.

³Reason for the quantum limit, the ultimate limit for coherent receivers.

In the far field of the telescope, the beam separation is:

$$\Theta = \frac{b_{\text{fp}}}{f} \quad (4.11)$$

where f is the effective focal length including all common mirrors or lenses and b_{fp} is the separation of the feed elements in the receiver focal plane (size of the pixel \approx beam spacing). In the current receiver the minimum beam spacing in the focal plane was imposed by the estimated size of the mixer blocks. Since the SIS balanced mixers are still being developed, it was decided to leave an area of 30 x 30 mm² for the future mixer blocks to be on the safe side in this respect. This provided area is bigger than the actual mixer-block area of 20 x 20 mm² used by the single-ended mixers.

The antenna illumination produced by a Gaussian feed distribution is described by the edge taper T_e , or by level of truncation at the edge of the aperture. The T_e , usually expressed in decibels with $T_e(\text{dB}) = -10\log_{10}(T_e)$, is the relative power density at a given radius of aperture and can be expressed as:

$$\frac{r_a}{w_a} = 0.3393\sqrt{T_e(\text{dB})} \quad (4.12)$$

where r_a is the radius of the antenna main dish and w_a is the beam radius of the Gaussian power pattern in the aperture plane.

A feed system generally employs a sequence of quasioptical components that affect the size and location of the final beam waist of the system, which produces the beam that actually illuminates the antenna. In [Goldsmith, 1998] can be found all the needed formulation to find the expression that satisfies the requirement of an appropriate illumination of the primary mirror by the feed system. Then, considering a primary mirror, which is circular and of diameter D , with a Gaussian beam and a telescope edge taper of $T_e(\text{dB})$, the required illumination beam waist radius in the receiver focal plane is given by:

$$w_{\text{ofp}} = 0.216\lambda\frac{f}{D}\sqrt{T_e(\text{dB})} \quad (4.13)$$

The main lobe of the radiation pattern of an antenna is usually described by the HPBW, which is the angle between points of the main beam where the normalized power pattern falls to half of the maximum. The expression for the HPBW (also called Full Width Half Maximum (FWHM)) of an in-focus, unblocked circular aperture with Gaussian illumination including truncation can be approximated by:

$$\text{HPBW} = [1.02 + 0.0135T_e(\text{dB})] \frac{\lambda}{D} \quad (4.14)$$

for the range of edge tapers of interest for radio telescope illumination ($0 \leq T_e \leq 25$ dB) [Goldsmith, 1998]. Then, we combine equations 4.11, 4.13 and 4.14 to express the beam separation as:

$$\frac{\Theta}{\text{HPBW}} = 0.216 \frac{b_{\text{fp}}}{w_{\text{ofp}}} \frac{\sqrt{T_e(\text{dB})}}{[1.02 + 0.0135T_e(\text{dB})]} \quad (4.15)$$

This shows clearly that the beam spacing on sky is defined by the ratio $b_{\text{fp}}/w_{\text{ofp}}$. Being T_e between 10 and 14 dB, the designer can only modify this ratio so that the FPU optics satisfies the requirements. In practice, the minimum size of the b_{fp} is already defined by other constraints, namely the size of the mixer blocks, leaving us with only the w_{ofp} as free parameter.

To continue with the analysis, first, we assume that the b_{fp} is equal to the circular aperture of radius r_{fp} (see figure 4.1). The ideal situation, seen from the last equation, is that the beam waist covers as much as possible the aperture, but the aperture should also let maximum radiation power go through, so it has to be a little bigger. This represents the difficulty in finding the best value for this ratio.

With respect of radiation power going through the aperture of radius r_{fp} , the fraction of power lost from the propagating fundamental mode beam is defined to be $F_{\text{lost}}(r_{\text{fp}})$ and is equal to the edge taper (power density at r_{fp} relative to that on axis) already discussed above and which can be used not only for the antenna aperture, but also to define the appropriate size of all mirrors, lenses and apertures in the optical path, it's described by equation 4.12. Then, $F(r_{\text{fp}})$, the fraction of power within the radius r_{fp} , can be calculated from:

$$F_{\text{lost}}(r_{\text{fp}}) = 1 - F(r_{\text{fp}}) = T_e(r_{\text{fp}}) \quad (4.16)$$

and should be as high as possible, minimizing losses due to truncation. This objective would lead the beam waist to smaller values causing an increase in the beam separation on sky. Then, to compensate this situation one would try to make the beam waist bigger, even to the expense of increasing some losses, to reduce this ratio value. A good compromise needs to be found.

However, beam truncation has more harmful effects than those due to the loss of power from the fundamental mode produced by the truncation itself. In [Goldsmith, 1998], the broadening of the main lobe of the beam is stated as a second effect of truncation. This is an effect equivalent to having a smaller effective beam waist radius ($w_{0\text{eff}}$) than that characterizing the original, untruncated beam and the following equation is used to approximate it:

$$\frac{w_{0\text{eff}}}{w_0} = \frac{0.40\sqrt{T_e(\text{dB})}}{1.6 + 0.021T_e(\text{dB})} \quad (4.17)$$

being T_e the equivalent edge taper of the $r_{\text{fp}}/w_{\text{ofp}}$ ratio, calculated from equation 4.12 and used with its corresponding value in decibels. For ratio values ≥ 1.6 ($T_e \geq 20$ dB), meaning low loss as well as accurate Gaussian beam design that will not be affected by truncation produced at the optical elements, the effect of truncation can be treated as a perturbation described by:

$$\frac{w_{\text{0eff}}}{w_0} = 1 - \sqrt{T_e} \quad (4.18)$$

This approximated formula, sufficient to give account of the phenomena, was obtained from [Belland and Crenn, 1982].

The best way to find the most appropriate ratio value and thereafter the w_{ofp} for the design, is to plot the $F(r_{\text{fp}})$ obtained from equation 4.16 and the ratio of the beam spacing on sky over HPBW (equation 4.15) for different ratio values and calculated for both, the original and the effective values of w_{ofp} . The later is obtained with equations 4.17 and 4.18. See these plots in figure 4.9 where it can be seen that for ratios smaller than 1.5 not only the included power starts to diminish strongly, but also that the smaller effective waist w_{0eff} limits the improvement of getting closer beams on sky.

When truncation is the only issue, the right choice is a ratio ≥ 2.0 , also known as the $4w$ -criterion, which means an included power of 99.97% and an equivalent edge taper of 34.75 dB, but as said before, in the FPU the beam spacing also matters. The chosen ratio for the design of the FPU optics was 1.625, this is a compromise between included power and distance on sky, considering also the effective-waist asymptotic effect. This $3.25w$ -criterion means an included power of 99.49% that corresponds to an edge taper of 22.94 dB and a ratio $w_{\text{0eff}}/w_{\text{ofp}} = 0.93$ according to equation 4.18. It's important to note that in [Lüthi et al., 2006] this ratio is estimated, based on simulations and confirmed by measurements, in 0.96. The resulting beam spacing on sky is of 2.2HPBW when considering the w_{0eff} .

The FPU optics, built for the 1.1 THz Array Receiver, has been designed to perform its task after the Compact Heterodyne Array Receiver Module (CHARM) concept [Lüthi et al., 2006] which is an expandable, purely reflective focal plane optics. In the case of SMART [Graf et al., 2003] another concept of only-reflecting mixer unit is used, but it is arranged in a 4x2 configuration making it more difficult to expand to a higher number of pixels than in the case of the CHARM concept.

The design was done using the fundamental-mode Gaussian beam formulation implemented in ProEngineer, a 3D CAD software. In the FPU optics setup the large collimation mirrors, and thus the beams, are arranged on a rectangular grid, with the horns and small illumination mirrors located in the gaps between the individual collimation mirrors and beams respectively (figure 4.10 left). In this manner, the array is scalable to an arbitrary number of pixels. The ratio $b_{\text{fp}}/w_{\text{ofp}}$ is defined in the focal plane which is located in

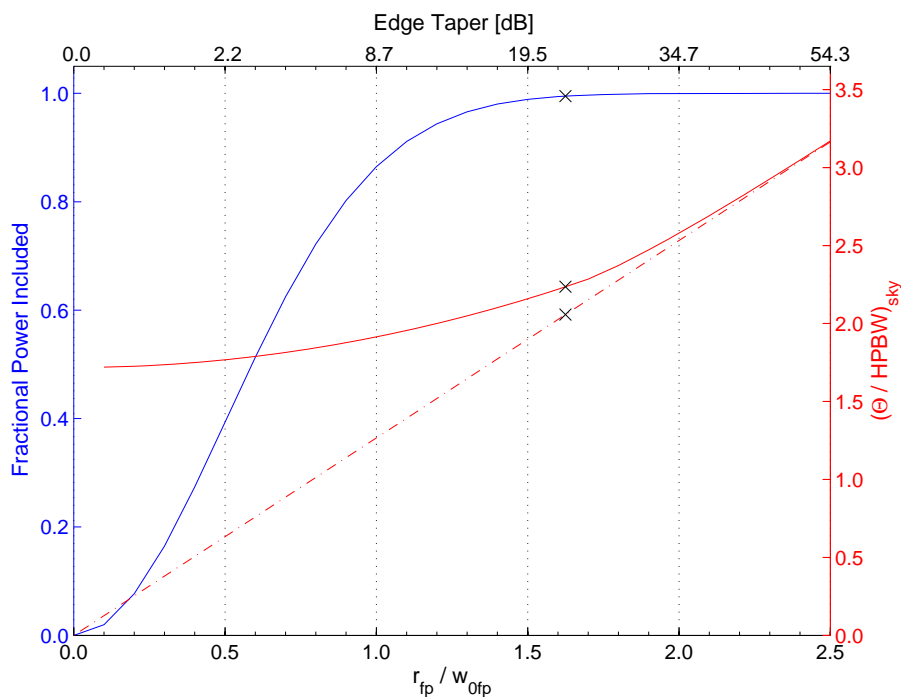


Figure 4.9: In blue, the fractional power of a fundamental mode Gaussian beam contained in a circular aperture of radius r_{fp} in the focal plane. The bottom x-axis is the ratio of this radius with respect of w_{0fp} and the top x-axis is the same, but represented in terms of edge taper in decibels. In red, two curves showing the effect of this ratio in the beam spacing on sky, both calculated for a telescope taper of 12 dB. The dashed line shows the results when considering the original w_{0fp} while the continuous line shows the effect of truncation that results in a smaller effective waist w_{0eff} that limits the improvement of getting closer beams on sky at smaller ratio values. The ratio, $r_{fp}/w_{0fp} = 1.625$, used for the current FPU optics design is shown with black crosses.

the FPU optics. For minimum beam truncation the focal plane, and thus the w_{ofp} , are located in the plane of the illumination mirror plate. In this common support plate with circular apertures of radius r_{fp} for the output beams, mechanical support is also provided to all the illumination mirrors fitted in the gaps of the apertures. The thickness s of the bars between the apertures should be kept as small as possible to prevent the beam separation from increasing.

In the FPU optics for the 1.1 THz Array Receiver, the pixels are arranged in a 3x3 configuration. The optics unit cell is formed by a two mirror collimator arranged as an off-axis Cassegrain system and a feed horn (figure 4.10 *top-right*). Thus, on each pixel, the divergent beam from the mixer feed horn, with a beam waist (w_{offh}) of 0.590 mm and located at 1 mm in front of the horn aperture, is reflected back by a hyperboloidal illumination mirror ($f = 227.04$) onto an ellipsoidal collimation mirror ($f = 63.74$) which then reflects the beam towards the focal plane producing a focal-plane beam waist (w_{ofp}) of 8.923 mm.

Name	f mm	$angle_r$ degree	d_{in} mm	w_{in} mm	d_{out} mm	w_{out} mm
M _{ill}	227.04	19.00	25.87	0.590	-29.10	0.666
M _{coll}	63.74	19.00	63.56	0.666	31.15	8.923

Table 4.3: Characteristics of the FPU optics. M_{ill} and M_{coll} are the illumination and collimation mirrors respectively. The w_{in} of the M_{ill} is also called w_{offh} and the w_{out} of the M_{coll} is also referred as w_{ofp} (see figure 4.10).

This last value was obtained as follows: the available space for each mixer-block is 30*30 mm², the thickness of the bars between the apertures is $s = 1$ mm and the diameter of the individual beam aperture is, for the reasons explained before, set to $3.25w_{\text{ofp}} = 29$ mm. Thus, when we do the exact calculation, $b_{\text{fp}} = 2r_{\text{fp}} + 1$, it makes the ratio $b_{\text{fp}}/w_{\text{ofp}} = 3.36$ and the resulting beam spacing on the sky equal to 13.5" (2.3HPBW) for the effective beam waist. The collimation was optimized to keep the mirrors as flat as possible, this together with the small reflection angles of 38° minimize optical aberrations.

We employ smoothed-wall spline-profile feed horns (figures 4.10 *bottom-right* and 4.11) optimized for the receiver's operating frequency of 1025 GHz ($\lambda = 293 \mu\text{m}$) to produce a beam with a high Gaussicity [Johansson, 1995] already at short distance of the illumination mirror. The optimization method of the spline profile is presented in [Granet et al., 2004]. An important characteristics of this kind of feed horns is that the beam waist is located well in front of the feed-horn aperture [Lüthi et al., 2006] so that the reflected beams are not truncated by the feed horn. An additional advantage of smooth-wall

feed horns is that they can be manufactured considerably easier and less expensive than the corrugated ones, especially at high frequencies. This is a very important factor when a large number of feed horns are required like it is the case in millimeter and sub-millimeter wavelengths array receivers.

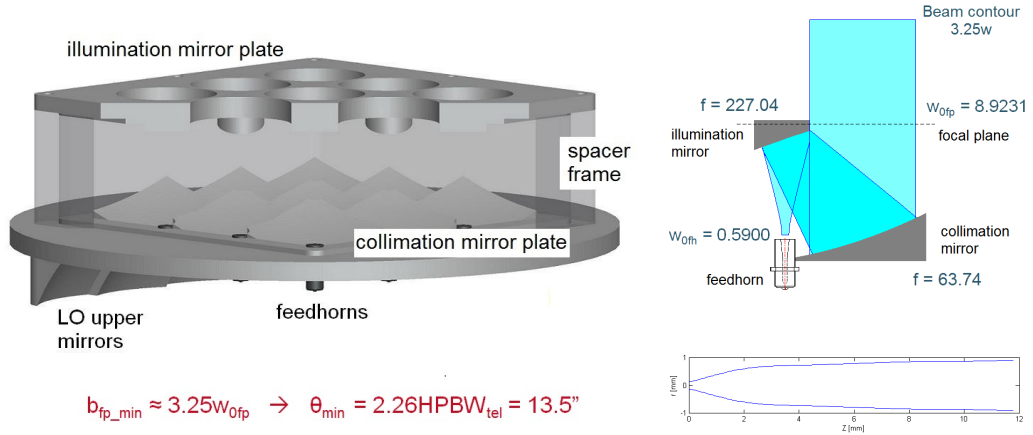


Figure 4.10: Left: CAD model of the 1.1 THz Array Receiver 3x3-beam FPU optics that consists, apart from the feed horns, of only three major parts: two plates with all the collimation and illumination mirrors and a spacer frame. Each sub-assembly is machined monolithically. The spacer frame keeps both plates at a distance of 40 mm and the diameter of the circular plate is 175 mm. The LO upper mirrors can be seen in the back side of the collimator mirror plate. These mirrors are part of the LO power distribution sub-system (see section 4.4) accommodated behind the FPU optics. Top-right: 2D drawing of the unit cell showing the optical beam path in each pixel with the 3.25w beam contour. Bottom-right: The smooth-walled spline-profile feed horn optimized for 1025 GHz.

The manufacture of each optical sub-assembly is carried out monolithically on our in-house 5-axis CNC-milling machine in a single machining cycle with very high precision, thus eliminating the need for an individual alignment. In the case of the FPU optics (pictures are shown in figure 4.12) which consists of three major parts, two plates with all the collimation and illumination mirrors respectively and a spacer frame, three machining cycles were needed. Due to the temperature difference between the manufacturing and operations temperature, scale versions of each part are built. The scaling factor takes into account the thermal expansion characteristics of the aluminum between 300 K and 4.2 K (see figure 3.2).

A similar FPU optics design for an operation frequency of 345 GHz was successfully built and tested. Its near field pattern simulations and measurements agreed very well ([Lüthi et al., 2006]). In this thesis, the 1.1 THz Array Receiver FPU optics performance was tested, independently and together with the Cold Optics, by doing beam measurements with HEB mixers working in direct detection mode. The results of this measurements are pre-

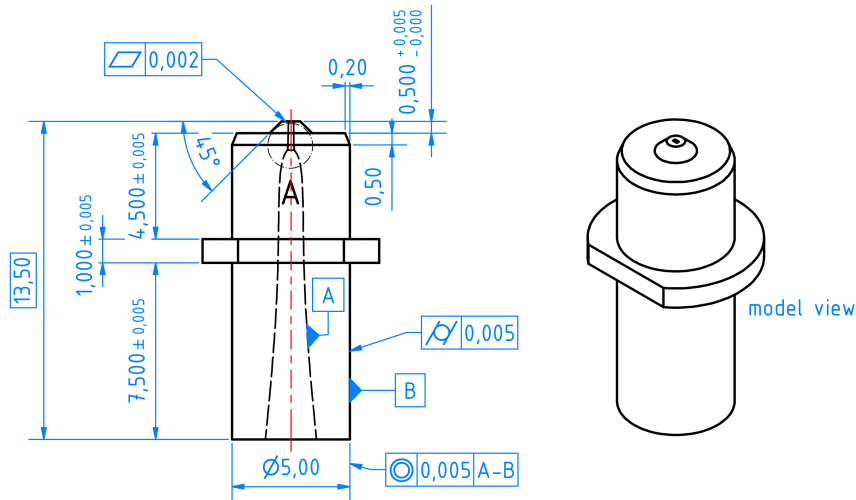


Figure 4.11: The 1025 GHz smooth-walled spline-profile feed horn: its dimensions and a model view. All feed horns are provided by [Radiometer Physics GmbH,].

sented in section 4.5.

Other integrated mixer concept is proposed in CHAMP⁺ [Kasemann et al., 2006]. There, a so called fly’s eye lens, a hexagonal arrangement of 7 individual crystal quartz lenses, coated with PTFE layers to minimize reflection losses, matches the common optics to the individual mixer-horns (corrugated feeds) of the array. This solution offers a simpler geometry.

4.4 LO Power Distribution

As said in section 1.3.4, the balanced mixers have two independent input ports, one for the RF and one for the LO radiation which implies that both signals can be combined without the need of an optical diplexer and thus, the LO power can be effectively used. Nevertheless, this means that the LO signal should have a separate distribution network.

In this thesis, this dedicated network is called the LO Power Distribution and is accommodated behind the FPU optics (section 4.3). It is divided in two main parts. The first one called LO Distribution Optics and the second one being the LO Distribution Plate. Both are explained in sections 4.4.1 and 4.4.2 respectively. See figure 4.13 to identify these parts in the cartridge set up.

The LO Power Distribution sub-system described here is only a proposed solution, it has not been built yet mainly due to the complexity of the LO Distribution Plate which is not ready yet. It is better to wait for the development of this plate, which is not part of this thesis, and then the LO Distribution Optics can be built directly or adjusted.



Figure 4.12: Pictures of the 1.1 THz Array Receiver FPU optics built in aluminum and based on the CHARM concept [Lüthi et al., 2006]. Top: The FPU optics ensemble. Bottom: The two plates with all the illumination (left) and collimation (right) mirrors, each is built out of one aluminum block in a machining cycle. The spacer frame that keeps both plates at a distance of 40 mm is not presented separately. The diameter of the circular plate is 175 mm.

4.4.1 LO Distribution Optics

The LO distribution optics is formed by a collimating Fourier grating ([Graf and Heyminck, 2001], [Heyminck and Graf, 2001]) and 2 sets of 3 mirrors, the LO lower and upper sets of mirrors. It works in the following manner: the divergent LO beam coming from the diagonal horn antenna, located after the LO multiplier chain, is split by a collimating Fourier grating into three identical well collimated beams, aligned on a horizontal plane. Each of these beams gets reflected by one of the LO lower mirrors and then by one of the LO upper mirrors. After that, each beam is coupled to one of the three diagonal feed horns located in the LO Distribution Plate (section 4.4.2). The central beam goes up directly and the two beams from the sides cross each other to allow a smaller hole in the 50 K cartridge plate (see figures 4.13 and 4.14). Diagonal horns' beam waists and their locations were calculated using [Johansson and Whyborn, 1992].

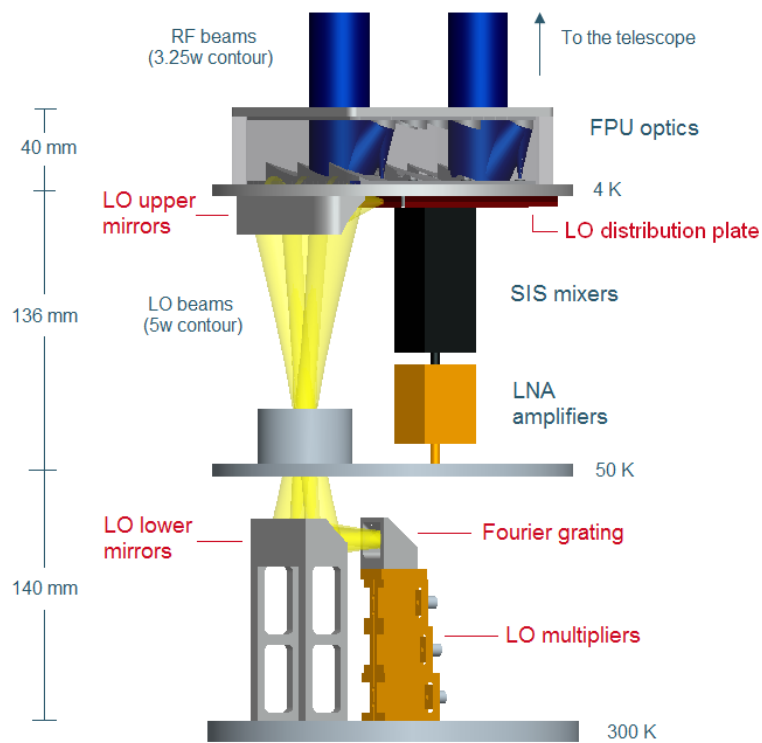


Figure 4.13: CAD model of the cartridge module showing the 3.25w beam contour of only 2 of the 9 RF beams in dark blue and the 5w beam contour of the LO beams in yellow. Only one pair of the nine SIS mixer - LNA amplifiers is included and represented as boxes to show their location and allocated space. The colored text points out the LO power distribution sub-system.

In table 4.4, the characteristics of these six mirrors are presented together with the mirror - a collimating parabola - on which the Fourier grating should be superimposed.

Name	f mm	$angle_r$ degree	d_{in} mm	w_{in} mm	d_{out} mm	w_{out} mm
M_{gr}	11.49	45.00	10.00	0.600	0.00	1.666
M_{lc}	40.88	45.00	50.00	1.666	56.26	2.189
M_{uc}	20.64	45.00	106.80	2.189	27.07	0.503
M_{us}	22.74	45.00	27.07	0.503	108.59	2.237
M_{ls}	42.45	42.26	61.73	2.237	53.14	1.666

Table 4.4: Characteristics of the LO distribution optics mirrors. M_{gr} is the parabolic mirror on which the Fourier grating structure should be added. M_{lc} and M_{uc} are the lower and upper mirrors in charge of propagating the central beam. And lastly, M_{ls} and M_{us} are the lower and upper mirrors for the side beams. Since, both side beams - which cross each other - are optically identical, two pairs of these mirrors are needed. They were designed starting from the upper part and are presented accordingly. The distance between beams in the lower mirrors is 18 mm and 30 mm in the upper ones.

The design of the collimating Fourier grating has not been done yet, but this should not present any problem since more complex ones have been developed in our institute and are now operational. For example, the two SMART collimating Fourier gratings for 810 GHz and 490 GHz described in [Heyminck and Graf, 2001].

4.4.2 LO Distribution Plate

The three LO beams that come from the LO Distribution Optics are then coupled to three diagonal feed horns in the LO Distribution Plate located at the rear side of the FPU optics. Then, each of these horns should feed a coupler structure, that provides with the LO power for a row of 3 mixers, thus supplying with LO signal to all 9 pixels of the array.

Figure 4.14 shows the case where this plate is one single square piece, it could also be, for example, 3 separate rectangular plates. Different options for the LO coupling design and fabrication are being analyzed and will be based on in-house hybrid waveguide/planar technology. The LO coupler is interfaced with the SIS balanced mixers.

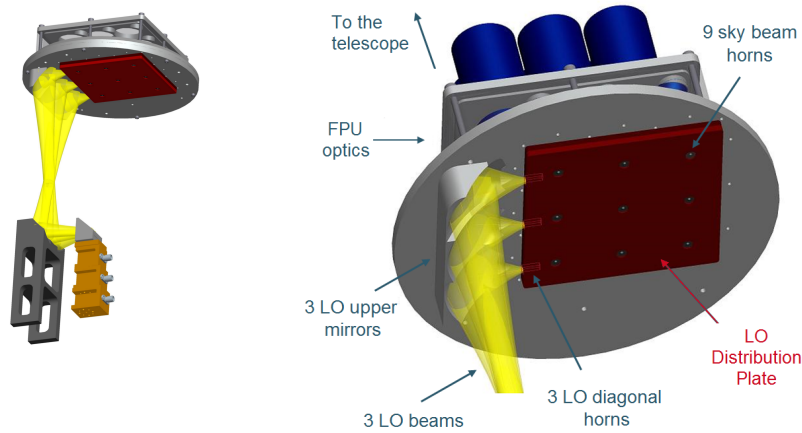


Figure 4.14: CAD design of a preliminary LO Distribution Plate. The three 5w-contour LO beams in yellow come up from the LO lower mirror (see insert on the left) and are reflected by the 3 LO upper mirrors towards the 3 diagonal horns that should couple each beam to a waveguide structure that distributes the LO power to the 3 mixers in a row, thus supplying with LO signal to the total of nine mixers in the array. Also in the image, the 9 sky beams in dark blue and on the left, a small insert of the whole LO Power Distribution on the rear side of the FPU optics.

4.5 Optics Tests

In this section, we present the results of the optics tests done in our laboratory. First, the beam measurements of the optics which are inside of the cryostat are described. Then, the tests performed to understand the encountered problems are explained and analyzed. Afterward, the beam measurements of the FPU optics done independently are presented; and an outlook of future tests is given.

4.5.1 Beam Measurements

We started by doing the beam measurements of the Cold Optics together with the FPU optics. To prepare for these tests, we installed the electronic boards and the necessary wiring, both developed by the electronics engineers of our group, on the cartridges. Each board can control 4 mixers. We were provided with 4 HEB mixers [Pütz et al., 2011] by the detectors group of our institute. The 4 mixers could be installed on one cartridge (figure 4.15) or on both, depending on the test we wanted to perform. To get to the operation point of the mixers, the temperature of the FPU had to be increased to ≈ 6.5 K. We decided to do the beam measurements with the HEBs in direct detection mode because it is simpler, for an heterodyne detection we would

have needed some extra equipment such as LO optics, bias-tees, LNAs, that would have required more time. Besides, there was the advantage that we were able to use the LO as a source for the tests.

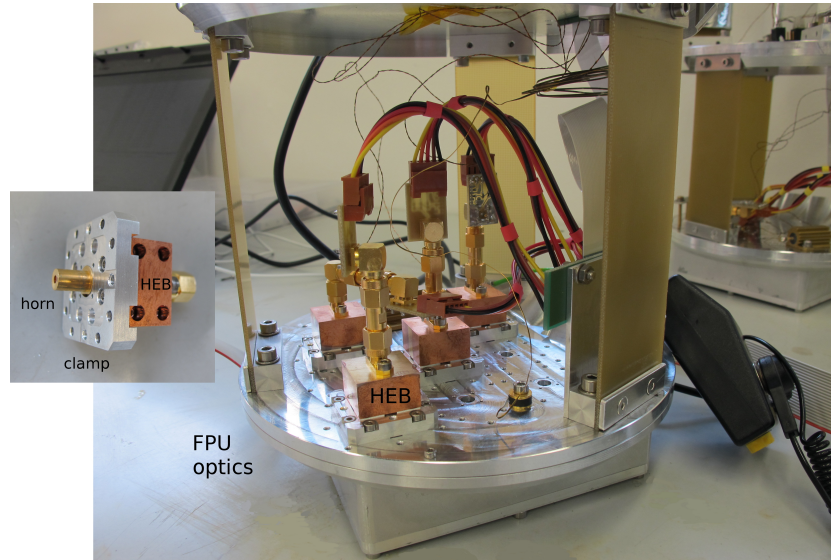


Figure 4.15: The HEB mixers, the wiring and electronic boards are installed in the cartridge. The 4 HEBs with their horns and clamps are mounted on the FPU optics rear side. One HEB is identified and a temperature sensor can be seen to its right. The insert shows the ensemble horn-clamp-HEB provided by the detectors group of our institute.

Then, we installed a source in an xy-stage which is controlled via a computer and can move horizontally and vertically to cover the area of the beam. The size of the map and the steps between the measured positions can be chosen in agreement with the size of the beam width being investigated.

We used two types of sources for the tests, a liquid nitrogen (LN_2) source which needs a chopper wheel and a lock-in amplifier that provide with the difference of the detection when looking at the hot (ambient temperature) and cold (LN_2 temperatures⁴), and the LO of the project that emits in the same range of frequencies. In this last case, since the emitted power is higher, between 30 and 100 μW (depending on the frequency), the chopper was not needed. Figure 4.16 shows the test set up when the LO is used as the source and figure 4.17 when the chopped LN_2 is used.

We started the measurements with the chopped- LN_2 source, but had some electronic coupling problems with the chopper and could not find the weak signal of the beam. Thus, we decided to use the LO as the source and set it to work at a frequency of 1035 GHz, where the maximum power is obtained. Most of the tests are done with this frequency, but also tests at 1012 GHz and 1025 GHz were performed.

⁴At atmospheric pressure, LN_2 boils at 77 K.

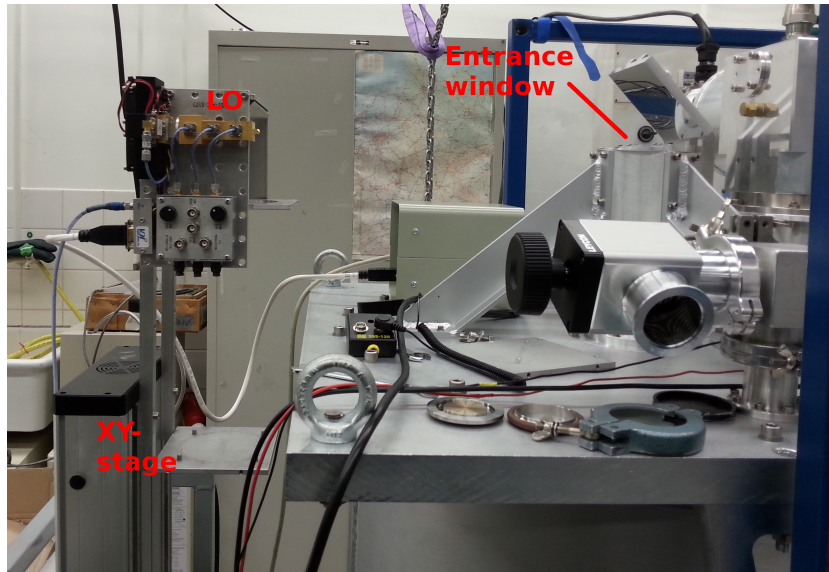


Figure 4.16: Beam measurement set-up with the LO as source, mounted on the xy-stage that can move vertically and horizontally to cover the beam that is being measured. In this picture, the entrance window is mounted in the tube.

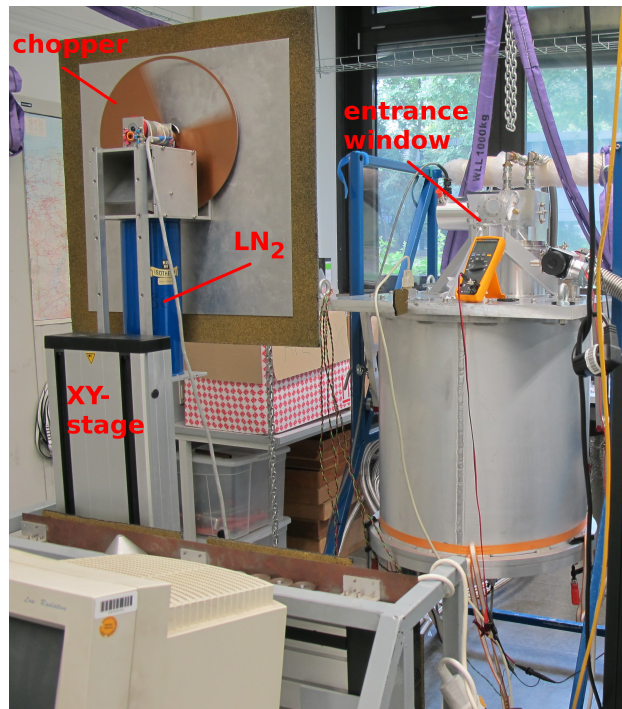


Figure 4.17: Beam measurement set-up with a chopped-LN₂ as source, mounted on the xy-stage that can move vertically and horizontally to cover the beam that is being measured. The square plate in front of the chopper contains a cone with an aperture that defines the size of the source. In this picture, the entrance window is mounted in the tube.

The first tests did not show a Gaussian beam profile, but rather an interference pattern (see figure 4.18), we tried with the mixers on different pixel positions on both FPU optics (for some we did not get any signal), measured the transmitted beams with and without polarizer, the result was similar. We put some sheets of paper in front of the source, all the maximum intensities were reduced. If the main maximum would have been the only one reduced, then we could have thought of standing waves as the cause of the fringes, but the latter was not the case. We also put some eccosorb (absorbers) around the entrance window to avoid any reflection that could contaminate the measurements, tried with the xy-stage in different angles with respect of the receiver, the outcome was similar.

During these tests, we found out that from the 4 HEB mixers only 2 were working correctly, this made the measurements very time consuming because every time that we needed to change a position of a mixer in the cartridge or move them to the other one, we had to warm up and cool-down the receiver. Here the cartridge concept was very useful because we only had to remove the cartridges to do the changes, and not open the whole cryostat.

After these results, the first thing to do was to verify the optics design which was checked and validated one more time with our usual tools and, in addition, with the use of the program General Reflector and Antenna Analysis Program (GRASP) [Graf, 2014]. Then, as the next step, we decided to remove the tube and installed the HDPE entrance window directly on the cryostat (see figure 2.10). The size of the window, in this position, allows only the center beam to pass through, so we installed a mixer on the central pixel of each FPU. The results of these tests can be seen on figures 4.19 and 4.20 for the CR and CT respectively. Both images show beams that are not completely clean, thus we still have to assume that they are partially vignetted and as a consequence they do not expand like the unvignetted designed beams. However, it is important to note that the vignetting is bigger for the CT than the CR. This is confirmed when comparing the measured and designed beam widths for the CR. The beams were measured at 349, 388 and 815 mm from the $w_0 = 6.064$ mm which is at 102 mm outside the entrance window, the measured beam widths are 9.3 mm, 10.7 mm and 11.8 mm and the designed beams are 8.1 mm, 8.5 mm and 13.9 mm respectively. The images for the first two tests are shown in figure 4.19.

While doing the previous measurements, we found out that the beams are not going through the center of the entrance window, but at the side of it. This happens when measuring on both cartridges (see figure 4.21). Therefore, we concluded that the problems encountered when doing the tests with the entrance window mounted on the tube (see figure 2.10) are due to a misalignment inside of the cryostat that causes the beam to go out tilted or shifted with respect to the original optical axis. Without the tube, the CT center pixel is somewhat elongated and some fringes are still present, but further out of the center. Thus, the misalignment could affect the CT more

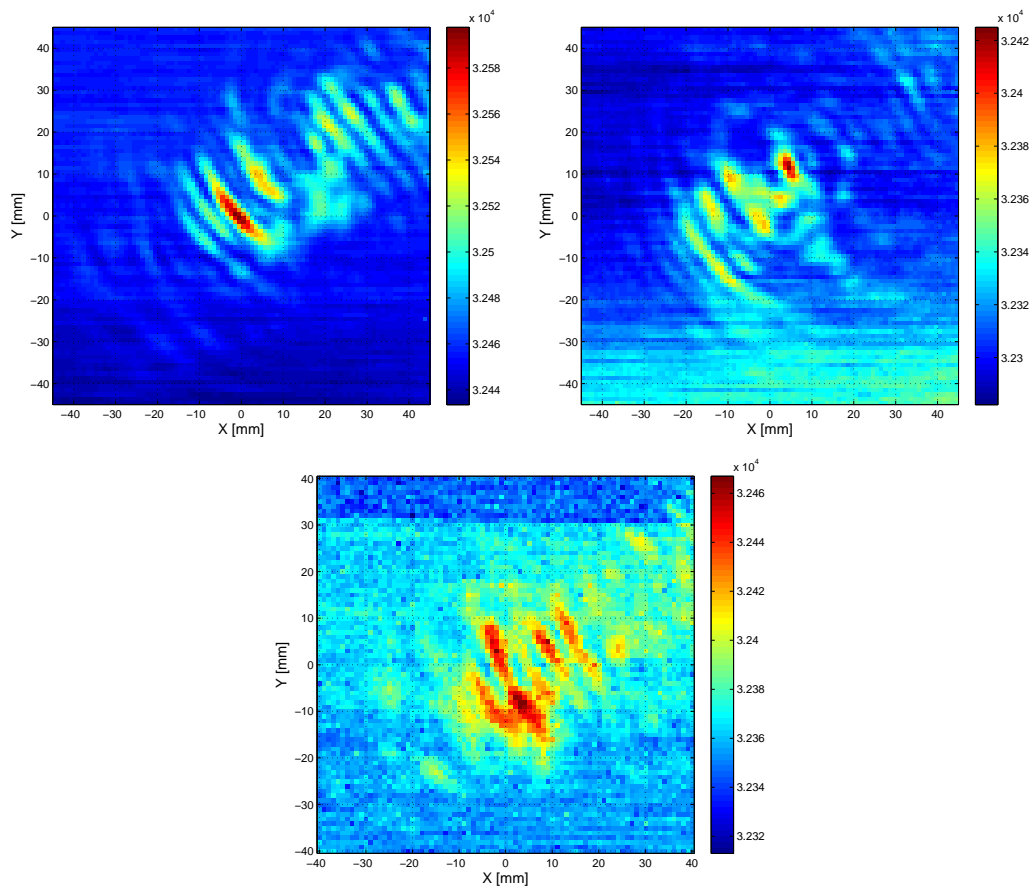


Figure 4.18: Examples of the non-Gaussian beam profile that were measured: center pixel (top left), corner pixel (top right) - both on the CR, and a center pixel (bottom) on the CT, without polarizer. Data was taken with a spacing of 1 mm and the source was the LO set at 1035 GHz.

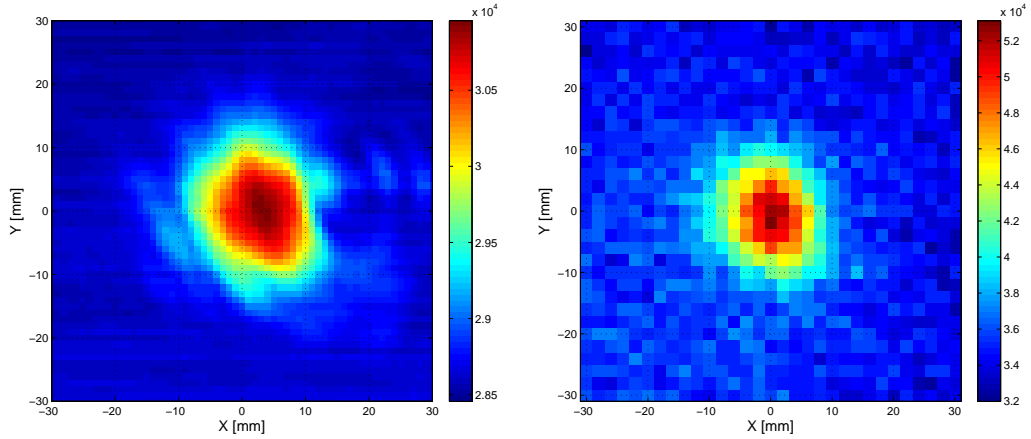


Figure 4.19: Beam measurement of the CR center pixel with the LO source set at 1035 GHz (left) and the chopped-LN2 source with a 10 mm aperture (right), the data was taken with a spacing of 1 mm. The sources are at 490 mm and at 451 mm from the entrance window respectively and the corresponding beam width, calculated from the fitted 2D-image, is 10.7 mm and 9.3 mm. The beam propagates from a $w_0 = 6.06$ mm which is located at 102 mm in front of the cryostat top plate (outside the cryostat). The beam is not really clean, thus we have to conclude that it is still partially vignetted, but less than the CT beam shown in figure 4.20.

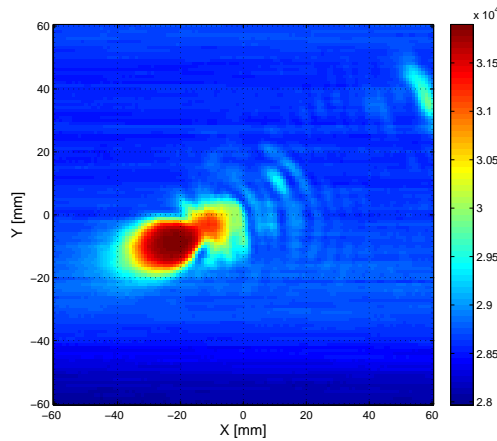


Figure 4.20: Beam measurement of the CT center pixel with the LO source set at 1035 GHz, the data was taken with a spacing of 1 mm. The polarizer was installed during the test. The source is at 451 mm from the entrance window and the corresponding measured beam width is 18.2 mm in the x-axis and 9.8 mm in the y-axis. The beam propagates from a $w_0 = 6.06$ mm which is located at 102 mm in front of the cryostat top plate (outside the cryostat). This beam map is elongated and some fringes are visible in the top right corner, this indicates that the misalignment present inside the cryostat affects more the CT than the CR (see figure 4.19).

than the CR.



Figure 4.21: The eccosorb marks the position where the center beam comes out of the cryostat in both cases, CR and CT. The diameter of the entrance window is 35 mm.

4.5.2 Alignment Tests and Analysis

Due to the misalignment inside the cryostat, we decided to do some tests to better identify the problem.

To start, we checked the alignment of the Cold Optics when warm and cold. An alignment piece was built and mounted on the Cold Optics instead of the polarizer. This piece has a polished surface which is parallel to the base of the Cold Optics and has a 0.5 mm hole positioned in the optical axis of the 3x3 array center beam (see figure 4.22). To continue, two movable mirrors and a laser were installed on the cryostat top plate (figure 4.23). In addition, to let the laser beam reach the alignment piece, the HDPE of the entrance window was changed by a Mylar of 50 μm thick and the Zitex[®] in the radiation shields were removed. Part of the laser beam goes through the hole and part is reflected by the surface.

First, at ambient conditions and with the cryostat open to be able to see the laser beam going into the alignment piece, we adjusted the movable mirrors until the laser beam was well positioned in the hole of the alignment piece and the reflected beam was on top of the incident one, back into the laser. In this way, the laser marks the optical axis of the Cold Optics. The laser was passing through the center of the cryostat window. The part of the beam that went through the hole was well in the center of the M1_t, as

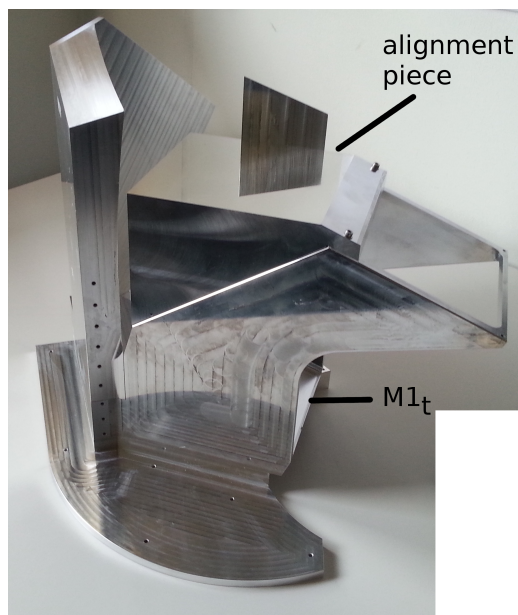


Figure 4.22: The Cold Optics with the alignment piece installed instead of the polarizer. The piece has a polished surface which is parallel to the bottom of the Cold Optics. A 0.5 mm hole, to mark the optical axis of the center beam, is made in this surface. Part of the laser beam goes through the hole allowing us to see where it hits the $M1_t$ and part of it is reflected making possible to follow it back and out of the cryostat. The dark quadrangle which is reflected in the alignment piece is part of the reflected-beams plane-mirror support.

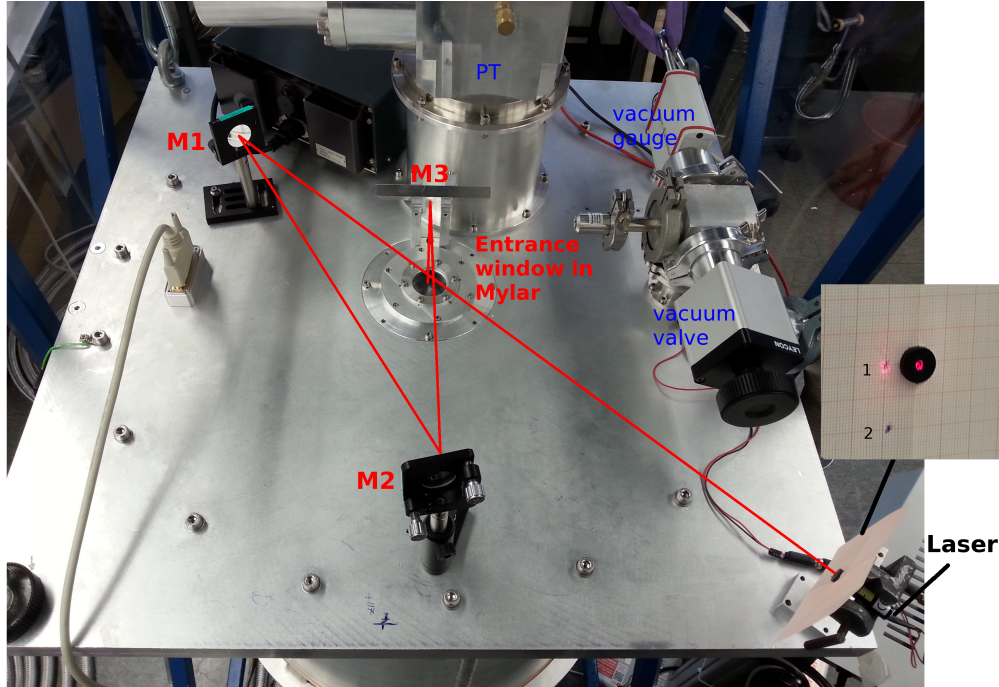


Figure 4.23: Laser beam set-up to check the alignment of the Cold Optics. The identified parts in red are part of the experiment, mirrors M1 and M2 are movable. Below the entrance window, the Cold Optics with the alignment piece is mounted (see figure 4.22). Two experiments were performed with this set up, the first one to check the alignment when the receiver is at ambient temperature and pressure and the second one to see what happens when the cryostat is evacuated and cooled down. The mirrors are adjusted until the laser beam goes in the hole and the incident and reflected beams are coincident. Thus, when the beam reflects back into the laser. In this way we find the normal to the surface of the alignment piece, the laser marks the optical axis of the Cold Optics. After the first test, the normal goes through the center of the entrance window, then we can conclude that the Cold Optics is well aligned. For the second test, we positioned the reflective laser beam on point number 1 (see insert), with the receiver at ambient pressure and temperature. During the evacuation, from ambient pressure down to 600 mbar, the reflected laser beam moved to point 2 and stayed there until the operations vacuum was reached (few 10^{-7}). This small movement is due to the bending of the cryostat top plate, mirrors and laser are mounted on it. Then, we moved the laser back to point 1 to be sure that it would stay inside the mirrors range and started the PT. The reflective beam did not move anymore as it can be seen in the insert picture which was taken when the receiver was already cold. Therefore, the Cold Optics does not move or tilt during cool down.

expected. These results showed that the Cold Optics is well centered and not tilted when the cryostat is at ambient temperature and pressure.

Secondly, we did a test to check what happens when the cryostat is evacuated and then cooled down. Before doing this, we had to complete the mounting of receiver to close the cryostat which required to turn it to the mounting position and then back to the operations one. Not sure about the alignment anymore, we decided to move the reflected beam to a position we could see (number 1 in figure 4.23), afterward we started the vacuum pump and the reflected laser beam moved only at the beginning of the evacuation and until 600 mbar (number 2 in the same figure). After that and during cool down the reflected laser beam did not move again. Thus, the Cold Optics and its support which comprises the 4 K and 50 K shields do not move during the cool down and are not responsible for the measured beam displacement at the entrance window.

To continue, we measured the bending of the vessel top plate, next to the entrance window. The result is 0.3 mm and it explains the movement of the reflected laser beam while the cryostat is being evacuated since the movable mirrors and the laser are installed on it. On the contrary, this bending is too small to explain the problem that we are trying to understand.

Then, we measured the bending of the vessel bottom plate where the cartridges are mounted, it is 0.5 mm. The tilting of the cartridge would produce a tilting of the FPU optics. By analyzing geometrically this situation, we found out that it would produce a shift of 2.3 mm from the center of the entrance window. To get a shift of 11.5 mm which is more or less what we see, a bending of ≈ 3 mm is needed in the center of the bottom vessel plate. The measured bending does not explain entirely the situation, but this result could, in addition to other things, explain it. For example, a tilt of the FPU optics could happened due, for example, to the misalignment of the epoxy strips, 0.9 mm of tilt would be needed to cause a shift of 9.2 mm. This scenario could be possible even if we pay a lot of attention when mounting the cartridges and installing the epoxy strips. For other tilts of the cartridges or FPU optics, that could happen when the cartridges are already mounted in the cryostat, such as the fact that the cartridges can move in the radial direction - to adjust to the shrinking of the radiation shields -, is something that has to be looked at in more detail.

After the previous analysis, we went back to have doubts about the Cold Optics manufacturing (because of its size it was only quasi monolithically built) and decided to do a 3D-scan of it to be able to compare the model with the manufactured part. Figure 4.24 show two comparisons of the CAD model and the built Cold Optics. We can conclude that the Cold Optics corresponds well to the model, there are no big differences. Besides, on both comparisons, the $M1_t$ (the M1 of the CT) has errors of ≈ 0.1 mm and the side that presents bigger differences in the comparison is either the polarizer or the $M1_r$ (the M1 of the CR), that would affect more the CR side, but

this one is the less affected. Nevertheless, a monolithically built Cold Optics would have better accuracy.

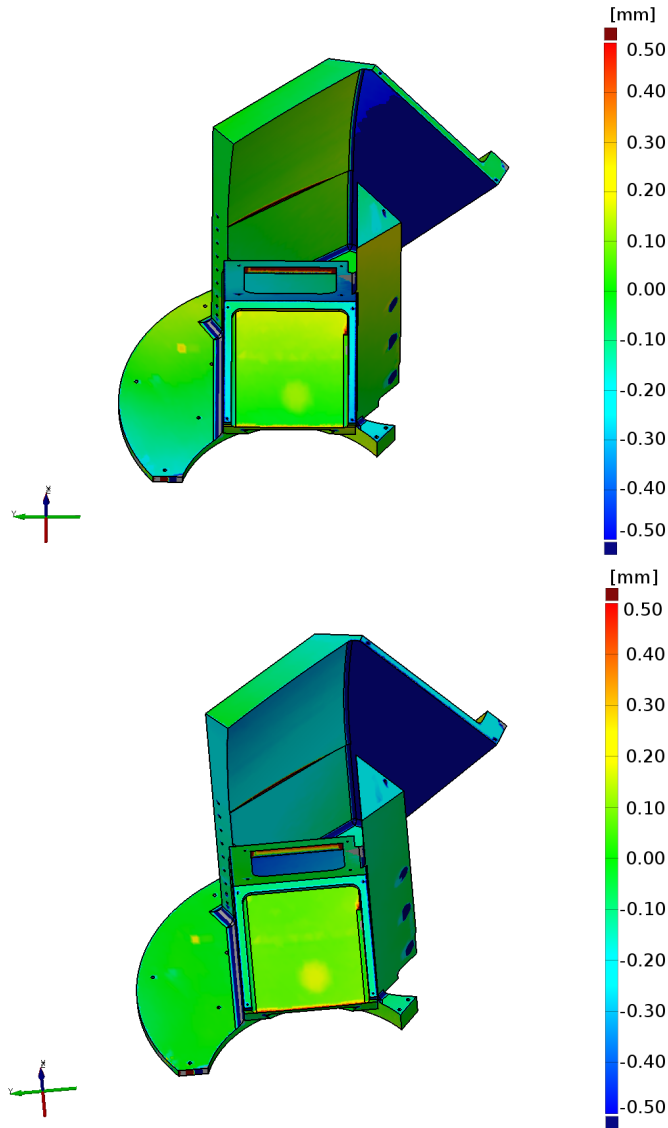


Figure 4.24: The Cold Optics CAD model compared with a 3D-scan of the built part. Top: a best fit comparison. Bottom: comparison with two defined planes, in this case the bottom plate and the vertical wall of the M_t mirror.

4.5.3 FPU Optics Beam Measurements

To measure the beams of the FPU optics alone, we removed the Cold Optics and installed the former, with two HEB mixers, directly on the 4 K top plate, right below the entrance of the shield (see figure 4.25). This plate is usually at 7.4 K, therefore extra OFHC braids were installed on the Al5N plates and

connected directly to the FPU optics to provide more cooling power.

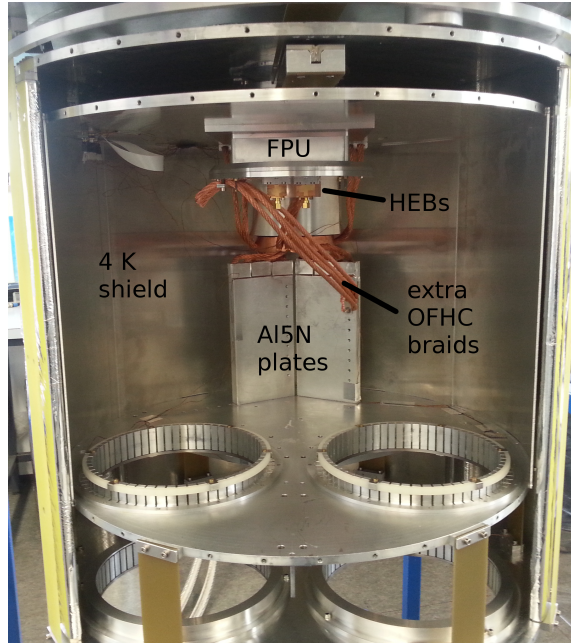


Figure 4.25: The FPU optics, with 2 HEB mixers, was installed directly on the 4 K shield entrance, the Cold Optics was dismantled to have enough space. Extra OFHC braids were installed from the Al5N plates to cool down the FPU below the needed 6.5 K.

Before the test was done, we checked the alignment of the FPU optics with respect of the entrance window. It is needed that the beam is well centered in the window because the size of the window is only $3.8w$. Using the same mirrors and laser set up mounted on the cryostat top cover (see figure 4.23) and an alignment piece, similar to the one for the Cold Optics, but appropriate for the FPU optics, we did the test and concluded that the FPU optics was well aligned with the entrance window.

During the first cool down to do the test, the temperature reached on the FPU was only 7.8 K, not cold enough to be able to operate the detectors. We had to put back the Zitex[®] filters that were removed to check the alignment with the laser beam. After this, the temperature went down to 5.6 K and the test could be performed.

The beam measurements results are presented in figures 4.26 and 4.27. The tests were performed with the LO source set at 1025 GHz and the spacing of the points is 4 mm. The first figure shows the results of the test with the LO source at 785 mm from the FPU optics where the $w_{\text{ofp}} = 8.923$ is located. The second figure shows the results when the LO source was at 1085 mm. The fit is done on the 2D-map, the results are a beam width equal to 11.877 mm in x and 14.142 mm in y for the first test and a beam width equal to 14.284 mm in x and 16.207 mm in y for the second one. Calculated beam

width according to the design are 12.122 mm and 14.430 mm respectively. It can be seen that the measured values are in very good agreement, particularly for the x values, with respect of the calculations for the designed FPU optics. Also, the optical axis seems well aligned with the beam.

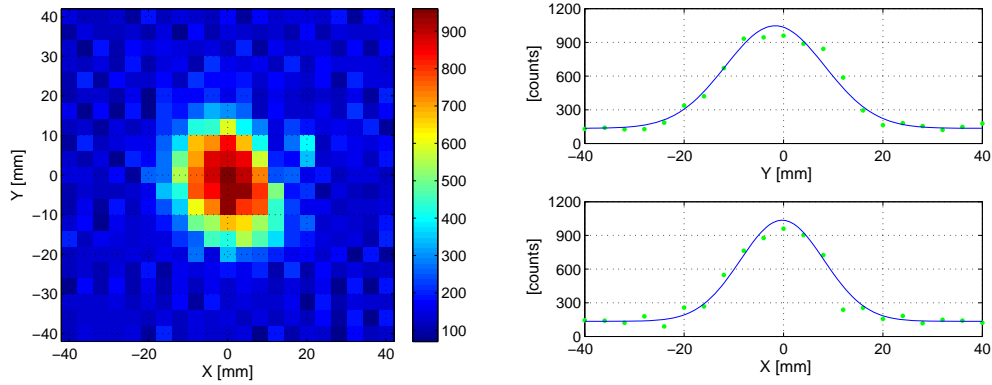


Figure 4.26: Beam measurement of the FPU optics center pixel (left) and a cut on the x-axis and y-axis, in the (0,0) position (not exactly the center) showing the measured points and the fit (right). The fit is done on the 2D-map. The fitted beam width is 11.877 mm in x and 14.142 mm in y. The LO source, set at 1025 GHz, is at ≈ 785 mm from the FPU optics where the $w_{\text{ofp}} = 8.923$ mm is located. The calculated beam width from these values is 12.122 mm.

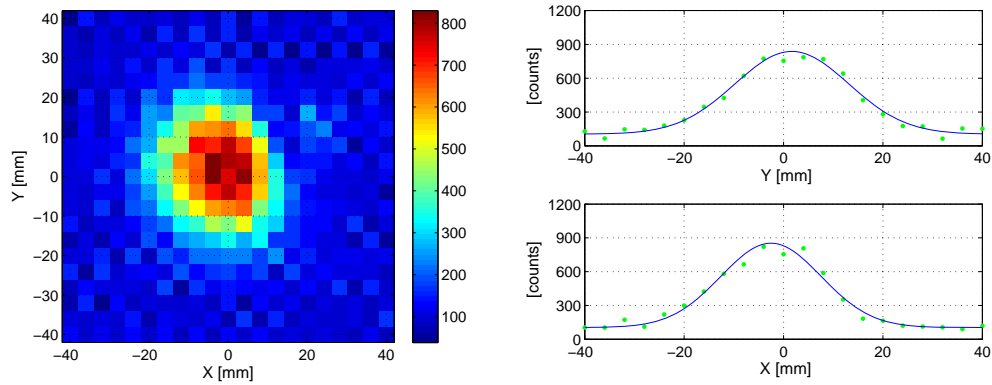


Figure 4.27: Beam measurement of the FPU optics center pixel (left) and a cut on the x-axis and y-axis, in the (0,0) position (not exactly the center) showing the measured points and the fit (right). The fit is done on the 2D-map. The fitted beam width is 14.284 mm in x and 16.207 mm in y. The LO source, set at 1025 GHz, is at ≈ 1085 mm from the FPU optics where the $w_{\text{ofp}} = 8.923$ mm is located. The calculated beam width from these values is 14.430 mm.

The way we found to measured the FPU optics in the receiver cryostat, allow us to test only one pixel at a time. The diameter of the entrance window

is 35 mm and the beam width at its current position (directly installed on the cryostat top plate) equals 9 mm. To test another beam one would have to dismount and move the FPU optics so the next beam to be measured is below the entrance window. Another alternative would be to make a bigger entrance window in HDPE, the biggest we can do to be installed in the current place, is 70 mm which would allow us to measure two beams at a time, but this would have to be tested because it means more heat load in the FPU optics and this one could end up being warmer than needed. Also, the measurements could be repeated with higher spatial resolution. In the limited amount of time of this thesis, these extra tests were not possible, but they could be included in future work. Nevertheless, the measured beam indicates that the FPU optics is behaving in agreement with the design.

4.6 Summary

In this chapter, we presented the optical design of the 1.1 THz Heterodyne Array Receiver for the APEX telescope which operation band is 1000 - 1080 GHz. The procedures for the optical design are described.

We designed the Relay Optics in charge of transforming the telescope focal plane into the receiver focal plane. The two sub-arrays are coupled to the telescope via a wire-grid polarizer, in which the incoming signal from the telescope is split into two orthogonal polarization components.

The implemented Relay Optics design has a frequency independent illumination of the secondary at 12 dB edge taper and fulfills the constraints with respect of the placement and limited allocated space for the instrument in the APEX telescope Nasmyth A cabin and consequently the RF beam clearance limitation by the elevation encoder with the $5w$ criterion. We use an edge taper of 12 dB because going to a higher value would mean that not all the Tertiary Optics mirrors could fulfill the $4w$ -criterion for all the beams.

The Relay Optics includes a diplexer to leave open the possibility of using single-ended HEB or SIS mixers. Removing this optical coupling to operate with SIS balanced mixers, and adjusting the warm optics, presents no problem.

The FPU optics is in charge of coupling the radiation from the receiver focal plane to the feed horns of the mixing elements. In order to keep the beams as close as possible on sky, when the minimum beam distance has been set (by the mixer-block size), it is necessary to increase the individual beam waists in the receiver focal plane before injecting them into the common optics. This is how the $3.25w$ criterion was chosen for the FPU optics.

All the optics is reflective to contribute minimally to the overall system temperature, this implies a Relay Optics design based on large off-axis mirrors to avoid absorption and reflection losses of refractive optics systems.

Scaled versions of the Cold Optics, the part of the Relay Optics that is

inside the cryostat, and the FPU optics were built because the manufacturing and operations temperature are different. The scaling factor takes into account the thermal expansion characteristics of the involved material and the temperature difference.

Some problems were found when the optics inside the cryostat (Cold Optics and FPU optics) were tested together. From what we know at the moment, we can say that the Cold Optics is well centered, not tilted and that this condition does not change when at operation temperature. It has also been built in agreement with the CAD model. Measurements of the center beam of both cartridges, with the entrance window on the cryostat top plate (i.e. without the tube), helped us conclude that there is a misalignment inside the cryostat that affects both cartridges and causes that the optical axis comes out at approximately 11 mm away from the center of the entrance window. However, we also concluded that the CT is more affected than the CR by the misalignment. The center beam of the former is more elongated and some fringes can still be seen farther away from the main beam.

In addition, all the test and analysis related to misalignment and tilt has helped us isolate the source of the problem. This would be the effect of the addition of different situations that could affect the cartridge as a whole or the FPU optics independently. The first one being the bending of the bottom vessel plate which causes a 2.3 mm tilt. Extra reinforcement has to be introduced. Other possible sources of tilt or misalignment of the FPU optics have to be looked at in more detail. A planned test, is to make a bigger entrance window to be installed also directly on the cryostat top plate to be able to see all the pixels at the same time, in this way, the propagation axes of all beams, from both cartridges, could be followed at the same time giving us information to track the source of misalignment. For this kind of test, we would need more HEB mixers.

The FPU optics works correctly. The beam measurement showed a beam width which corresponds to a propagation from the beam-waist designed value which is located in the FPU optics, as well as the beam propagation direction in agreement with the optical axis of the FPU.

The LO power distribution is also part of this chapter mainly because it includes an optics assembly of the array receiver. We presented a designed LO Distribution Optics that would work with the preliminary proposed schematic-solution for the LO Distribution Plate which is not ready yet and is not part of this thesis. For this reason, this optics assembly was not built neither tested. Most probably, it will have to be adapted. The necessary space for the dedicated LO distribution network has been allocated on the cartridge module.

To summarize, there is still work to do to find out and correct the problems encountered while testing the optics, but improvement has been done, we have isolated the area that is, most probably, the cause of the problems and have also positive results from independently measured optics assembly.

Chapter 5

Conclusions and Outlook

We have presented the optics and the cryogenics for the 1.1 THz Heterodyne Array Receiver that will be mounted in the Nasmyth A cabin of the Atacama Pathfinder Experiment (APEX) telescope, located on the Chajnantor plateau at 5100 meters altitude in northern Chile.

Observing in the 1.1 THz band with high resolution spectroscopy will bring new knowledge of the structure and chemistry of star formation regions as well as distant starburst galaxies.

The THz range is a still largely unexplored area in astrophysics because of two major limitations: the opacity of the atmosphere with only some windows of transmission open from the ground and the technological challenge for the receiver and telescope.

The APEX telescope with its 12 m dish, surface accuracy of 17 r.m.s and location is the largest submillimeter single-dish telescope in the world for THz frequencies.

Observations with APEX at 1.1 THz are outstanding additions of the observations done with the Herschel Space Observatory and Stratospheric Observatory For Infrared Astronomy (SOFIA). Additionally, after the Herschel space observatory was decommissioned in 2012, there is no instrument observing in this frequency band.

We designed, built and tested the cartridge-type cryostat, the cartridge modules and the all-metal thermal links that does not require a permanent mechanical attachment. This modularity provides a significant operational advantage in that a withdrawal of a cartridge module to modify or service it, can be simply performed at room temperature and ambient atmospheric pressure without having to open the whole cryostat or disturb the rest of the receiver. As a consequence this brings benefits at the telescope, reducing observing downtime, and also at the laboratory during tests.

The receiver optics is fully reflective and follows a monolithically approach as much as possible. The Relay Optics transforms the Nasmyth A focal plane into the the receiver focal plane and the Focal Plane Unit (FPU) optics couples the radiation from the receiver focal plane into the feed horns of the the

mixers. The incoming signal from the telescope is split into two orthogonal polarization components via a wire-grid polarizer. A dual diplexer, that can be easily removed, is present to leave open the possibility to use single-ended mixers.

The implemented Relay Optics design has a frequency independent illumination of the secondary at 12 dB edge taper and satisfies the constraints with respect of the allocated space in the cabin of the telescope. We use an edge taper of 12 dB because going to a higher value would mean that not all the Tertiary Optics mirrors could fulfill the $4w$ -criterion for all the beams. This shows that the 1.1 THz Array Receiver is suitable for operation in the Nasmyth A cabin of the APEX telescope.

The cryostat together with the cartridges, Thermal Links (TLs) and optics were assembled and tested in the laboratory. When the temperature in the focal plane reached 4.8 K, we started doing the beam measurements of the optics with the Superconducting Hot Electron Bolometer (HEB) mixers in direct-detection mode, their operation temperature was around 6.5 K. However, we continued trying to reduce the temperature to the one required by the Superconductor-Isolator-Superconductor (SIS) mixers (below 4.5 K).

Since the temperature provided to the FPUs also depends in the thermal conductance of the TLs, initially made of Al-5083, we designed a new TL made of higher conductivity aluminum (Al-1050). Unfortunately, the result was not as good as expected, obtaining a thermal conductance of 0.19 W/K, similar to the one of the initial version. The thermal conductance is dominated by the contact between the TL and the cartridge, which is not improved by a different choice of aluminum. We decided to incorporate a nylon ring to the TL made of Al-1050 and after that, the thermal conductance was increased to 0.45 W/K and allowed the best performance of the cryostat.

The lowest temperature in the focal plane of the receiver, reached during the latest cool downs, was 4.4 K in the Cartridge of Reflected beams (CR). The temperature of the other cartridge, the Cartridge of Transmitted beams (CT), could not be measured because the FPU optics of the transmitted beams was being tested and thus mounted below the entrance of the 4 K radiation.

If one needs this Nylon ring on the 4 K TLs will depend in the amount of heat load that will be present in the receiver focal plane and the operation temperature of the detectors. In other words, if the thermal conductance of our all-metal TLs is enough for the receiver to operate, there is no need to add the nylon ring.

The TL of the 50 K stage are made of Al-5083 and have to be used with a cover made in aluminum to block the radiation from the 300 K to pass through, the finger spacing, directly into the 4 K stage. This solution worked very well and helped to reduce the temperature of the 4K stage.

The first tests of the optics, when the Cold Optics and FPU optics were

tested together, revealed a misalignment inside the cryostat that caused an interference pattern when the entrance window was installed in its support tube. When the tube is removed, we are able to see a Gaussian beam, but not completely clean indicating that there is still some vignetting which affects more the transmitted beams. This problem is still not solved, but all the tests and analysis related to the misalignment has helped us isolate the source of the problem which is most probably due to the positioning of the cartridges and not due to the optics.

We measured the FPU optics independently and found out that it works correctly. The beam measurement showed a beam width which corresponds to a propagation from the designed beam-waist located in the FPU optics. Also, the beam propagation direction is in agreement with the optical axis of the FPU.

The source(s) of the tilt or misalignment of the cartridges have to be fixed. A planned test to investigate in this respect is to make a bigger entrance window and install it directly on the cryostat top plate. This will allow to see all the pixels at the same time and help to find their propagation axes. It would be convenient to be able to test more beams at the same time, from both cartridges. For this kind of test, more mixers are needed. This would give us information to track the source of the misalignment.

The calculated heat load of the current receiver version is similar to the one estimated for the final state, when the receiver will be fully populated with 18 SIS balanced mixers. The main reason for this, is that in the current version, the heat load produced by the wiring (particularly the white ribbon cables) is too high and can be reduced by changing the wires. We can conclude that the cryostat is suitable for the use with HEB mixers and it should also be the case with SIS balanced mixers, provided that the adequate wiring is used.

Once the final mixers are ready, depending if they are balanced or single-ended, HEBs or SIS, the warm optics has to be built and maybe also adjusted. In the case of the balance mixers, the LO distribution network also needs to be ready and the final wiring has to be implemented.

Even though, the 1.1 THz Heterodyne Array Receiver was conceived to perform observations with APEX, it could also work with other telescopes. In particular, with the future Cerro Chajnantor Atacama Telescope (CCAT), planned to be located on Cerro Chajnantor, at 5600 m altitude, in the Chilean Atacama Desert where the transparency of the atmosphere is unique; it should have a primary mirror of 25 m which would bring unprecedented high spatial resolution and sensitivity at this frequencies.

Appendix A

Cryostat Temperature Data

Two examples of cool downs, the first one showing the temperature of the 50 K CH of the PT which was measured only at the beginning. The second example includes temperatures of both cartridges.

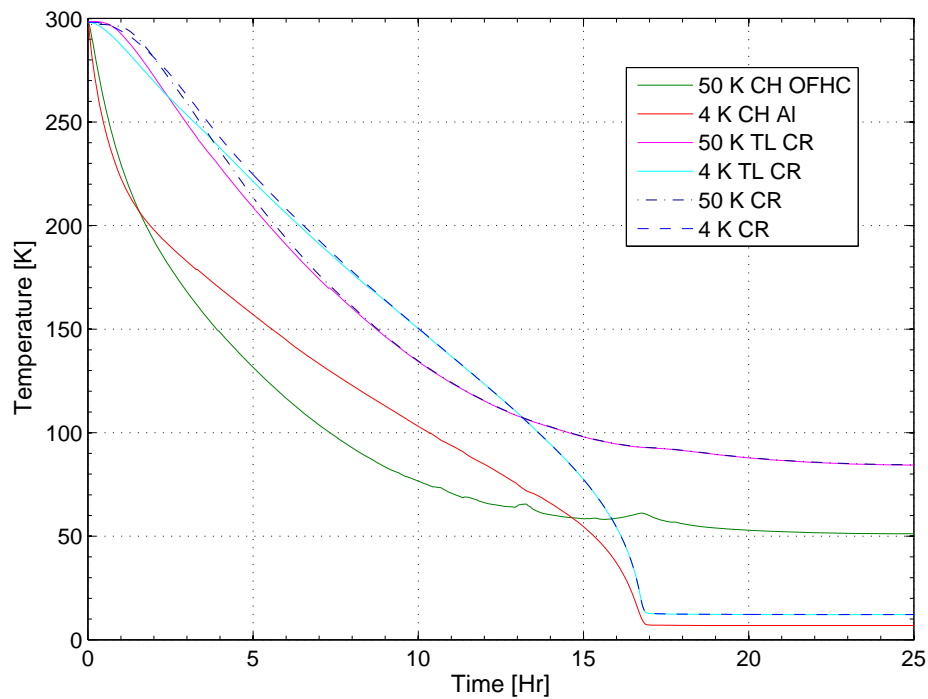


Figure A.1: Cool down cycle performed on the 26.06.2013, one of the first cool downs when the cryostat was closed to external radiation, the Cold Optics was not installed yet and the 50 K TLs had no covers. It shows the temperatures of both CHs of the PT, taken at there interfaces (not directly in the CH).

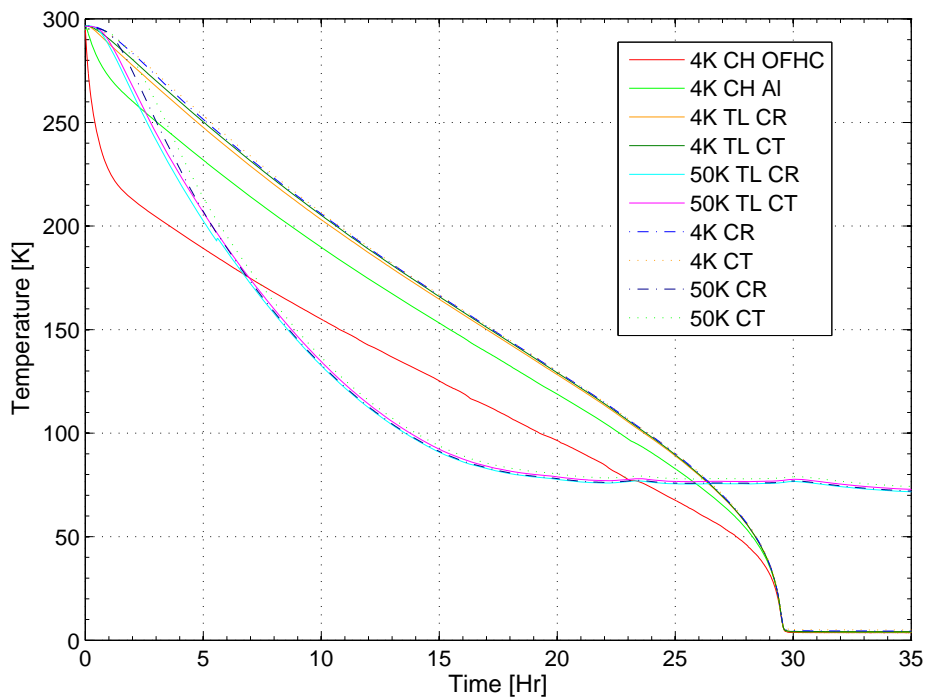


Figure A.2: Cool down cycle performed on the 11.06.2014, one of the last cool downs when the Cold Optics was installed, the 50 K TLs had their covers and the PT 50 K entrance was also cover with an Al-plate. The new 4 K CH interface and the 4 K TLs in Al-1050 were also installed.

Appendix B

Thermal Links Data

Here we present the TLs data obtained during the 31 cool downs, out of a total of 35, done during this thesis. The data is presented chronologically and the plots have some information on changes like, for example, when the Cold Optics was installed, when the 4 K TL was installed, when the mixers were installed, etc. These cool downs were done first to reach the necessary temperature on the receiver focal plane and then to test the receiver optics. I decided to show the TL data to record all the cool downs, but it could have also been done with other cryostat data, like the ones shown in the previous appendix.

The cryostat was closed to external radiation until the cool down of 09.12.2013 and between the 27.02.2014 and 06.08.2014. For the rest of the cool downs, the cryostat was open to astronomical signal (RF), using the High Density Polyethylene (HDPE) entrance window.

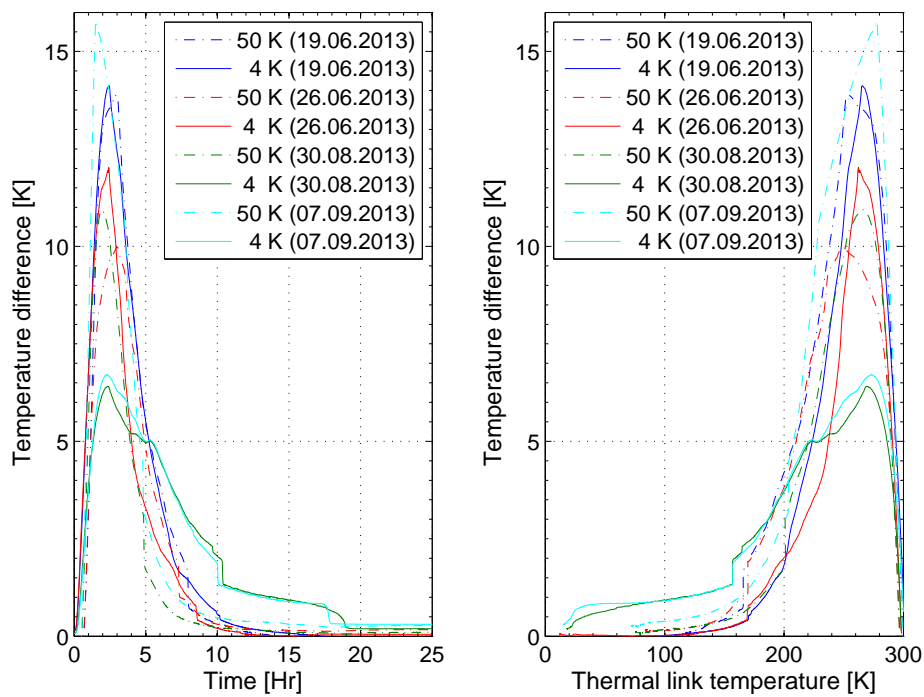


Figure B.1: Left: Temperature difference between 4 K or 50 K the TL and the corresponding cartridge plates versus the cooling down time. Right: Temperature difference between the 4 K or 50 K TL and the corresponding cartridge plates versus the TL temperature.

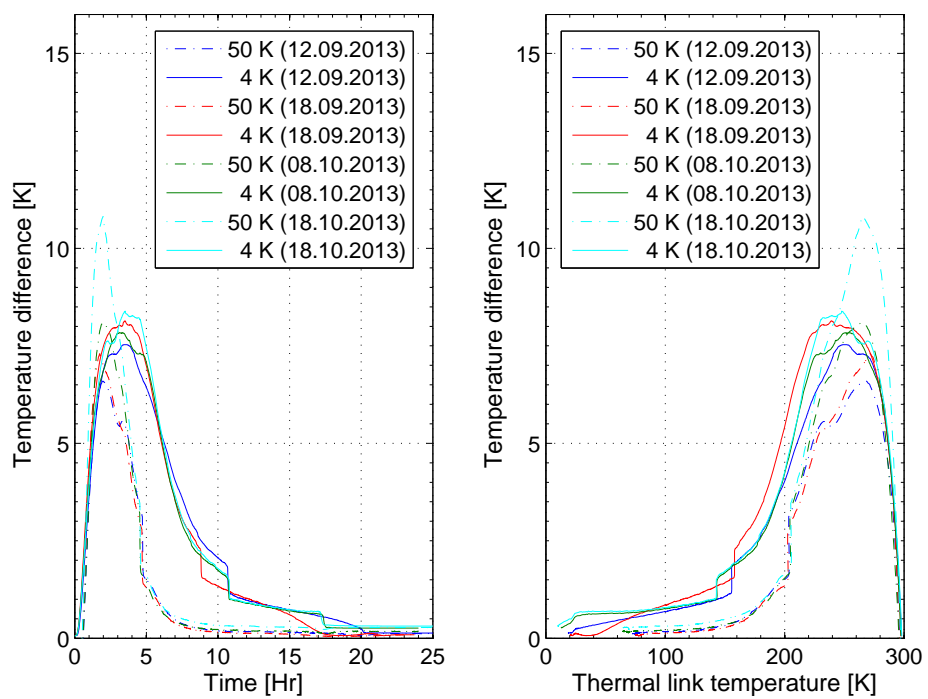


Figure B.2: Left: Temperature difference between 4 K or 50 K the TL and the corresponding cartridge plates versus the cooling down time. Right: Temperature difference between the 4 K or 50 K TL and the corresponding cartridge plates versus the TL temperature.

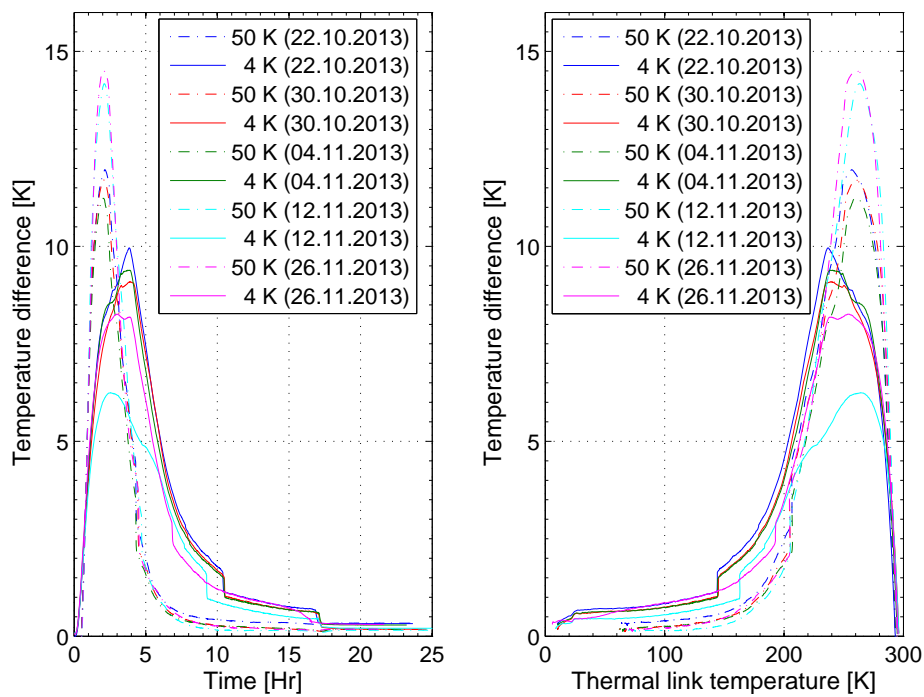


Figure B.3: Left: Temperature difference between 4 K or 50 K the TL and the corresponding cartridge plates versus the cooling down time. Right: Temperature difference between the 4 K or 50 K TL and the corresponding cartridge plates versus the TL temperature.

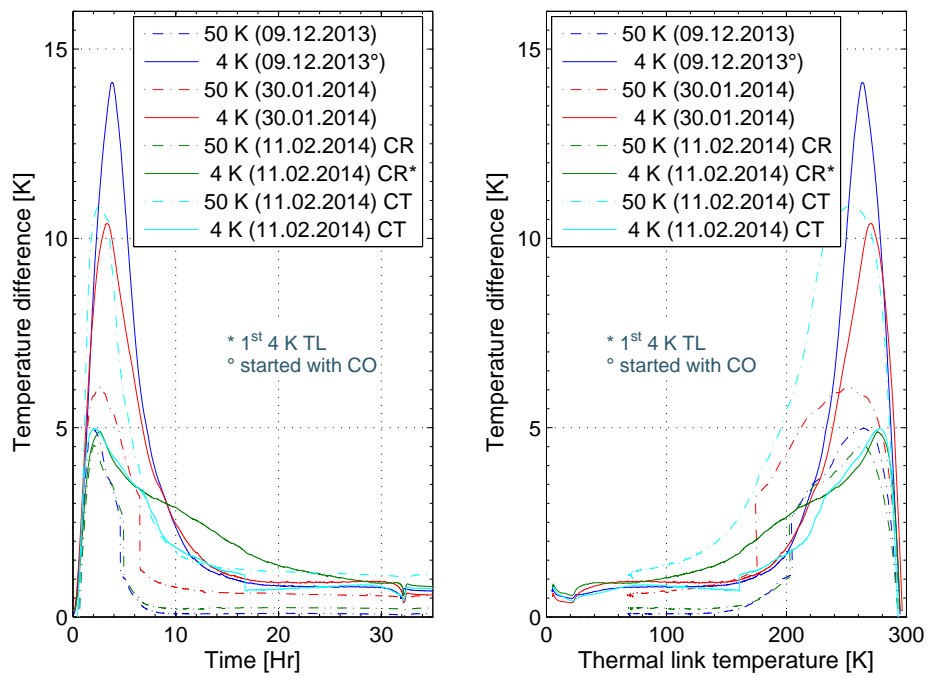


Figure B.4: Left: Temperature difference between 4 K or 50 K the TL and the corresponding cartridge plates versus the cooling down time. Right: Temperature difference between the 4 K or 50 K TL and the corresponding cartridge plates versus the TL temperature. CO stands for Cold Optics.

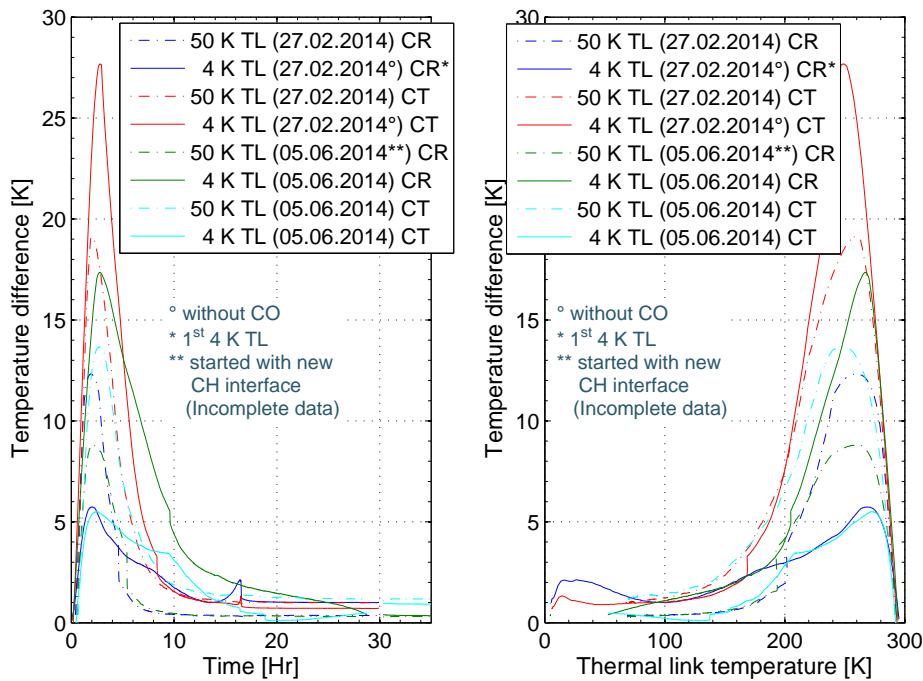


Figure B.5: Left: Temperature difference between 4 K or 50 K the TL and the corresponding cartridge plates versus the cooling down time. Right: Temperature difference between the 4 K or 50 K TL and the corresponding cartridge plates versus the TL temperature. In the data from 05.06.2014, there are approximately two hours missing due to a problem with the temperature recording, but the steady state temperature is recorded. CO stands for Cold Optics.

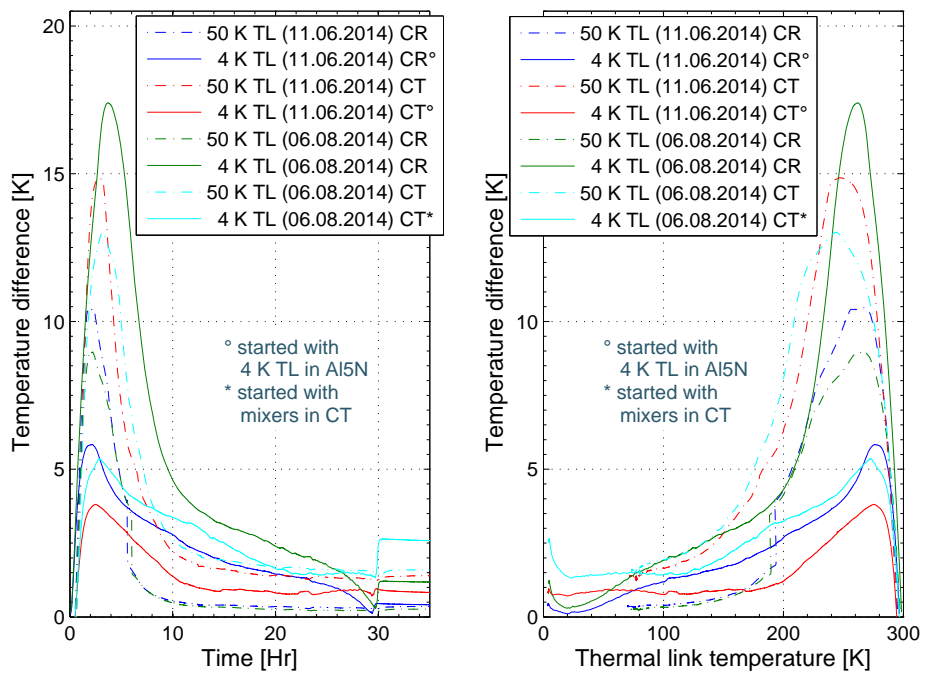


Figure B.6: Left: Temperature difference between 4 K or 50 K the TL and the corresponding cartridge plates versus the cooling down time. Right: Temperature difference between the 4 K or 50 K TL and the corresponding cartridge plates versus the TL temperature.

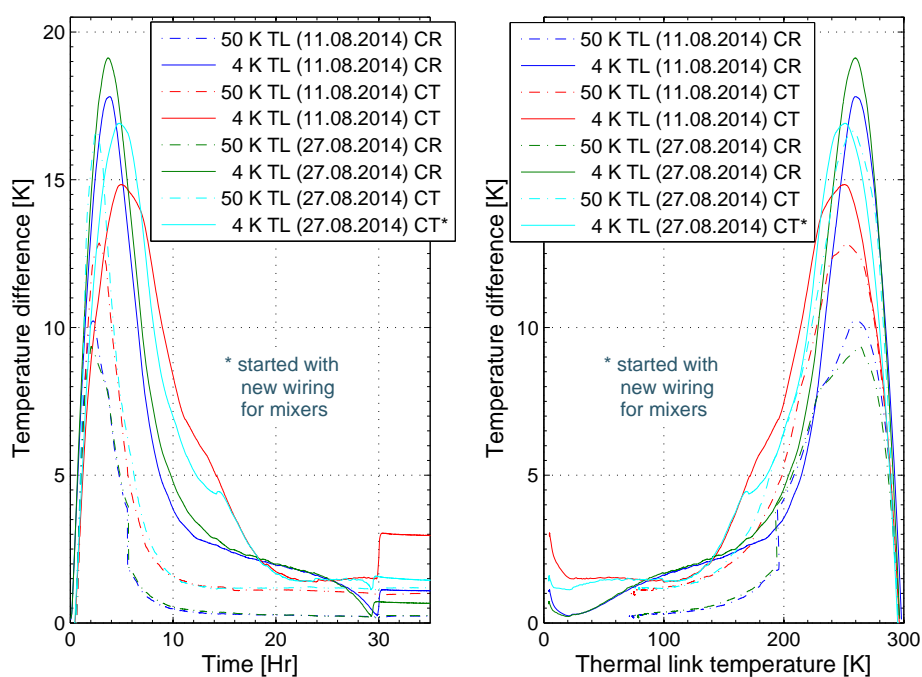


Figure B.7: Left: Temperature difference between 4 K or 50 K the TL and the corresponding cartridge plates versus the cooling down time. Right: Temperature difference between the 4 K or 50 K TL and the corresponding cartridge plates versus the TL temperature.

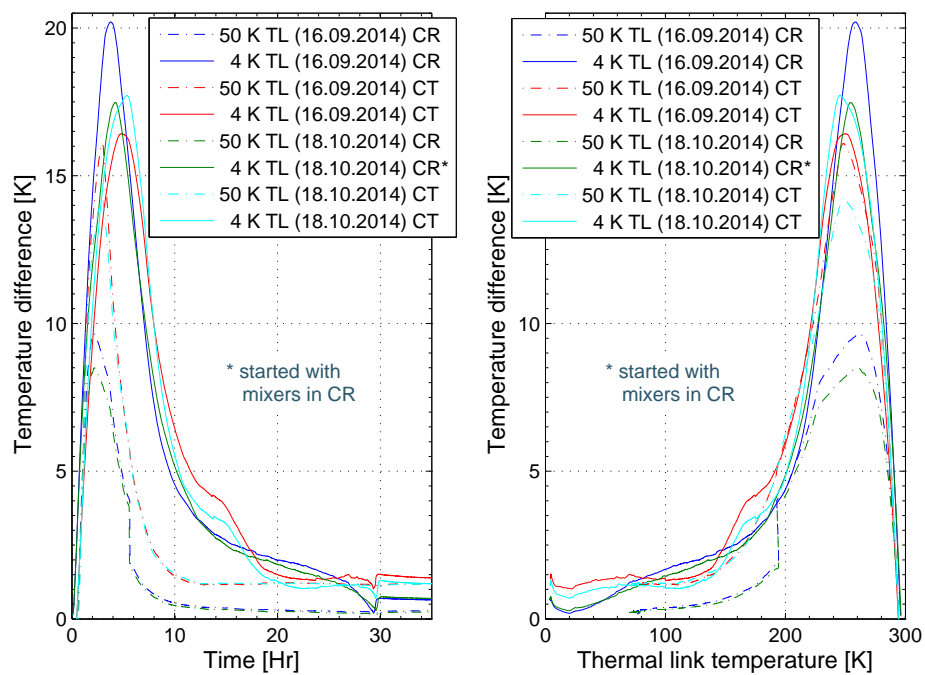


Figure B.8: Left: Temperature difference between 4 K or 50 K the TL and the corresponding cartridge plates versus the cooling down time. Right: Temperature difference between the 4 K or 50 K TL and the corresponding cartridge plates versus the TL temperature.

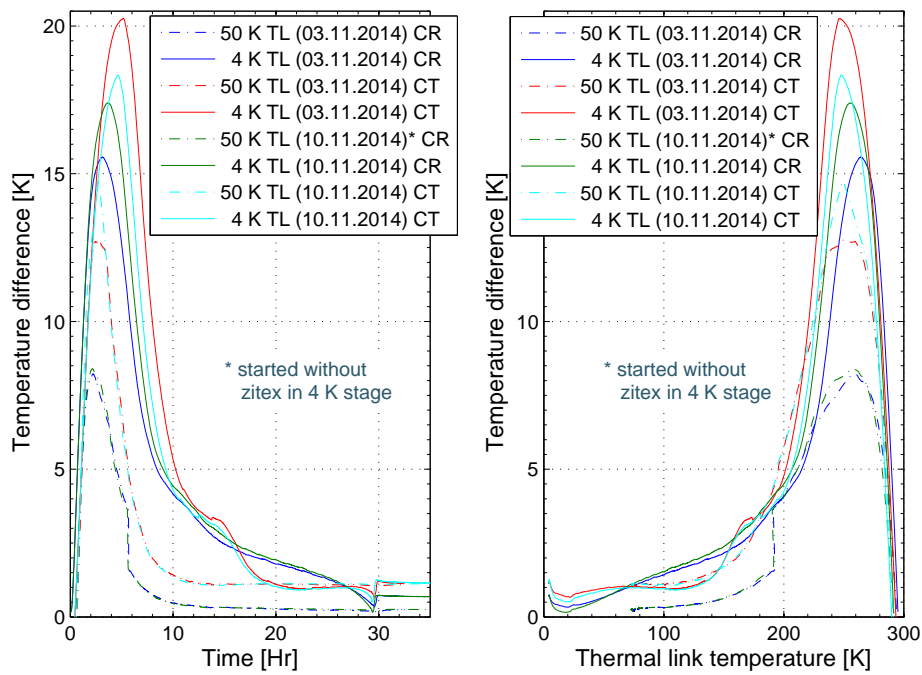


Figure B.9: Left: Temperature difference between 4 K or 50 K the TL and the corresponding cartridge plates versus the cooling down time. Right: Temperature difference between the 4 K or 50 K TL and the corresponding cartridge plates versus the TL temperature.

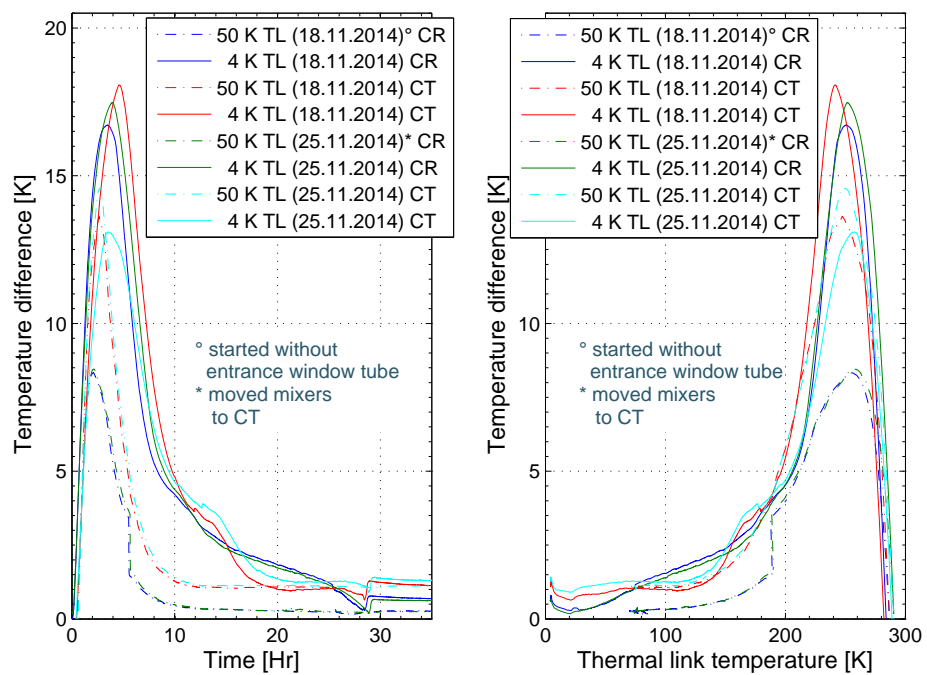


Figure B.10: Left: Temperature difference between 4 K or 50 K the TL and the corresponding cartridge plates versus the cooling down time. Right: Temperature difference between the 4 K or 50 K TL and the corresponding cartridge plates versus the TL temperature.

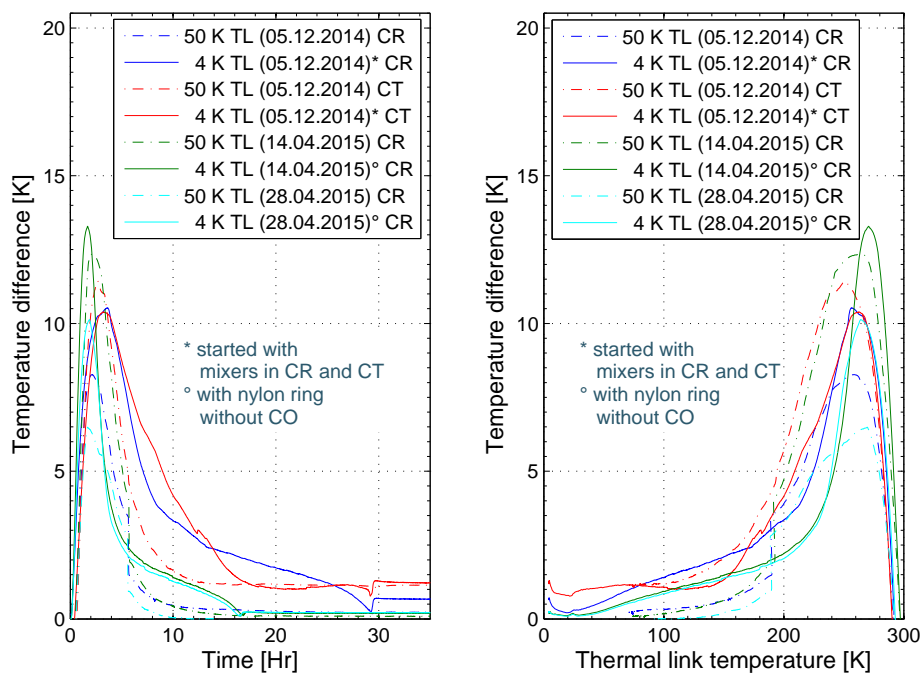


Figure B.11: Left: Temperature difference between 4 K or 50 K the TL and the corresponding cartridge plates versus the cooling down time. Right: Temperature difference between the 4 K or 50 K TL and the corresponding cartridge plates versus the TL temperature.

Bibliography

- ALMA observatory (2014). <http://almaobservatory.org/>.
- APEX telescope (2014). <http://www.apex-telescope.org/>.
- Ashcroft, N. W. and Mermin, N. D. (1976). *Solid State Physics*. Saunders College, first edition edition.
- ASM Aerospace Specification Metals, Inc. (2014). <http://www.aerospacemetals.com/>.
- Becklin, E. E. and Moon, L. J. (2004). Stratospheric Observatory For Infrared Astronomy (SOFIA). In Caroff, L., Moon, L. J., Backman, D., and Praton, E., editors, *Debris Disks and the Formation of Planets*, volume 324 of *Astronomical Society of the Pacific Conference Series*, page 197.
- Belland, P. and Crenn, J. P. (1982). Changes in the characteristics of a Gaussian beam weakly diffracted by a circular aperture. *Applied Optics*, 21(3):522–527.
- Benford, D. J., Gaidis, M. C., and Kooi, J. W. (2003). Optical properties of Zitex in the infrared to submillimeter. *Applied Optics*, 42(25):5118–5122.
- Blundell, R., Barrett, J. W., Gibson, H., Gottlieb, C., Hunter, T. R., Kimber, R., Leiker, S., Marrone, D., Meledin, D., Paine, S., Papa, D. C., Plante, R. J., Riddle, P., Smith, M. J., Sridharan, T. K., Tong, C. E., Wilson, R. W., Diaz, M. A., Bronfman, L., May, J., Otarola, A., and Radford, S. J. E. (2002). Prospects for Terahertz Radio Astronomy from Northern Chile. In *Thirteenth International Symposium on Space Terahertz Technology*, page 159.
- Born, M. and Wolf, E. (1989). *Principles of Optics. Electromagnetic Theory of Propagation Interference and Diffraction of Light*. Pergamon Press, sixth (corrected) edition.
- Bründermann, E., Hübers, H.-W., and Kimmitt, M. F. (2012). *Terahertz Techniques*. Springer Series in Optical Sciences.
- CCAT observatory (2014). <http://www.ccatobservatory.org/>.

- Clark, J. S. and D'Addario, L. R. (1999). *Test of Materials for use in multi-layer infrared filters in cryogenic application*. NRAO. ALMA Memo Series No. 269.
- Day, P. K., LeDuc, H. G., Mazin, B. A., Vayonakis, A., and Zmuidzinas, J. (2003). A broadband superconducting detector suitable for use in large arrays. *Nature*, 425:817–821.
- de Graauw, T., Helmich, F. P., Phillips, T. G., Stutzki, J., Caux, E., Whyborn, N. D., Dieleman, P., Roelfsema, P. R., Aarts, H., Assendorp, R., Bachiller, R., Baechtold, W., Barcia, A., Beintema, D. A., Belitsky, V., Benz, A. O., Bieber, R., Boogert, A., Borys, C., Bumble, B., Caïs, P., Caris, M., Cerulli-Irelli, P., Chattopadhyay, G., Cherednichenko, S., Ciechanowicz, M., Coeur-Joly, O., Comito, C., Cros, A., de Jonge, A., de Lange, G., Delforges, B., Delorme, Y., den Boggende, T., Desbat, J.-M., Diez-González, C., di Giorgio, A. M., Dubbeldam, L., Edwards, K., Eggens, M., Erickson, N., Evers, J., Fich, M., Finn, T., Franke, B., Gaier, T., Gal, C., Gao, J. R., Gallego, J.-D., Gauffre, S., Gill, J. J., Glenz, S., Golstein, H., Goulooze, H., Gunsing, T., Güsten, R., Hartogh, P., Hatch, W. A., Higgins, R., Honingh, E. C., Huisman, R., Jackson, B. D., Jacobs, H., Jacobs, K., Jarchow, C., Javadi, H., Jellema, W., Justen, M., Karpov, A., Kasemann, C., Kawamura, J., Keizer, G., Kester, D., Klapwijk, T. M., Klein, T., Kollberg, E., Kooi, J., Kooiman, P.-P., Kopf, B., Krause, M., Krieg, J.-M., Kramer, C., Kruizenga, B., Kuhn, T., Laauwen, W., Lai, R., Larsson, B., Leduc, H. G., Leinz, C., Lin, R. H., Liseau, R., Liu, G. S., Loose, A., López-Fernandez, I., Lord, S., Luinge, W., Marston, A., Martín-Pintado, J., Maestrini, A., Maiwald, F. W., McCoey, C., Mehdi, I., Megej, A., Melchior, M., Meinsma, L., Merkel, H., Michalska, M., Monstein, C., Moratschke, D., Morris, P., Muller, H., Murphy, J. A., Naber, A., Natale, E., Nowosielski, W., Nuzzolo, F., Olberg, M., Olbrich, M., Orfei, R., Orleanski, P., Ossenkopf, V., Peacock, T., Pearson, J. C., Peron, I., Phillip-May, S., Piazzo, L., Planesas, P., Rataj, M., Ravera, L., Risacher, C., Salez, M., Samoska, L. A., Saraceno, P., Schieder, R., Schlecht, E., Schlöder, F., Schmülling, F., Schultz, M., Schuster, K., Siebertz, O., Smit, H., Szczerba, R., Shipman, R., Steinmetz, E., Stern, J. A., Stokroos, M., Teipen, R., Teyssier, D., Tils, T., Trappe, N., van Baaren, C., van Leeuwen, B.-J., van de Stadt, H., Visser, H., Wildeman, K. J., Wafelbakker, C. K., Ward, J. S., Wesselius, P., Wild, W., Wulff, S., Wunsch, H.-J., Tielens, X., Zaal, P., Zirath, H., Zmuidzinas, J., and Zwart, F. (2010). The Herschel-Heterodyne Instrument for the Far-Infrared (HIFI). *A&A*, 518:L6.

ES&S Solutions GmbH (2014). <http://en.esskabel.de/ffc-fdc/C21>.

-
- Everest Interscience (2014). <http://www.everestinterscience.com/info/emissivitytable.htm>.
- Flynn, T. M. (2005). *Cryogenic Engineering*. Taylor & Francis, second edition, revised and expanded edition.
- Frey, H., Haefer, R. A., Eder, F. X., and Timmerhaus, K. D. (1981). *Tieftemperaturtechnologie*. VDI-Verlag.
- Gatesman, A. J., Waldman, J., Ji, M., Musante, C., and Yngvesson (2000). An anti-reflection coating for silicon optics at terahertz frequencies. *IEEE Microwave and Guided Wave Letters*, 10:264–266.
- Goldsmith, P. F. (1998). *Quasioptical Systems, Gaussian Beam Quasioptical Propagation and Applications*. IEEE Press.
- Goodfellow (2014). <http://www.goodfellow.com/>.
- Graf, U. U. (2014). Personal communication.
- Graf, U. U., Haas, S., Honingh, C. E., Jacobs, K., Schieder, R., and Stutzki, J. (1998). Array receiver development at KOSMA for the submillimeter and terahertz spectral range. In Phillips, T. G., editor, *Advanced Technology MMW, Radio, and Terahertz Telescopes*, volume 3357 of *Society of Photo-Optical Instrumentation Engineers (SPIE) Conference Series*, pages 159–166.
- Graf, U. U. and Heyminck, S. (2001). Fourier gratings as submillimeter beam splitters. *IEEE Trans. AP*, 49(4):542–546.
- Graf, U. U., Heyminck, S., Michael, E. A., Stanko, S., Honingh, C. E., Jacobs, K., Schieder, R. T., Stutzki, J., and Vowinkel, B. (2003). SMART: The KOSMA sub-millimeter array receiver for two frequencies. In Phillips, T. G. and Zmuidzinas, J., editors, *Society of Photo-Optical Instrumentation Engineers (SPIE) Conference Series*, volume 4855 of *Society of Photo-Optical Instrumentation Engineers (SPIE) Conference Series*, pages 322–329.
- Granet, C., Graeme, L. J., Bolton, R., and Moorey, G. (2004). A smooth-walled spline-profile horn as an alternative to the corrugated horn for wide band millimeter-wave applications. *IEEE Transactions on Antennas and Propagation*, 52(3):795–800.
- Griffin, M. J., Abergel, A., Abreu, A., Ade, P. A. R., André, P., Augueres, J.-L., Babbedge, T., Bae, Y., Baillie, T., Baluteau, J.-P., Barlow, M. J., Bendo, G., Benielli, D., Bock, J. J., Bonhomme, P., Brisbin, D., Brockley-Blatt, C., Caldwell, M., Cara, C., Castro-Rodriguez, N.,

Cerulli, R., Chaniel, P., Chen, S., Clark, E., Clements, D. L., Clerc, L., Coker, J., Communal, D., Conversi, L., Cox, P., Crumb, D., Cunningham, C., Daly, F., Davis, G. R., de Antoni, P., Delderfield, J., Devin, N., di Giorgio, A., Didschuns, I., Dohlen, K., Donati, M., Dowell, A., Dowell, C. D., Duband, L., Dumaye, L., Emery, R. J., Ferlet, M., Ferrand, D., Fontignie, J., Fox, M., Franceschini, A., Frerking, M., Fulton, T., Garcia, J., Gastaud, R., Gear, W. K., Glenn, J., Goizel, A., Griffin, D. K., Grundy, T., Guest, S., Guillemet, L., Hargrave, P. C., Harwit, M., Hastings, P., Hatziminaoglou, E., Herman, M., Hinde, B., Hristov, V., Huang, M., Imhof, P., Isaak, K. J., Israelsson, U., Ivison, R. J., Jennings, D., Kiernan, B., King, K. J., Lange, A. E., Latter, W., Laurent, G., Laurent, P., Leeks, S. J., Lellouch, E., Levenson, L., Li, B., Li, J., Lilienthal, J., Lim, T., Liu, S. J., Lu, N., Madden, S., Mainetti, G., Marliani, P., McKay, D., Mercier, K., Molinari, S., Morris, H., Moseley, H., Mulder, J., Mur, M., Naylor, D. A., Nguyen, H., O'Halloran, B., Oliver, S., Olofsson, G., Olofsson, H.-G., Orfei, R., Page, M. J., Pain, I., Panuzzo, P., Papageorgiou, A., Parks, G., Parr-Burman, P., Pearce, A., Pearson, C., Pérez-Fournon, I., Pinsard, F., Pisano, G., Podosek, J., Pohlen, M., Polehampton, E. T., Pouliquen, D., Rigopoulou, D., Rizzo, D., Roseboom, I. G., Roussel, H., Rowan-Robinson, M., Rownd, B., Saraceno, P., Sauvage, M., Savage, R., Savini, G., Sawyer, E., Scharnberg, C., Schmitt, D., Schneider, N., Schulz, B., Schwartz, A., Shafer, R., Shupe, D. L., Sibthorpe, B., Sidher, S., Smith, A., Smith, A. J., Smith, D., Spencer, L., Stobie, B., Sudiwala, R., Sukhatme, K., Surace, C., Stevens, J. A., Swinyard, B. M., Trichas, M., Tourette, T., Triou, H., Tseng, S., Tucker, C., Turner, A., Vaccari, M., Valtchanov, I., Vigroux, L., Virique, E., Voellmer, G., Walker, H., Ward, R., Waskett, T., Weilert, M., Wesson, R., White, G. J., Whitehouse, N., Wilson, C. D., Winter, B., Woodcraft, A. L., Wright, G. S., Xu, C. K., Zavagno, A., Zemcov, M., Zhang, L., and Zonca, E. (2010). The Herschel-SPIRE instrument and its in-flight performance. *A&A*, 518:L3.

Güsten, R., Booth, R., Cesarsky, C., Menten, K. M., Agurto, C., Anciaux, M., Azagra, F., Belitsky, V., Belloche, A., Bergman, P., De Breuck, C., Comito, C., Dumke, M., Duran, C., Esch, W., Fluxa, J., Greve, A., Hafok, H., Häupl, W., Helldner, L., Henseler, A., Heyminck, S., Johansson, L. E., Kasemann, C., Klein, B., Korn, A., Kreysa, E., Kurz, R., Lapkin, I., Leurini, S., Lis, D., Lundgren, A., Mac-Auliffe, F., Martinez, M., Melnick, J., Morris, D., Muders, D., Nyman, L. A., Olberg, M., Olivares, R., Pantaleev, M., Patel, N., Pausch, K., Philipp, S. D., Philipps, S., Sridharan, T. K., Polehampton, E., Reveret, V., Risacher, C., Roa, M., Sauer, P., Schilke, P., Santana, J., Schneider, G., Sepulveda, J., Siringo, G., Spyromilio, J., Stenvers, K.-H., van der Tak, F., Torres, D., Vanzi, L., Vassilev, V., Weiss, A., Willmeroth, K., Wunsch, A., and

- Wyrowski, F. (2006). APEX: the Atacama Pathfinder EXperiment. In *Society of Photo-Optical Instrumentation Engineers (SPIE) Conference Series*, volume 6267 of *Society of Photo-Optical Instrumentation Engineers (SPIE) Conference Series*.
- Hecht, E. (1987). *Optics*. Addison-Wesley Publishing Company, second edition edition.
- Heyminck, S. and Graf, U. U. (2001). Array-receiver LO unit using collimating fourier-gratings. In Mehdi, I., editor, *Twelfth International Symposium on Space Terahertz Technology*, pages 563–570.
- Heyminck, S., Graf, U. U., Güsten, R., Stutzki, J., Hübers, H. W., and Hartogh, P. (2012). GREAT: the SOFIA high-frequency heterodyne instrument. *A&A*, 542:L1.
- Heyminck, S., Kasemann, C., and Belitsky, V. (2004). *Interface Control Document for receivers operated in the APEX Nasmyth A Cabin*.
- Hurtado, N., Leriche, B., and Visticot, F. (2007). Spectral response in transmission at ambient temperature of candidate materials to be used in the sub-millimetric range. Technical report, Service d’Astrophysique, CEA-Saclay, France. Work done in the context of the ArTeMiS Project (a bolometer camera for APEX), and in particular of its prototype P-ArTeMiS.
- Indriolo, N., Neufeld, D. A., Gerin, M., Schilke, P., Benz, A. O., Winkel, B., Menten, K. M., Chambers, E. T., Black, J. H., Bruderer, S., Falgarone, E., Godard, B., Goicoechea, J. R., Gupta, H., Lis, D. C., Ossenkopf, V., Persson, C. M., Sonnentrucker, P., van der Tak, F. F. S., van Dishoeck, E. F., Wolfire, M. G., and Wyrowski, F. (2015). Herschel Survey of Galactic OH⁺, H₂O⁺, and H₃O⁺: Probing the Molecular Hydrogen Fraction and Cosmic-Ray Ionization Rate. *ApJ*, 800:40.
- Jin, Y., Kim, G., and Jeon, S. (2006). Terahertz dielectric properties of polymers. *Journal of the Korean Physical Society*, 49(2):513–517.
- Johansson, J. F. (1995). A comparison of some feed types. In Emerson, D. T. and Payne, J. M., editors, *Multi-Feed Systems for Radio Telescopes*, volume 75 of *Astronomical Society of the Pacific Conference Series*, page 82.
- Johansson, J. F. and Whyborn, N. D. (1992). The diagonal horn as a sub-millimeter wave antenna. *IEEE Transactions on Microwave Theory Techniques*, 40:795–800.

- Kasemann, C., Güsten, R., Heyminck, S., Klein, B., Klein, T., Philipp, S. D., Korn, A., Schneider, G., Henseler, A., Baryshev, A., and Klapwijk, T. M. (2006). CHAMP⁺: a powerful array receiver for APEX. In *Society of Photo-Optical Instrumentation Engineers (SPIE) Conference Series*, volume 6275 of *Society of Photo-Optical Instrumentation Engineers (SPIE) Conference Series*.
- Lake Shore Cryogenics, Inc. (2014). <http://www.lakeshore.com/>.
- Lamb, J. W., Baryshev, A., Carter, M. C., D'Addario, L. R., Ellison, B. N., Grammer, W., Lazareff, B., Sekimoto, Y., and Tham, C. Y. (2001). *ALMA Receiver Optics Design*. NRAO. ALMA Memo Series No. 362.
- Lee, Y. (2009). *Principles of Terahertz Science and Technology*. Springer Science+Business Media.
- Leinz, C., Caris, M., Klein, T., de Lange, G., Zijlstra, T., Klapwijk, T. M., Wunsch, H. J., and Güsten, R. (2010). A 1THz Receiver System at APEX. In *Twenty-First International Symposium on Space Terahertz Technology*, pages 130–135.
- Lienhard IV, J. H. and Lienhard V, J. H. (2008). *A heat transfer textbook*. Phlogiston Press, third edition edition.
- Lüthi, T., Rabanus, D., Graf, U. U., Granet, C., and Murk, A. (2006). Expandable fully reflective focal plane optics for millimeter- and submillimeter-wave array receivers. *Review of Scientific Instruments*, **77** 014702.
- Marquardt, E. D., Le, J. P., and Radebaugh, R. (2000). Cryogenic material properties database. In *11th International Cryocooler Conference*.
- Marrone, D. P., Battat, J., Bensch, F., Blundell, R., Diaz, M., Gibson, H., Hunter, T., Meledin, D., Paine, S., Papa, D. C., Radford, S., Smith, M., and Tong, E. (2004a). A Map of OMC-1 in CO J = 9-8. *ApJ*, 612:940–945.
- Marrone, D. P., Blundell, R., Gibson, H., Paine, S., Papa, D. C., and Tong, C.-Y. E. (2004b). Characterization and Status of a Terahertz Telescope. In Narayanan, G., editor, *Fifteenth International Symposium on Space Terahertz Technology*, page 426.
- Marrone, D. P., Blundell, R., Tong, E., Paine, S. N., Loudkov, D., Kawamura, J. H., Lühr, D., and Barrientos, C. (2005). Observations in the 1.3 and 1.5 THz Atmospheric Windows with the Receiver Lab Telescope. In *Sixteenth International Symposium on Space Terahertz Technology*, pages 64–67.

- Moore, J. H., Davis, C. C., and Coplan, M. A. (1989). *Building Scientific Apparatus. A practical guide to design and construction*. Addison Wesley, second edition.
- NIST Cryogenics (2014). <http://cryogenics.nist.gov/MPropsMAY/materialproperties.htm>.
- Orlowska, A., Harman, M., and Ellison, B. (2002). *ALMA Project Book version 5.5, Chapter 6: Receiver Cryogenic System*. <https://www.cv.nrao.edu/~demerson/almabk/construc/chap6/chap6.pdf>.
- Persson, C. M., De Luca, M., Mookerjea, B., Olofsson, A. O. H., Black, J. H., Gerin, M., Herbst, E., Bell, T. A., Coutens, A., Godard, B., Goicoechea, J. R., Hassel, G. E., Hily-Blant, P., Menten, K. M., Müller, H. S. P., Pearson, J. C., and Yu, S. (2012). Nitrogen hydrides in interstellar gas. II. Analysis of Herschel/HIFI observations towards W49N and G10.6 - 0.4 (W31C). *A&A*, 543:A145.
- Pilbratt, G. L., Riedinger, J. R., Passvogel, T., Crone, G., Doyle, D., Gageur, U., Heras, A. M., Jewell, C., Metcalfe, L., Ott, S., and Schmidt, M. (2010). Herschel Space Observatory. An ESA facility for far-infrared and submillimetre astronomy. *A&A*, 518:L1.
- Poglitsch, A., Waelkens, C., Geis, N., Feuchtgruber, H., Vandenbussche, B., Rodriguez, L., Krause, O., Renotte, E., van Hoof, C., Saraceno, P., Cepa, J., Kerschbaum, F., Agnèse, P., Ali, B., Altieri, B., Andreani, P., Augueres, J.-L., Balog, Z., Barl, L., Bauer, O. H., Belbachir, N., Benedettini, M., Billot, N., Boulade, O., Bischof, H., Blommaert, J., Callut, E., Cara, C., Cerulli, R., Cesarsky, D., Contursi, A., Creten, Y., De Meester, W., Doublier, V., Doumayrou, E., Duband, L., Exter, K., Genzel, R., Gillis, J.-M., Grözinger, U., Henning, T., Herreros, J., Huygen, R., Inguscio, M., Jakob, G., Jamar, C., Jean, C., de Jong, J., Katterloher, R., Kiss, C., Klaas, U., Lemke, D., Lutz, D., Madden, S., Marquet, B., Martignac, J., Mazy, A., Merken, P., Montfort, F., Morbidelli, L., Müller, T., Nielbock, M., Okumura, K., Orfei, R., Ottensamer, R., Pezzuto, S., Popesso, P., Putzeys, J., Regibo, S., Reveret, V., Royer, P., Sauvage, M., Schreiber, J., Stegmaier, J., Schmitt, D., Schubert, J., Sturm, E., Thiel, M., Tofani, G., Vavrek, R., Wetzstein, M., Wieprecht, E., and Wiezorrek, E. (2010). The Photodetector Array Camera and Spectrometer (PACS) on the Herschel Space Observatory. *A&A*, 518:L2.
- Pon, A., Caselli, P., Johnstone, D., Kaufman, M., Butler, M. J., Fontani, F., Jiménez-Serra, I., and Tan, J. C. (2015). Mid-J CO Shock Tracing Observations of Infrared Dark Clouds I. *A&A*, *in press*.

- PTC (2014). <http://www.ptc.com/products/>.
- Pütz, P., Jacobs, K., Justen, M., Schomaker, F., Schultz, M., Wulff, S., and Honingh, C. E. (2011). NbTiN hot electron bolometer waveguide mixers on Si₃N₄ membranes at THz frequencies. *IEEE Trans. Appl. Supercond.*, 21(3):636–639.
- Qiu, K., Wyrowski, F., Menten, K. M., Güsten, R., Leurini, S., and Leinz, C. (2011). CO (9-8) Mapping of an Extremely High Velocity and Jet-like Outflow in a High-mass Star-forming Region. *ApJ*, 743:L25.
- QMC Instruments Ltd. (2014). <http://www.terahertz.co.uk/>.
- Radebaugh, R. (2000). Pulse tube cryocoolers for cooling infrared sensors. In Andresen, B. F., Fulop, G. F., and Strojnik, M., editors, *Infrared Technology and Applications XXVI*, volume 4130 of *Society of Photo-Optical Instrumentation Engineers (SPIE) Conference Series*, pages 363–379.
- Radiometer Physics GmbH (2014). <http://www.radiometer-physics.de>.
- Rodriguez-Morales, F., Yngvesson, K. S., Gerecht, E., Wadefalk, N., Nicholson, J., Gu, D., Zhao, X., Goyette, T., and Waldman, J. (2004). A Prototype Focal Plane Array with HEB Mixer Elements and MMIC IF Amplifiers. In Narayanan, G., editor, *Fifteenth International Symposium on Space Terahertz Technology*, page 165.
- Roeser, H. P., Schmid-Burgk, J., Schwaab, G. W., and Titz, R. U. (1990). Airborne heterodyne receiver for the range 600 GHz to 3,000 GHz. In Kaldeich, B., editor, *Liege International Astrophysical Colloquia*, volume 29 of *Liege International Astrophysical Colloquia*, pages 369–373.
- RUAG Space Division (2014). http://www.ruag.com/en/Space/Space_Home.
- Schuster, K.-F., Boucher, C., Brunswig, W., Carter, M., Chenu, J.-Y., Foulieux, B., Greve, A., John, D., Lazareff, B., Navarro, S., Perrigouard, A., Pollet, J.-L., Sievers, A., Thum, C., and Wiesemeyer, H. (2004). A 230 GHz heterodyne receiver array for the IRAM 30 m telescope. *Astronomy and Astrophysics*, 423:1171–1177.
- Schwarzwälder Metallhandel GmbH (2014). <http://www.smh-metalle.de/internet/de/lagerprogramm/aluminium/aluminium.jsp>.
- Sekimoto, Y., Kamba, T., Yokogawa, S., Sugimoto, M., Okuda, T., Kandori, R., Takematsu, K., Muraoka, K., Ueda, A., Nishino, T., Okada, N., Fukuda, T., Kaneko, K., Ogawa, H., Kimura, K., Noda, K., Narasaki, K., and Suzuki, K. (2003). *Cartridge Test Cryostat for ALMA Front End*. NRAO. ALMA Memo Series No. 455.

- SHI Cryogenics Group (2014). <http://www.shicryogenics.com/>.
- Stutzki, J. (1994). Molecular cloud structure traced by submm- and far-IR spectral line observations. *Infrared Physics and Technology*, 35:493–501.
- Sugimoto, M., Sekimoto, Y., Yokogawa, S., Okuda, T., Kamba, T., Ogawa, H., Kimura, K., Nishino, T., Noda, K., and Narasaki, K. (2003). Thermal link for cartridge-type cryostat. *Cryogenics*, 43:435–439.
- Tydex Optics (2014). http://www.tydexoptics.com/en/products/thz_optics/thz_materials/.
- van der Werf, P. P., Isaak, K. G., Meijerink, R., Spaans, M., Rykala, A., Fulton, T., Loenen, A. F., Walter, F., Weiß, A., Armus, L., Fischer, J., Israel, F. P., Harris, A. I., Veilleux, S., Henkel, C., Savini, G., Lord, S., Smith, H. A., González-Alfonso, E., Naylor, D., Aalto, S., Charmandaris, V., Dasyra, K. M., Evans, A., Gao, Y., Greve, T. R., Güsten, R., Kramer, C., Martín-Pintado, J., Mazzarella, J., Papadopoulos, P. P., Sanders, D. B., Spinoglio, L., Stacey, G., Vlahakis, C., Wiedner, M. C., and Xilouris, E. M. (2010). Black hole accretion and star formation as drivers of gas excitation and chemistry in Markarian 231. *A&A*, 518:L42.
- VDI Virginia Diodes, Inc. (2014). <http://www.vadiodes.com/>.
- Verdier, J. and Locatelli, M. (1986). *Notes de cryogénie*. CEA, France. SBT/LCT/1-86 C.E.A.-C.E.N.G.-D.R.F.-S.B.T. 2nd edition.
- Verhoeve, P., Ter Meulen, J. J., Leo Meerts, W., and Dyamanus, A. (1986). Observation of the lowest rotational transition of NH⁺ with resolved hyperfine structure. *Chemical Physics Letters*, 132:213–217.
- Wagner-Gentner, A., Graf, U. U., Rabanus, D., and Jacobs, K. (2005). Low loss THz window. In *Sixteenth International Symposium on Space Terahertz Technology*, pages 360–363.
- Walmsley, C. M., Bertout, C., Combes, F., Forveille, T., and Shore, S. N. (2012). GREAT special feature. *Astronomy & Astrophysics*, 542:E1.
- Westig, M. P., Jacobs, K., Stutzki, J., Schultz, M., Justen, M., and Honingh, C. E. (2011). Balanced superconductor-insulator-superconductor mixer on a 9 μm silicon membrane. *Superconductor Science Technology*, 24(8):085012.
- Westig, M. P., Justen, M., Jacobs, K., Stutzki, J., Schultz, M., Schomacker, F., and Honingh, N. (2012). A 490 GHz planar circuit balanced Nb-Al₂O₃-Nb quasiparticle mixer for radio astronomy: Application to quantitative local oscillator noise determination. *Journal of Applied Physics*, 112(9):093919.

- Westig, M. P., Selig, S., Jacobs, K., Klapwijk, T. M., and Honingh, C. E. (2013). Improved Nb SIS devices for heterodyne mixers between 700 GHz and 1.3 THz with NbTiN transmission lines using a normal metal energy relaxation layer. *Journal of Applied Physics*, 114(12):124504.
- Wieching, G. (2006). *CONDOR: a Heterodyne Receiver for Astronomical Observations at 1.5 THz*. PhD thesis, Universität zu Kön.
- Wild, W. and Payne, J. (2002). *ALMA Project Book version 5.5, Chapter 5: ALMA Front Ends*. <https://www.cv.nrao.edu/~demerson/almabk/construct/chap5/chap5.pdf>.
- Woodcraft, A. L. (2005a). Predicting the thermal conductivity of aluminium alloys in the cryogenic to room temperature range. *Cryogenics*, 45:421–431.
- Woodcraft, A. L. (2005b). Recommended values for the thermal conductivity of aluminum of different purities in the cryogenic to room temperature range, and a comparison with copper. *Cryogenics*, 45:626–636.
- Yokogawa, S., Sekimoto, Y., Sugimoto, M., Okuda, T., Sekiguchi, T., Kamba, T., Takematsu, K., Nishino, T., Ogawa, H., Kimura, K., Noda, K., and Narasaki, K. (2003). Plug-in cryogenic system for cartridge-type SIS receivers. *Publ. Astron. Soc. Japan*, 55:519–525.
- Young, W. C. and Budynas, R. G. (2002). *Roark's Formulas for Stress and Strain*. Mc Graw Hill, seventh edition.
- Zmuidzinas, J. and Richards, P. L. (2004). Superconducting detectors and mixers for millimeter and submillimeter astrophysics. *IEEE Proceedings*, 92:1597–161.

Acronyms

<i>GBT</i>	Gaussian Beam Telescope.
ALMA	Atacama Large Millimeter Array.
AMC	Amplified Multiplier Chain.
APEX	Atacama Pathfinder Experiment.
ArTeMiS	Architectures de bolomètres pour des Télescopes à grand champs de vue dans le domaine sub-Millimétrique au Sol.
ATM	Atmospheric Transmission at Microwaves.
CAD	Computer-Aided Design.
CCAT	Cerro Chajnantor Atacama Telescope.
CH	Cold Head.
CHAMP ⁺	The Carbon Heterodyne Array of the MPIfR.
CHARM	Compact Heterodyne Array Receiver Module.
CNC	Computer Numerical Control.
CR	Cartridge of Reflected beams.
CT	Cartridge of Transmitted beams.
DC	Direct Current.
ESO	European Southern Observatory.
FFTS	Fast Fourier Transform Spectrometer.
FOV	Field of View.
FPU	Focal Plane Unit.
FTS	Fourier Transform Spectrometer.
FWHM	Full Width Half Maximum.
GM	Gifford-McMahon.
GRASP	General Reflector and Antenna Analysis Program.
GREAT	German Receiver for Astronomy at Terahertz Frequencies.

Acronyms

HDPE	High Density Polyethylene.
HEB	Superconducting Hot Electron Bolometer.
HEMT	High Electron Mobility Transistor.
HIFI	Heterodyne Instrument for the Far Infrared.
HPBW	Half Power Beam Width.
IF	Intermediate Frequency.
IR	Infrared.
ISM	Interstellar Medium.
KAO	Kuiper Airborne Observatory.
KOSMA	Köln Observatorium für SubMillimeter Astronomie.
LABOCA	Large Apex BOLometer CAmera.
LNA	Low Noise Amplifier.
LO	Local Oscillator.
MKID	Microwave Kinetic Inductance Detector.
MLI	Multi Layer Insulation.
MPIfR	Max-Planck-Institut für Radioastronomie.
NIST	National Institute of Standards and Technology.
OFHC	Oxygen Free High Conductivity Copper.
OMC	Orion Molecular Cloud.
OSO	Onsala Space Observatory.
PACS	Photodetecting Array Camera and Spectrometer.
PDR	Photon Dominated Region.
PT	Pulse Tube.
PTFE	Polytetrafluoroethylene (teflon).
PWV	Precipitable Water Vapor.
RAL	Rutherford Appleton Laboratory.
RF	astronomical signal.
RLT	Receiver Lab Telescope.
SHeFI	Swedish Heterodyne Facility Instrument.
SHI	Sumitomo Heavy Industries.
SIS	Superconductor-Isolator-Superconductor.
SMA	SubMiniature version A.
SMART	SubMillimeter Array Receiver for Two Frequencies.
SOFIA	Stratospheric Observatory For Infrared Astronomy.
SPIRE	Spectral and Photometric Imaging Receiver.

TL	Thermal Link.
TPX	Polymethylpentene.
UHMW	Ultra High Molecular Weight polyethylene.
VDI	Virginia Diodes Inc..

Acknowledgment

I would like to conclude this dissertation by expressing my gratitude to all the people that helped me and supported me during these last years.

I'm very grateful of Prof. Dr. Jürgen Stutzki for giving me the opportunity to work on this project, for all the support and advice, and for keeping his door open to any discussions and questions I had. Many thanks for the feedback on my manuscript.

Special thanks to Dr. Urs Graf for supervising my work and for all that he taught me. Many thanks for the comments on my manuscript.

I thank Henning Adams for all the work and time he invested in this project. As well as the nice talk while working in the laboratory.

I thank Bernhard Schmidt for the good disposition when I needed some wiring, sensors, etc.

I thank the Workshop for all the pieces built, specially for the complicated ones.

I thank Dr. Netty Honingh for her support and guidance when I needed it.

I would like to thank Prof. Dr. Jan Jolie and Prof. Dr. Susanne Crewel for being part of my thesis committee as second referee and chair respectively.

I'm really grateful to Dr. Markus Rölig for translating the abstract into German.

I thank Bettina Krause for all her help during these years, for making all the bureaucratic issues much easier.

To my colleagues in the green floor, thank you for the wonderful working atmosphere, for the friendly chats over lunch or in the corridors.

Thanks to the group of PhD students, Pablo, Philipp, Zoltan, Michael, Oliver, Christian, Cristian, Anika, Timo and Silke. Many good memories come to my mind. Thanks for the fun and also for the many conversations about our PhD work. I think that in some way we all supported each other. Pablo and Silke, it was great finishing this thesis at the same time as you two.

Special thanks to the Chilean crew, Pablo and Cristian, nice to be able to talk in Chilean between us, celebrate the important Chilean dates and support each other far from home.

I thank all my friends that live in different parts of the world and that no matter the distance keep in contact and are part of my life. In particular to Angela, Constanza, Marie-Hélène, Marcia, Monica, Michel, Marcelo, Nicola, Christophe, Jeanne, Sole, Camila, Ivonne, Diana, Paula and the whole "Ameba".

Many thanks to Tía Irma, the first person that put in my mind the possibility of doing a PhD. Unfortunately, you left this world already, but you live in all of us that love you. I thank you for all your support.

Special thanks to my parents Norma and Ernesto for always being there and for helping me when it was necessary.

I want to thank my son Dervan for his love and understanding (not easy to have a mom who is a PhD student!) and to Paulina, his girlfriend.

This last paragraph is dedicated to Florent, for his company, love and support. Without you, I would not have succeeded. Merci mille fois.

Financial Support

This work was supported by the Bundeministerium für Bildung und Forschung (BMBF) within the Verbundforschung Astronomie program under grant number 05A08PK2.

Erklärung

Ich versichere, dass ich die von mir vorgelegte Dissertation selbständig angefertigt, die benutzten Quellen und Hilfsmittel vollständig angegeben und die Stellen der Arbeit - einschließlich Tabellen, Karten und Abbildungen -, die anderen Werken im Wortlaut oder dem Sinn nach entnommen sind, in jedem Einzelfall als Entlehnung kenntlich gemacht habe; dass diese Dissertation noch keiner anderen Fakultät oder Universität zur Prüfung vorgelegen hat; dass sie- abgesehen von unten angegebenen Teilpublikationen - noch nicht veröffentlicht worden ist sowie, dass ich eine solche Veröffentlichung vor Abschluss des Promotionsverfahrens nicht vornehmen werde. Die Bestimmungen dieser Promotionsordnung sind mir bekannt. Die von mir vorgelegte Dissertation ist von Prof. Dr. Jürgen Stutzki betreut worden.

Köln, den 27. April 2015

Norma Hurtado

Teilpublikationen

Hurtado, N., Graf, U. U., Adams, H., Honingh, C. E., Jacobs, K., Pütz, P., Güsten, R. and Stutzki, J. 2014, "*Optics and cryogenics for the 1.1 THz multi-pixel heterodyne receiver for APEX*", Proc. SPIE, 9153, 915327

Hurtado, N., Adams, H. and Graf, U. U. 2014, "*All-metal thermal link developed for cartridge-type cryostats*", Proc. ISSTT (abstract)

Hurtado, N., Graf, U. U., Honingh, C. E., Jacobs, K., Westig, M. P., Güsten, R. and Stutzki, J. 2011, "*The 1.1 multi-pixel heterodyne receiver for APEX*", Proc. ISSTT, page 100 (abstract)

Lebenslauf

Norma Hurtado

Geburtsdatum 18. May 1964
Geburtsort Antofagasta, Chile
Staatsangehörigkeit chilenisch
E-mail norma.hurtado@gmail.com
Wohnort Sürther Str. 59
50996 Köln

Schulausbildung

08.1981 - 1982 Liceo de Niñas, Antofagasta, Chile
09.1980 - 07.1981 Dulles High School, Missouri City, Texas, USA
1978 - 08.1980 Liceo de Niñas, Antofagasta, Chile

Studium

August 2009 Beginn des Promotionsstudiums am I. Physikalischen Institut, Universität zu Köln
09.2005 - 09.2006 Master in Astronomie und Astrophysik, Université Paris XI, Frankreich
Masterarbeit: “*Preparation of a Bolometer Wide Field Imager for Ground Based Sub-millimetric Telescopes*”, Service d’Astrophysique, CEA-Saclay, Frankreich
1983 - 1990 Diplom Elektroingenieurwesen, Universidad de Chile, Santiago, Chile
1983 - 06.1988 Bachelor in Ingenieurwissenschaften, Fachrichtung Elektroingenieurwesen, Universidad de Chile, Santiago, Chile

Berufserfahrung

seit 08.2009 Wissenschaftliche Mitarbeiterin
I. Physikalischen Institut, Universität zu Köln
04.2009 - 07.2009 Projektierungsingenieur (Ingénieur d’études)
Institut d’Astrophysique Spatiale, Orsay, Frankreich
10.2006 - 01.2008 Forschungsingenieur (Ingénieur Chercheur)
Service d’Astrophysique, CEA-Saclay, Frankreich
01.2001 - 09.2005 Head of the Telescope Instrument Operators Group
Paranal Observatory, ESO - Chile
12.1998 - 2000 Telescope Instrument Operator
Paranal Observatory, ESO - Chile

- 11.1996 - 11.1998 Telescope Instrument Operator
La Silla Observatory, ESO - Chile
- 11.1993 - 10.1996 Projektmanager
Transbank S.A, Santiago, Chile
- 10.1992 - 10.1993 Telekommunikationsingenieur
Transbank S.A, Santiago, Chile
- 10.1991 - 09.1992 Vertriebsingenieur
PRAGMA S.A., Agent von IBM de Chile S.A.C.
Santiago, Chile
- 01.1991 - 09.1992 Ingenieur in der IT-Abteilung
Informatik und EDV-Service der Universidad de Chile
Santiago, Chile

Publikationsliste

- Hurtado, N., Graf, U. U., Adams, H., Honingh, C. E., Jacobs, K., Pütz, P., Güsten, R. and Stutzki, J. 2014, "*Optics and cryogenics for the 1.1 THz multi-pixel heterodyne receiver for APEX*", Proc. SPIE, 9153, 915327
- Dubreuil, D., Martignac, J., Toussaint, J. C., Visticot, F., Delisle, C., Gallais, P., Le Penneç, J., Lerch, T., André, P., Lortholary, M., Maffei, B., Haynes, V., Hurtado, N., Pisano, G., Revéret, V., Rodriguez, L. and Talvard, M. 2014, "*Optical design for the 450, 350, and 200 μm ArTeMiS camera*", Proc. SPIE, 9153, 915319
- Haynes, V., Maffei, B., Pisano, G., Dubreuil, D., Delisle, C., Le Penneç, J. and Hurtado, N. 2014, "*Spectral definition of the ArTeMiS instrument*", Proc. SPIE, 9153, 915325
- Mathys, G., Gilmozzi, R., Hurtado, N., Kaufer, A., Lidman, C. and Parra, J. 2002, "*Paranal science operations: running the four 8m unit telescopes of ESO*", Proc. SPIE, 4844, 25
- Hainaut, O. R., Meech, K. J., Bauer, J., Martin, P., Mueller, K., van de Steene, G., Hurtado, N., Miranda, J., Schubart, J., Nakano, S., Hasegawa, I. and Yeomans, D. K., 1997, "*Comet 55P/1997 E1 (Tempel-Tuttle)*", IAU Circ., 6579, 1

